



**NATIONAL TECHNICAL UNIVERSITY OF ATHENS
SCHOOL OF CIVIL ENGINEERING**

DESIGN OF CLADDING TO MITIGATE BLAST EFFECTS ON THE SUPPORTING STRUCTURE

**DOCTORAL THESIS OF
ORESTIS K. IOANNOU**

Supervised by
CHARIS J. GANTES
Professor NTUA



**Operational Programme
Human Resources Development,
Education and Lifelong Learning**
Co-financed by Greece and the European Union



This research is co-financed by Greece and the European Union (European Social Fund- ESF) through the Operational Programme «Human Resources Development, Education and Lifelong Learning» in the context of the project “Strengthening Human Resources Research Potential via Doctorate Research - 2nd Cycle” (MIS-5000432), implemented by the State Scholarships Foundation (IKY)

Athens, July 2022



ΕΘΝΙΚΟ ΜΕΤΣΟΒΙΟ ΠΟΛΥΤΕΧΝΕΙΟ
ΣΧΟΛΗ ΠΟΛΙΤΙΚΩΝ ΜΗΧΑΝΙΚΩΝ

ΣΧΕΔΙΑΣΜΟΣ ΕΠΙΚΑΛΥΨΕΩΝ ΚΤΙΡΙΩΝ
ΓΙΑ ΜΕΙΩΣΗ ΤΩΝ ΣΥΝΕΠΕΙΩΝ ΑΠΟ ΕΚΡΗΞΕΙΣ
ΣΤΟΝ ΥΠΟΚΕΙΜΕΝΟ ΦΟΡΕΑ

ΔΙΔΑΚΤΟΡΙΚΗ ΔΙΑΤΡΙΒΗ
ΟΡΕΣΤΗΣ Κ. ΙΩΑΝΝΟΥ

Επιβλέπων
ΧΑΡΗΣ Ι. ΓΑΝΤΕΣ
Καθηγητής ΕΜΠ



Ευρωπαϊκή Ένωση
Ευρωπαϊκό Κοινωνικό Ταμείο

Επιχειρησιακό Πρόγραμμα
Ανάπτυξη Ανθρώπινου Δυναμικού,
Εκπαίδευση και Διά Βίου Μάθηση

Με τη συγχρηματοδότηση της Ελλάδας και της Ευρωπαϊκής Ένωσης



Το έργο συγχρηματοδοτείται από την Ελλάδα και την Ευρωπαϊκή Ένωση (Ευρωπαϊκό Κοινωνικό Ταμείο) μέσω του Επιχειρησιακού Προγράμματος «Ανάπτυξη Ανθρώπινου Δυναμικού, Εκπαίδευση και Διά Βίου Μάθηση», στο πλαίσιο της Πράξης «Ενίσχυση του ανθρώπινου ερευνητικού δυναμικού μέσω της υλοποίησης διδακτορικής έρευνας - 2^{ος} κύκλος» (MIS-5000432), που υλοποιεί το Ίδρυμα Κρατικών Υποτροφιών (ΙΚΥ)

Αθήνα, Ιούλιος 2022



**NATIONAL TECHNICAL UNIVERSITY OF ATHENS
SCHOOL OF CIVIL ENGINEERING**

**DESIGN OF CLADDING
TO MITIGATE BLAST EFFECTS
ON THE SUPPORTING STRUCTURE**

**DOCTORAL THESIS OF
ORESTIS K. IOANNOU**

Diploma in Civil Engineering, Aristotle University of Thessaloniki (2015)

MSc in Analysis and Design of Structures, National Technical University of Athens (2017)

The thesis is submitted to the School of Civil Engineering
of the National Technical University of Athens
in fulfilment of the requirements for the Degree of Doctor of Philosophy

ADVISORY COMMITTEE:

1. C. GANTES, Professor NTUA (supervisor)
2. N. LAGAROS, Professor NTUA
3. D. VAMVATSIKOS, Associate Professor NTUA

EXAMINATION COMMITTEE:

1. C. GANTES, Professor NTUA (supervisor)
2. N. LAGAROS, Professor NTUA
3. D. VAMVATSIKOS, Associate Professor NTUA
4. C.A. ZERIS, Professor NTUA
5. K.D. TSAVDARIDIS, Professor City University, UK
6. H. MOUZAKIS, Associate Professor NTUA
7. V. KARLOS, Scientific Project Officer JRC, Italy

Athens, July 2022

© Copyright 2022 by Orestis K. Ioannou
All Rights Reserved

Neither the whole nor any part of this doctoral thesis may be copied, stored in a retrieval system, distributed, reproduced, translated, or transmitted for commercial purposes, in any form or by any means now or hereafter known, electronic or mechanical, without the written permission from the author. Reproducing, storing and distributing this doctoral thesis for non-profitable, educational or research purposes is allowed, without prejudice to reference to its source and to inclusion of the present text. Any queries in relation to the use of the present doctoral thesis for commercial purposes must be addressed to its author.

Approval of this doctoral thesis by the School of Civil Engineering of the National Technical University of Athens (NTUA) does not constitute in any way an acceptance of the views of the author contained herein by the said academic organization (L. 5343/1932, art. 202).



ΕΘΝΙΚΟ ΜΕΤΣΟΒΙΟ ΠΟΛΥΤΕΧΝΕΙΟ
ΣΧΟΛΗ ΠΟΛΙΤΙΚΩΝ ΜΗΧΑΝΙΚΩΝ

ΣΧΕΔΙΑΣΜΟΣ ΕΠΙΚΑΛΥΨΕΩΝ ΚΤΙΡΙΩΝ
ΓΙΑ ΜΕΙΩΣΗ ΤΩΝ ΣΥΝΕΠΕΙΩΝ ΑΠΟ ΕΚΡΗΞΕΙΣ
ΣΤΟΝ ΥΠΟΚΕΙΜΕΝΟ ΦΟΡΕΑ

ΔΙΔΑΚΤΟΡΙΚΗ ΔΙΑΤΡΙΒΗ
ΟΡΕΣΤΗΣ Κ. ΙΩΑΝΝΟΥ

Δίπλωμα Πολιτικού Μηχανικού, Αριστοτέλειο Πανεπιστήμιο Θεσσαλονίκης (2015)

Μεταπτυχιακό Δίπλωμα Ειδίκευσης, Εθνικό Μετσόβιο Πολυτεχνείο (2017)

Η διατριβή υποβλήθηκε στη Σχολή Πολιτικών Μηχανικών του Εθνικού Μετσόβιου Πολυτεχνείου προς εκπλήρωση των προϋποθέσεων του τίτλου του Διδάκτορος Μηχανικού

ΤΡΙΜΕΛΗΣ ΣΥΜΒΟΥΛΕΥΤΙΚΗ ΕΠΙΤΡΟΠΗ:

1. Χ. ΓΑΝΤΕΣ, Καθηγητής ΕΜΠ (επιβλέπων)
2. Ν. ΛΑΓΑΡΟΣ, Καθηγητής ΕΜΠ
3. Δ. ΒΑΜΒΑΤΣΙΚΟΣ, Αν. Καθηγητής ΕΜΠ

ΕΠΤΑΜΕΛΗΣ ΕΞΕΤΑΣΤΙΚΗ ΕΠΙΤΡΟΠΗ:

1. Χ. ΓΑΝΤΕΣ, Καθηγητής ΕΜΠ (επιβλέπων)
2. Ν. ΛΑΓΑΡΟΣ, Καθηγητής ΕΜΠ
3. Δ. ΒΑΜΒΑΤΣΙΚΟΣ, Αν. Καθηγητής ΕΜΠ
4. Χ. ΖΕΡΗΣ, Καθηγητής ΕΜΠ
5. Κ.Δ. ΤΣΑΒΔΑΡΙΔΗΣ, Καθηγητής City University, Αγγλία
6. Χ. ΜΟΥΖΑΚΗΣ, Αν. Καθηγητής ΕΜΠ
7. Β. ΚΑΡΛΟΣ, Scientific Project Officer JRC, Ιταλία

Αθήνα, Ιούλιος 2022

© Copyright 2022 by Ορέστης Κ. Ιωάννου

Με επιφύλαξη παντός δικαιώματος

Απαγορεύεται η αντιγραφή, αποθήκευση σε αρχείο πληροφοριών, διανομή, αναπαραγωγή, μετάφραση ή μετάδοση της παρούσας εργασίας, εξ ολοκλήρου ή τμήματος αυτής, για εμπορικό σκοπό, υπό οποιαδήποτε μορφή και με οποιοδήποτε μέσο επικοινωνίας, ηλεκτρονικό ή μηχανικό, χωρίς την προηγούμενη έγγραφη άδεια του συγγραφέα. Επιτρέπεται η αναπαραγωγή, αποθήκευση και διανομή για σκοπό μη κερδοσκοπικό, εκπαιδευτικής ή ερευνητικής φύσης, υπό την προϋπόθεση να αναφέρεται η πηγή προέλευσης και να διατηρείται το παρόν μήνυμα. Ερωτήματα που αφορούν στη χρήση της εργασίας για κερδοσκοπικό σκοπό πρέπει να απευθύνονται προς το συγγραφέα.

Η έγκριση της διδακτορικής διατριβής από την Ανώτατη Σχολή Πολιτικών Μηχανικών του Εθνικού Μετσόβιου Πολυτεχνείου δεν υποδηλώνει αποδοχή των απόψεων του συγγραφέως (Ν. 5343/1932, Άρθρο 202).

Acknowledgments

My doctoral studies were by far the hardest thing I had to do in my life. It is a bit heavy to start my acknowledgments section with such a statement, isn't it? Let me rephrase, my doctoral studies were absolutely fantastic! A typical thing I used to say all this time was that if, instead of my PhD research, I enrolled on two masters each year of my studies, then I would end up with ten masters and it would still be an easier thing to do. Yes, I admit it, I am bit grouchy... My father always told me that (from zero years old).

Fortunately, my academic advisor, Professor Charis Gantes, was also my psychologist. The amount of time that he spent every week on my scientific guidance was enormous. It would be impossible to finish my research without his continuous assistance and endless support. Mr. Gantes thanks a million, you are the best!

I would also like to express my deepest appreciation to the other members of my doctoral thesis committee, Professor Nikos Lagaros and Associate Professor Dimitris Vamvatsikos. Our interaction has always been inspirational and fruitful. Their unwavering enthusiasm for civil engineering, as emerged through our discussions and their papers, kept me constantly focused on my research.

My sincere gratitude to my research buddy Michalis Hadjioannou, who lives halfway across the world and is a fellow countryman (Cyprus <3 | Θέκκιο!). Michalis you can't imagine how grateful I am for your help, time and constant assistance throughout my PhD studies. You are wonderful and deserve the best.

The capstone of my studies was the experimental test, which took place in May 2021. My gratitude is expressed to Mr. Papavasileiou, who was there for me all the way through and made it possible. Three distinct parties were involved, each one playing a crucial role in the process: (1) The army team; (2) The fabricator team; (3) The research team. I am extremely thankful to all the participants. Without all of them, we would not be able to make it:

Mr. Petrakis
*Land Minefield Clearance and
EOD Battalion*

Mr. Adamopoulos
*Engineer Officers'
Technical School*

Mr. Krikelis
*Land Minefield Clearance and
EOD Battalion*

Mr. Gkologiannis
*Design & Application
Engineers SA*

Mr. Dimitriou
*Kataskevastiki
J. Dimitriou*

Mrs. Orologopoulou
*Armos
Precast SA*

Mr. Lignos
*Institute of
Steel Structures*

Mr. Katsatsidis
*Institute of
Steel Structures*

Mr. Spiliopoulos
*Institute of
Steel Structures*

Last but not least, lots of thanks to my fiancée, family, colleagues and friends for their constant support and beneficial discussions during this journey. Moral of the story: Life is good and the best is yet to come...

Orestis Ioannou,
Athens, Wednesday, May 25th, 2022

For the experimental investigation of the response of steel cladding subjected to blast loading, which was conducted by NTUA's Institute of Steel Structures, the explosions were performed by the Land Minefield Clearance and EOD Battalion in the context of the memorandum of cooperation between the National Technical University of Athens (NTUA) and the Engineer Officers' Technical School (EOTS) of the Greek Army. Sponsors and fabricators of the experimental setup were the companies Armos Precast SA (precast reinforced concrete ground slab) and Kataskevastiki J. Dimitriou (steel cladding specimens, main steel support structure). Their support is gratefully acknowledged.

*to my parents,
Kostas and Eleni*



National Technical University of Athens
School of Civil Engineering

Doctoral Thesis of Orestis K. Ioannou

Design of cladding to mitigate blast effects on the supporting structure

Supervisor: Professor Charis J. Gantes
Athens, July 2022

Abstract

The main aim of this doctoral thesis is to gain insight into the role of building cladding to mitigate blast effects on the supporting structure. This can be achieved by utilizing two different mechanisms, i.e., the mechanism of inertial resistance and the mechanism of plastic energy absorption, which, if properly exploited, may lead to the same result. More specifically, the initial blast load profile on the cladding is converted from a high-amplitude and short-duration time history into a lower-amplitude and longer-duration time history of the dynamic reactions of the cladding that are transferred to the supporting structure. In this way, the load demand on the supporting structure is decreased, thus reducing its deflections, increasing the chances of maintaining its integrity, achieving life safety, and limiting damages. The mechanism of inertial resistance is activated through increased mass and decreased stiffness in the cladding, while the mechanism of plastic energy absorption is activated through plastic strains in the cladding.

In this context, a combined numerical, analytical and experimental investigation of the capacity of cladding to mitigate blast effects is performed. The investigation is conducted along four distinct lines of action. In the first one, the influence of cladding mass, stiffness, ultimate resistance and ductility on the supporting structure is theoretically explored. In the second, the influence of cladding membrane action on the supporting structure is researched. Next, the results of the theoretical investigation are verified with the experimental investigation of two steel cladding types and the respective numerical models are validated. Finally, a methodology is proposed for the calculation of the potential of any cladding to mitigate blast effects on the supporting structure, when subjected to a variety of blast loadings.

Hence, the originality of the doctoral thesis and its contribution to the advancement of engineering practice is multilevel. More specifically, novel scientific conclusions are extracted and guidelines for structural engineers are formulated about the properties that cladding should have in order to offer increased mitigation potential capabilities. The above are initially verified with an experimental investigation of two steel cladding-to-girt systems. The relevant numerical models are validated on the basis of experimental results, and guidelines for the preparation of proper, detailed numerical models regarding blast loading are presented. Finally, a methodology is developed for the direct comparison of different cladding types, in order to estimate their strength characteristics and mitigation potential capacity of the blast effects on the supporting structure.



Εθνικό Μετσόβιο Πολυτεχνείο
Σχολή Πολιτικών Μηχανικών

Διδακτορική Διατριβή Ορέστη Κ. Ιωάννου

Σχεδιασμός επικαλύψεων κτιρίων για μείωση των συνεπειών από εκρήξεις στον υποκείμενο φορέα

Επιβλέπων: Καθηγητής Χάρης Ι. Γαντές
Αθήνα, Ιούλιος 2022

Περίληψη

Αντικείμενο της παρούσας διδακτορικής διατριβής αποτελεί η διερεύνηση της δυνατότητας των στοιχείων επικάλυψης των κατασκευών να μειώνουν τις συνέπειες εκρήξεων στον υποκείμενο φορέα. Αυτή η δυνατότητα της επικάλυψης μπορεί να πραγματοποιείται μέσω δύο ξεχωριστών μηχανισμών, οι οποίοι, εφόσον αξιοποιηθούν κατάλληλα, μπορούν να οδηγήσουν σε κοινό αποτέλεσμα. Πρόκειται για τον μηχανισμό αδρανειακής αντίστασης και τον μηχανισμό πλαστικής απορρόφησης ενέργειας. Πιο συγκεκριμένα, η ιστορία της ασκούμενης πίεσης επί της επικάλυψης μετατρέπεται από υψηλής τιμής και σύντομης διάρκειας σε μια χαμηλότερης τιμής και μεγαλύτερης διάρκειας ιστορία των αντιδράσεων στήριξης της επικάλυψης, οι οποίες αποτελούν φορτία επί του υποκείμενου φορέα. Με αυτόν τον τρόπο, μειώνεται η απαίτηση στον υποκείμενο φορέα και, άρα, μειώνονται οι παραμορφώσεις του, και αυξάνονται οι πιθανότητες διατήρησης της ακεραιότητάς του, διασφάλισης της προστασίας της ανθρώπινης ζωής, και περιορισμού των βλαβών. Ο μηχανισμός αδρανειακής αντίστασης ενεργοποιείται μέσω αυξημένης μάζας και μειωμένης δυσκαμψίας της επικάλυψης, ενώ ο μηχανισμός πλαστικής απορρόφησης ενέργειας ενεργοποιείται μέσω πλαστικών παραμορφώσεων της επικάλυψης.

Για τον σκοπό αυτό, πραγματοποιείται συνδυασμός αριθμητικής, αναλυτικής και πειραματικής διερεύνησης αυτών των δυνατοτήτων των στοιχείων επικάλυψης. Η διερεύνηση γίνεται σε τέσσερις διακριτούς άξονες. Στον πρώτο άξονα αναζητείται θεωρητικά ο τρόπος επιρροής της επικάλυψης μέσω των δύο μηχανισμών και των ζωνών ενεργοποίησής τους, καθώς και της συμβολής της μάζας, της δυσκαμψίας, της αντίστασης και της ολκιμότητας. Στη συνέχεια αναζητείται θεωρητικά ο τρόπος επιρροής της μεμβρανικής λειτουργίας της επικάλυψης στη συμπεριφορά του υποκείμενου φορέα. Στον τρίτο άξονα επιβεβαιώνονται τα θεωρητικά συμπεράσματα μέσω πειραματικής διερεύνησης σε δύο τύπους επικάλυψης από δομικό χάλυβα και πιστοποιούνται τα αποτελέσματα των αριθμητικών προσομοιωμάτων. Τελικά, προτείνεται μεθοδολογία μέσω της οποίας μπορεί να υπολογιστεί η δυνατότητα μιας επικάλυψης να οδηγεί σε μείωση των συνεπειών έκρηξης στον υποκείμενο φορέα.

Επομένως, η πρωτοτυπία της διατριβής και η συμβολή της στην επαγγελματική πρακτική είναι πολυεπίπεδη. Προκύπτουν πρωτότυπα επιστημονικά συμπεράσματα που μετουσιώνονται σε τεχνικές οδηγίες προς τους μηχανικούς, όσον αφορά στις ιδιότητες που πρέπει να έχει η επικάλυψη για την επίτευξη του στόχου μείωσης των συνεπειών έκρηξεων. Τα παραπάνω επιβεβαιώνονται αρχικά μέσω της πειραματικής διερεύνησης δύο συστημάτων επικάλυψης-υποκείμενου φορέα. Με βάση τα πειραματικά αποτελέσματα, πιστοποιούνται αντίστοιχα αριθμητικά προσομοιώματα και διατυπώνονται οδηγίες σύνταξης

αριθμητικών προσομοιωμάτων έναντι έκρηξης. Τέλος, διατυπώνεται μεθοδολογία για τη συγκριτική ανάλυση διαφόρων ειδών επικάλυψης έναντι έκρηξης, προκειμένου να διαπιστωθεί η ικανότητά τους για μείωση των συνεπειών στον υποκείμενο φορέα.

Table of contents

List of figures	v
List of tables	xi
Notation	xiii
Chapter 1 Introduction	1
1.1. Background	1
1.2. Blast resistant cladding	5
1.3. Problem statement and objective	7
1.4. Outline of thesis	8
1.5. References.....	9
Chapter 2 Blast loading and structural response	11
2.1. Introduction	11
2.2. Blast loading.....	12
2.2.1. Pressure–time profile	12
2.2.2. Blast wave parameters.....	14
2.2.3. Blast loading over buildings	16
2.3. Structural response	19
2.3.1. Analysis of an elastic SDOF	20
2.3.2. Analysis of an elastic-perfectly plastic SDOF.....	22
2.3.3. Strain-rate effects	22
2.3.4. Response limits	23
2.4. Conclusions.....	25
2.5. References.....	25
Chapter 3 Mechanisms for cladding mitigation potential and literature review	27
3.1. Introduction	27
3.2. Philosophy of cladding design	27
3.3. Cladding response to blast loading.....	28
3.4. Activated mechanisms for cladding mitigation potential	29
3.5. Literature findings about cladding with mitigation potential	32
3.5.1. Cladding-to-framing.....	32
3.5.2. Sacrificial cladding.....	35
3.5.3. Energy-absorbing connectors	37
3.6. Conclusions.....	37
3.7. References.....	37

Chapter 4	Influence of cladding mass, stiffness, ultimate resistance and ductility ...	41
4.1.	Introduction.....	41
4.2.	Proposed 2DOF model and response regimes.....	42
4.2.1.	Derivation of equations of motion and applied blast loading	42
4.2.2.	Mapping the properties of the cladding–supporting structure system in the 2DOF model	45
4.2.3.	Assumptions and limitations	45
4.3.	Analysis methodology	46
4.4.	Validation of the 2DOF model	46
4.4.1.	Validation of the 2DOF model with detailed finite element analysis results of a cladding-to-framing system.....	46
4.4.2.	Validation of the 2DOF model with experimental and analytical results of sacrificial cladding.....	51
4.5.	Results of the 2DOF model response to blast loading.....	52
4.5.1.	Effects of cladding ultimate resistance on the supporting structure	52
4.5.2.	Effects of cladding ductility on the supporting structure	55
4.5.3.	Effects of cladding mass and stiffness on the supporting structure	56
4.5.4.	The special case of similar natural periods	57
4.6.	Interpretation of the 2DOF results and design remarks	59
4.7.	Conclusions	61
4.8.	References	61
Chapter 5	Influence of cladding membrane action	65
5.1.	Introduction.....	65
5.2.	Dimensionless SDOF analysis.....	66
5.2.1.	Derivation of equations of motion	66
5.2.2.	Assumptions and limitations	69
5.3.	Influence of cladding with both bending and membrane stiffness	69
5.4.	Influence of cladding as a membrane structure	74
5.5.	Case study	75
5.6.	Conclusions.....	80
5.7.	References	82
Chapter 6	Experimental investigation	85
6.1.	Introduction.....	85
6.2.	Description of the experimental setup and instrumentation	86
6.2.1.	Description of the reacting frame.....	86
6.2.2.	Instrumentation	86
6.2.3.	Field configuration of the experimental setup.....	89
6.2.4.	Explosive charge weight.....	90
6.3.	Description of the test specimens	90

6.3.1. Specimen geometry	90
6.3.2. Specimen design	91
6.3.3. Material properties	92
6.4. Experimental test results	93
6.5. Numerical modeling	95
6.5.1. Description of analysis models	95
6.5.2. Material models	96
6.5.3. Blast load simulation	96
6.5.4. Extension of the analysis with an elastic model	99
6.6. Interpretation of the results	99
6.7. Conclusions	100
6.8. Acknowledgements	101
6.9. References	102
Chapter 7 Evaluation of mitigation potential	105
7.1. Introduction	105
7.2. Characteristics of cladding response to blast loads	106
7.3. Description of the proposed methodology	107
7.3.1. Implementation	107
7.3.2. Assumptions and limitations	111
7.4. Case study	112
7.4.1. Cladding description	112
7.4.2. Finite element models of claddings	112
7.4.3. Step 1: Calculation of the pressure–impulse diagrams	114
7.4.4. Step 2: Calculation of the dynamic reaction time histories	117
7.4.5. Step 3: Calculation of the response of the supporting structure	118
7.4.6. Step 4: Calculation of the mitigation potential at each natural period and for each reaction time history	119
7.4.7. Step 5: Calculation of the mitigation potential over a range of selected natural periods of the supporting structure	119
7.4.8. Step 6: Addition of the mitigation potential values to the pressure–impulse diagrams	120
7.4.9. Discussion of the results	120
7.5. Conclusions	122
7.6. References	123
Chapter 8 Conclusions	127
8.1. Summary	127
8.2. Concluding remarks	129
8.3. Research contribution	130
8.4. Suggestions for future research	130

8.5. References	131
Appendix A Code fragments	133
A1. Matlab code for SDOF	133
A2. Matlab code for 2DOF	137
A3. Matlab code for dimensionless SDOF.....	140
Appendix B Extended summary (in Greek).....	149
B1. Εισαγωγή.....	149
B2. Μηχανισμοί λειτουργίας και βιβλιογραφική επισκόπηση.....	151
B3. Επιρροή της μάζας, δυσκαμψίας, αντοχής και ολκιμότητας της επικάλυψης	155
B4. Επιρροή της μεμβρανικής δράσης της επικάλυψης	161
B5. Πειραματική διερεύνηση μεταλλικής επικάλυψης σε έκρηξη.....	163
B6. Μεθοδολογία εκτίμησης της ικανότητας της επικάλυψης για μείωση των συνεπειών από έκρηξη.....	167
B7. Σύνοψη και συμπεράσματα.....	170
B8. Πρωτότυπη συμβολή και προτάσεις για περαιτέρω έρευνα	170
B9. Βιβλιογραφία	171

List of figures

Figure 1-1: Explosion at the Alfred P. Murrah Federal Building [reprinted from FEMA (1996)]: (a) Photo before the explosion; (b) Photo after the explosion; (c) Damage induced to the front side of the building; (d) Damage induced to the surrounding buildings	2
Figure 1-2: Location of explosions with regard to the Khobar Towers [reprinted from Grant (1998)]	2
Figure 1-3: Damages from the explosions in the Tianjin Harbour [reprinted from Yu et al. (2022)]: (a) Map of overpressure and damages; (b) Damages at 200 m; (c) Damages at 300 m; (d) Damages at 400 m; (e) Damages at 500 m; (f) Damages at 1000 m	3
Figure 1-4: Damage around the Port of Beirut after the explosion [reprinted from Sivaraman and Varadharajan (2021)]	4
Figure 1-5: Global aggressor attacks from 2000 to 2014 [reprinted from IEP (2015)]	4
Figure 1-6: USA aggressor attacks from 1994 to 2020 by threat type [reprinted from Jones and Doxsee (2020)]: (a) Right-wing aggressor attacks; (b) Left-wing aggressor attacks; (c) Religious aggressor attacks	4
Figure 1-7: Failures in the Beirut explosion [reprinted from Lekkas et al. (2020)]: (a) Metal sheets; (b) Masonry walls	5
Figure 1-8: Blast-resistant cladding manufactured with the use of innovative materials: (a) High-strength sandwich panel [reprinted from Foamtech Global (2021)]; (b) Aluminium-foam blast-resistant product [reprinted from Foamtech Global (2021)]; (c) FRP and CFRP panels with closed-cell aluminium foam [reprinted from Beihai Composite Materials Co. Ltd. (2021)]; (d) Stone bonded to a honeycomb matrix [reprinted from StonePly Co. (2022)]	6
Figure 1-9: Innovative core layouts for blast-resistant cladding [reprinted from Fleck and Deshpande (2004)]	6
Figure 2-1: Detonation pressure time history	12
Figure 2-2: Deflagration pressure time history	12
Figure 2-3: Equivalent triangle of detonation pressure time history	13
Figure 2-4: Equivalent triangle of deflagration pressure time history	13

Figure 2-5: Pressure time histories for close-in, mid-field range and far-field range detonations.....	14
Figure 2-6: Incident pressure and reflected pressure magnitude with regard to distance	14
Figure 2-7: Positive-phase parameters of a spherical detonation (DoD, 2008)	15
Figure 2-8: Positive-phase parameters of a hemispherical detonation (DoD, 2008)	16
Figure 2-9: Negative-phase parameters of a spherical detonation (DoD, 2008).....	17
Figure 2-10: Negative-phase parameters of a hemispherical detonation (DoD, 2008).....	18
Figure 2-11: Effect of angle of incidence on the reflection coefficient (DoD, 2002)	18
Figure 2-12: Blast loading on a rectangular-in-plan structure	19
Figure 2-13: SDOF model and blast loading	20
Figure 2-14: Response of an elastic SDOF subjected to blast loading:	
(a) Quasi-static response;	
(b) Impulsive response;	
(c) Dynamic response	21
Figure 2-15: DLF of an elastic SDOF subjected to a triangular detonation blast loading	22
Figure 2-16: Ductility of an elastic-perfectly plastic SDOF subjected to triangular detonation blast loading (Biggs, 1964)	23
Figure 2-17: Ductility of an elastic-perfectly plastic SDOF subjected to triangular deflagration blast loading (Biggs, 1964)	24
Figure 3-1: Typical quasi-static load (P) versus deflection (δ) curves for different cladding types:	
(a) Steel sandwich panels with clamped supports [data from Xue and Hutchinson (2004)];	
(b) Monolithic steel plate with clamped supports [data from Xue and Hutchinson (2004)];	
(c) Steel sandwich panels with insignificant membrane action [data from Khalifa, Tait and El-Dakhkhni (2017)];	
(d) Concrete panels with clamped supports [data from Gouverneur, Caspee and Taerwe (2013)];	
(e) Concrete panels with insignificant membrane action [data from Gouverneur, Caspee and Taerwe (2013)];	
(f) Laminated glass [data from Zobec et al. (2015)]	29
Figure 3-2: Typical response of steel cladding subjected to blast loading:	
(a) Reaction time history;	
(b) Power Spectral Density	30
Figure 3-3: Types of response in terms of the DLF and the t_d/T ratio in an elastic SDOF	31
Figure 3-4: Qualitative illustration of reaction time histories of the cladding with two different governing response mechanisms; the plastic energy absorption and the inertial resistance	31
Figure 3-5: Plastic energy dissipation of four different sandwich panel types [reprinted from Xue and Hutchinson (2004)].....	33
Figure 3-6: Schematic section diagram of typical curved panels [reprinted from Chen and Hao (2012)]	33
Figure 3-7: Schematic diagram of rotational hinge devices with spring incorporated in the sandwich panels [reprinted from Chen and Hao (2013)]	33
Figure 3-8: Model of the cladding and its supporting structure [reprinted from Hoffmeister et al. (2015)]	34
Figure 3-9: Stiffener configurations of rectangular plates subjected to blast loading [reprinted from Goel, Matsagar and Gupta (2011)].....	34

Figure 3-10: Calculation model of an hexagonal sandwich panel [reprinted from Sun et al. (2019)].....	35
Figure 3-11: Sacrificial cladding with Y-frame formulation [reprinted from Guruprasad and Mukherjee (2000)].....	35
Figure 3-12: Core topologies: diamond folded, Y-frame folded, triangular folded, hexagonal honeycomb, square honeycomb, triangular honeycomb [reprinted from (Alberdi, Przywara and Khandelwal (2013))].....	36
Figure 3-13: Concept of proposed sacrificial cladding with empty recyclable beverage cans [reprinted from Palanivelu et al. (2011)].....	36
Figure 3-14: Conceptual placement of energy-absorbing connection in building [reprinted from Oswald (2018)].....	37
Figure 4-1: Representation of the 2DOF model: (a) Notation of the applied mass, stiffness, ultimate resistance and displacement parameters; (b) Force–displacement diagram of the spring connecting mass m_1 (cladding) to mass m_2 (supporting structure)	43
Figure 4-2: Typical and equivalent pressure–time profile for blast wave passing through a fixed point in space	44
Figure 4-3: Cladding-to-framing geometry and numerical model.....	47
Figure 4-4: Material model for S355 steel	48
Figure 4-5: Equivalent triangular pressure time history for the numerical and the 2DOF model.....	48
Figure 4-6: Results of the numerical model when subjected to the pressure time history: (a) Vertical displacements; (b) Plastic strains	49
Figure 4-7: Computed response with 2DOF and finite element model: (a) Comparison of the finite element model with the 2DOF model; (b) Comparison of the finite element model with alternatives A and B.....	50
Figure 4-8: Representation of the PU sacrificial cladding model: (a) Experimental set-up [data from Ousji et al. (2017)]; (b) Equivalent 2DOF model as considered in the present study	51
Figure 4-9: Reaction force time history between the second DOF and the main structure in the experimental tests [reprinted from (Ousji et al., 2017)] and the 2DOF model.....	52
Figure 4-10: Front plate displacement time history in the experimental tests [reprinted from (Ousji et al., 2017)], the analytical approaches [reprinted from (Ousji et al., 2017)] and the 2DOF model.....	53
Figure 4-11: Supporting structure DLF_2 for mass ratios $m_2/m_1 = 0.1, 1.0$, for resistance ratios $R_u/P_o = 0.1 - 2.0$ (black curve represents the $R_u/P_o = 2.0$ curve) and typical stiffness ratios k_2/k_1	54
Figure 4-12: Supporting structure DLF_2 for mass ratios $m_2/m_1 = 10.0, 100.0$, for resistance ratios $R_u/P_o = 0.1 - 2.0$ (black curve represents the $R_u/P_o = 2.0$ curve) and typical stiffness ratios k_2/k_1	55
Figure 4-13: Achieved ductility of the cladding for $m_2/m_1 = 1.0$, $k_2/k_1 = 10.0$ and $R_u/P_o = 0.1 - 2.0$	56
Figure 4-14: Supporting structure DLF_2 for typical mass and stiffness ratios corresponding to resistance ratio $R_u/P_o = 2$	58
Figure 4-15: $R_u/P_o = 2$ curves when cladding and its supporting structure are in dynamic interaction	58
Figure 4-16: Limits and activation zones of the mechanisms of plastic energy absorption and inertial resistance.....	60

Figure 5-1: Dimensionless SDOF analysis:	
(a) Pressure time profile for blast loading;	
(b) Two step SDOF analysis	66
Figure 5-2: Force–displacement diagram of cladding with both bending and membrane stiffness	67
Figure 5-3: Force–displacement diagram of cladding at multiple membrane stiffness ratios ($k_{1,3}/k_{1,1} = 0.10, 0.25, 0.50, 0.75, 1.00, 2.00$)	70
Figure 5-4: DLF_2 of supporting structure for typical mass, bending stiffness, and membrane stiffness arrangements ($m_2/m_1 = 0.1, 1.0, k_2/k_{1,1} = 10.0, 100.0,$ and $k_{1,3}/k_{1,1} = 0.1, 0.5, 1.0$) at resistance ratios $R_u/P_o = 0.1, 1.0, 2.0$	71
Figure 5-5: DLF_2 of supporting structure for typical mass, bending stiffness, and membrane stiffness arrangements ($m_2/m_1 = 0.1, 1.0, k_2/k_{1,1} = 10.0, 100.0,$ and $k_{1,3}/k_{1,1} = 0.1, 0.5, 1.0$) at resistance ratios $R_u/P_o = 0.5, 1.5, 2.0$	72
Figure 5-6: DLF_2 of supporting structure for mass ratio $m_2/m_1 = 0.1$, bending stiffness ratio $k_2/k_{1,1} = 10.0$, and various membrane stiffness ratios ($k_{1,3}/k_{1,1} = 0.10, 0.25,$ 0.50, 0.75, 1.00, 2.00) at resistance ratios $R_u/P_o = 0.1, 0.5, 1.0, 1.5$	73
Figure 5-7: DLF_2 of supporting structure when cladding is considered to be a membrane structure with $k_{1,3}/k_{1,1} = 1.0, 2.0$ at mass ratios $m_2/m_1 = 0.1, 1.0$ and bending stiffness ratios $k_2/k_{1,1} = 10.0, 100.0$	74
Figure 5-8: Geometry of the trapezoidal sheet considered in the case study	75
Figure 5-9: Static pressure–displacement curve (resistance curve) of the trapezoidal sheet considered in the case study.....	76
Figure 5-10: 3D view of the cladding-to-column arrangement that was implemented in the case study	77
Figure 5-11: Combinations of maximum blast pressure and positive phase duration applied to the cladding of the case study.....	77
Figure 5-12: Two-step SDOF analysis and numerical model results of the case study (a) cladding and (b) columns, when subjected to maximum blast pressure of 200 kPa and positive phase duration of 15 ms	79
Figure 5-13: Meshing and results of the case study numerical model when cladding is subjected to 200 kPa maximum blast pressure and 1500 kPa ms impulse (15 ms positive phase duration)	80
Figure 5-14: Numerical-model transverse displacements of the case-study cladding and column at increasing positive phase duration	81
Figure 6-1: Views of the experimental setup:	
(a) 3D view;	
(b) Plan view;	
(c) Front view;	
(d) Side view.....	87
Figure 6-2: Displacement "comb" devices for the measurement of maximum transient deflection:	
(a) Experimental-setup location of the devices in plan;	
(b) 3D view of the devices' fastening points below the experimental setup;	
(c) Geometry of the devices;	
(d) Photo of the devices before their fastening	88
Figure 6-3: Installation of the prefabricated experimental setup in the pit.....	89
Figure 6-4: Wooden strips for volume relief below the experimental setup	89
Figure 6-5: View of the experimental setup prior to the detonation.....	90
Figure 6-6: Views of the two specimens sA and sB	91
Figure 6-7: Static pressure–displacement curves of the two cladding types	91
Figure 6-8: Tensile tests in the laboratory:	

(a) Specimen in Universal Testing Machine (UTM);	
(b) Specimens after the tensile test	92
Figure 6-9: Snapshot of explosion.....	93
Figure 6-10: Photo of the specimens after the explosion.....	94
Figure 6-11: Displacement device, before and after the explosion.....	94
Figure 6-12: Permanent deflections after the explosion:	
(a) Visual representation of the deflection of the central girt of the panel with stiffeners;	
(b) Points of interest in plan for the determination of maximum and permanent displacement (solid plate - left, panel with stiffeners - right)	95
Figure 6-13: Numerical model of both cladding types and their girts:	
(a) Discretization and partial modeling of the experimental setup;	
(b) Points of interest at the bottom side of the specimens.....	96
Figure 6-14: True plastic stress–true plastic strain diagrams of the tensile tests accompanied by their fitted Johnson-Cook strain hardening curve. The tensile-test values correspond to the elongation of the specimens up to their ultimate strength, i.e., the post-necking elongation is neglected.....	97
Figure 6-15: Blast pressure over the cladding:	
(a) Plan distribution of maximum blast pressure over the cladding;	
(b) Blast pressure time history of points S1, S2, S3 over the cladding	98
Figure 6-16: Numerical model and experimental results:	
(a) Vertical displacements in the numerical model at instances $t = 4.5$ ms (peak displacement) and $t = 100.0$ ms (permanent displacement);	
(b) Plastic strains at instance 100.0 ms (permanent displacement);	
(c) Numerical model displacement time histories at points P1, P2, P3, P4, P5 and P6 and comparison to experimental measurements	100
Figure 6-17: Results of the numerical model with elastic girts:	
(a) Discretization of the numerical model with elastic girts;	
(b) Vertical displacements in the numerical model at instances of $t = 3.9$ ms (peak displacement) and $t = 14.7$ ms (rebound);	
(c) Numerical model displacement time histories at points P1, P2, P3, P4, P5 and P6	101
Figure 7-1: Implementation of the proposed methodology through six steps	108
Figure 7-2: Illustration of the four case study cladding types: (a) CT1; (b) CT2; (c) CT3; (d) CT4	113
Figure 7-3: Mesh sensitivity study for cladding type CT2 with pressure 5.0 MPa and impulse 2.0 MPa-ms:	
(a) Maximum displacement;	
(b) Reaction time history	113
Figure 7-4: Description of the blast loading.....	114
Figure 7-5: Description of:	
(a) The maximum ductility ratio at a section of the examined cladding;	
(b) The in-plane slippage at the plan view of the examined cladding.....	115
Figure 7-6: Pressure–impulse diagrams for all case study cladding types	116
Figure 7-7: Transverse displacements, plastic strains and in-plane displacements of the case study cladding types subjected to a pressure–impulse combination of 1.0 MPa and 3.0 MPa-ms.....	117
Figure 7-8: Reaction time histories for the case study cladding types.....	118
Figure 7-9: $DLF(T)$ at different natural periods of the dimensionless SDOF for the examined cladding types for pressure 5.0 MPa and impulse 2.0 MPa-ms	118
Figure 7-10: Mitigation potential for different natural periods of the dimensionless SDOF for	

the case study cladding types with pressure 5.0 MPa and impulse 2.0 MPa-ms.....	119
Figure 7-11: Pressure–Impulse diagrams including the mitigation potential values for the case study cladding types	121
Figure 7-12: Static resistance curves for the case study cladding types in combination with the respective static damage levels and the associated performance goals.....	122

List of tables

Table 2-1: Response criteria for explosive safety design (DoD, 2008).....	24
Table 2-2: Response criteria for upper bound of each damage level (PDC, 2008b; Dusenberry, 2010)	25
Table 2-3: Response criteria for antiterrorism design (PDC, 2008a).....	25
Table 2-4: Response criteria for blast-resistant design of petrochemical facilities (ASCE, 2010).....	25
Table 4-1: Parameters of the equivalent cladding-to-framing 2DOF system	49
Table 5-1: Parameters values of the Johnson-Cook and the Cowper-Symonds models (Cadoni et al., 2018; Mortazavi and Heo, 2018).....	76
Table 5-2: Parameters of the two-step SDOF analysis.....	78
Table 6-1: Experimental measurements of the tensile tests	93
Table 6-2: Experimental measurements of the maximum and permanent displacements of the points of interest.....	95
Table 7-1: Parameters of the Cowper-Symonds Strength model	114
Table 7-2: Pressure–impulse hyperbola parameters	115

Notation

Abbreviations and acronyms

2DOF	Two degrees of freedom
DOF	Degree of freedom
FE	Finite element
FFT	Fast Fourier transform
FP	Front plate
FSI	Fluid–Structure interaction
NTFEA	Nonlinear transient finite element analysis
PI	Pressure–Impulse
PU	Polyurethane
PVB	Polyvinyl butyral
PSD	Power spectral density
SDOF	Single degree of freedom
SEA	Specific energy absorption
TNT	Trinitrotoluene

Symbols

A	Yield stress
B	Strain hardening coefficient
C_r	Reflection coefficient
D	Strain-rate effects coefficient
DIF	Dynamic increase factor
DLF	Dynamic load factor
DLF_i	Dynamic load factor of the i^{th} degree of freedom
$DLF_{rh}(T)$	Dynamic load factor of the dynamic reaction time history
$DLF_{or}(T)$	Dynamic load factor of the original blast pressure time history
E	Modulus of elasticity
I_i	Moment of inertia of the i^{th} member
I_{yy}	Moment of inertia
K_{LM}	Load - mass transformation factor
K_{LMi}	Load - mass transformation factor of the i^{th} degree of freedom
L	Length of component
L_i	Length of the i^{th} member
L_w	Blast wavelength
\bar{M}	Mass per unit area
M_{pl}	Plastic moment resistance
$MP(T)$	Mitigation potential at the corresponding natural period
MP_{avg}	Mitigation potential mean across a range of natural periods
N_p	Axial resistance
P	Blast pressure

$P(t)$	Blast pressure time history
P_o	Positive peak pressure
P_o^-	Negative peak pressure
P_r	Positive peak reflected pressure
P_r^-	Negative peak reflected pressure
$P_r(t)$	Reflected pressure time history
P_s	Positive peak incident pressure
P_s^-	Negative peak incident pressure
$P_s(t)$	Incident pressure time history
P_φ	Peak pressure as affected by φ
$P_\varphi(t, \varphi)$	Pressure time history as affected by φ
R	Stand-off distance
$R(t)$	Resistance time history
R_u	Ultimate/Maximum resistance
T	Natural period
T_1	Natural period of the cladding
T_c	Duration of the first oscillation cycle
T_i	Natural period of the i^{th} degree of freedom
U_s	Blast-wave velocity
\overline{U}_p	Plastic energy dissipated per unit area
$V(t)$	Reaction time history
W	Explosive weight
Z	Scaled distance
a_0	Sonic sound speed in air
$a_{i,j}$	Coefficients of the reaction time history
b	Blast-wave decay coefficient
$b_{i,j}$	Coefficients of the reaction time history
c	Viscous damping coefficient
i	Impulse
i_o	Impulse at a specific PI combination
i_s	Positive incident impulse
i_s^-	Negative incident impulse
i_r	Positive reflected impulse
i_r^-	Negative reflected impulse
i_φ	Impulse as affected by φ
k	Stiffness
k_1	Stiffness of the cladding
$k_{1,1}$	Bending stiffness of cladding
$k_{1,2}$	Zero stiffness along the horizontal branch of the cladding
$k_{1,3}$	Membrane stiffness of the cladding
k_2	Stiffness of the supporting structure
k_i	Stiffness of the i^{th} spring
m	Mass of a structural component or of an explosive (magnitude)
m_i	Mass assigned to the i^{th} degree of freedom
n	Non-dimensional form of displacement
n_h	Hudson's non dimensional length scale

n_i	Non-dimensional form of displacement of the i_{th} degree of freedom
\dot{n}	Non-dimensional form of velocity
\ddot{n}	Non-dimensional form of acceleration
\ddot{n}_i	Non-dimensional form of acceleration of the i_{th} degree of freedom
n_{iel}	Non-dimensional form of elastic displacement limit of the i_{th} degree of freedom
q	Strain-rate effects coefficient
q_s	Dynamic pressure
s	In-plane slippage
t	Time
t_1	Time of the reflected pressure appearance at the front wall
t_2	Time of pressure appearance at the side walls and roof
t_3	Time of pressure appearance at the rear wall
t'	Time when the pressure time history reaches the stagnation pressure
t_a	Time of arrival
t_d	Equivalent blast duration
t_d^+	Positive phase duration
t_d^-	Negative phase duration
w_i	Weight per unit length of the i_{th} member
x	Displacement
x_1	Yield displacement at the first yield point of the resistance function
$x_{1,el}$	Elastic displacement limit of cladding
$x_{1,mem}$	Displacement of initiation of the cladding membrane action
x_2	Yield displacement at the second yield point of the resistance function
x_{edge}	Distance between the point of interest and the free edge of the setup
x_{el}	Elastic displacement
x_i	Displacement of the i_{th} degree of freedom
x_{iel}	Elastic displacement limit of the i_{th} degree of freedom
x_{max}	Maximum displacement
x_{maxi}	Maximum displacement of the i_{th} degree of freedom
x_{st}	Static displacement
x_{sti}	Static displacement of the i_{th} degree of freedom
\dot{x}	Velocity
\ddot{x}	Acceleration
\ddot{x}_i	Acceleration of the i_{th} degree of freedom
β_N	Beta factor for the Newmark method
γ_N	Gamma factor for the Newmark method
δ	Deflection
δ_h	Hudson's time scale
δ_{punch}	Punch displacement
ϵ_{pl}	Plastic strain
$\dot{\epsilon}_{pl}$	Plastic strain rate
ζ	Damping ratio
θ	Strain hardening coefficient
θ_m	Maximum support rotation
μ	Maximum ductility ratio
ξ	Non-dimensional form of time

ρ	Material density
σ	Plastic stress
σ_Y	Yield stress
φ	Angle of incidence
ω	Natural frequency

Chapter 1

Introduction

1.1. Background

Explosions are of great concern in modern societies, as they lead to severe damages and human casualties. More specifically, the blast loads exerted on structures due to external explosions are typically of high amplitude and short duration, thus triggering different structural response mechanisms, compared to response mechanisms resulting from more typical loads such as wind, snow or earthquake, and causing structural failures. As a consequence, blast loads are critical for buildings in the vicinity of possible explosions.

Explosions may occur due to aggressor attacks against buildings or due to human error in industrial zones. There are numerous blast events in both categories which have historically attracted the attention of the media and induced societal and government-wise setback.

Two representative examples regarding the category of aggressor attacks are the explosions at the Alfred P. Murrah Federal Building in Oklahoma City, USA (1995) and the Khobar Towers in Dhahran, Saudi Arabia (1996). In the first incident, a truck containing explosives equivalent to 1800 kg of TNT detonated in close proximity to the target building. Approximately one third of the building collapsed (Figure 1-1) and numerous other buildings in the surrounding area were destroyed or damaged (FEMA, 1996). In the second incident, a truck filled with explosives equivalent to 9000 kg of TNT detonated in a parking lot next to a U.S. Military housing (Figure 1-2). In the aftermath, nineteen military personnel were killed and severe damages were induced in the building (Grant, 1998).

Two representative examples regarding the category of human errors are the accidental explosions at the Tianjin Harbour in China (2015) and the Port of Beirut in Lebanon (2020). In the first incident, an

overheated container of dry nitrocellulose was the cause of the initial explosion leading to a series of larger in magnitude explosions, which caused extensive destruction in the area of the warehouse (Yu et al., 2022). The explosions were so intense that their hazardous consequences were observed hundreds of meters away from the detonation centre (Figure 1-3). A similar pattern was also observed in the second incident, where a large amount of ammonium nitrate was stored without proper protection measures. The substance, which was equivalent to 1100000 kg of TNT, was finally triggered by a fire and a stored stash of fireworks (Sivaraman and Varadharajan, 2021). The explosion that occurred was so massive (Figure 1-4) that it was even felt in Cyprus (located more than 240 km away), forcing the Lebanese government to declare a two-week state of emergency.

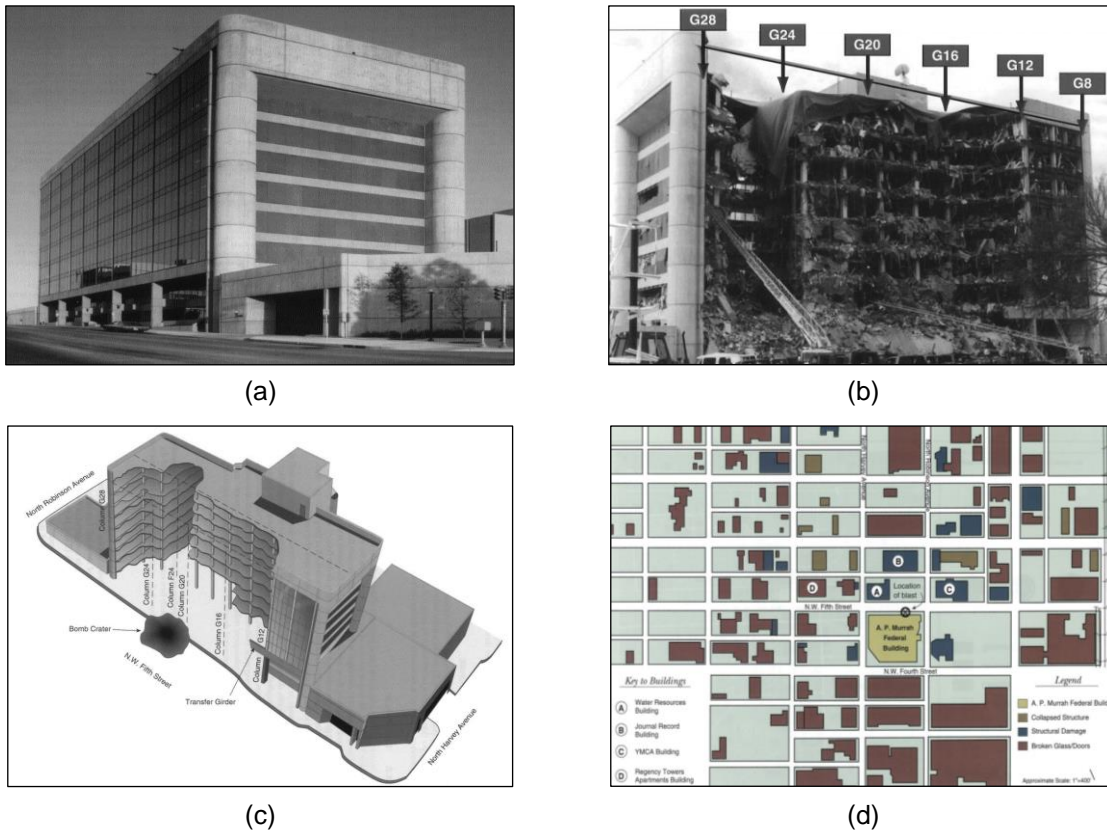


Figure 1-1: Explosion at the Alfred P. Murrah Federal Building [reprinted from FEMA (1996)]: (a) Photo before the explosion; (b) Photo after the explosion; (c) Damage induced to the front side of the building; (d) Damage induced to the surrounding buildings

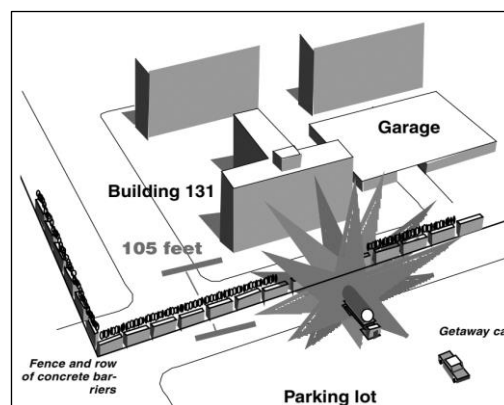
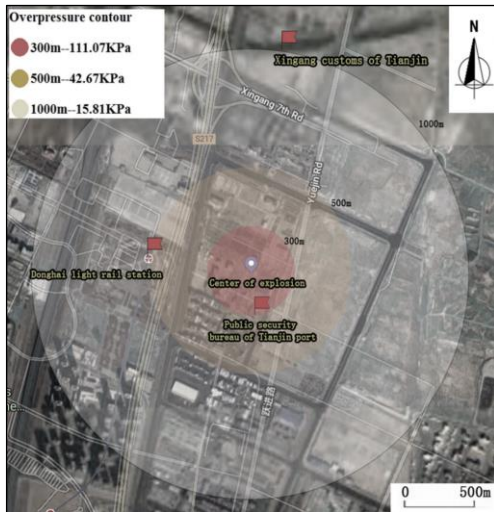


Figure 1-2: Location of explosions with regard to the Khobar Towers [reprinted from Grant (1998)]



(a) - Map



(b) - Damages at 200 m



(c) - Damages at 300 m



(d) - Damages at 400 m



(e) - Damages at 500 m



(f) - Damages at 1000 m

Figure 1-3: Damages from the explosions in the Tianjin Harbour [reprinted from Yu et al. (2022)]: (a) Map of overpressure and damages; (b) Damages at 200 m; (c) Damages at 300 m; (d) Damages at 400 m; (e) Damages at 500 m; (f) Damages at 1000 m

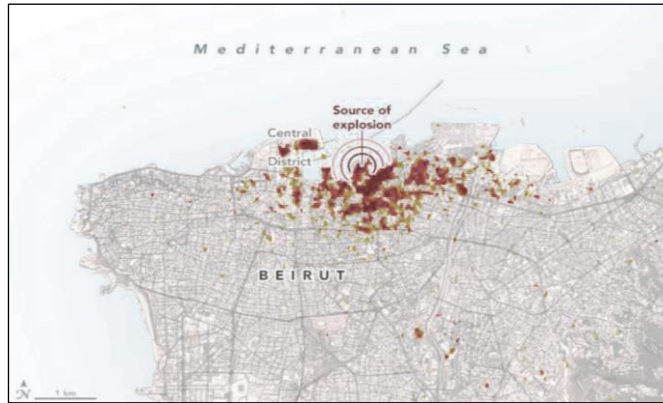


Figure 1-4: Damage around the Port of Beirut after the explosion [reprinted from Sivaraman and Varadharajan (2021)]

There are various parameters affecting the likelihood and magnitude of both intentional and accidental explosions, e.g., industrial activity, use of explosion-sensitive materials, integrity of equipment, public policies, regulations, radicalization, extremism, organized crime, etc. Starting as a rare occurrence, explosions have evolved into a relatively frequent problem in regard to these reasons (Mlakar et al., 1998; Abouzeid et al., 2020). Especially for aggressors, the frequency of attacks seems to follow an increasing trend globally (Figure 1-5), with particular growth in underdeveloped countries. A large proportion of these attacks occurs from explosives (Figure 1-6).

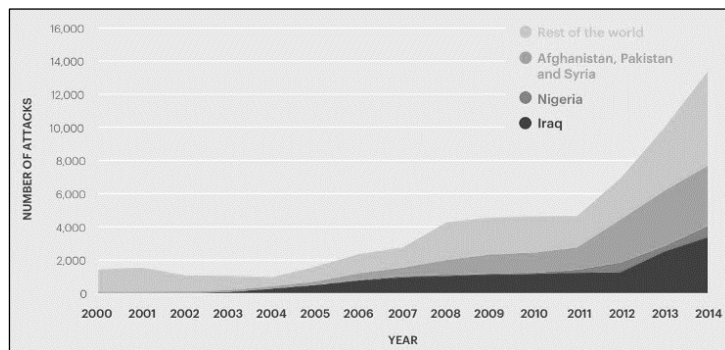


Figure 1-5: Global aggressor attacks from 2000 to 2014 [reprinted from IEP (2015)]

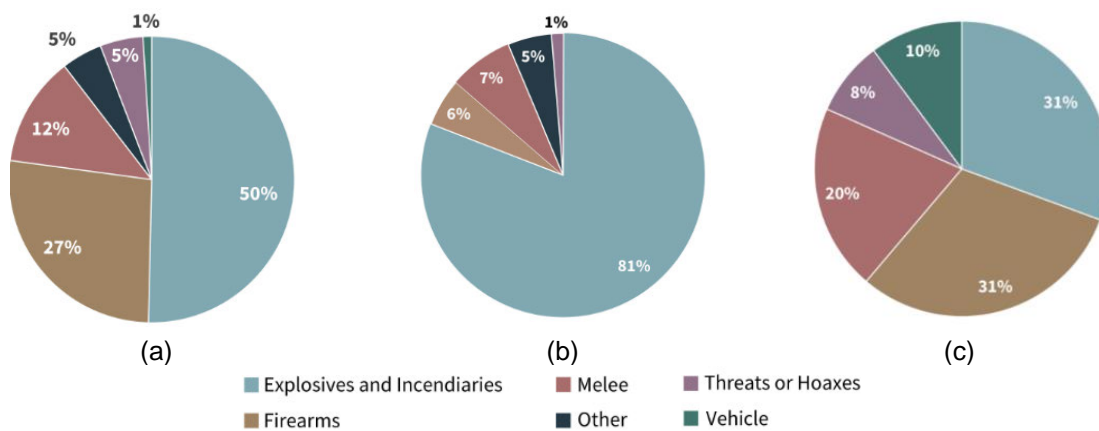


Figure 1-6: USA aggressor attacks from 1994 to 2020 by threat type [reprinted from Jones and Doxsee (2020)]: (a) Right-wing aggressor attacks; (b) Left-wing aggressor attacks; (c) Religious aggressor attacks

The reoccurring incidents have allowed the identification of blast intensity levels, the observation of failure mechanisms and the assessment of the relevant consequences. The findings enabled the research community and the public protection agencies to implement design strategies in order to effectively mitigate blast loading, develop protection measures against explosions and improve life safety.

1.2. Blast resistant cladding

Typically, the first component that receives the blast load from an external explosion is the building envelope, which may comprise of curtainwalls, windows, and generally other types of exterior wall claddings. However, the usually applied cladding components (e.g., corrugated metal sheets or masonry infill walls) have been proved to be inadequate, as observed in the recent Beirut explosion (Figure 1-7). In the occasions of cladding failure, the blast wave entered the building and caused significant injuries as well as extensive damage in the interior.



Figure 1-7: Failures in the Beirut explosion [reprinted from [Lekkas et al. \(2020\)](#)]: (a) Metal sheets; (b) Masonry walls

Thus, in an effort to maintain the strength of the building envelope, cladding components should generally have increased capacity for blast-resistant applications. Furthermore, cladding should be designed in order to be able to block flying debris from entering the building interior as well as to sustain its integrity. As noted by [Dusenberry \(2010\)](#), the latter is necessary because cladding may be converted into pieces of hazardous projectiles (e.g., fragile glass panels) for the occupied space.

The application of these principles has become complex and cumbersome in blast engineering practice. This is critical when investigating the response of building cladding susceptible to blast loads, i.e., in high-risk structures, such as public buildings, military structures and industrial plants.

In this direction, special cladding systems (which follow the described design strategy) have been recently researched and manufactured with the use of innovative materials (e.g., Figure 1-8) and geometric layouts (e.g., Figure 1-9). These systems have sufficient strength to withstand the corresponding blast design pressure. Moreover, they exhibit significant energy absorption capacity that enables them to deform in a ductile manner and, thus, deter the need to be designed elastically, which could lead to increased cost.

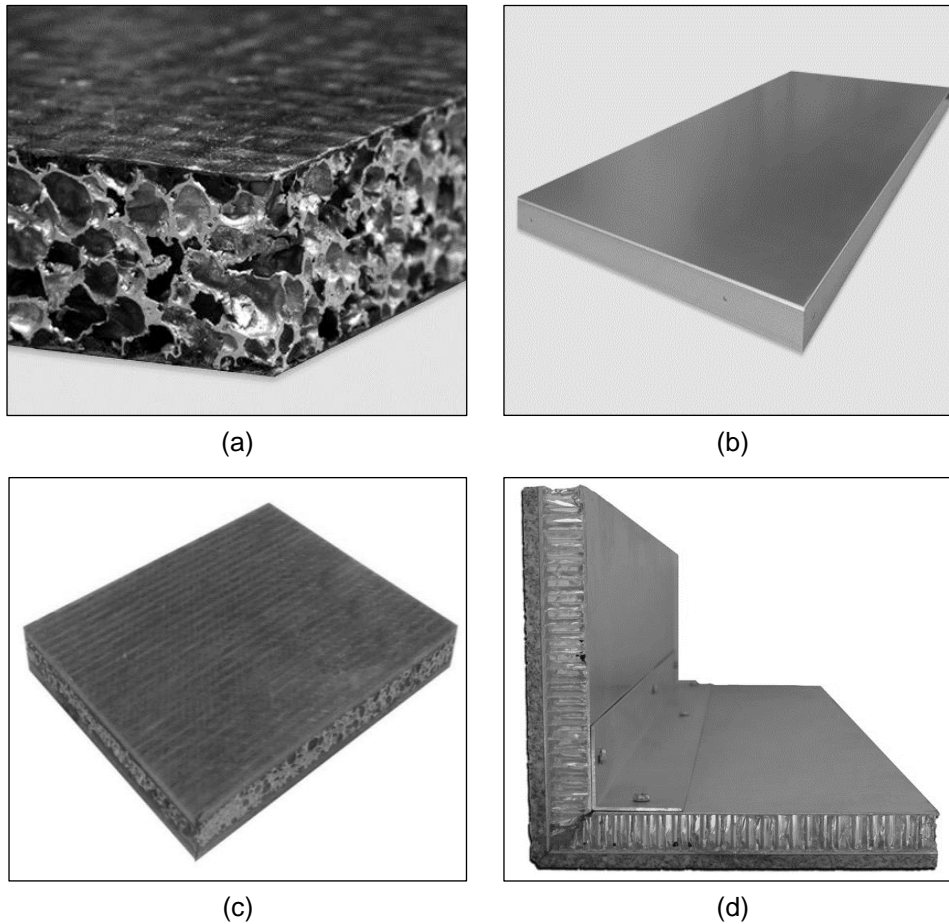


Figure 1-8: Blast-resistant cladding manufactured with the use of innovative materials: (a) High-strength sandwich panel [reprinted from [Foamtech Global \(2021\)](#)]; (b) Aluminium-foam blast-resistant product [reprinted from [Foamtech Global \(2021\)](#)]; (c) FRP and CFRP panels with closed-cell aluminium foam [reprinted from [Beihai Composite Materials Co. Ltd. \(2021\)](#)]; (d) Stone bonded to a honeycomb matrix [reprinted from [StonePly Co. \(2022\)](#)]

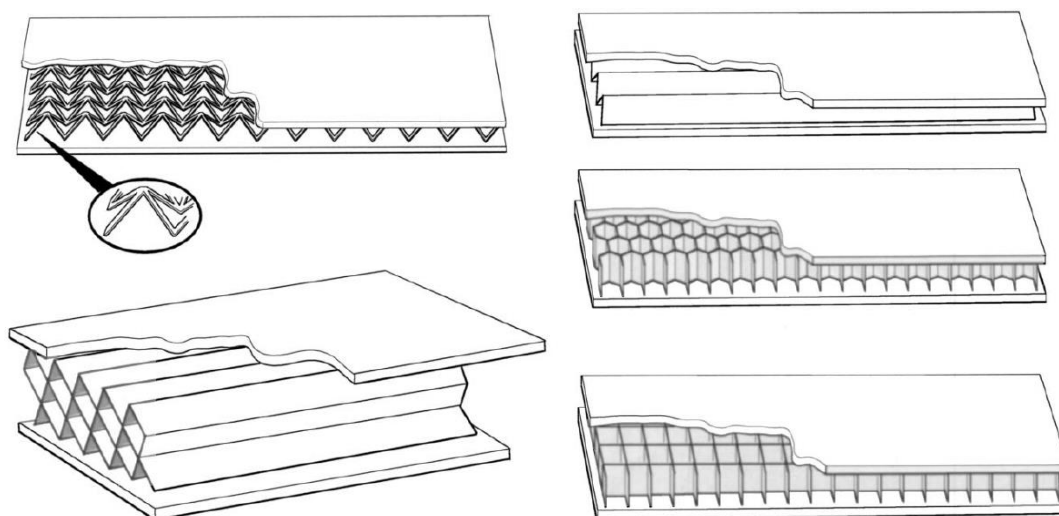


Figure 1-9: Innovative core layouts for blast-resistant cladding [reprinted from [Fleck and Deshpande \(2004\)](#)]

1.3. Problem statement and objective

As aforementioned, when buildings are subjected to an external explosion, the blast pressure initially impinges the exterior cladding. The cladding should meet the described structural design criteria in order to be sufficient for blast applications. In addition to these criteria, a recent design trend regarding the cladding is its ability to enhance blast-resistant performance on the supporting structure, i.e., the components where the cladding is supported to.

More specifically, after the impingement of blast pressure over the cladding, dynamic reactions from the cladding supports are transferred to the supporting structural components, i.e., the components where the cladding is connected to, and eventually to the structural frame of the building. Typical examples of this application are the exterior cladding-to-framing system and the sacrificial cladding that is installed as protection around a column.

According to [Chengqing et al. \(2011\)](#), [Hanssen et al. \(2002\)](#) a high amplitude and short duration blast load can be converted into a reaction with lower amplitude and larger duration due to plastic energy absorption and ductility. The reaction amplitude can thereby be decreased. Along with the plastic energy absorption mechanism, inertial resistance to the blast pressure wave is also an important response mechanism. As explained by [Rutner and Wright \(2016\)](#), energy absorption and inertial effects comprise a duality. In some cases, mass and stiffness have a larger effect on the protected structure than energy dissipation and may mitigate blast pressure without the need to enable plasticity.

In this context, there are some issues which need to be resolved in order to effectively implement the described design trend:

- The range of possible cladding configurations, which could be applied over a building susceptible to blast loading, is vast. Hence, proper design guidance should be given with regard to the cladding properties that could lead to effective mitigation potential.
- The results of the cladding-to-supporting-structure numerical models should be experimentally validated in order to verify that they are realistic.
- A methodology is needed for evaluating the cladding mitigation potential of a designed cladding with specific geometric and material properties, as there is no generalized way of examining the effectiveness of a specific cladding type.

Observing these research gaps, the main scope of the present thesis is to offer further insight into the structural behavior of blast-resistant cladding by:

- a. Calculating with quantitative and qualitative diagrams the blast effects of cladding mass, stiffness, ultimate resistance and ductility on the supporting structure.
- b. Calculating with quantitative and qualitative diagrams the blast effects of cladding membrane action on the supporting structure.
- c. Experimentally investigating a steel-cladding-to-supporting-structure system with a real explosion and employing the respective numerical model calibrated to the experimental results.
- d. Describing a methodology for the generalized estimation of the mitigation potential of a cladding, which could enable the direct comparison between different cladding types.

Thus, a combined experimental, numerical and analytical investigation is conducted in order to achieve these research goals. Aim of this thesis is to develop novel scientific methods and tools, and to contribute

to structural engineering practice, regarding the response and design of cladding with blast mitigation effects for the supporting structure .

1.4. Outline of thesis

The thesis is divided into nine chapters. Chapters 2 to 7 are considered to be self-contained. However, a thorough study of the key concepts in blast engineering (summarized in Chapter 2) is suggested for the readers who are not familiar with the basic concepts of blast effects on structures.

- Chapter 1: Purpose of the thesis

A brief introduction is made about the significance of cladding and its characteristics in relation to blast-resistant applications. The capacity of cladding to mitigate blast consequences for the supporting structure is highlighted as one of the main characteristics.

- Chapter 2: Basic concepts in blast engineering used throughout the thesis

Basic properties of blast loading, shock wave phenomena and their effects on structures are presented in this chapter with an emphasis on the methods used for evaluating the load and response parameters. A review of the performance criteria of cladding subjected to blast loading is also given in association with the thesis research goals.

- Chapter 3: Mechanisms of cladding mitigation potential and notes from literature

Literature findings on the design trend of mitigating blast effects to the supporting structure are explored and notes are made about the relevant activated mechanisms. Particular emphasis is given on the works of other researchers about the mitigation potential of blast resistant cladding.

- Chapter 4: Study for the influence of cladding mass, stiffness, ultimate resistance and ductility

An extensive two-degrees-of-freedom (2DOF) parametric study is carried out for examining the effects of cladding mass, stiffness, ultimate resistance and ductility to the supporting structure. The cladding and supporting structure are represented by the 1st and 2nd degrees of freedom (DOFs), respectively. The determination of the effects of these parameters are important for the design of cladding components with mitigation potential capacity. It is noted that the cladding is considered to be elastic-perfectly plastic with no membrane branch.

- Chapter 5: Study for the influence of cladding membrane action

The effects of the cladding membrane action on the supporting structure are investigated. The membrane action is explored in two forms: (a) As the secondary stiffening phase of a cladding with significant bending stiffness; and (b) As the main stiffness branch of a cladding behaving as a membrane structure.

- Chapter 6: Experimental investigation of cladding mitigation potential

An experimental investigation on the response of a steel cladding and its supporting structure subjected to a real explosion is presented. Finite element simulations of the aforementioned

experimental test are presented for the calibration of the numerical model and the verification of the results of the parametric studies.

- Chapter 7: Methodology for the evaluation of cladding mitigation potential

A design methodology for the calculation of the blast mitigation potential of a cladding component is proposed. The methodology is implemented with the use of the reaction time histories of a cladding component subjected to various combinations of peak pressure and impulse. It is also generalized for all possible geometric and material types of cladding components.

- Chapter 8: Conclusions and contributions of the thesis

A summary of the conducted research, the conclusions, the contributions of the thesis and recommendations for future research are included in this chapter.

- Appendix A: Code fragments used in the thesis

Code fragments are included for the implementation of the Chapter 7 methodology and the further theoretical investigation of the 2DOF studies of Chapter 4 and 5.

- Appendix B: Extended summary of the thesis in Greek

A summary of the introduction, primary findings and conclusions of the thesis are provided in Greek for the benefit of native Greek readers. It is noted that the Institute of Steel Structures, where the research was conducted, is a Greek institute belonging to the National Technical University of Athens.

1.5. References

Abouzeid, M. et al. (2020) 'Lebanon's humanitarian crisis escalates after the Beirut blast', *The Lancet*, pp. 1380–1382. doi: 10.1016/S0140-6736(20)31908-5.

Beihai Composite Materials Co. Ltd. (2021) Aluminum foam composite panels. Available at: chinabeihai.net.

Chengqing, W., Liang, H. and John, O. D. (2011) 'Blast testing of aluminum foam – protected reinforced concrete slabs', *Journal of Performance of Constructed Facilities*, 25(5), pp. 464–474. doi: 10.1061/(ASCE)CF.1943-5509.0000163.

Dusenberry, D. O. (2010) *Handbook for blast resistant design of buildings*. John Wiley & Sons. doi: 10.1002/9780470549070.

Federal Emergency Management Agency (1996) 'FEMA 277: The Oklahoma city bombing: Improving building performance through multi-hazard mitigation'.

Fleck, N. A. and Deshpande, V. S. (2004) 'The resistance of clamped sandwich beams to shock loading', *Journal of Applied Mechanics, Transactions ASME*. doi: 10.1115/1.1629109.

Foamtech Global (2021) Military industry and general industry products. Available at: foamtechglobal.co.kr/product#military.

Grant, R. (1998) 'Khobar Towers', *Air Force Magazine*, pp. 41–77.

- Hanssen, A. G., Enstock, L. and Langseth, M. (2002) 'Close-range blast loading of aluminium foam panels', *International Journal of Impact Engineering*, 27(6), pp. 593–618. doi: 10.1016/S0734-743X(01)00155-5.
- Institute for Economics and Peace (2015) 'Global Terrorism Index 2015, measuring the impact of terrorism'.
- Jones, S. G. and Doxsee, C. (2020) 'The tactics and targets of domestic terrorists', *Center for Strategic and International Studies*.
- Lekkas, E. et al. (2020) 'The August 4, 2020 Beirut (Lebanon) explosion: a technological disaster within crises', *Newsletter of Environmental, Disaster and Crises Management Strategies*, p. Issue No. 18.
- Mlakar, P. F. et al. (1998) 'The Oklahoma city bombing: Analysis of blast damage to the Murrah building', *Journal of Performance of Constructed Facilities*, 12(3), pp. 113–119. doi: 10.1061/(asce)0887-3828(1998)12:3(113).
- Rutner, M. P. and Wright, J. P. (2016) 'Duality of energy absorption and inertial effects: Optimized structural design for blast loading', *International Journal of Protective Structures*, 7(1), pp. 18–44. doi: 10.1177/2041419615622726.
- Sivaraman, S. and Varadharajan, S. (2021) 'Investigative consequence analysis: A case study research of beirut explosion accident', *Journal of Loss Prevention in the Process Industries*, 69, p. 104387. doi: <https://doi.org/10.1016/j.jlp.2020.104387>.
- StonePly Co. (2022) Stone backing options. Available at: stoneply.com/es/.
- Yu, G. et al. (2022) 'Holistic case study on the explosion of ammonium nitrate in Tianjin port', *Sustainability*. doi: 10.3390/su14063429.

Chapter 2

Blast loading and structural response

2.1. Introduction

When an explosion takes place, shock waves are generated. These waves have adverse effects over buildings, as they are characterized by relatively high-pressure magnitude, accompanied with short duration (in the order of ms). Multiple experimental tests and computational fluid dynamic models have been performed in order to determine the characteristics and values of the corresponding blast pressure time histories [Karlos and Solomos \(2013\)](#). Furthermore, building envelope generally affects the corresponding blast wave. When encountering a sufficiently large structure, the blast wave is reflected. This interaction between the building and the blast wave is a function of both the blast wave characteristics and the dimensions of the structure. Thus, the pressure time history that is applied throughout the building envelope is accordingly modified ([Cormie, Mays and Smith, 2009](#)).

In addition, structural response of a building subjected to blast loading can be calculated through a variety of methods, the most important of which are the Single-Degree-of-Freedom (SDOF) analyses. These design methods are based on the evaluation of the component adequacy by considering the dynamic nature of blast loading. A brief analysis of the aforementioned blast loading characteristics and the blast effects over buildings is presented in this chapter. The analyzed theoretical background is considered as known in the next chapters of the thesis.

2.2. Blast loading

2.2.1. Pressure–time profile

Explosions are characterized by sudden release of energy, volume expansion and waves, which lead to temperature and, most importantly, pressure increase (far beyond ambient pressure, which is approximately 101.3 kPa). The pressure increase is referred to as overpressure.

Regarding the wave speed, explosions can be separated into two different categories: Detonations and deflagrations. Detonations are characterized by sudden pressure increase (Figure 2-1), while deflagrations are characterized by gradual pressure increase (Figure 2-2). The waves created from detonations are shock waves, while the waves created from deflagrations are pressure waves. In detonations and, in some cases, in deflagrations the pressure time history also includes a negative phase. The negative phase exists due to the fact that the waves move the air forwards, thus leaving a vacuum (lack of air) behind them, with pressure lower than the ambient pressure (negative pressure) (ASCE, 2010).

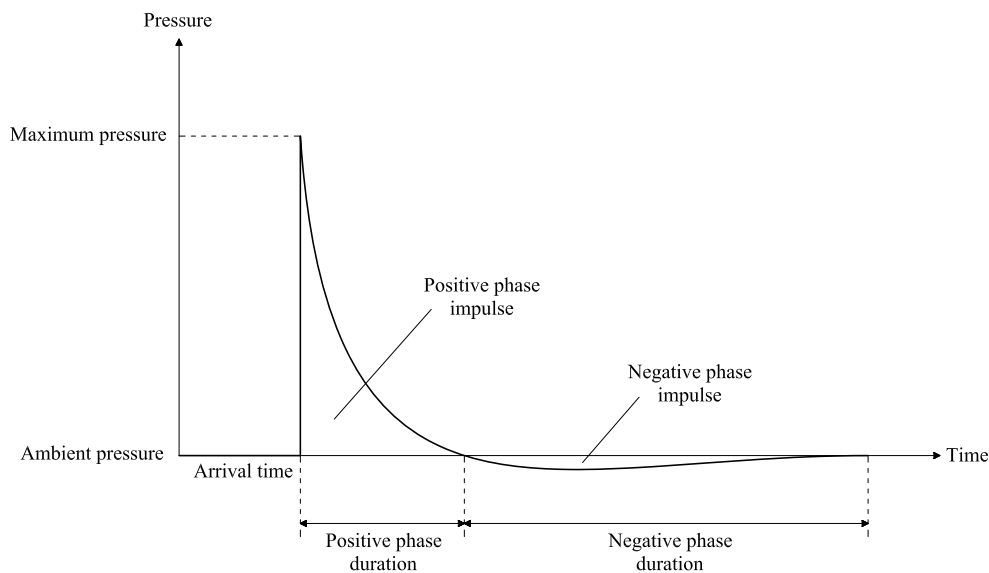


Figure 2-1: Detonation pressure time history

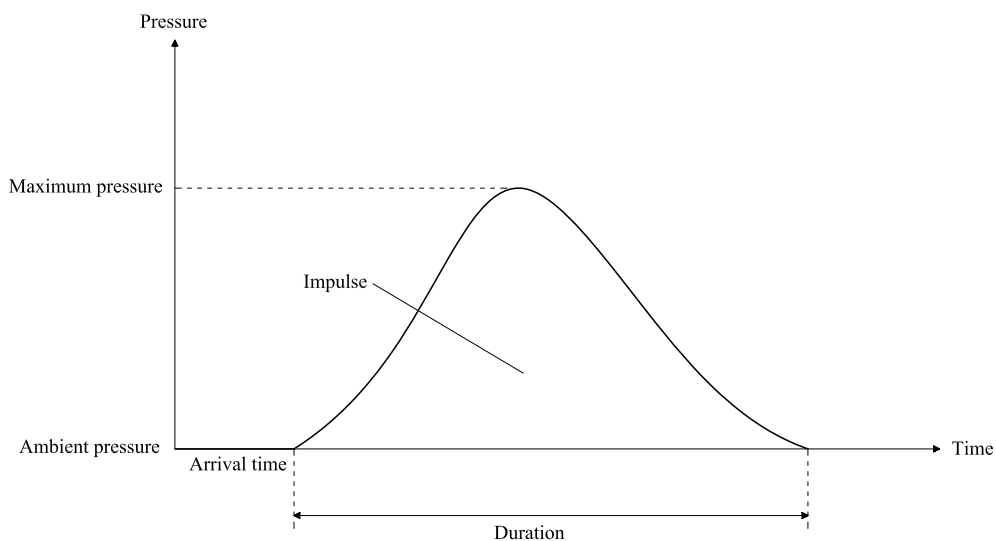


Figure 2-2: Deflagration pressure time history

Impulse denotes the integral of pressure over time. By keeping the same positive phase impulse, the same maximum pressure and neglecting the negative phase, the pressure time history can be idealized with triangles in both cases of detonations and deflagrations (Hoffmeister et al., 2015). Illustratively, these approximations are presented in Figure 2-3 and Figure 2-4.

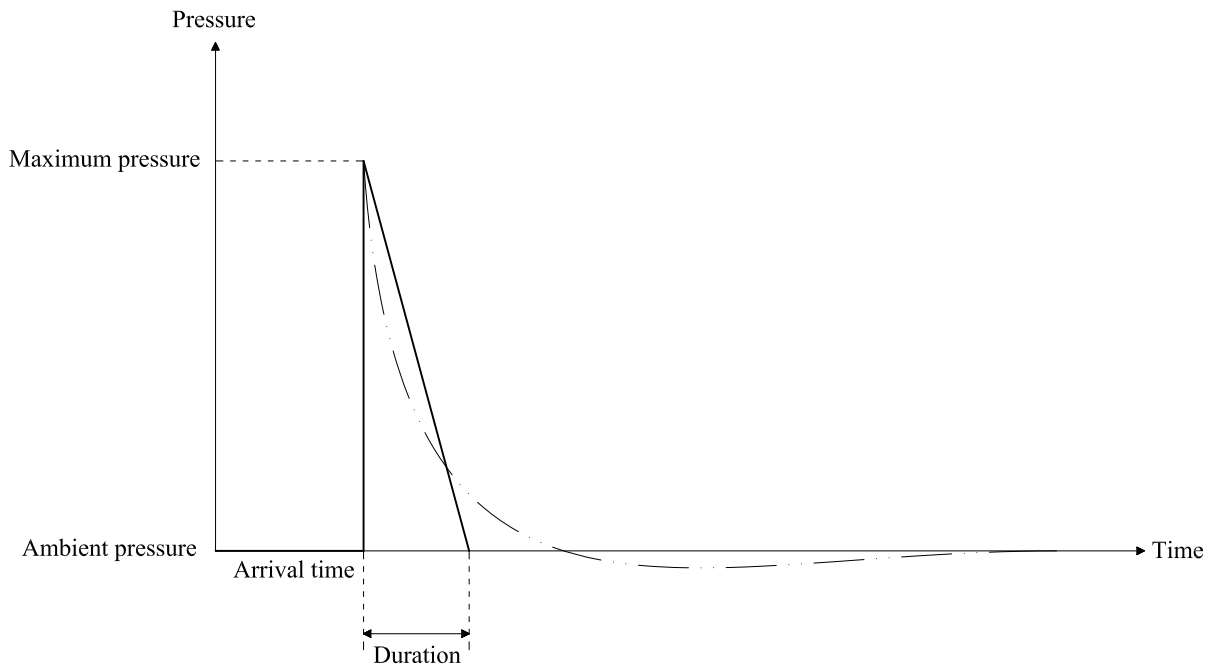


Figure 2-3: Equivalent triangle of detonation pressure time history

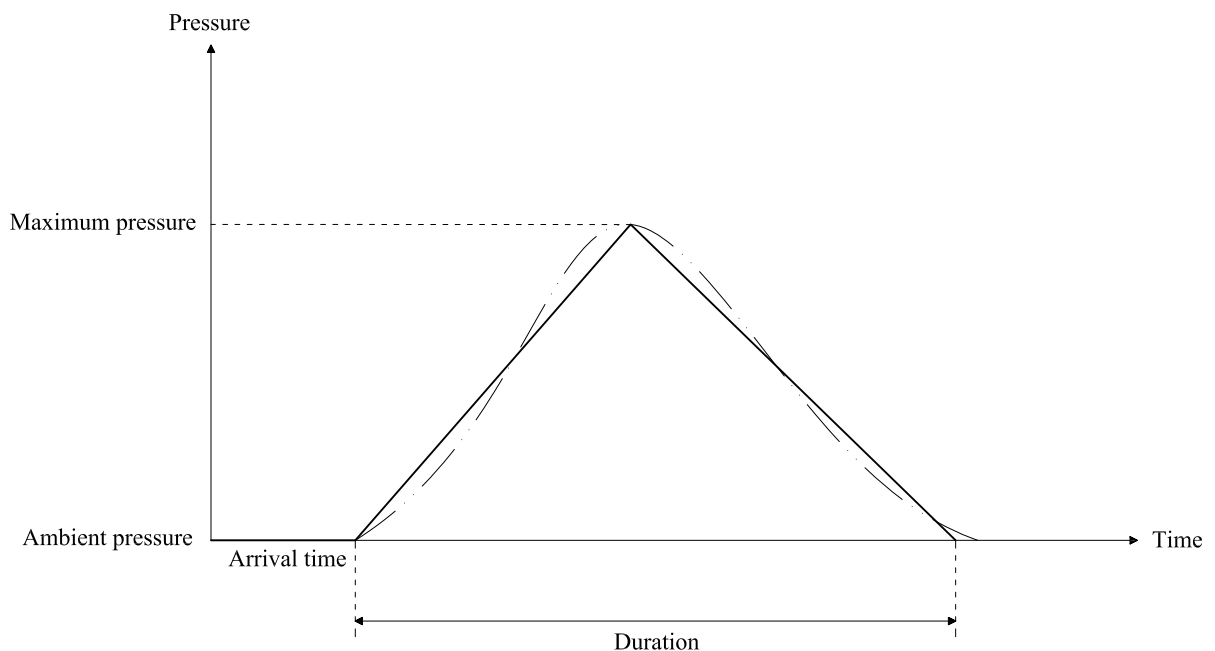


Figure 2-4: Equivalent triangle of deflagration pressure time history

Furthermore, pressure magnitude decreases as distance from the blast source is increased. The time at which the wave reaches the corresponding object is referred to as arrival time. As observed through Figure 2-5 (where the negative phase has not been included for simplicity reasons), the further the blast source is, the larger the arrival time and the longer the positive phase duration is.

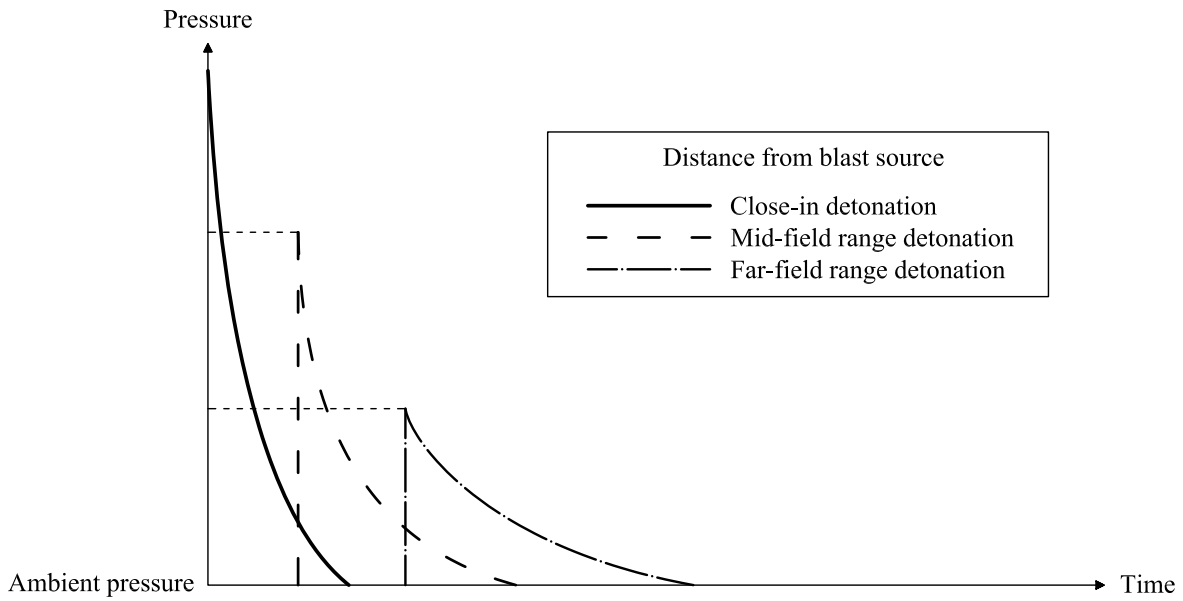


Figure 2-5: Pressure time histories for close-in, mid-field range and far-field range detonations

2.2.2. Blast wave parameters

Blast waves are reflected when they face an object with sufficiently large dimensions. Buildings can be such objects. Blast waves impinge on them and transfer part of their energy. The air is locally compressed and due to momentum difference, pressure increases significantly. The increased pressure is called reflected pressure, while the original pressure is called incident pressure. Incident pressure represents the pressure that is exhibited when the examined surface is parallel to the direction of blast wave propagation. Typical differences between the two pressures are presented in Figure 2-6 in logarithmic scale.

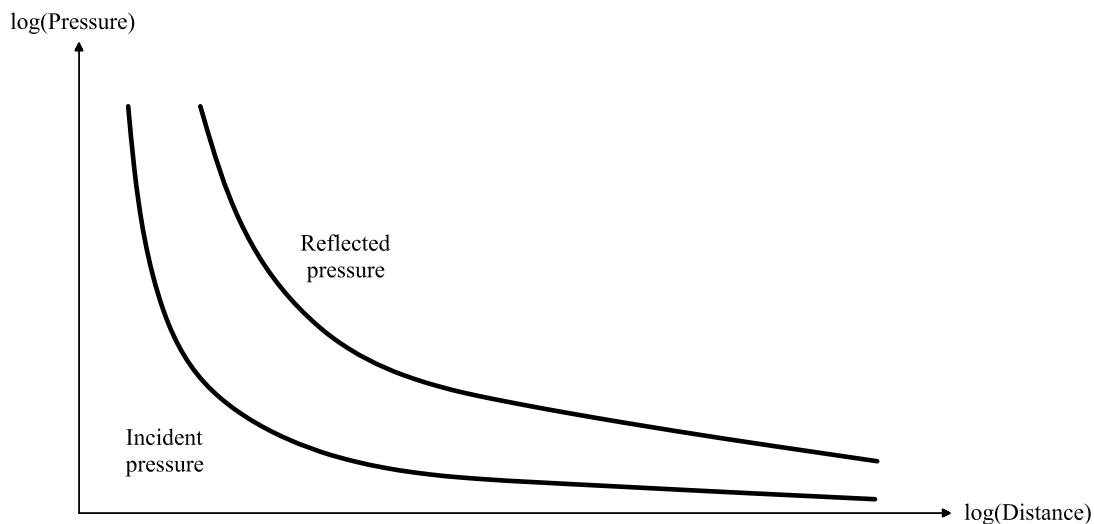


Figure 2-6: Incident pressure and reflected pressure magnitude with regard to distance

Along with reflected pressure, dynamic or drag pressure, which is the pressure that refers to the velocity of the air moving around the corresponding object, is also applied to buildings. The calculation of all

these blast parameters can generally be performed through empirical expressions or diagrams, which have been produced by experimental blast tests and/or computational fluid dynamics models. Such diagrams are given in Figure 2-7 to Figure 2-10 about detonations with the use of scaled distance. Scaled distance Z can be expressed by Equation (2-1). R and W stand for the stand-off distance and the equivalent TNT mass, respectively.

$$Z = \frac{R}{W^{1/3}} \quad (2-1)$$

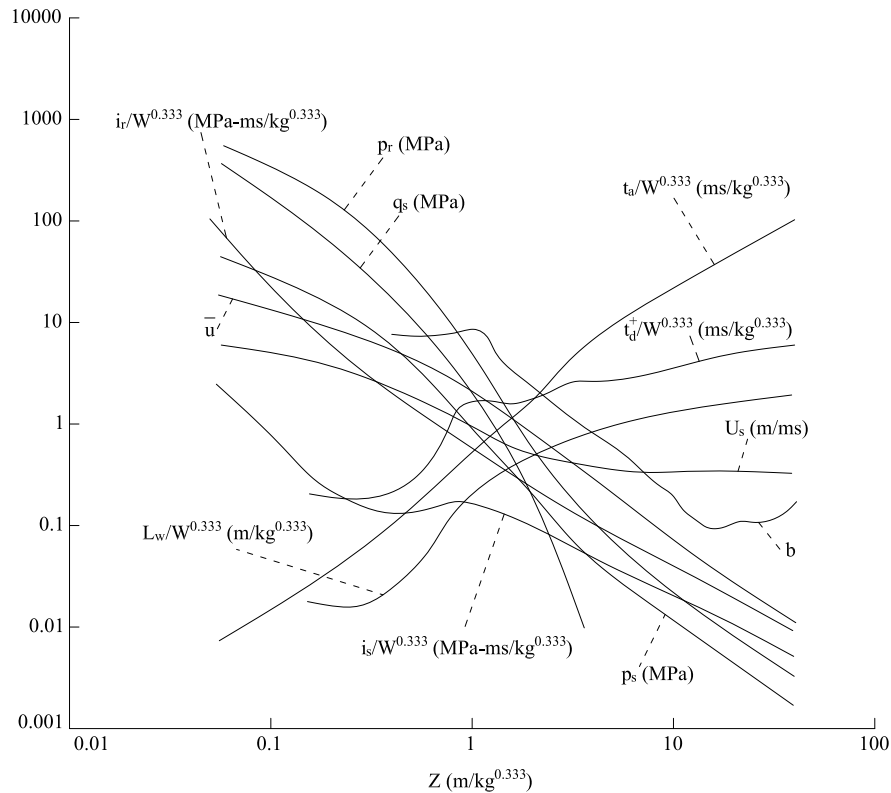


Figure 2-7: Positive-phase parameters of a spherical detonation (DoD, 2008)

The symbols refer to:

- P_s : Positive peak incident pressure
- P'_s : Negative peak incident pressure
- P_r : Positive peak reflected pressure
- P'_r : Negative peak reflected pressure
- i_r : Positive reflected impulse
- i'_r : Negative reflected impulse
- i_s : Positive incident impulse
- i'_s : Negative incident impulse
- L_w : Blast wavelength
- U_s : Blast-wave velocity
- t_a : Time of arrival
- t_d^+ : Positive phase duration
- t_d^- : Negative phase duration
- q_s : Dynamic pressure

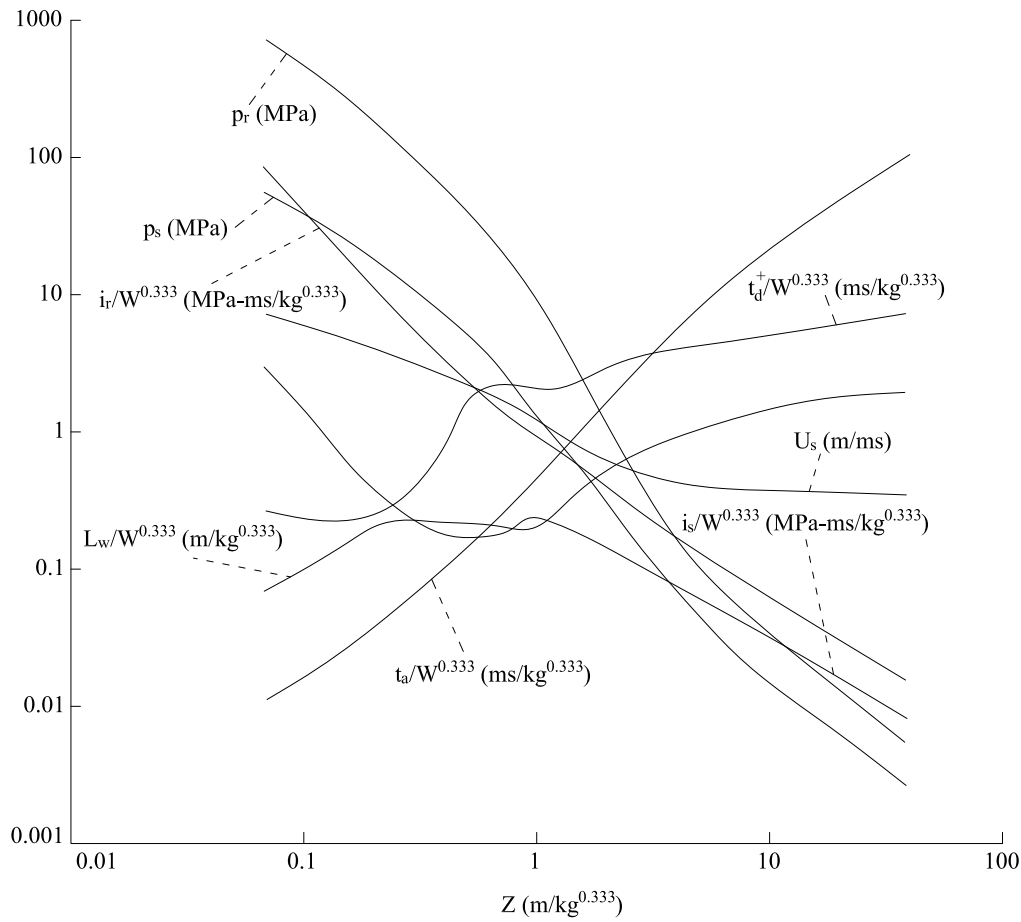


Figure 2-8: Positive-phase parameters of a hemispherical detonation (DoD, 2008)

Detonations are generally described by a pressure time history that follows an exponential form [Equation (2-2)] at the positive phase (namely the Friedlander equation), while they follow the Cubic function [Equation (2-3)], as found by Rigby et al., (2014) to be more precise, at the negative phase. As a whole, the pressure time history $P(t)$ is a function of time t , positive peak pressure P_o , negative peak pressure P_o^- , positive phase duration t_d^+ , negative phase duration t_d^- and blast wave decay coefficient b .

$$P(t) = P_o \cdot \left(1 - \frac{t}{t_d^+}\right) \cdot \exp\left(-b \cdot \frac{t}{t_d^+}\right) \quad (2-2)$$

$$P(t) = -P_o^- \cdot \left(\frac{6.75 \cdot (t - t_d^+)}{t_d^-}\right) \cdot \left(1 - \frac{(t - t_d^+)}{t_d^-}\right)^2 \quad (2-3)$$

2.2.3. Blast loading over buildings

As aforementioned, when a blast wave encounters with an object with sufficiently large dimensions, it is reflected. The angle of incidence towards the object has a key role over the amount of reflected pressure that will occur. In this context, reflection coefficient C_r is defined as the ratio between the reflected pressure and the incident pressure. C_r can reach large values depending on the angle of incidence and the value of incident pressure. An indicative representation of values of C_r can be found in Figure 2-11. The maximum value of C_r is observed when the blast wave is perpendicular to the corresponding object and the minimum value is observed when the blast wave is parallel to the object. It is worth noting that there

is a peak of C_r in the intermediate angles of incidence because of Mach reflection (Cormie, Mays and Smith, 2009).

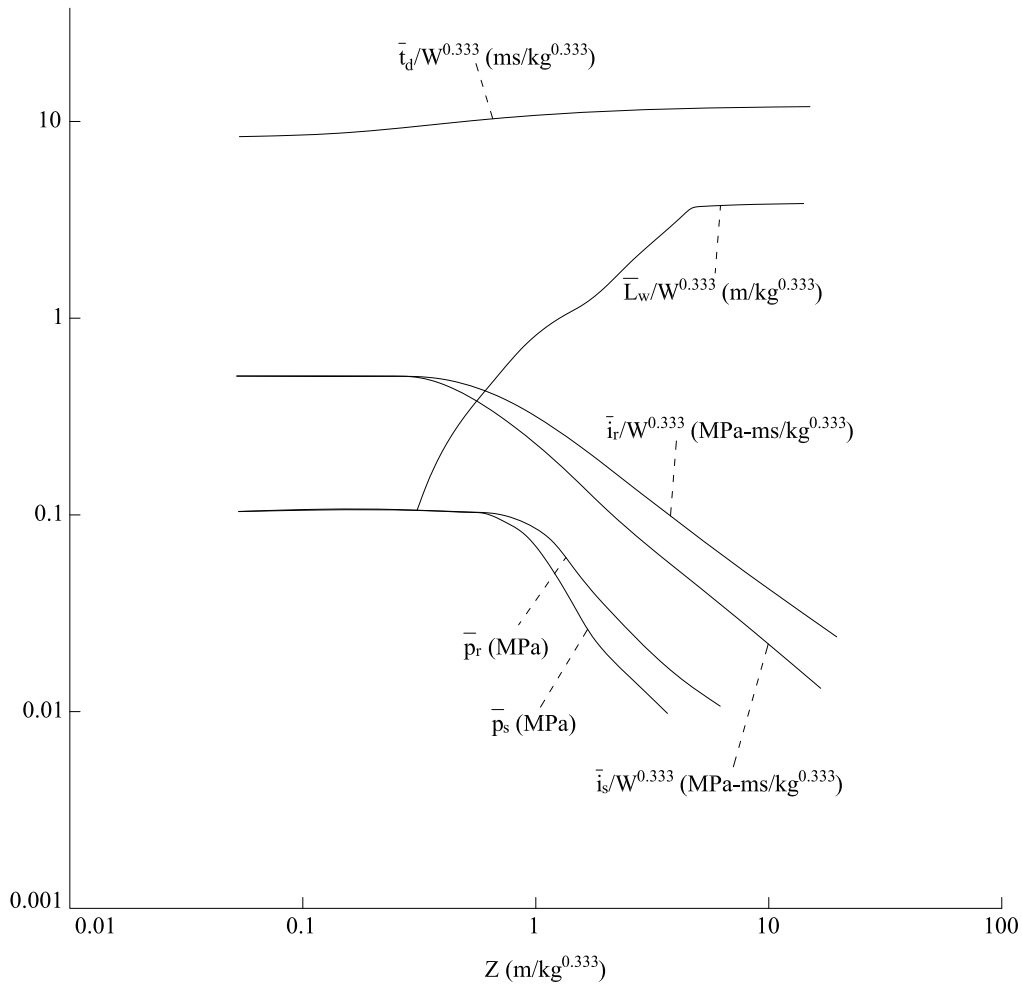


Figure 2-9: Negative-phase parameters of a spherical detonation (DoD, 2008)

According to Hyde (1993), the reflected pressure and impulse can simplistically be calculated by the approximations shown in Equations (2-4) and (2-5), regarding the angle of incidence φ .

$$P_{\varphi} = \begin{cases} P_s \cdot (1 + \cos\varphi - 2\cos^2\varphi) + P_r \cdot \cos^2\varphi, & \cos\varphi \geq 0 \\ P_s, & \cos\varphi < 0 \end{cases} \quad (2-4)$$

$$i_{\varphi} = \begin{cases} i_s \cdot (1 + \cos\varphi - 2\cos^2\varphi) + i_r \cdot \cos^2\varphi, & \cos\varphi \geq 0 \\ i_s, & \cos\varphi < 0 \end{cases} \quad (2-5)$$

Typically, structures are engulfed by the corresponding blast wave. The blast wave is diffracted around them and squashes the exposed surfaces (walls and roof) of the building envelope. As shown in Figure 2-12, the pressure that is initially experienced at time t_1 is the reflected pressure of the front wall. This pressure rapidly decays because blast wave passes around the roof and side walls until time t' . At time t' pressure reaches stagnation pressure, which is the sum of the time-varying incident and dynamic pressure. This is a process called clearing and its main function is the reduction of the impulse delivered to the front wall. At time t_2 the side walls and roof are pushed inside by the blast wave pressure and at time t_3 the blast wave reaches the rear wall, which is loaded by both the diffraction loads and the drag loads.

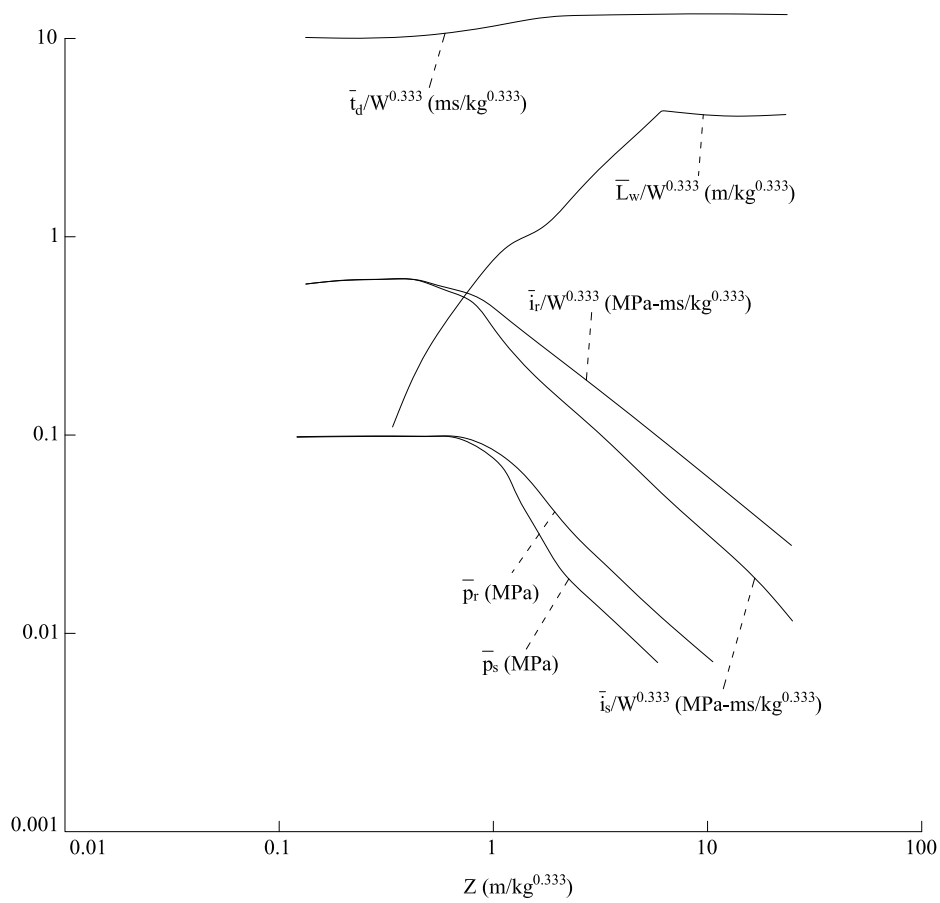


Figure 2-10: Negative-phase parameters of a hemispherical detonation (DoD, 2008)

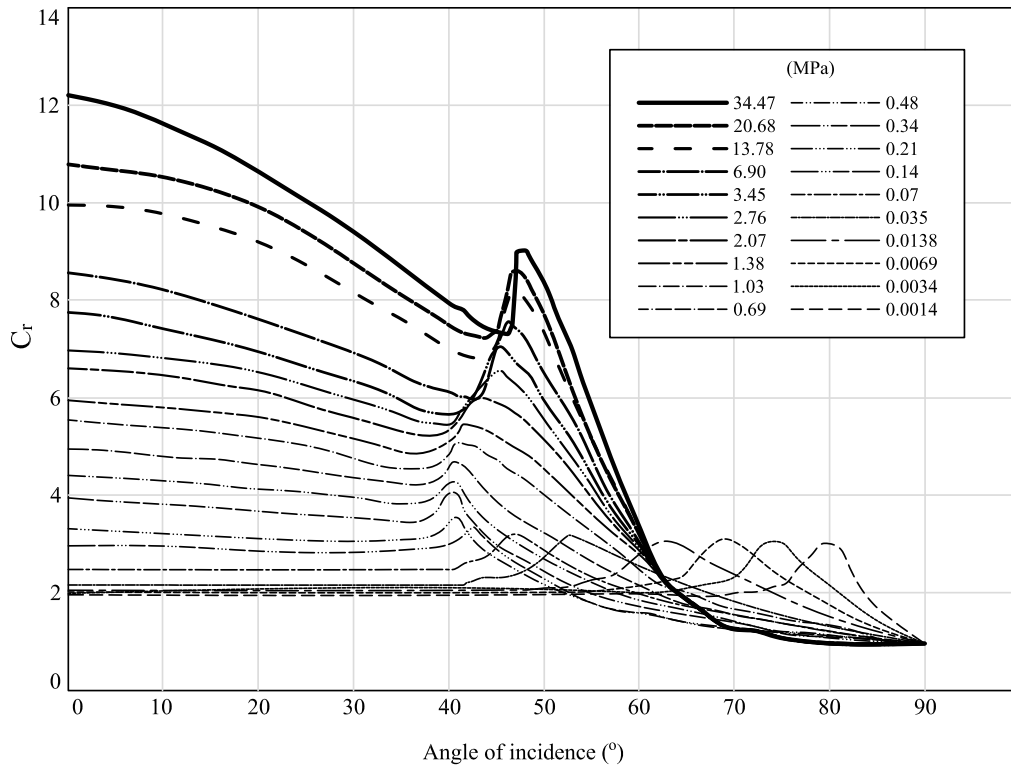


Figure 2-11: Effect of angle of incidence on the reflection coefficient (DoD, 2002)

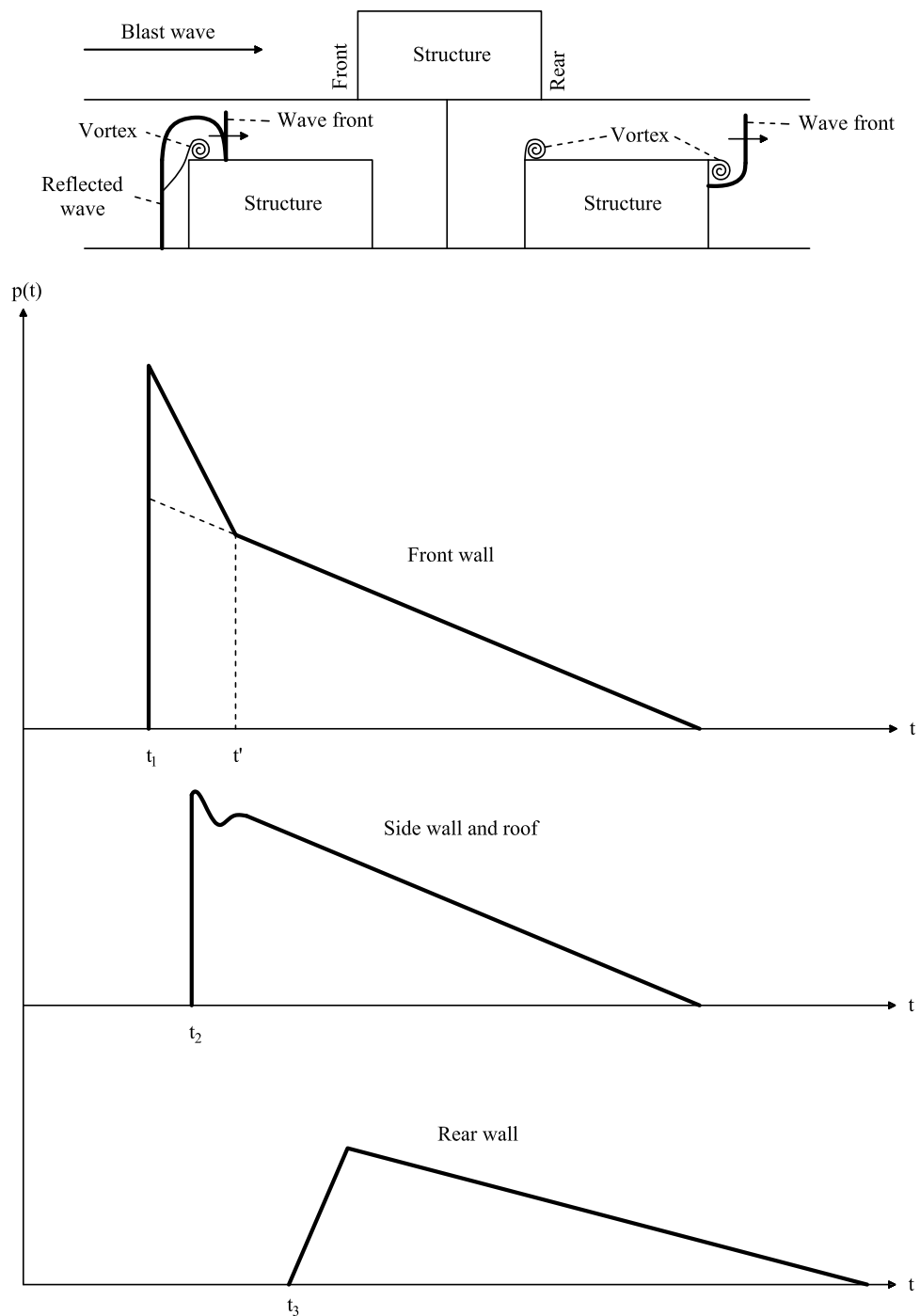


Figure 2-12: Blast loading on a rectangular-in-plan structure

2.3. Structural response

Structural response to blast loading is highly dependent upon (1) the peak pressure, (2) the applied impulse and (3) the pressure time history, as well as the characteristics of the structure itself (T). A brief description of the dependency of structural response to the complex nature of the applied loading can be found in this section.

2.3.1. Analysis of an elastic SDOF

The simplest possible case of a component subjected to blast loading is the case of an equivalent lumped-mass SDOF model. This model is considered equivalent to an actual structural component, by considering its displacement equal with the SDOF displacement. As shown in Figure 2-13, blast loading $P(t)$ is considered to be an equivalent triangular loading and refers to the resultant blast pressure, by taking into account the corresponding tributary area of the element.

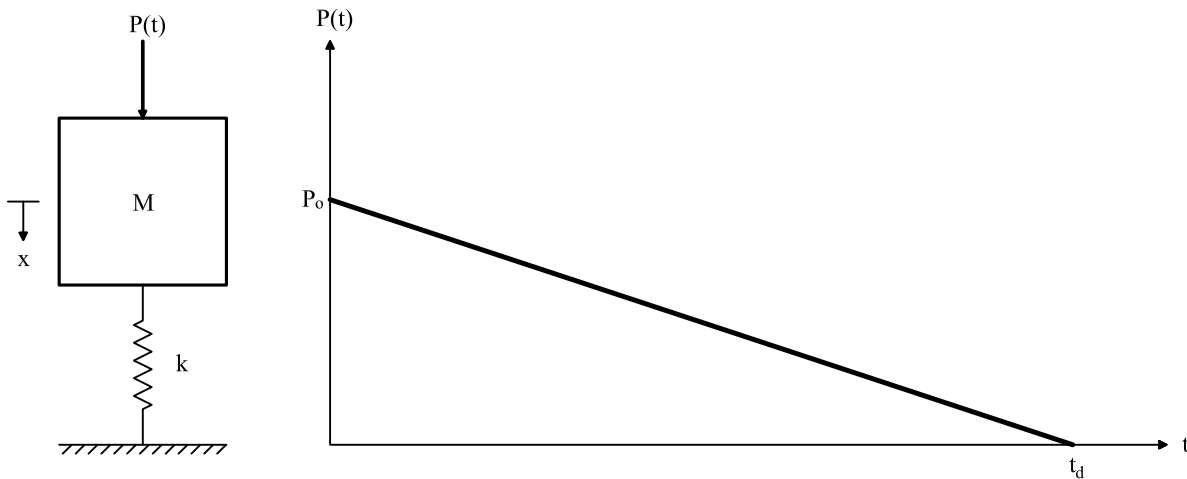


Figure 2-13: SDOF model and blast loading

In this case, the response $R(t)$ of the SDOF (resistance time history) can be characterized by three response regimes. These regimes depend on the ratio of the blast load duration t_d to the SDOF natural period T :

- $t_d/T < 0.1$: Impulsive response
- $0.1 < t_d/T < 10$: Dynamic response
- $10 < t_d/T$: Quasi-static response

As presented through Figure 2-14, the maximum displacement in the impulsive regime occurs after the application of the blast loading is completed. On the contrary, the maximum displacement in the quasi-static regime occurs before the blast loading ceases. In the intermediate region, the response is considered to be dynamic. It is worth noting that quasi-static response is dictated only by peak pressure P_0 , while impulsive response is dictated only by impulse i , as calculated by Equation (2-6).

$$i = \frac{1}{2} \cdot P_0 \cdot t_d \quad (2-6)$$

In this context, useful conclusions can be drawn with regard to the dynamic response of the elastic SDOF in comparison to the static response (i.e., the response of the elastic SDOF as if blast loading was applied statically). This comparison can be illustrated with the use of the Dynamic Load Factor (DLF), which is calculated by the ratio of the maximum dynamic displacement x_{max} to the static displacement x_{st} . As observed in Figure 2-15, the maximum DLF is 2.0 and it appears as the quasi-static asymptote. On the contrary, DLF at the impulsive asymptote is a function of the ratio of blast duration to the SDOF natural period. This function can be expressed through Equation (2-7).

$$DLF = \frac{x_{max}}{x_{st}} = \pi \cdot \frac{t_d}{T} \quad (2-7)$$

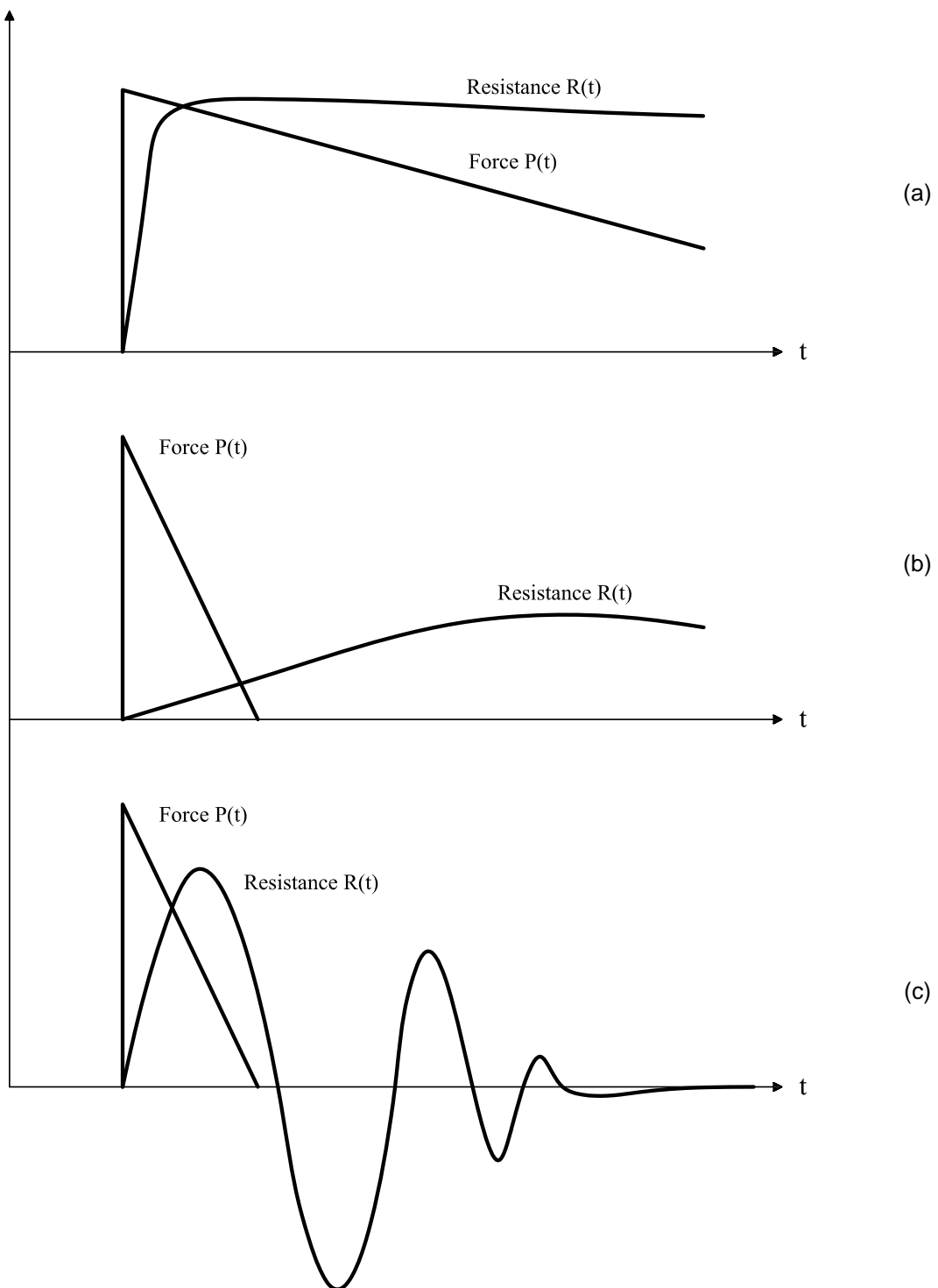


Figure 2-14: Response of an elastic SDOF subjected to blast loading: (a) Quasi-static response; (b) Impulsive response; (c) Dynamic response

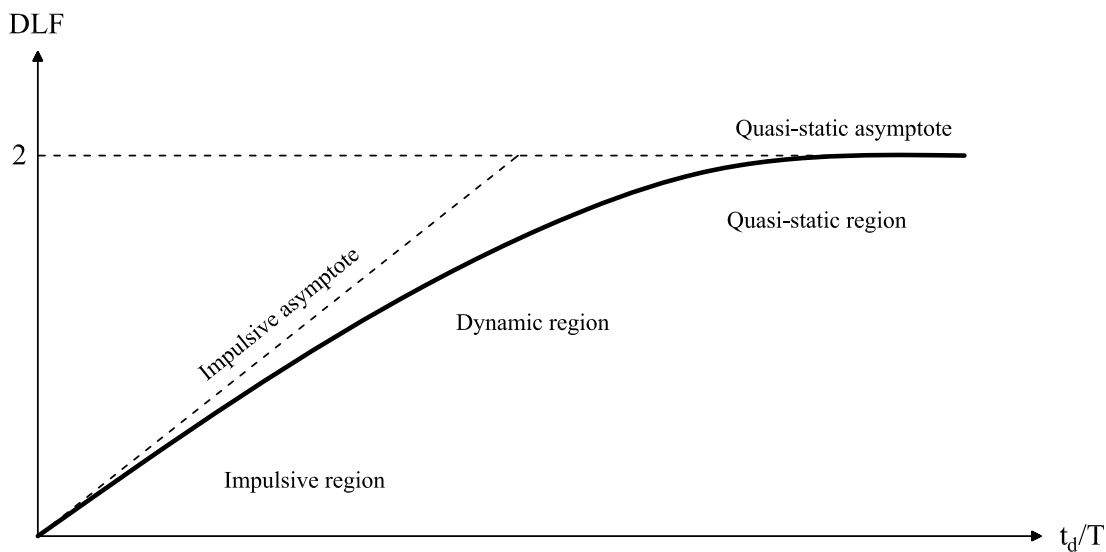


Figure 2-15: DLF of an elastic SDOF subjected to a triangular detonation blast loading

2.3.2. Analysis of an elastic-perfectly plastic SDOF

When designing a component against blast loading, there is the option of designing it not to enter into plasticity and behave elastically. However, this approach generally leads to large section properties and overconservative designs. A way to overcome this issue is to design the components with elastoplastic response exhibiting acceptable plastic strains.

As shown by Biggs (1964), if the aforementioned elastic SDOF is replaced by an elastic-perfectly plastic SDOF with maximum resistance R_u and ductility $\mu = x_{max}/x_{el}$, the diagrams of Figure 2-16 and Figure 2-17 occur. Elastic displacement is denoted by x_{el} . The diagrams refer to detonation and deflagration blast loading, respectively. Furthermore, they are shown in a non-dimensional form by using the ratio of blast load duration to the natural period t_d/T in the horizontal axis and the ratio of maximum resistance to peak pressure R_u/P_o for the distribution of the curves. It is noted that ductility can reach large values for low R_u/P_o ratios, which are not acceptable for structural applications, while for $R_u/P_o = 2$, the same curve as the one of the elastic SDOF is presented. Thus, the response of an elastoplastic component subjected to blast loading can be quickly estimated by using these diagrams.

2.3.3. Strain-rate effects

When it comes to blast loading, the duration is extremely small (in the order of ms) and the strain rate, which appears over the respective structural components, is high. It is well known (Dusenberry, 2010) that increased strain rate leads to higher strength characteristics in construction materials, such as structural steel or reinforced concrete.

In order to account for the strain-rate effects, a modification can simplistically be applied with an increase factor to the strength of the corresponding components, namely the Dynamic Increase Factor (DIF). More sophisticated material laws, calibrated with experimental tests, can also be used. Such a plastic flow material model is the Cowper-Symonds (1957) strength model, as expressed through Equation (2-8), with σ being the plastic stress, ϵ_{pl} being the plastic strain and $\dot{\epsilon}_{pl}$ the plastic strain rate. It comprises of the Johnson-Cook (1983) model for the hardening effects (through yield stress A and hardening coefficients B , θ) and the Cowper-Symonds coefficients D , q for the strain-rate effects.

$$\sigma = (A + B \cdot \varepsilon_{pl}^\theta) \cdot \left(1 + \left(\frac{\varepsilon_{pl}}{D}\right)^{1/q}\right) \tag{2-8}$$

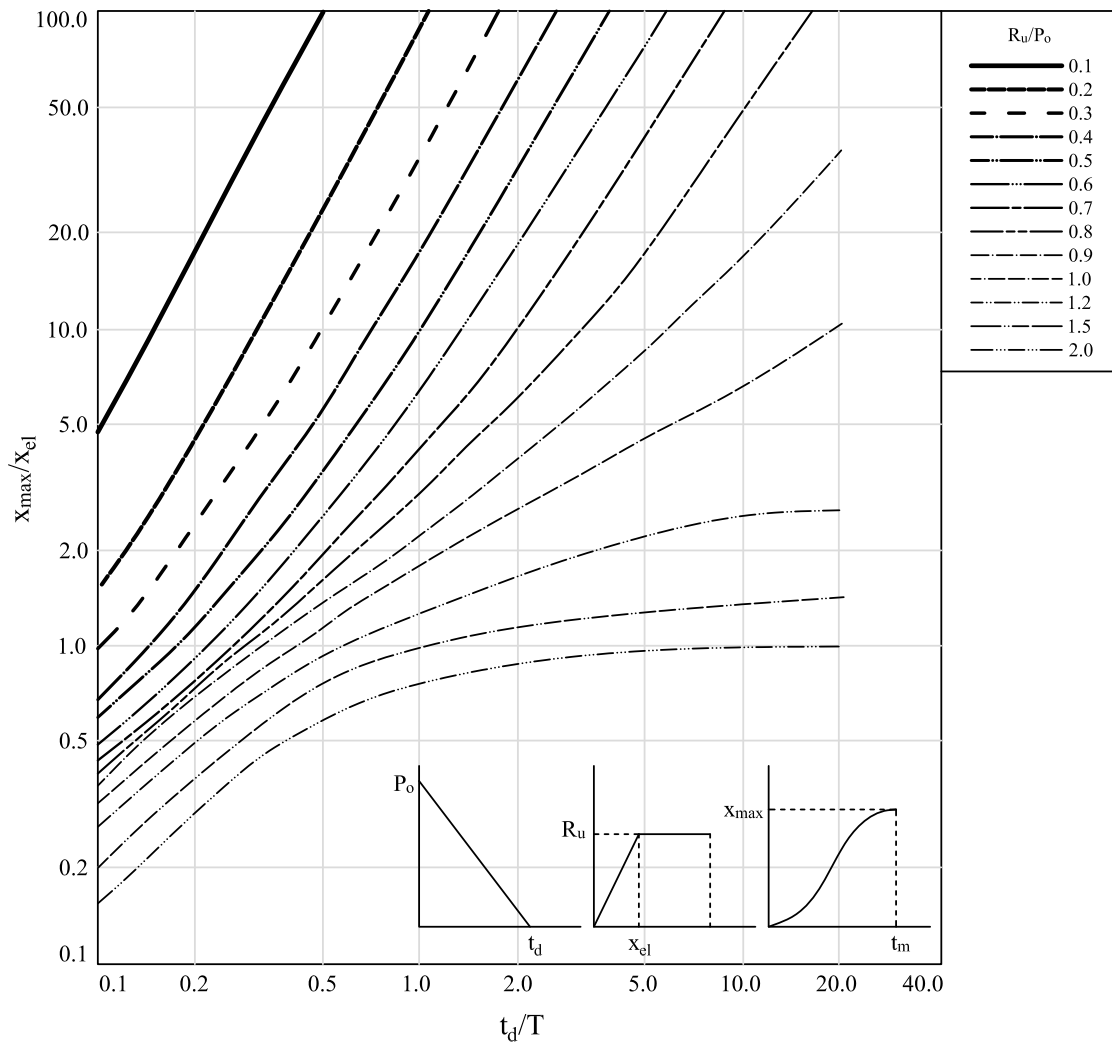


Figure 2-16: Ductility of an elastic-perfectly plastic SDOF subjected to triangular detonation blast loading (Biggs, 1964)

2.3.4. Response limits

The adequacy or not of structural components subjected to blast loading can generally be determined by a variety of engineering demand parameters, which may be maximum displacement, maximum support rotation, maximum plastic strains, maximum ductility, etc. The values of these parameters and the respective limit states are prescribed by structural guidelines, client requirements or detailed damage analyses.

As an indicative example, the response limits regarding the case of steel cladding are presented in Table 2-1 to Table 2-4, with θ_m being the maximum support rotation, as calculated through Equation (2-9), and L being the length of the examined component.

$$\theta_m = \tan^{-1}\left(\frac{x_{max}}{L/2}\right) \tag{2-9}$$

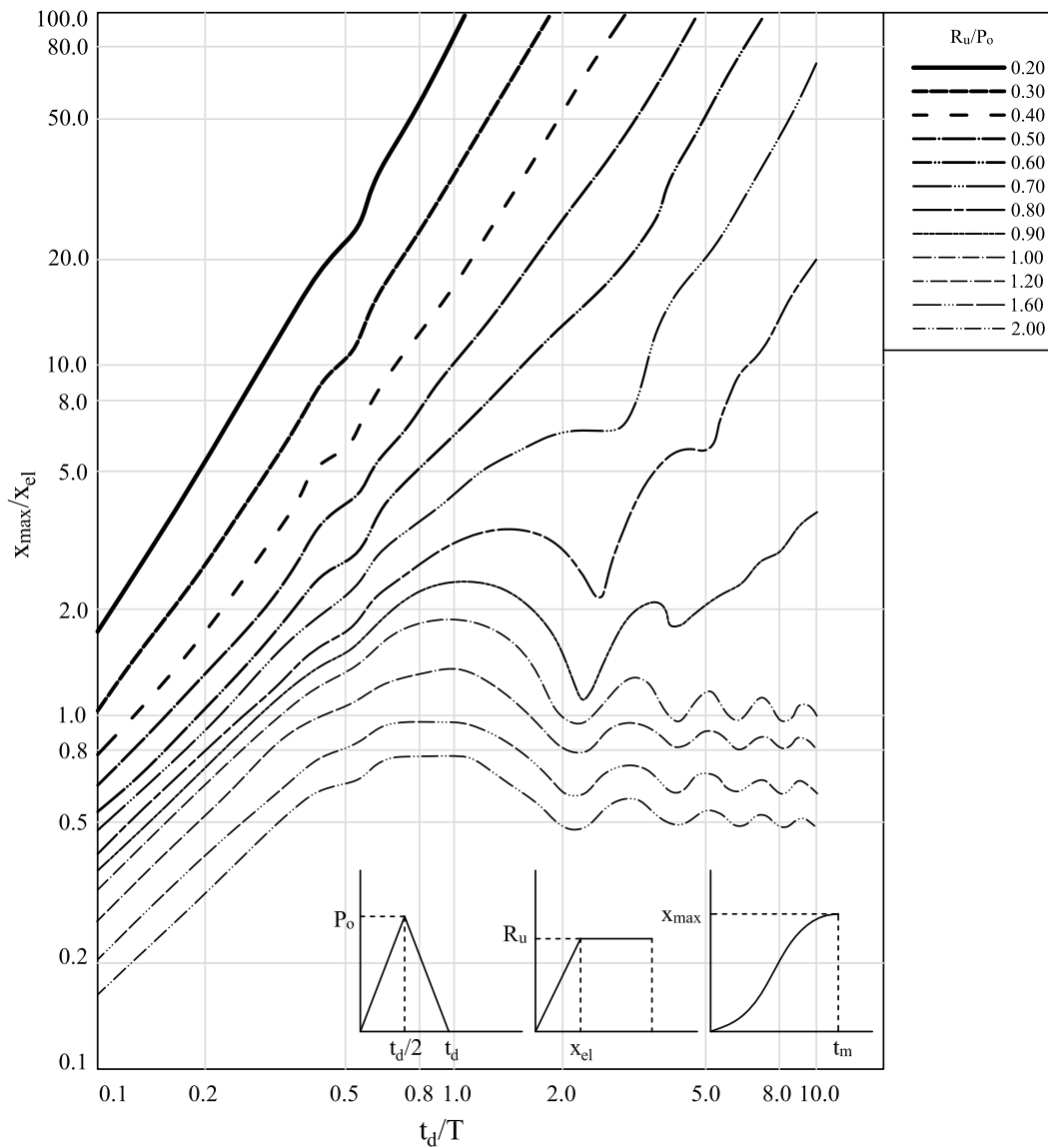


Figure 2-17: Ductility of an elastic-perfectly plastic SDOF subjected to triangular deflagration blast loading (Biggs, 1964)

Table 2-1: Response criteria for explosive safety design (DoD, 2008)

	Category 1		Category 2	
	μ	θ_m	μ	θ_m
Structural steel plates	10	2°	20	12°
Cold-formed wall panels without tension membrane action	1.75	1.25°	(-)	(-)
Cold-formed wall panels with tension membrane action	6	4°	(-)	(-)

Category 1: Attenuate blast pressures and structural motion to a level consistent with personnel tolerances

Category 2: Protect equipment, supplies, and stored explosives from fragment impact, blast pressures, and structural response

Table 2-2: Response criteria for upper bound of each damage level (PDC, 2008b; Dusenberry, 2010)

	μ			θ_m		
	Moderate	Heavy	Hazardous	Moderate	Heavy	Hazardous
One-way corrugated metal panel	3	6	12	3°	6°	10°

Table 2-3: Response criteria for antiterrorism design (PDC, 2008a)

	Superficial		Moderate		Heavy		Hazardous	
	μ	θ_m	μ	θ_m	μ	θ_m	μ_{max}	θ_m
Corrugated panel (1-way) with full tension membrane	1	(-)	3	3°	6	6°	10	12°
Corrugated panel (1-way) with some tension membrane	1	(-)	(-)	1°	(-)	4°	(-)	8°
Corrugated panel (1-way) with limited tension membrane	1	(-)	1.8	1.3°	3	2°	6	4°
Built-up blast doors (composite plate and stiffeners)	3	1°	10	6°	20	12°	(-)	(-)
Plate blast doors (solid)	3	1°	20	6°	40	12°	(-)	(-)

Table 2-4: Response criteria for blast-resistant design of petrochemical facilities (ASCE, 2010)

	Low response		Medium response		High response	
	μ	θ_m	μ	θ_m	μ	θ_m
Steel plates	5	3°	10	6°	20	12°
Cold-formed light-gage steel panels (with secured ends)	1.75	1.25°	3	2°	6	4°
Cold-formed light-gage steel panels (with unsecured ends)	1	(-)	1.8	1.3°	3	2°

2.4. Conclusions

A brief introduction into blast loading and its effects on structures was presented in this chapter. The following information was discussed:

- The actual and equivalent blast pressure time histories.
- The interaction of a building with a blast wave.
- The response of an elastic SDOF subjected to blast loading.
- The response of an elastic-perfectly plastic SDOF subjected to blast loading.
- The strain-rate effects of blast loading with relevant material models.
- The response limits to blast loading with emphasis on steel cladding.

The presented theoretical background is used throughout the thesis.

2.5. References

American Society of Civil Engineers (2010) Design of blast-resistant buildings in petrochemical facilities. doi: 10.1061/9780784410882.

- Biggs, J. M. (1964) Introduction to structural dynamics. United States of America: McGraw-Hill.
- Cormie, D., Mays, G. and Smith, P. (2009) Blast effects on buildings. ICE Publishing. doi: 10.1680/beob.61477.
- Cowper, G. and Symonds, P. (1957) 'Strain hardening and strain-rate effects in the impact loading of cantilever beam', Brown University Division of Applied Mathematics.
- Dusenberry, D. O. (2010) Handbook for blast resistant design of buildings. John Wiley & Sons. doi: 10.1002/9780470549070.
- Hoffmeister, B. et al. (2015) 'Advanced design methods for blast loaded steel structures', European Commission Directorate-General for Research and Innovation.
- Hyde, D. (1993) 'User's guide for microcomputer program CONWEP, applications of TM 5-855-1, "Fundamentals of protective design for conventional weapons"', U.S. Army Engineer Waterways Experiment Station.
- Johnson, G. R. and Cook, W. H. (1983) 'A constitutive model and data from metals subjected to large strains, high strain rates and high temperatures', in *Proceedings of the Seventh International Symposium on Ballistics*. The Hague, Netherlands.
- Karlos, V. and Solomos, G. (2013) Calculation of blast loads for application to structural components, Publications Office of the European Union.
- Protective Design Center (2008a) 'PDC TR-06-08: Single degree of freedom structural response limits for antiterrorism design', U.S. Army Corps of Engineers. Available at: <https://pdc.usace.army.mil/library/tr/06-08>.
- Protective Design Center (2008b) 'PDC TR-08-07: Component explosive damage assessment workbook', U.S. Army Corps of Engineers.
- Rigby, S. E. et al. (2014) 'The negative phase of the blast load', *International Journal of Protective Structures*, 5(1), pp. 1–19. doi: 10.1260/2041-4196.5.1.1.
- U.S. Department of Defense (2002) 'UFC 03-340-01: Design and analysis of hardened structures to conventional weapon effects'.
- U.S. Department of Defense (2008) 'UFC 03-340-02: Structures to resist the effects of accidental explosions'.

Chapter 3

Mechanisms for cladding mitigation potential and literature review

3.1. Introduction

A description of the mechanisms, which could render cladding components beneficial for the supporting structure in terms of response to blast loading, is included in the present chapter. Furthermore, significant literature findings correlated with these mechanisms are shown. Complete overview of all research studies, which refer to the structural behavior of cladding subjected to blast loading, is not feasible because of the vast amount of the performed scientific research, especially if research is viewed from a multidisciplinary perspective. More specifically, except for civil engineering, cladding under shock and impact also constitutes a primary research field in aerospace engineering, naval architecture, military protection, etc. Furthermore, excellent sources can be found in the literature about the theoretical background, structural design and structural assessment of cladding subjected to blast loading. The theoretical basis of structural components subjected to blast loading and calculation of their response through simplified models has been demonstrated by [DA \(1957\)](#), [Biggs \(1964\)](#) and is summarized in Chapter 2. Extensive design guidance over the design of cladding subjected to blast loading can be found in [DoD \(2008\)](#). Moreover, the key parameters, which determine the response of structural elements subjected to blast loading, can be found in [Cormie, Mays and Smith \(2009\)](#), with multi-material examples, and an overview of the structural assessment of cladding subjected to blast loading with reference to code specifications can be found in [Dusenberry \(2010\)](#). Chapters 3-8 also contain references to literature that are specific to their content.

3.2. Philosophy of cladding design

Cladding components can sustain different levels of damage, depending on the magnitude of the possible blast loads and their capacity, ranging from purely elastic response to minimal damage, permanent

plastic deformation, up to complete failure. Detailed information about the pressure pulses and their interaction with the corresponding building envelope can be found in Chapter 2. Particular emphasis should be given to the cladding components because they are critical for blast-resistant applications. This is not in agreement with typical structural engineering practice, according to which cladding components are considered secondary elements and are given small attention in terms of both man-made imposed loads and environmental loads, such as in the cases of wind, snow or earthquake.

The fact that the cladding components are the first to receive the blast pressure, has led to the following key design strategies according to [Hetherington and Smith \(1994\)](#), [Dusenberry \(2010\)](#) and [Palanivelu et al. \(2011\)](#):

- 1) Prevent component failure: The response of cladding components protecting personnel and equipment should be limited to levels below those causing failure or extensive damage.
- 2) Maintain building envelope: The cladding components should have the strength to resist blast loading because, if blast overpressure enters the interior, it can cause significant damage and injuries.
- 3) Minimize flying debris: The cladding components should have the ability not to become hazardous projectiles to the occupied space. This is applied in an effort to mitigate extensive injuries to the building occupants by minimizing flying debris.
- 4) Blast containment in the cladding: The main load bearing members should be safeguarded by containing blast consequences in the cladding. Design strategies (1) to (3) should be in effect in case cladding enters into plasticity when containing blast consequences.

The present thesis is focused on the fourth design strategy, namely blast containment in the cladding. The mitigation of blast consequences to the main loading bearing members is further discussed in the next sections. It is noted that the main load bearing members are denoted as the supporting structure in the context of this thesis.

3.3. Cladding response to blast loading

Regarding the design strategy of blast containment in the cladding, cladding can be divided into three types: (1) Cladding-to-framing type, where the structural system of the cladding is composed of a surface supported at its edges to the supporting structure; (2) Sacrificial cladding type, where the cladding is attached directly to the supporting structure (e.g., a column) as a layer; and (3) Energy-absorbing connectors type, where the energy absorption is facilitated in the connections of the cladding to the supporting structure.

In all three types, the static response of cladding can be characterized by load (P) versus deflection (δ) curves, commonly known as resistance curves. Typical profiles of resistance curves of the cladding-to-framing type are shown in Figure 3-1 ([Xue and Hutchinson, 2004](#); [Gouverneur, Caspeepele and Taerwe, 2013](#); [Zobec et al., 2015](#); [Khalifa, Tait and El-Dakhakhni, 2017](#)). Resistance curves are critical for blast attenuation, as they control the maximum applied load to the supporting components through the value of resistance corresponding to the maximum reached deflection. As observed in Figure 3-1, the cladding's resistance, i.e., initial elastic stiffness, maximum resistance, post-elastic characteristics, depends on the mechanical properties of the materials and boundary conditions, thus their proper selection is critical for the supporting structure. The applied blast load is typically characterized by a wide range of peak pressure and impulse combinations. Each pressure–impulse pair generates a unique response profile, thereby resulting in different cladding dynamic reaction histories. Consequently, the response of

the underlying components supporting the cladding is also unique and specific to the: (1) Cladding's resistance, mass and stiffness, (2) Blast load profile.

In other words, the cladding can be considered as an oscillator that is transforming the applied blast load history into a new load profile, the dynamic reaction time history, that is exerted to the supporting structure. The cladding's dynamic reaction time history depends on the blast load profile, the cladding's natural frequency and its resistance (Figure 3-1). A representative reaction time history, as computed with the finite element (FE) analysis of a simply supported steel cladding subjected to blast, is shown in Figure 3-2(a). It can be observed from the reaction time history plot of Figure 3-2(a) that the cladding enters its plastic range, as there is an approximately constant maximum reaction force for a relatively long period of time in the first cycle. By applying a Fast Fourier Transform (FFT) (Yang, 2009) to the reaction time history and extracting its Power Spectral Density (PSD), it can be observed that the time history is not characterized by a unique frequency [Figure 3-2(b)]. Instead, the reaction history can be decomposed into different frequencies with varying power densities.

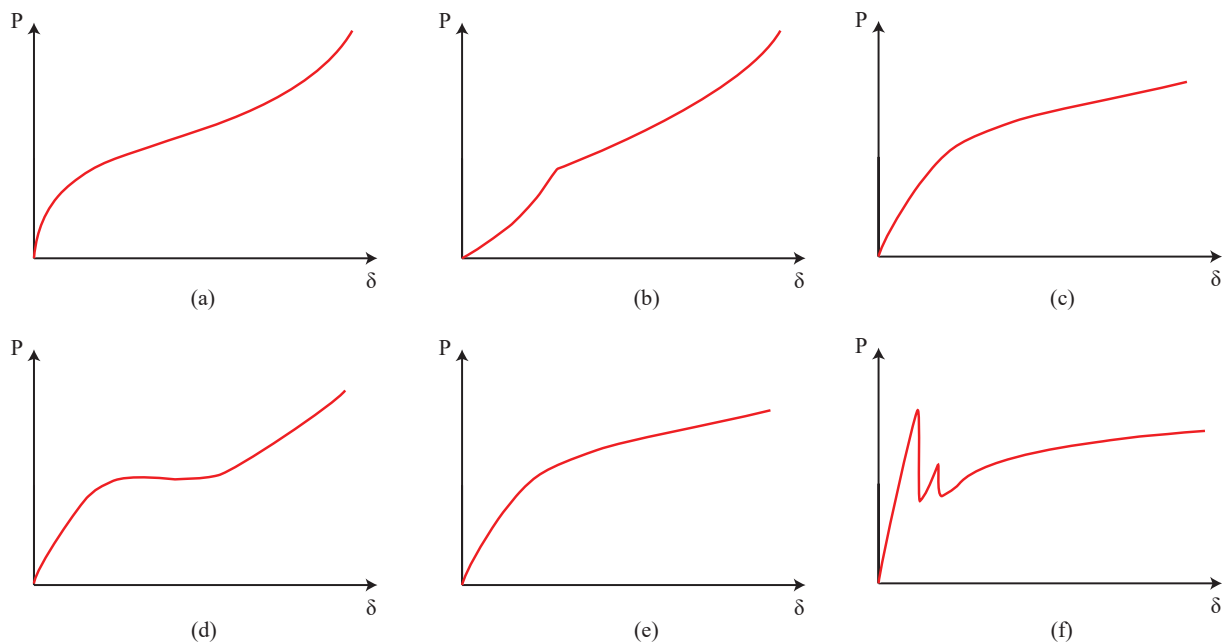


Figure 3-1: Typical quasi-static load (P) versus deflection (δ) curves for different cladding types: (a) Steel sandwich panels with clamped supports [data from Xue and Hutchinson (2004)]; (b) Monolithic steel plate with clamped supports [data from Xue and Hutchinson (2004)]; (c) Steel sandwich panels with insignificant membrane action [data from Khalifa, Tait and El-Dakhkhni (2017)]; (d) Concrete panels with clamped supports [data from Gouverneur, Caspeepe and Taerwe (2013)]; (e) Concrete panels with insignificant membrane action [data from Gouverneur, Caspeepe and Taerwe (2013)]; (f) Laminated glass [data from Zobec et al. (2015)]

3.4. Activated mechanisms for cladding mitigation potential

Depending on the cladding characteristics, the plastic energy absorption and inertial resistance mechanisms may be activated (Rutner and Wright, 2016), which can lead to a dynamic reaction on the supporting structure with significantly lower peak force and longer duration than the applied blast loading. More specifically, the peak force is typically reduced, while the blast impulse remains approximately the same (Palanivelu et al., 2011; Bornstein and Ackland, 2013). The plastic energy absorption mechanism is mainly dictated by the cladding's ultimate resistance, which is responsible for the conversion of blast energy into plastic energy, while the inertial resistance mechanism is mainly dictated by the cladding's

mass and stiffness and renders the response against blast loading slower, thus leading to reduced peak reactions.

Furthermore, in accordance with Chapter 2, the response of a component subjected to blast pressure is characterized by three well-defined response regimes. These regimes are the impulsive (with $t_d/T < 0.1$ ratios), dynamic (with $0.1 < t_d/T < 10.0$ ratios) and quasi-static (with $t_d/T > 10.0$ ratios) (Cormie, Mays and Smith, 2009), which are shown in Figure 3-3. Assuming a cladding-to-supporting-structure system, these three response regimes are directly correlated with the inertial resistance mechanism. When the cladding is subjected to blast loading it can have a quasi-static (no significant inertial resistance), an impulsive (significant inertial resistance) or a dynamic (moderate inertial resistance) response. Time histories of the three response types are illustrated in Figure 3-4, along with the applied blast load history (the supporting structure has been considered as rigid), where T_1 is the natural period of the cladding.

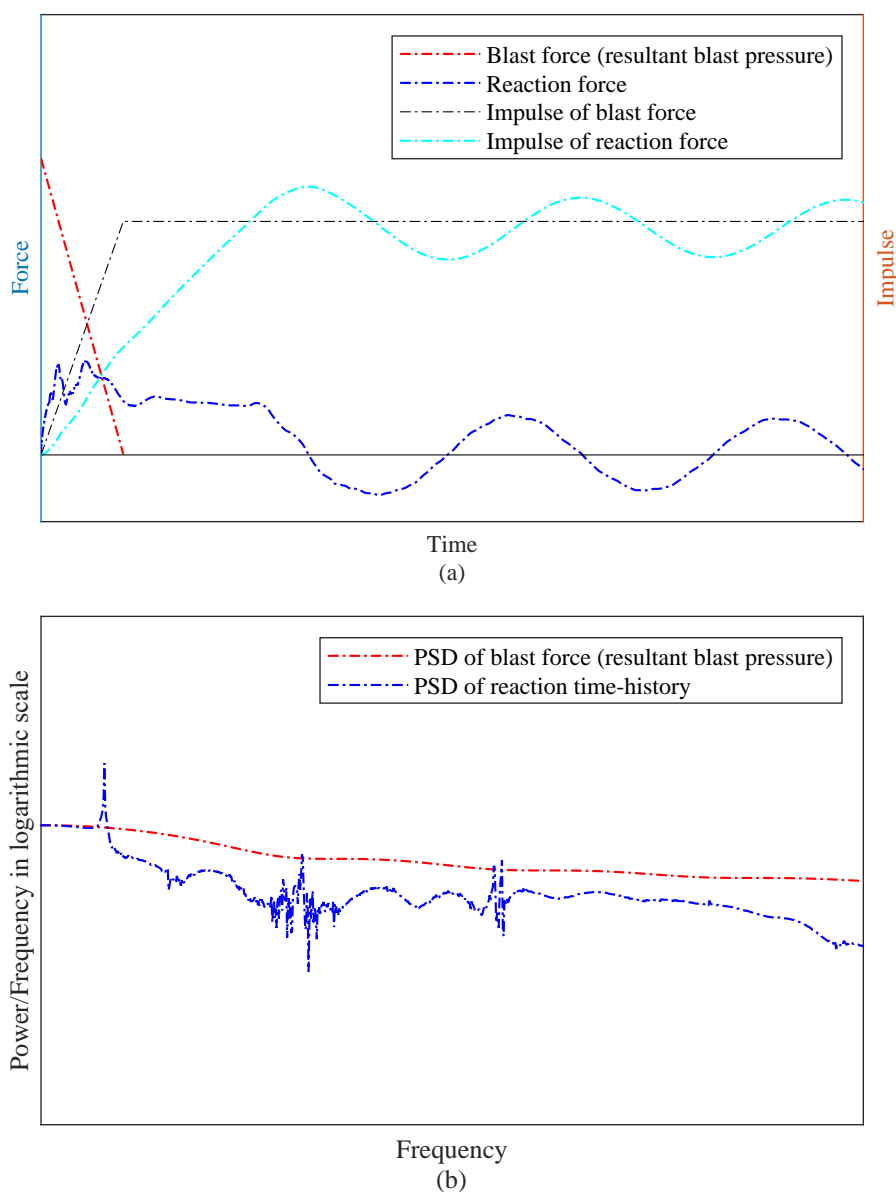


Figure 3-2: Typical response of steel cladding subjected to blast loading: (a) Reaction time history; (b) Power Spectral Density

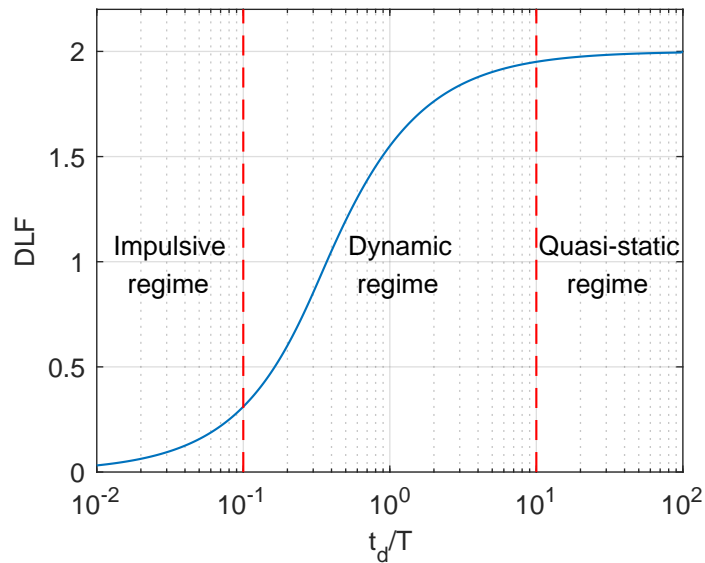


Figure 3-3: Types of response in terms of the DLF and the t_d/T ratio in an elastic SDOF

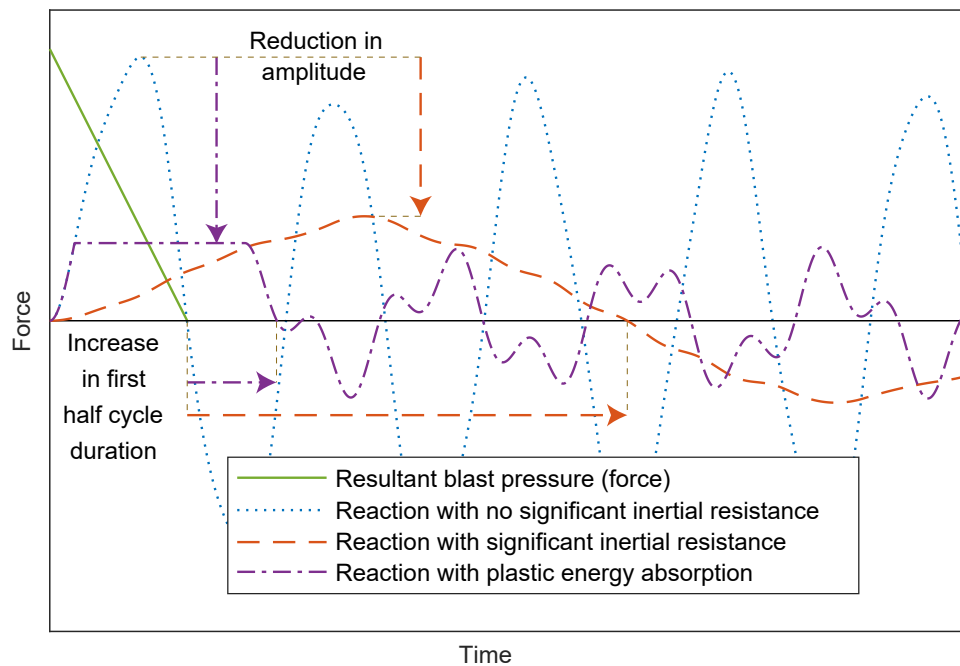


Figure 3-4: Qualitative illustration of reaction time histories of the cladding with two different governing response mechanisms; the plastic energy absorption and the inertial resistance

Generally, the reaction of the cladding is associated with the cladding's natural period. In the case of a cladding with a significantly smaller natural period than the duration of the applied load (quasi-static response), the maximum displacement and the corresponding maximum reaction, which is approximately equal to the peak blast pressure P_o , occur rapidly and before the excitation ceases. In other words, the time of peak response is lower than the duration of the applied blast load (cladding reaction without significant inertial resistance in Figure 3-4). In the case of a cladding with considerably higher natural period compared to the duration of the blast load (impulsive response), the displacement and the corresponding dynamic reaction, continue to increase past the duration of the applied blast load. The time of peak displacement and reaction is higher than the duration of the applied blast load (cladding reaction with significant inertial resistance in Figure 3-4). Interestingly, in the impulsive behavior, where

cladding responds slowly to the blast load, the period of the reaction oscillation is increased, while the amplitude is decreased. This represents the inertial resistance mechanism.

Similar behavior takes place when the resistance R_u of the cladding is reached during the oscillation. When a structural component is subjected to a pressure of large amplitude, it usually reaches its yield capacity and subsequently enters into the plastic regime. The amplitude of the reactions is limited due to the yield capacity of the cladding. Thus, portion of the blast energy is dissipated in the cladding through plastic deformation and the duration of at least the first cycle of the oscillation is increased (cladding reaction with plastic energy absorption in Figure 3-4). This represents the plastic energy absorption mechanism.

For the plastic energy absorption and the inertial resistance mechanisms, the resulting effects in terms of dynamic reaction are similar. That is, the amplitude of the cladding reactions is decreased, while their duration is increased. However, this effect is attained through a different mechanism.

3.5. Literature findings about cladding with mitigation potential

A brief overview of research studies investigating the response of specific cladding systems subjected to blast loading is presented in this section. The literature findings are analyzed regarding the cladding mitigation potential. The section is divided into three paragraphs, each one of them representing a cladding type: (1) Cladding-to-framing type; (2) Sacrificial cladding type; and (3) Energy-absorbing connectors type.

3.5.1. Cladding-to-framing

The cladding-to-framing type refers to the claddings, which are supported at their edges to their supporting structure. A primarily bending and membrane behavior is normally anticipated in this type of cladding systems. This type is analyzed in the present section through six research studies.

Xue and Hutchinson (2004) investigated different types of sandwich panels subjected to impulsive loads and compared them with the equivalent solid plates in terms of maximum displacement and plastic energy absorption. More specifically, multiple core geometries were examined, with each one leading to a different plastic dissipation curve. The energy absorption was measured by using the averaged plastic energy dissipated per unit area \overline{U}_p , with L being half the panel length, σ_Y the yield stress, δ_{punch} the punch displacement, ρ the material density and \overline{M} the mass per unit area (Figure 3-5). The sandwich panels were found to have the potential to dissipate more plastic energy than the equivalent material and mass solid plates due to the ability of their core to behave plastically.

Chen and Hao (2012) performed a numerical study of a multi-arch double-layered blast-resistant door (Figure 3-6) subjected to close-in blast loading. Multiple geometries were examined by differentiating the thicknesses of the arched and internal layers. The internal energy and the maximum force support reactions in all three directions were calculated during the dynamic time history solutions. It was shown that increase of thickness led to reduced peak reactions.

Chen and Hao (2013) performed a numerical study of rotational hinge devices, which were incorporated into the core of sandwich panels (Figure 3-7). The rotational hinge devices were applied in order to improve operational performance of sandwich door panels against close-in blast loading. The effect of these devices was presented in comparison with the effects of the equivalent monolithic plates. A 75.6%

reduction was observed in the peak reaction force by comparing the respective reaction time histories, when subjecting the claddings to blast loading induced from 500 g of TNT at a distance of 300 mm.

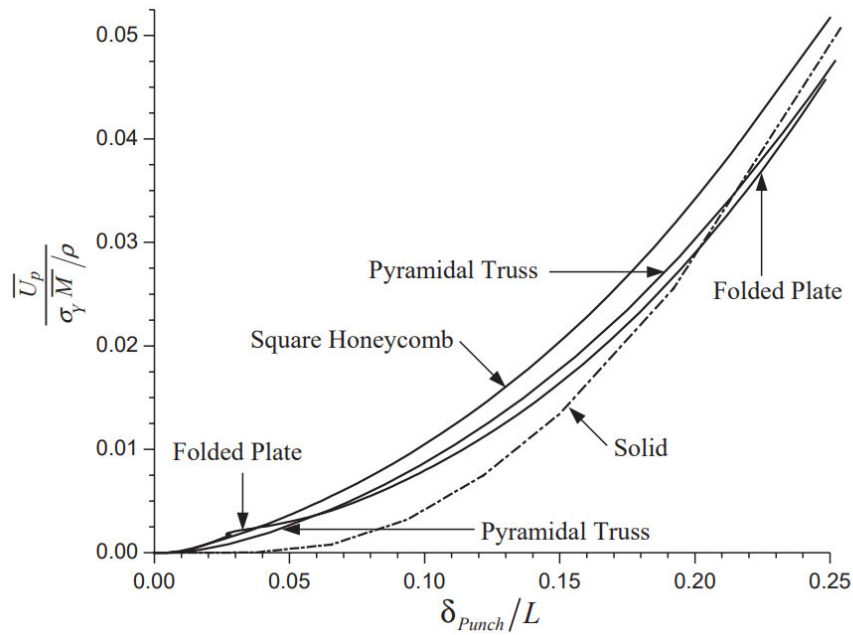


Figure 3-5: Plastic energy dissipation of four different sandwich panel types [reprinted from Xue and Hutchinson (2004)]

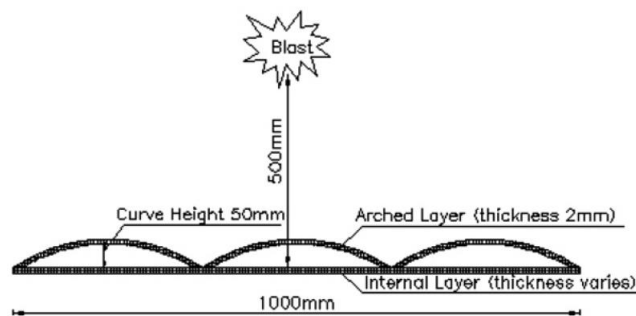


Figure 3-6: Schematic section diagram of typical curved panels [reprinted from Chen and Hao (2012)]

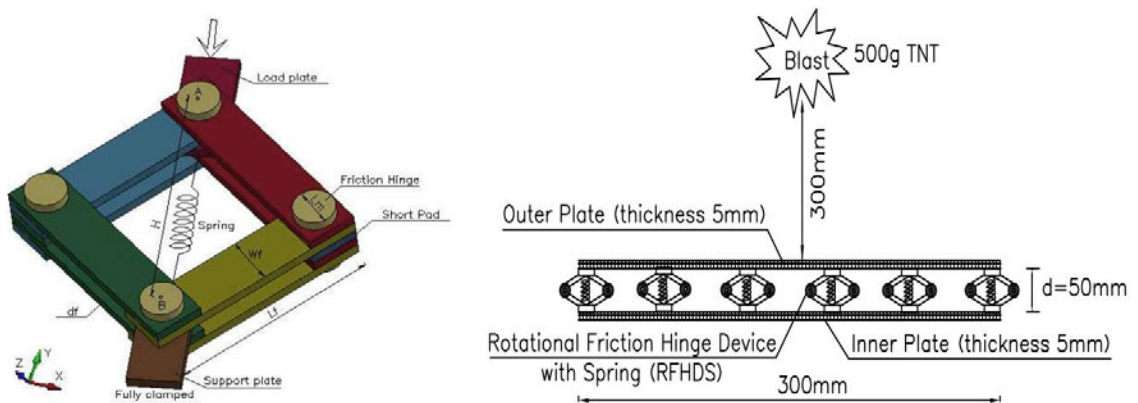


Figure 3-7: Schematic diagram of rotational hinge devices with spring incorporated in the sandwich panels [reprinted from Chen and Hao (2013)]

Hoffmeister et al. (2015) examined typical cladding used in industrial facilities (Figure 3-8), which are susceptible to accidental explosions. After performing an investigation about the structural configuration (type, section properties and material), the load transfer function was explored regarding the cladding energy absorption capacity. The experimental results along with the respective computational models were used in order to derive the failure modes and analytical solutions, taking into account the membrane effects. It was shown that when cladding was subjected to blast loading, the peak reaction force was significantly decreased and the reaction duration was increased by keeping the same impulse with the initial blast pressure time history.

Goel, Matsagar and Gupta (2011) investigated the effects of different stiffener configurations on the response of rectangular plates (Figure 3-9) subjected to close-in airblast loading. Their plastic-energy-absorption capacity was examined by presenting the respective plastic energy time histories.

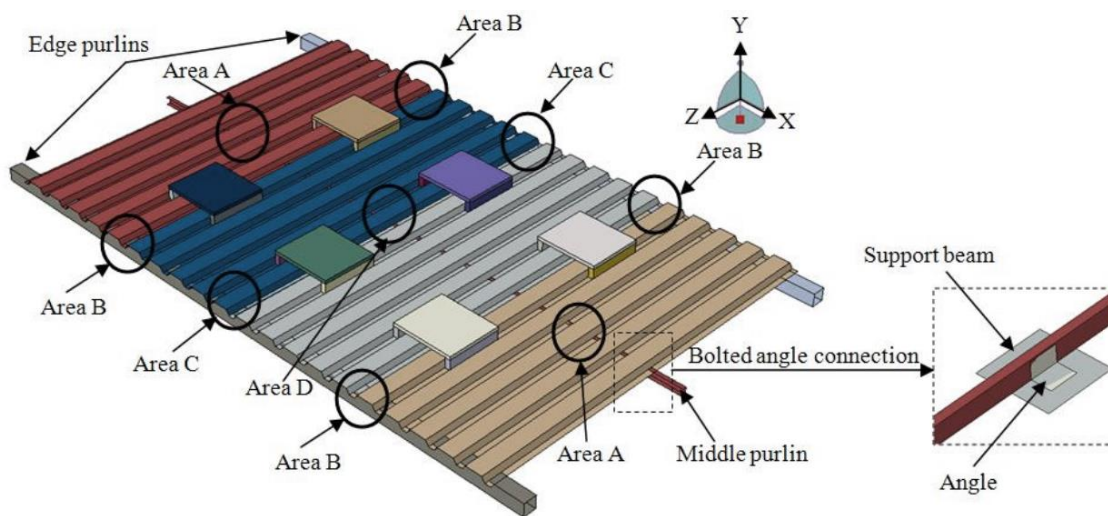


Figure 3-8: Model of the cladding and its supporting structure [reprinted from Hoffmeister et al. (2015)]

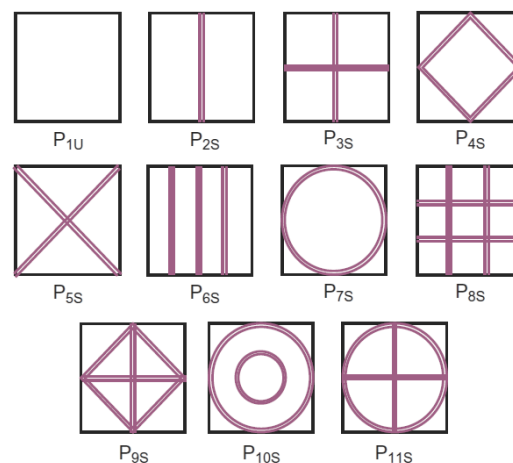


Figure 3-9: Stiffener configurations of rectangular plates subjected to blast loading [reprinted from Goel, Matsagar and Gupta (2011)]

Sun et al. (2019) introduced a novel hexagonal-cell hierarchical-core sandwich panel (Figure 3-10). The mitigation potential was calculated through the Specific Energy Absorption (SEA), which represents the ratio of the absorbed energy to the core mass. It was shown that regular honeycombs lead to higher SEA than hierarchical honeycombs.

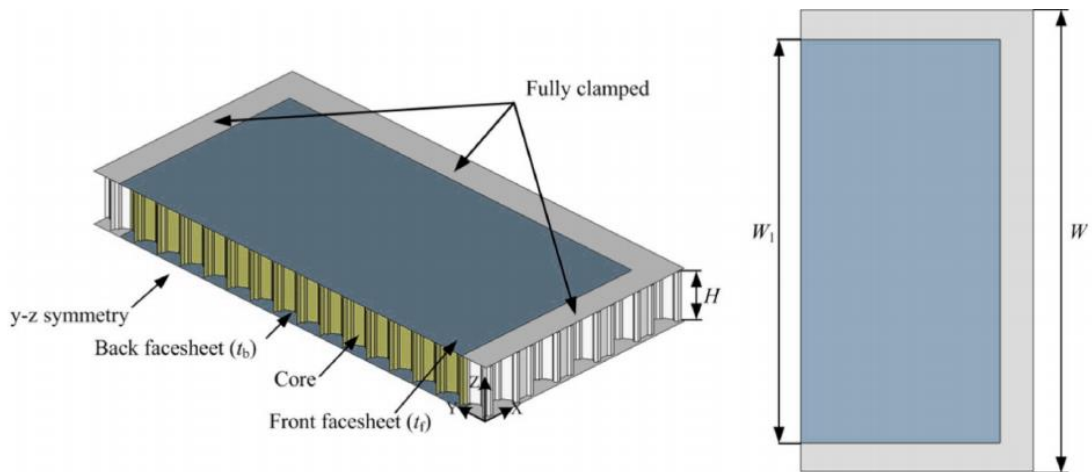


Figure 3-10: Calculation model of an hexagonal sandwich panel [reprinted from Sun et al. (2019)]

3.5.2. Sacrificial cladding

The sacrificial cladding type refers to the claddings that are attached directly to their supporting structure. More specifically, in this type of claddings a generally axial behavior is anticipated, according to which the failure load of the core is kept at low levels in order to be able to absorb energy and deform plastically. This type is analyzed in the present paragraph with three research studies.

Guruprasad and Mukherjee (2000) investigated a sacrificial cladding with Y-frame formulation (Figure 3-11) directly attached to a non-sacrificial frame. The effects of the formulation were calculated through the force reaction time history, that exhibited significant magnitude reduction. Furthermore, it was shown that the force reaction was largely increased through a stiffening phase, which was activated at high strains.

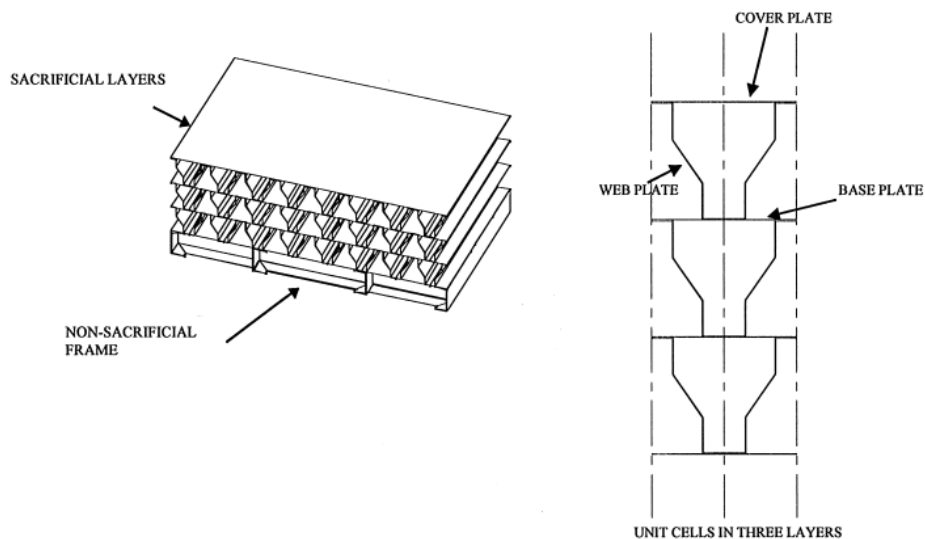


Figure 3-11: Sacrificial cladding with Y-frame formulation [reprinted from Guruprasad and Mukherjee (2000)]

Alberdi, Przywara and Khandelwal (2013) made a performance evaluation of sandwich systems (Figure 3-12) for blast mitigation under close-in blasts. The plate deflection, the energy dissipated through plastic

deformation and the maximum transferred force were used as performance indicators. It was found that increased front plate thickness led to decreased peak reaction force.

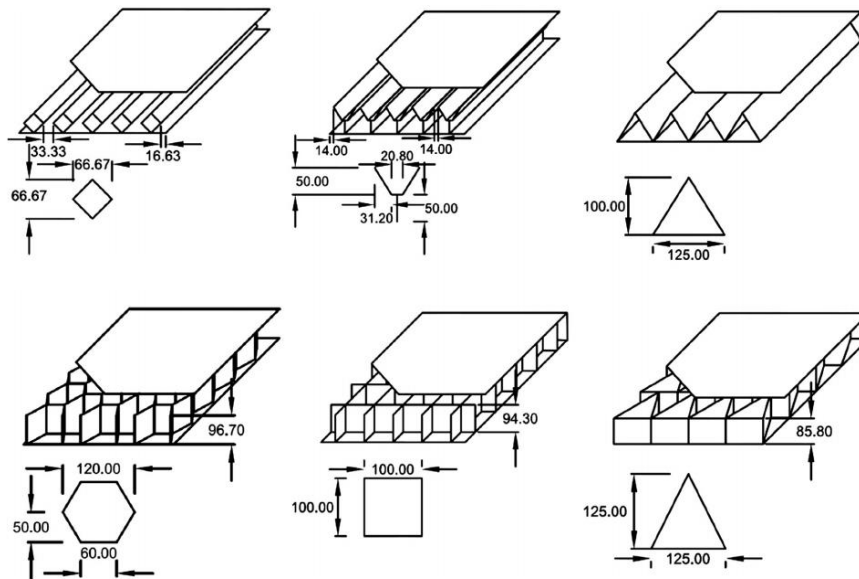


Figure 3-12: Core topologies: diamond folded, Y-frame folded, triangular folded, hexagonal honeycomb, square honeycomb, triangular honeycomb [reprinted from (Alberdi, Przywara and Khandelwal (2013))]

Palanivelu et al. (2011) conducted an experimental and numerical study about the use of empty recyclable metal-beverage cans as sacrificial cladding (Figure 3-13). The respective effects were measured through the energy absorption of the core structure and the comparison of the top face pressure and impulse (blast loading) to the bottom face pressure and impulse (reaction loading).

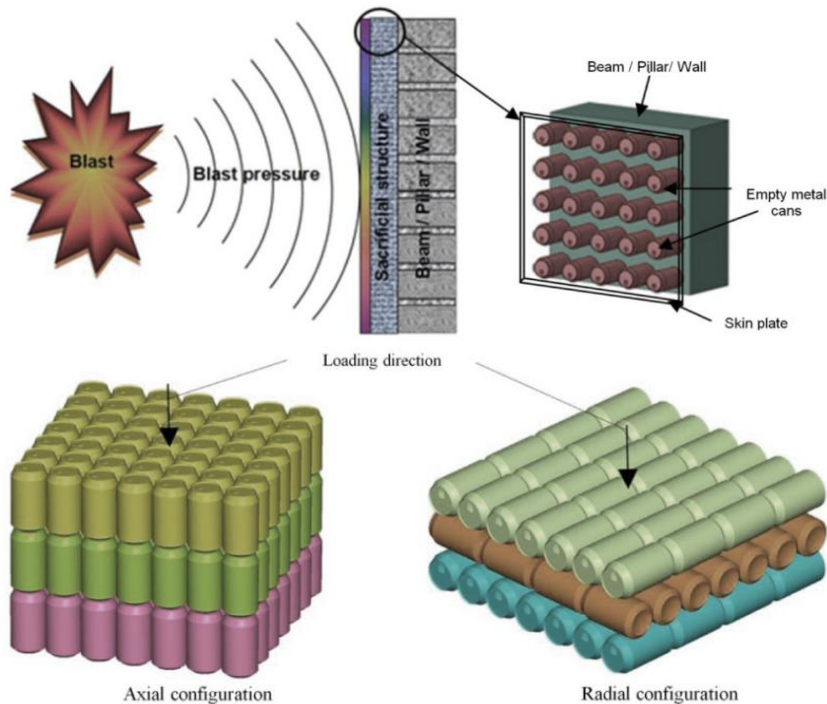


Figure 3-13: Concept of proposed sacrificial cladding with empty recyclable beverage cans [reprinted from Palanivelu et al. (2011)]

3.5.3. Energy-absorbing connectors

The energy-absorbing connectors type refers to the claddings that are connected to their supporting structure with the use of energy-absorbing devices. More specifically, in this type of claddings plastic dissipation is exhibited in their connections. This type is analyzed in the present paragraph with one research study.

Oswald (2018) performed an experimental study in order to examine the mitigation potential of energy absorbing devices at the connections of blast-loaded precast panels. The devices were designed to absorb blast energy by limiting the peak reactions transferred to the supporting structure. The absorption of blast energy was achieved through the ductile yield in flexure of the devices. According to the measurements, it was observed that the peak reaction forces were reduced by 25-40%.

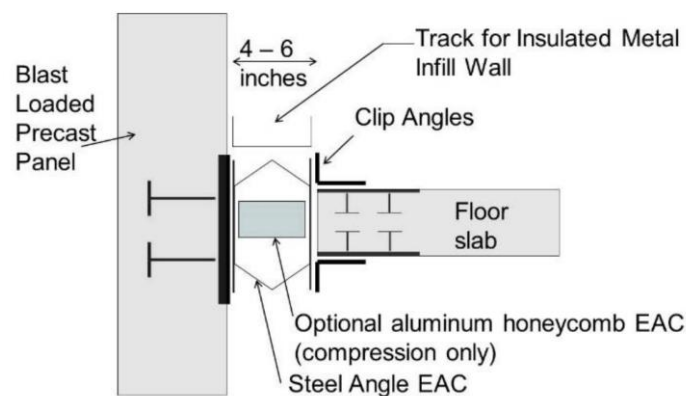


Figure 3-14: Conceptual placement of energy-absorbing connection in building [reprinted from Oswald (2018)]

3.6. Conclusions

The mechanisms of plastic energy absorption and inertial resistance were described thoroughly in the present chapter. As shown previously, the plastic energy absorption mechanism is based on the cladding ultimate resistance and ductility, while the inertial resistance mechanism is based on the cladding mass and stiffness. The effect of both mechanisms is the same, i.e., the initial high-amplitude and short-duration blast loading is converted into a low-amplitude and long-duration reaction time history through the cladding. Three types of cladding were analyzed: (1) The cladding-to-framing type; (2) The sacrificial cladding type; and (3) The energy-absorbing connectors type. A literature review of these types was made in order to show the mitigation potential that has been exhibited in claddings from various research studies.

3.7. References

- Alberdi, R., Przywara, J. and Khandelwal, K. (2013) 'Performance evaluation of sandwich panel systems for blast mitigation', *Engineering Structures*, 56, pp. 2119–2130. doi: <https://doi.org/10.1016/j.engstruct.2013.08.021>.
- Biggs, J. M. (1964) *Introduction to structural dynamics*. United States of America: McGraw-Hill.
- Bornstein, H. and Ackland, K. (2013) 'Evaluation of energy absorbing materials under blast loading', in *WIT Transactions on Engineering Sciences*, pp. 125–136. doi: 10.2495/MC130111.

- Chen, W. and Hao, H. (2012) 'Numerical study of a new multi-arch double-layered blast-resistance door panel', *International Journal of Impact Engineering*, 43, pp. 16–28. doi: 10.1016/j.ijimpeng.2011.11.010.
- Chen, W. S. and Hao, H. (2013) 'Preliminary study of sandwich panel with rotational friction hinge device against blast loadings', in *Advances in Engineering Plasticity XI*. Trans Tech Publications Ltd (Key Engineering Materials), pp. 530–533. doi: 10.4028/www.scientific.net/KEM.535-536.530.
- Cormie, D., Mays, G. and Smith, P. (2009) *Blast effects on buildings*. ICE Publishing. doi: 10.1680/beob.61477.
- Dusenberry, D. O. (2010) *Handbook for blast resistant design of buildings*. John Wiley & Sons. doi: 10.1002/9780470549070.
- Goel, M. D., Matsagar, V. A. and Gupta, A. K. (2011) 'Dynamic response of stiffened plates under air blast', *International Journal of Protective Structures*, 2(1), pp. 139–156. doi: 10.1260/2041-4196.2.1.139.
- Gouverneur, D., Caspeelee, R. and Taerwe, L. (2013) 'Experimental investigation of the load–displacement behaviour under catenary action in a restrained reinforced concrete slab strip', *Engineering Structures*, 49, pp. 1007–1016. doi: <https://doi.org/10.1016/j.engstruct.2012.12.045>.
- Guruprasad, S. and Mukherjee, A. (2000) 'Layered sacrificial claddings under blast loading Part I — Analytical studies', *International Journal of Impact Engineering*, 24(9), pp. 957–973. doi: [https://doi.org/10.1016/S0734-743X\(00\)00004-X](https://doi.org/10.1016/S0734-743X(00)00004-X).
- Hetherington, J. and Smith, P. (1994) *Blast and ballistic loading of structures*. New York: Taylor & Francis.
- Hoffmeister, B. et al. (2015) 'Advanced design methods for blast loaded steel structures', European Commission Directorate-General for Research and Innovation.
- Khalifa, Y. A., Tait, M. J. and El-Dakhakhni, W. W. (2017) 'Out-of-plane behavior of lightweight metallic sandwich panels', *Journal of Performance of Constructed Facilities*, 31(5), p. 4017056. doi: 10.1061/(ASCE)CF.1943-5509.0001018.
- Oswald, C. (2018) 'Blast testing of energy absorbing connectors for blast resistant design', *WIT Transactions on the Built Environment*, 180, pp. 57–67. doi: 10.2495/SUSI180061.
- Palanivelu, S. et al. (2011) 'Close-range blast loading on empty recyclable metal beverage cans for use in sacrificial cladding structure', *Engineering Structures*, 33(6), pp. 1966–1987. doi: <https://doi.org/10.1016/j.engstruct.2011.02.034>.
- Rutner, M. P. and Wright, J. P. (2016) 'Duality of energy absorption and inertial effects: Optimized structural design for blast loading', *International Journal of Protective Structures*, 7(1), pp. 18–44. doi: 10.1177/2041419615622726.
- Sun, G. et al. (2019) 'Dynamic response of sandwich panel with hierarchical honeycomb cores subject to blast loading', *Thin-Walled Structures*. doi: 10.1016/j.tws.2019.04.029.
- U.S. Department of Defense (2008) 'UFC 03-340-02: Structures to resist the effects of accidental explosions'.
- U.S. Department of the Army (1957) 'TM5-856-3: Design of structures to resist the effects of atomic weapons'.
- Xue, Z. and Hutchinson, J. W. (2004) 'A comparative study of impulse-resistant metal sandwich plates',

International Journal of Impact Engineering, 30(10), pp. 1283–1305. doi: 10.1016/j.ijimpeng.2003.08.007.

Yang, W. Y. (2009) Signals and systems with MATLAB, Signals and Systems with MATLAB. doi: 10.1007/978-3-540-92954-3.

Zobec, M. et al. (2015) 'Innovative design tool for the optimization of blast-enhanced facade systems', Journal of Facade Design and Engineering, 2(3–4), pp. 183–200. doi: 10.3233/fde-150019.

Chapter 4

Influence of cladding mass, stiffness, ultimate resistance and ductility

This chapter is a slightly modified version of the following paper:

Ioannou, O., Hadjioannou, M. and Gantes, C.J. (Forthcoming) 'A 2DOF method to study the influence of cladding characteristics on the response of the supporting structure under blast loading', Journal of Structural Engineering. doi: 10.1061/(ASCE)ST.1943-541X.0003494.

4.1. Introduction

As mentioned in chapter 2, a widely used method for the analysis and design of structural components against blast loading is the Single-Degree-of-Freedom (SDOF) method, according to which the structural components of a structure are analyzed as isolated members, using appropriate boundary conditions. In the case of building cladding, the response of the cladding, the supporting structure, and any other underlying components along the load path are typically modelled with a series of SDOF models, either using the dynamic reactions from the supported members or by directly applying the blast load to each member using the tributary area approach. This is the prevalent state-of-practice method, which is nowadays further explored and developed, as discussed by [Cormie et al. \(2009\)](#), in order to include more sophisticated SDOF models that can account for the contribution of catenary effects, different moment capacities, partial rotational fixities, etc. In SDOF models, the dependence of maximum displacement and corresponding peak time (i.e., the time when maximum displacement occurs) on the main SDOF parameters (i.e., mass, stiffness, ultimate resistance and ductility) has been investigated in depth in [DA \(1957\)](#), where non-dimensionalization of the maximum SDOF displacement is performed using the Dynamic Load Factor (*DLF*). *DLF* is defined in Equation (4-1), as the ratio of the maximum dynamic displacement x_{max} to the static displacement x_{st} , computed by dividing force P_o (resultant blast peak pressure) to stiffness k . SDOF ductility μ is defined in Equation (4-2), as the ratio of x_{max} to the elastic displacement limit x_{el} being equal to the resistance R_u over stiffness k .

$$DLF = x_{max}/x_{st} = x_{max}/(P_o/k) \quad (4-1)$$

$$\mu = x_{max}/x_{el} = x_{max}/(R_u/k) \quad (4-2)$$

In this chapter, the key parameters affecting the behavior of the supporting structure are thoroughly explored in terms of the maximum supporting structure displacement, by implementing a Two Degrees of Freedom (2DOF) model that can directly account for the interaction of cladding and supporting structure, instead of two uncoupled SDOF models, thus describing the dynamic interaction more accurately. A non-dimensional formulation is used, and the concept of dynamic load factor, as defined in Equation (4-1), is adopted to describe the response. Thereby, the main design principles that can be applied in the cladding parameters in order to mitigate blast effects in the supporting structure are described herein.

More specifically, the purpose of the described content is to supplement blast-resistant-cladding research studies in terms of their applicability range, by taking into account the two mechanisms of plastic energy absorption and inertial resistance. In this context, an improved qualitative understanding of the mechanisms for mitigating the blast effects on the supporting structure, as well as quantitative estimations for the contribution of each cladding parameter to the response of the supporting structure, are provided. Response diagrams are developed that can be used in the structural design of the cladding and its connections, leading to more efficient and safe solutions for the cladding–supporting structure system, applicable to new structures as well as for retrofitting of existing buildings with new cladding.

To that effect, the 2DOF model is first developed, and its theoretical background and pertinent assumptions are discussed. The 2DOF model and its results are validated numerically, through nonlinear dynamic finite element analyses of a typical cladding-to-framing system. Results of the 2DOF model are also validated against experimental and analytical results of a typical polyurethane sacrificial cladding (Ousji et al., 2017). Parametric analyses, with the use of the 2DOF model, are then performed in order to study the effects of all key parameters on the system's response and conclusions are drawn. Finally, the benefits of the developed solutions, for optimizing the blast performance of such systems, are highlighted.

4.2. Proposed 2DOF model and response regimes

4.2.1. Derivation of equations of motion and applied blast loading

The cladding–supporting structure system is idealized as a 2DOF system that consists of two masses m_1 and m_2 connected with two springs in series, k_1 and k_2 , as shown in Figure 4-1. The masses (m_1 , m_2) and spring constants (k_1 , k_2) used for the 2DOF model are derived using the same approach as for the SDOF analysis, using mass and stiffness coefficients (Biggs, 1964), that depend on the boundary conditions of the cladding and the supporting structure. It is, therefore, noted that the mass terms, referred to herein for the 2DOF model, correspond to the factored mass and not the total mass of the cladding and supporting structure. Likewise, the spring constant, referred to herein, is associated with the stiffness at the location that displacements are measured, which is typically at the midspan of the two components in the case of the cladding-to-framing system.

Specifically, mass m_1 and spring k_1 represent the cladding, while mass m_2 and spring k_2 represent the structure that supports the cladding (Figure 4-1). The degrees of freedom for the cladding and supporting structure are denoted as x_1 and x_2 , respectively. The stiffness k_1 of the nonlinear spring between the two masses is idealized as elastic-perfectly plastic, as shown in Figure 4-1. The resistance of the cladding is approximated with a nonlinear spring that comprises of two branches: (a) Elastic branch for the early elastic response; (b) Perfectly plastic branch for the post-yield response, which can account for yielding of the cladding. The yield capacity of the spring is referred as ultimate resistance R_u . The spring properties are assumed to be the same for inward and outward deformation. On the other hand, the

spring that connects mass m_2 to a rigid support is linear elastic, with stiffness k_2 . This assumption is made on the basis that cladding is the sacrificial element, while the supporting structure is considered non-sacrificial (Guruprasad and Mukherjee, 2000; Hanssen, Enstock and Langseth, 2002) and it is desirable to remain elastic.

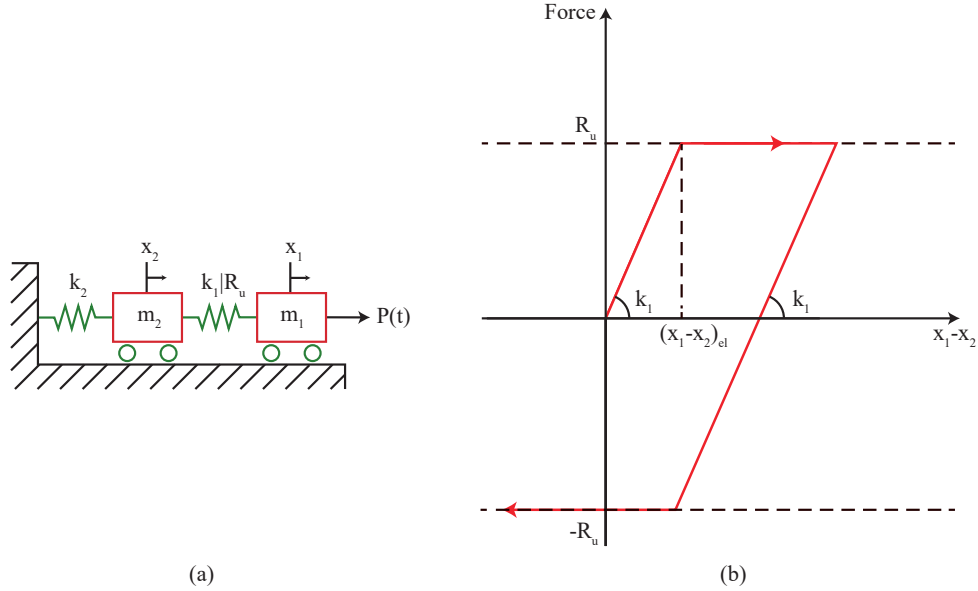


Figure 4-1: Representation of the 2DOF model: (a) Notation of the applied mass, stiffness, ultimate resistance and displacement parameters; (b) Force–displacement diagram of the spring connecting mass m_1 (cladding) to mass m_2 (supporting structure)

Equations (4-3)-(4-6) describe the motion of the 2DOF system (Chopra, 2007). The mass terms represent the inertial forces, while the stiffness terms represent the spring forces. Damping has not been taken into account for simplicity, considering that small damping ratios have minimal effect on the first few response cycles, which is typically where maximum displacement occurs for blast loads (Krauthammer and Altenberg, 2000; Rigby, Tyas and Bennett, 2012). Moreover, ignoring damping is conservative and the energy dissipated through plastic deformation is greater than that through structural damping. Equations (4-3)-(4-6) are separated into elastic and plastic regions to account for the elastoplastic response of the first degree of freedom (Figure 4-1).

$$m_1 \cdot \ddot{x}_1 + k_1 \cdot (x_1 - x_2) = P(t), \quad x_1 - x_2 < (x_1 - x_2)_{el} \quad (4-3)$$

$$m_1 \cdot \ddot{x}_1 + R_u = P(t), \quad x_1 - x_2 \geq (x_1 - x_2)_{el} \quad (4-4)$$

$$m_2 \cdot \ddot{x}_2 + k_2 \cdot x_2 - k_1 \cdot (x_1 - x_2) = 0, \quad x_1 - x_2 < (x_1 - x_2)_{el} \quad (4-5)$$

$$m_2 \cdot \ddot{x}_2 + k_2 \cdot x_2 - R_u = 0, \quad x_1 - x_2 \geq (x_1 - x_2)_{el} \quad (4-6)$$

The external force $P(t)$ is applied to mass m_1 , representing the cladding system, which is herein assumed to receive the applied blast load $P(t)$. The blast load is idealized as a triangular load with peak pressure P_o at the time of arrival, that linearly decays to zero pressure over a duration t_d . The peak pressure P_o is equal to the peak pressure of the actual explosion and the duration t_d is calculated based on positive impulse pressure equivalency. It is noted that the idealization of the blast load profile as triangular results in minimal loss of accuracy compared to the more typical exponential decay profile, which is shown in Figure 4-2 (Gantes and Pnevmatikos 2004; DoD 2008). The triangular force profile $P(t)$ is described by Equation (4-7).

$$P(t) = P_o \cdot \left(1 - t/t_d\right) \quad (4-7)$$

The equations of motion can be written in non-dimensional form by replacing x_1, x_2 with n_1, n_2 , as defined in Equations (4-8) and (4-9), adopting a similar approach as the one used by Biggs (1964) for SDOF systems.

$$n_1 = \frac{x_1}{(P_o/k_2)} \quad (4-8)$$

$$n_2 = \frac{x_2}{(P_o/k_2)} \quad (4-9)$$

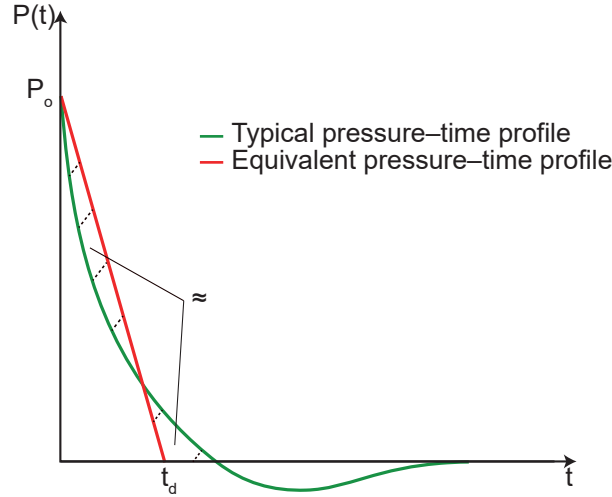


Figure 4-2: Typical and equivalent pressure-time profile for blast wave passing through a fixed point in space

Time t is also replaced according to Equation (4-10), where T_2 is the natural period of the supporting structure, assuming that it is decoupled from mass m_1 and spring k_1 . Then, Equations (4-3)-(4-6) are written in non-dimensional form, as Equations (4-11)-(4-14).

$$\xi = t/T_2 = t / (2\pi\sqrt{m_2/k_2}) \quad (4-10)$$

$$\frac{m_1}{m_2} \cdot \frac{1}{4\pi^2} \cdot \ddot{n}_1 + \frac{k_1}{k_2} \cdot (n_1 - n_2) = 1 - \xi \cdot T_2/t_d, \quad n_1 - n_2 < (n_1 - n_2)_{el} \quad (4-11)$$

$$\frac{m_1}{m_2} \cdot \frac{1}{4\pi^2} \cdot \ddot{n}_1 + \frac{R_u}{P_o} = 1 - \xi \cdot T_2/t_d, \quad n_1 - n_2 \geq (n_1 - n_2)_{el} \quad (4-12)$$

$$\frac{1}{4\pi^2} \cdot \ddot{n}_2 + n_2 - \frac{k_1}{k_2} \cdot (n_1 - n_2) = 0, \quad n_1 - n_2 < (n_1 - n_2)_{el} \quad (4-13)$$

$$\frac{1}{4\pi^2} \cdot \ddot{n}_2 + n_2 - \frac{R_u}{P_o} = 0, \quad n_1 - n_2 \geq (n_1 - n_2)_{el} \quad (4-14)$$

It is observed that the 2DOF system can be uniquely described by the ratios m_2/m_1 , k_2/k_1 , t_d/T_2 and R_u/P_o . Using these ratios as design variables, the 2DOF system of differential equations was solved in Matlab (The Mathworks Inc, 2018) by employing the Newmark average acceleration method ($\gamma_N = 0.5$ and $\beta_N = 0.25$). A sufficiently small time-step was used to ensure accuracy and sufficiently large total duration was allowed to capture the maximum displacement of the second degree of freedom. The nonlinearity of spring k_1 was considered using the Modified Newton-Raphson method. The obtained maximum values of variables n_1 and n_2 have the same meaning as the Dynamic Load Factor (DLF) of the SDOF models described by Biggs (1964). It is noted that the maximum displacement was captured at the first oscillation cycle. Since the design objective is to control the maximum displacement of the

second degree of freedom, so that the structure supporting the cladding remains elastic, the maximum value of n_2 was monitored and calculated from each 2DOF analysis. Cladding ductility was quantified by using Equation (4-15).

$$\mu = \frac{\max(|x_1 - x_2|)}{x_{el}} = \frac{\max(|x_1 - x_2|)}{R_u/k_1} = \frac{\max(|n_1 - n_2|) \cdot (k_1/k_2)}{R_u/P_o} \quad (4-15)$$

4.2.2. Mapping the properties of the cladding–supporting structure system in the 2DOF model

The input parameters of the 2DOF system depend on the actual properties of the cladding–supporting structure system (i.e., mass, stiffness, load, and ultimate resistance) but are not identical to them. In reality, the cladding and supporting structure have distributed mass with various deflection shapes, especially if nonlinearity takes place, which has to be converted into an equivalent lumped mass for the 2DOF system. For that purpose, proper transformation factors, which are available in the literature for SDOF systems, should be applied. For the cases of cladding-to-framing systems, these factors are provided by [Cormie et al. \(2009\)](#), denoted as K_{LM} factors. The K_{LM} factors are applied to the properties of a SDOF system, so that it will have approximately the same displacement time history as the actual system. This operation is performed by selecting the appropriate load pattern, component configuration, boundary conditions and deformed shape, which ideally describe the actual behavior of the components with tolerable deviations. An alternative solution would be to perform a modal and a load–deflection analysis in order to extract the equivalent properties of the 2DOF system, as proposed by [HSE \(2006\)](#). In the case of connections with an upper bound strength or a specific load–deformation diagram, the aforementioned factors should be combined with the properties of the connection. A similar process can be performed in the case of sacrificial cladding, probably with less effort, as the sacrificial cladding–supporting structure system matches directly with the 2DOF system, as shown by [Rutner and Wright \(2016\)](#).

4.2.3. Assumptions and limitations

The 2DOF system, described herein, has a number of simplifying assumptions, which are summarized below:

- The transformation factors (K_{LM}) used to match the displacements of the physical cladding-to-framing system with the 2DOF displacements are approximate. The K_{LM} factors can be intrinsically included in the 2DOF equations and the results, by multiplying masses m_1 and m_2 with K_{LM1} and K_{LM2} , respectively.
- The transformation factors are considered uniform throughout the response of the 2DOF system. In reality, the deflected shape of the actual component changes as it transitions from elastic to plastic, which will thereby change the transformation factor.
- In the 2DOF system, plasticity is approximated with an elastic–perfectly plastic spring, while the actual structural system has a smooth force–displacement curve, which may include bilinear regions, hardening and/or softening branches.
- The 2DOF system cannot capture possible catenary action or second stiffening phase, such as the densification phase of sacrificial cladding. The influence of these effects are discussed by [Ioannou and Gantes \(2021\)](#).
- Resistance R_u and stiffnesses k_1 and k_2 are considered symmetric in both 2DOF directions, i.e., inbound and rebound deformation. In some structural components, they may be different, e.g., they may have different positive and negative flexure capacities.

- Strength and stiffness deterioration due to cyclic loading or buckling are not included. Therefore, effects, such as low cycle fatigue, concrete cracking, lateral buckling, etc., are not considered.
- The negative phase of the blast load is not included, and explosive charge is considered to be applied at sufficient distance from the cladding, such that the cladding is uniformly loaded.
- Strain-rate effects can be incorporated in the 2DOF resistance R_d with dynamic increase factors, per the commonly used approach for SDOF analysis (DoD 2008).

These assumptions may limit the accuracy of the 2DOF results, but overall their effects are considered to be relatively small and the qualitative results, presented in section 4.4, are not significantly affected by them, as demonstrated also by comparison to nonlinear transient analysis results of a detailed finite element model as well as to experimental and analytical results, described in section 4.4.

4.3. Analysis methodology

As already noted in section 4.2, each analysis corresponds to a set of dimensionless ratios m_2/m_1 , k_2/k_1 , t_d/T_2 and R_d/P_o . The extracted quantity from each analysis is DLF_2 , which is the DLF of the second degree of freedom, and is equal to the absolute maximum value of the non-dimensional displacement n_2 [Eq. (4-9)]. Depending on the geometry, material and section properties, the natural period of the supporting structure may vary significantly. Moreover, the blast loading may have different standoff distances, resulting in a wide range of blast durations. Thus, response diagrams were generated for a wide range of t_d/T_2 values to capture all possible natural periods and blast durations. Specifically, the non-dimensional load duration parameter t_d/T_2 was used in the horizontal axis and DLF_2 in the vertical axis. The effects of the other system parameters were presented through several diagrams, each one representing different ratios m_2/m_1 and k_2/k_1 as well as family of R_d/P_o ratio curves. Each curve was constructed from a series of 320 data points, with each point representing the calculated response from a different 2DOF analysis.

The dimensionless 2DOF model is employed to examine the influence of the cladding characteristics (i.e., m_2/m_1 , k_2/k_1 and R_d/P_o) over the supporting structure. The effects of cladding ultimate resistance (R_u/P_o), cladding ductility (μ) and cladding mass and stiffness (m_2/m_1 , k_2/k_1) are discussed extensively in the subsequent sections by varying the 2DOF model parameters.

4.4. Validation of the 2DOF model

4.4.1. Validation of the 2DOF model with detailed finite element analysis results of a cladding-to-framing system

Description of the structure

To validate the 2DOF model, comparisons were performed with results from three-dimensional finite element simulations of a cladding-to-framing system. The modeled cladding-to-framing system, shown in Figure 4-3, comprises of an 8-mm thick steel panel with 92-mm tall and 8-mm thick stiffeners, spaced at 250 mm. The panel is supported by two beams with rectangular hollow sections, having a height of 400 mm, a width of 200 mm and a wall thickness of 10 mm. The panel width is 1000 mm and the beam length is 3750 mm. The stiffeners are welded to the beams, thus their connections can transfer shear and axial forces. Each beam is simply supported, with the longitudinal degree of freedom free to prevent the development of catenary action under large deformations.

Finite element model

The numerical model was developed and analyzed with the ANSYS Explicit Dynamics software (ANSYS Inc, 2017), by employing material and geometric nonlinearity (Nonlinear Transient Finite Element Analysis – NTFEA). The time-step was automatically calculated to ensure numerical stability per the Courant number criterion (ANSYS Inc, 2017).

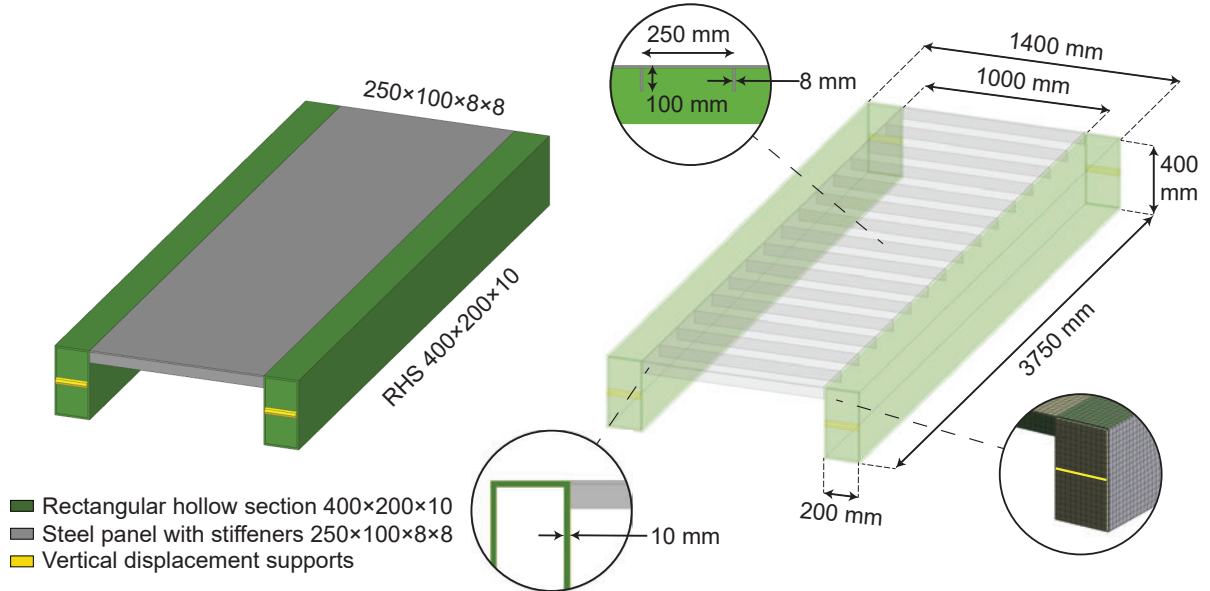


Figure 4-3: Cladding-to-framing geometry and numerical model

To model the behavior of steel, the Cowper-Symonds Strength model (ANSYS Inc, 2017) was employed, that allows to take into account the post-yield behavior of steel and strain-rate effects. The Cowper-Symonds Strength model is described by Equation (4-16), with ϵ_{pl} being the plastic strain and $\dot{\epsilon}_{pl}$ the plastic strain rate, and comprises of the Johnson-Cook model (Johnson and Cook, 1983) for the hardening effects (through yield stress A and hardening coefficients B , θ) and the Cowper-Symonds coefficients for the strain-rate effects. The material of all the steel parts was steel S355 (BSI, 2019), by accounting for the mean strength per Braconi et al. (2015). Figure 4-4 shows the material law in true stress–true strain terms. The strain-rate coefficients q and D were adopted from Cadoni et al. (2018), Mortazavi and Heo (2018) and are indicated in Figure 4-4.

$$\sigma = (A + B \cdot \epsilon_{pl}^{\theta}) \cdot \left(1 + \left(\frac{\dot{\epsilon}_{pl}}{D} \right)^{1/q} \right) \quad (4-16)$$

The applied pressure time history was approximated with an equivalent triangular load with peak pressure and impulse that results from a hemi-spherical explosion of 5 kg TNT-equivalent at a stand-off distance of 4 m, as shown in Figure 4-5. The blast profile parameters were calculated according to the Kingery and Bulmash (1984) equations. Furthermore, the load was applied on the steel panel as uniformly distributed over the panel area. All steel parts utilized shell elements with 20.0-mm edge length. Each shell element had five through-thickness integration points.

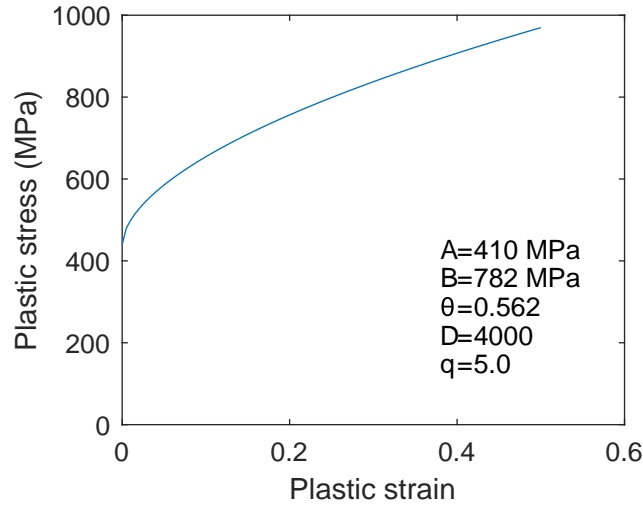


Figure 4-4: Material model for S355 steel

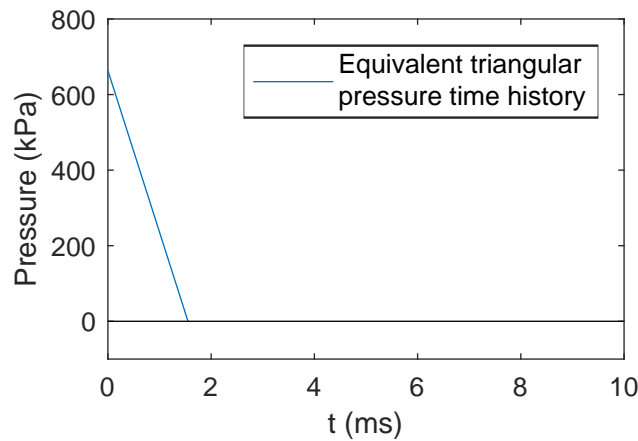


Figure 4-5: Equivalent triangular pressure time history for the numerical and the 2DOF model.

2DOF model

The same cladding-to-framing system (Figure 4-3) was analyzed with the 2DOF model using transformation factors from [Cormie et al. \(2009\)](#) for the SDOF systems. These transformation factors (K_{LM}) were applied in order to account for the distribution of the load, stiffness, mass, and ultimate resistance of both degrees of freedom according to [Dusenberry \(2010\)](#), as described in Equations (4-17)-(4-20). The stiffness and mass properties of the two beams were lumped into one and were represented by the second degree of freedom. The strain-rate effects were included in the 2DOF model by increasing the resistance R_u by 10%, as recommended by [Cormie et al. \(2009\)](#), [Dusenberry \(2010\)](#). Moreover, in the 2DOF model, the initial (elastic) stiffness was simplified with the nonlinear spring k_1 . The equivalent triangular pressure time history is presented in Figure 4-5.

$$K_{LM1} \cdot m_1 \cdot \ddot{x}_1 + k_1 \cdot (x_1 - x_2) = P(t), \quad (x_1 - x_2) < (x_1 - x_2)_{el} \quad (4-17)$$

$$K_{LM1} \cdot m_1 \cdot \ddot{x}_1 + R_u = P(t), \quad (x_1 - x_2) \geq (x_1 - x_2)_{el} \quad (4-18)$$

$$K_{LM2} \cdot m_2 \cdot \ddot{x}_2 + k_2 \cdot x_2 - k_1 \cdot (x_1 - x_2) = 0, \quad (x_1 - x_2) < (x_1 - x_2)_{el} \quad (4-19)$$

$$K_{LM2} \cdot m_2 \cdot \ddot{x}_2 + k_2 \cdot x_2 - R_u = 0, \quad (x_1 - x_2) \geq (x_1 - x_2)_{el} \quad (4-20)$$

The parameters of the 2DOF system are summarized in Table 4-1. The K_{LM} factors were calculated by considering the beam and cladding as simply supported with uniform distribution of load and mass.

Computed response with finite element model and 2DOF

The obtained panel and beam displacements, as well as plastic strains at different time steps, when subjected to the pressure time history, are presented in Figure 4-6. Time $t = 5.5$ ms corresponds to the first peak inbound panel response with maximum displacement at midspan of -6.7 mm, while time $t = 12.5$ ms corresponds to the first peak rebound panel response with maximum displacement at midspan of 7.7 mm. The displacement due to rebound of the panel is larger because of partial loss of the capacity of the stiffeners due to lateral buckling (presented at the close-up views of Figure 4-6(b)). Furthermore, limited plastic strains are exhibited at the panel stiffeners. The maximum displacement at the midspan of the beams is -6.9 mm and occurs during inbound, while the beam displacement at midspan during rebound is slightly less, at 5.8 mm at time $t = 11.0$ ms.

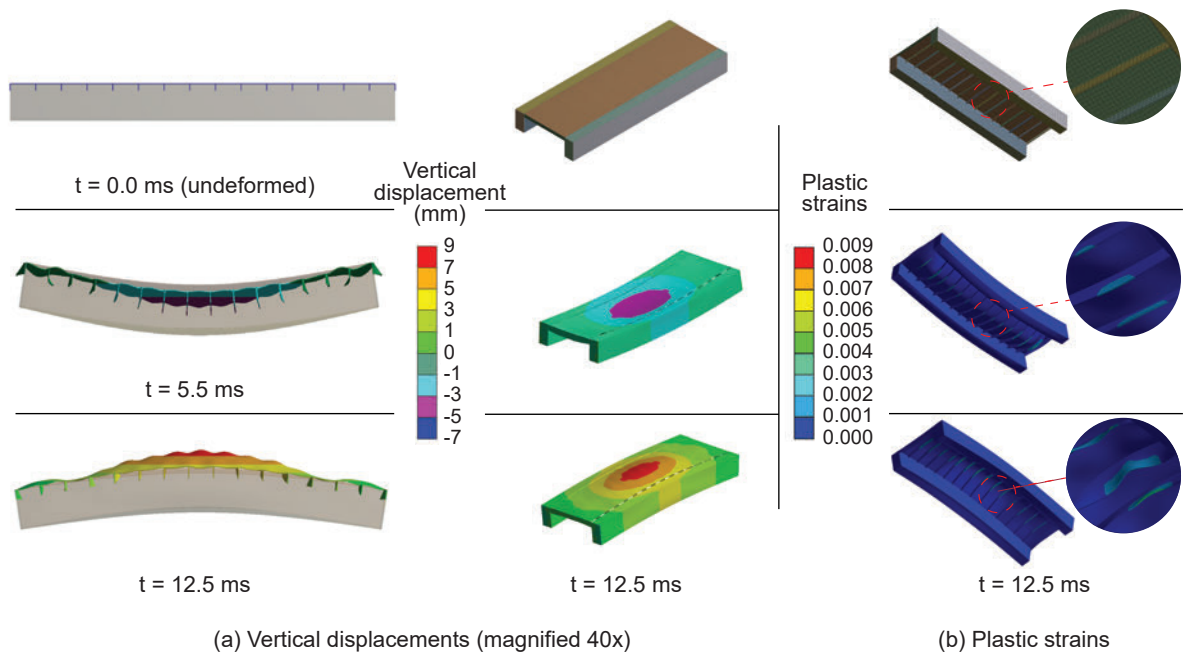


Figure 4-6: Results of the numerical model when subjected to the pressure time history: (a) Vertical displacements; (b) Plastic strains

Table 4-1: Parameters of the equivalent cladding-to-framing 2DOF system

Parameter	Note/Equation	Value
Stiffness k_1	$384/5 \cdot (EI_1/L_1^3)$	262472 N/mm
Stiffness k_2	$384/5 \cdot (EI_2/L_2^3)$	148990 N/mm
Resistance R_u	$8 \cdot (M_p/L_1) \cdot DIF$	2178871 N
Elastic limit	R_u/k_1	8.3 mm
Mass m_1	$w_1 \cdot L_1$	322500 gr
Mass m_2	$w_2 \cdot L_2$	683250 gr
K_{LM1}	Uniformly distributed load and mass	0.78 approx.
K_{LM2}	Uniformly distributed load and mass	0.78 approx.
t_d/T_2		0.13
R_u/P_0		0.93

The results of the 2DOF analysis and their comparison with the numerical model results are presented in Figure 4-7(a). It can be seen that there are only minor deviations between the displacement time histories of the panel and the beams (4.9% and 7.5% maximum difference in the peak displacements of the cladding and girts, respectively). Hence this comparison suggests that the 2DOF model is fairly accurate. The minor differences between the 2DOF system and the detailed numerical model are attributed to the reasons described in section 4.2.3.

In order to further examine the effects of the plastic energy absorption and the inertial resistance mechanisms, two alternatives to the previously examined cladding-to-framing system were considered:

- Alternative A: Steel grade was changed from S355 to S235 (BSI, 2019).
- Alternative B: The panel stiffeners were shortened to 50 mm height and the panel thickness was increased to 20 mm.

The results of the numerical models prepared for the two alternatives are presented in Figure 4-7(b). Regarding the two alternatives, insignificant difference is exhibited in Alternative A, while substantial reduction is achieved in Alternative B.

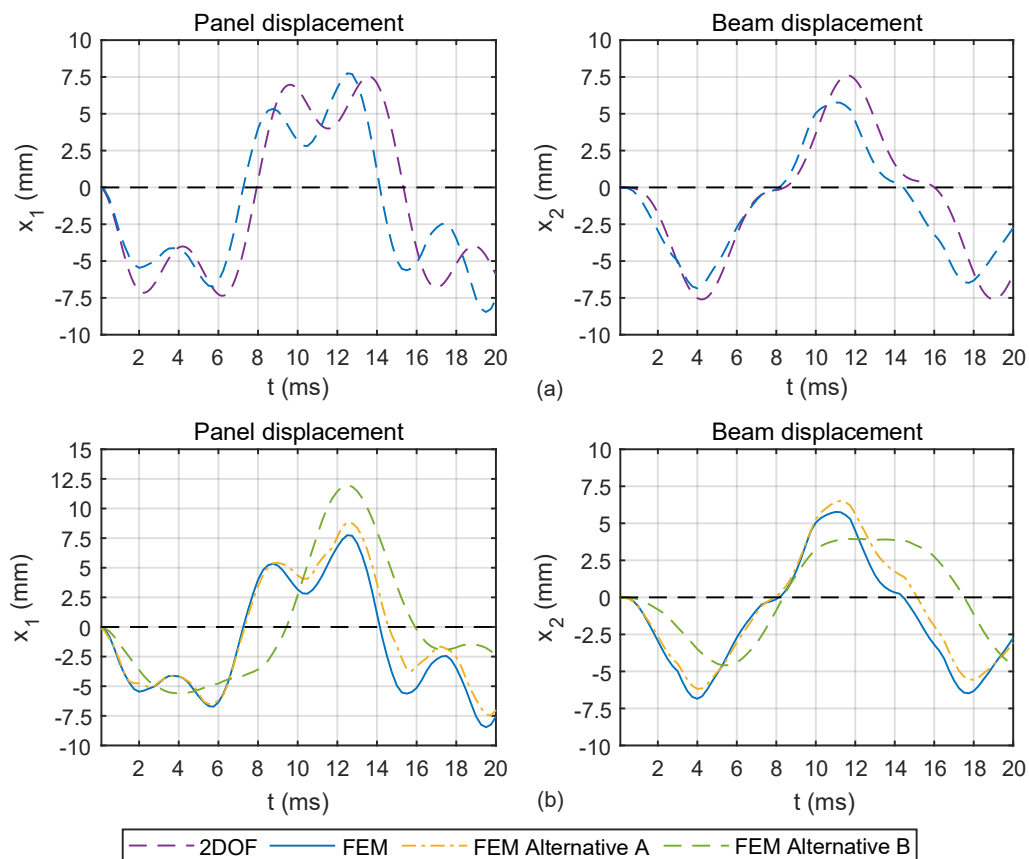


Figure 4-7: Computed response with 2DOF and finite element model: (a) Comparison of the finite element model with the 2DOF model; (b) Comparison of the finite element model with alternatives A and B

4.4.2. Validation of the 2DOF model with experimental and analytical results of sacrificial cladding

The 2DOF model was also validated against experimental and analytical results. Specifically, results by [Ousji et al. \(2017\)](#) for a typical polyurethane (PU) sacrificial cladding were used for the validation. Out of twenty different configurations of front plate (FP) thickness and material as well as PU density and thickness, type PU30-50-FP3 was selected, because it was the only one for which detailed results in terms of load time history, deformation time history and load-deformation curve were available. A representative overview of the sacrificial cladding concept is shown in Figure 4-8. With respect to the 2DOF, the first DOF represents the front plate and the PU sacrificial cladding, while the second DOF represents the rear plate that is attached to a rigid structure. The connection of the cladding to the rear plate is represented by a nonlinear spring with the same resistance as the resistance of the polyurethane.

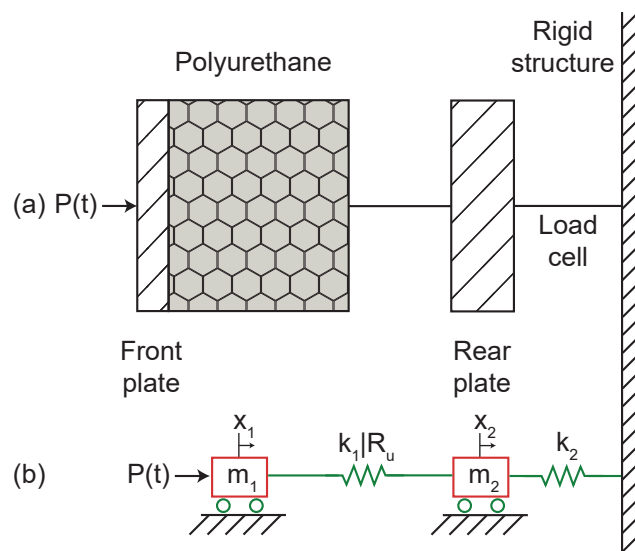


Figure 4-8: Representation of the PU sacrificial cladding model: (a) Experimental set-up [data from [Ousji et al. \(2017\)](#)]; (b) Equivalent 2DOF model as considered in the present study

In the selected configuration, PU30-50-FP3, FP material was steel S355, FP mass was 339 g, PU density was 30 kg/m^3 and PU thickness was 50 mm. Each specimen had a cross sectional area of $80 \times 80 \text{ mm}^2$ and a pressure loaded area of $74 \times 74 \text{ mm}^2$. Regarding the other PU properties, it was assumed that Young's modulus was 6.16 MPa, the densification strain was 0.59 and the quasi-static plateau stress was 323 kPa. Furthermore, PU thickness was sufficient for blast energy to be fully absorbed in the PU foam before its full densification, which would lead to sudden increase in the transmitted pressure.

As indicated by [Ma and Ye \(2007\)](#), the plateau stress used in the calculations should be adjusted to the actual resistance. Hence, increase in quasi-static plateau stress, due to strain rate effects, should be considered. In the 2DOF calculations the resistance was increased by 33%, as indicated by the experimental results summary of [Ousji et al. \(2017\)](#) for this specific type.

Furthermore, significant difference was observed by [Ousji et al. \(2017\)](#) between the reflected impulse at the front plate and the transmitted impulse at the rear plate. This difference was attributed to Fluid Structure Interaction (FSI) effects, as discussed extensively by [Aleyaasin et al. \(2015\)](#), [Kambouchev et al. \(2006\)](#), [Turkyilmazoglu \(2016\)](#). In the present study, these effects were accounted by reducing the

applied impulse at the first DOF, as calculated experimentally by Ousji et al. (2017), from 7.25 Ns to 6.51 Ns (10.21 % decrease) while peak pressure was 6.58 MPa.

The 2DOF applied pressure time history was triangular (Figure 4-2) with 0.386 ms positive phase duration and the force-displacement diagram was considered elastic-perfectly plastic (Figure 4-1). Regarding the analytical calculations of Ousji et al. (2017), multiple literature approaches were employed for the loadings and equations of motion. These were the Hanssen (Hanssen, Enstock and Langseth, 2002), Taylor–Without FSI (Taylor, 1963), Taylor–FSI (ETT) (Aleyaasin, Harrigan and Reid, 2015) and Taylor–FSI (KNR) (Kambouchev, Noels and Radovitzky, 2006) approaches.

The supporting structure consisted of a thick 80×80 mm² steel rear plate. Due to lack of more detailed information from Ousji et al. (2017), the supporting structure was modeled with axial stiffness (10⁸ N/mm) and mass (1000 g), with a thickness of 20 mm that was estimated with photo processing. The rear plate was attached to a rigid structure through a force load cell measuring the transmitted reacting load.

The results of the 2DOF approach, along with the experimental results and the aforementioned analytical approaches, are presented in Figure 4-9 and Figure 4-10. In the reaction time history between the rear plate and the rigid structure (Figure 4-9), obtained by the 2DOF model, it is observed that the initial elastic region is followed by a constant transmitted load curve, which was also identified in the experimental results. Regarding the front plate displacement time history (Figure 4-10), as also noted by Ousji et al. (2017), there was significant deviation between the analytical approaches and the experimental results. In this context, the maximum displacement exhibited in the 2DOF model is considered acceptable. Furthermore, the time of maximum response was approximately identical between the 2DOF model and the experimental results. The *DLF* of the rear plate was estimated to be 0.08 through the 2DOF analysis. This shows the beneficial effects of sacrificial cladding for the protected structure by activating ductility and plastic energy absorption.

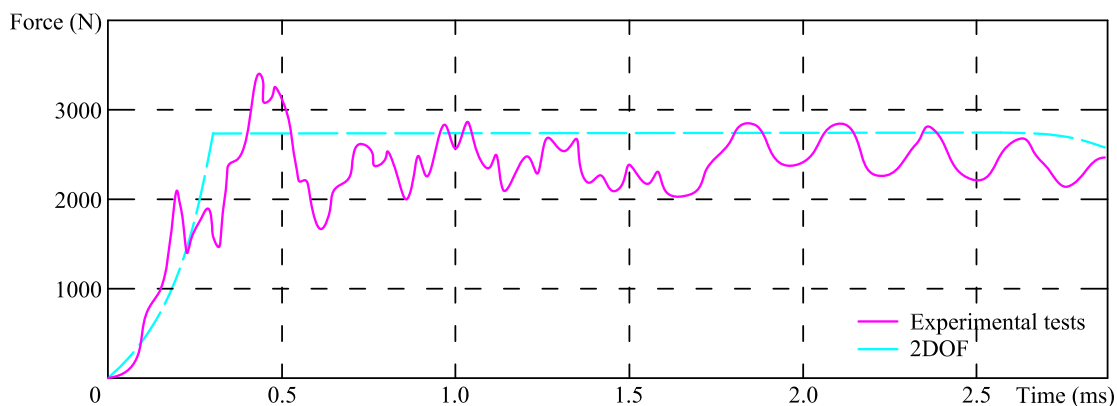


Figure 4-9: Reaction force time history between the second DOF and the main structure in the experimental tests [reprinted from (Ousji et al., 2017)] and the 2DOF model

4.5. Results of the 2DOF model response to blast loading

4.5.1. Effects of cladding ultimate resistance on the supporting structure

In the examined problem of the cladding-to-supporting-structure system, the plastic energy absorption mechanism allows the cladding to dissipate blast energy and, thereby, reduce the load demand on the main structure. This behavior is discussed in this section based on the results of the response of the

2DOF system, illustrated in Figure 4-11 and Figure 4-12, which were obtained from parametric analyses for a wide range of dimensionless parameters. As already noted, the positive effect of the cladding can be facilitated through the reduction of DLF_2 , which is illustrated on the vertical axis of Figure 4-11 and Figure 4-12.

The black (envelope) curve in each diagram of Figure 4-11 and Figure 4-12 corresponds to $R_u/P_o = 2.0$. The value of 2.0 generally constitutes the maximum DLF which is exhibited in elastic SDOF models (Cormie, Mays and Smith, 2009). It is observed that, mainly in the impulsive region ($t_d/T_2 < 0.1$) and partly in the dynamic region ($0.1 < t_d/T_2 < 10.0$), a number of curves with different ratios of R_u/P_o coincide with the black curve. Consequently, for all these R_u/P_o ratios, the maximum displacement of the second degree of freedom is the same. It is thus inferred that resistance R_u and the corresponding ductility and plastic energy absorption mechanism of the cladding do not have appreciable effects in these regions. The envelope curves represent the points where the response is mainly affected by the inertial resistance mechanism, while the areas below these curves represent the points where the response is mainly governed by the plastic energy absorption mechanism. Most importantly, it is noted that in the quasi-static and partly in the dynamic region, where the resistance R_u controls the response, the reduction of DLF_2 is substantial. The lower the resistance R_u is, the lower DLF_2 is, which is desirable. However, when the resistance R_u is lowered, the ductility requirements increase.

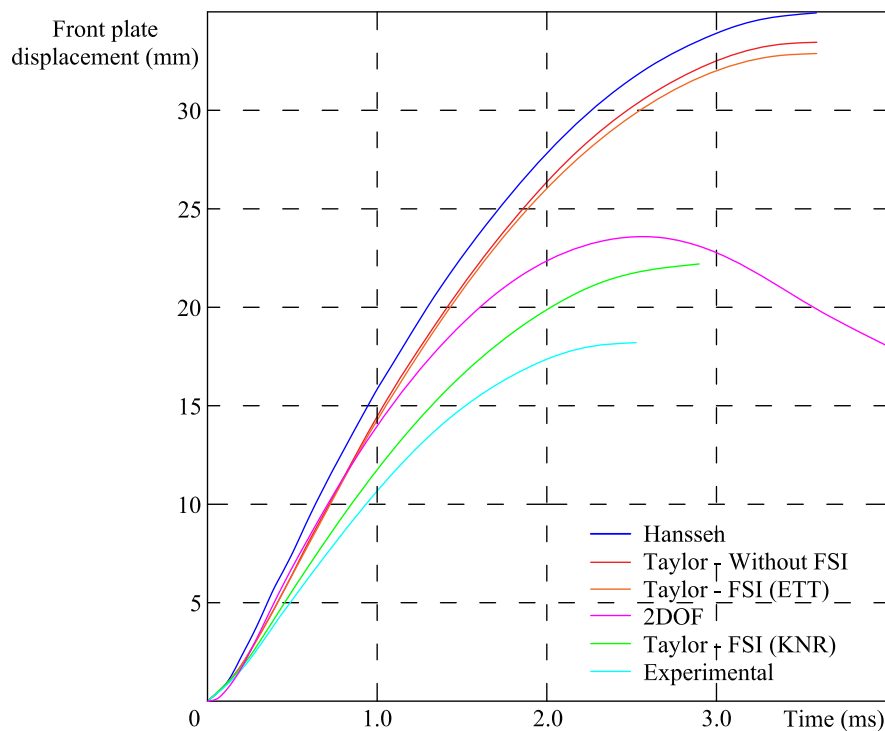


Figure 4-10: Front plate displacement time history in the experimental tests [reprinted from (Ousji et al., 2017)], the analytical approaches [reprinted from (Ousji et al., 2017)] and the 2DOF model

Generally, the R_u/P_o curves form an approximately horizontal line to the right of the envelope curve. Hence, the positive effect on DLF_2 is constant, regardless of the parameter t_d/T_2 . This is attributed to the nonlinear spring k_1 reaching its peak resistance R_u . In the quasi-static region, where the response is mainly affected by the maximum force and not by impulse, this lower reaction force value, which is limited by the resistance R_u of the first degree of freedom (cladding), controls the response of the sup-

porting structure. For each R_u/P_o curve, the resistance R_u , with respect to the maximum force P_o , remains constant, hence this is the reason why DLF_2 also remains constant at the portion where the R_u/P_o curve exits the envelope curve.

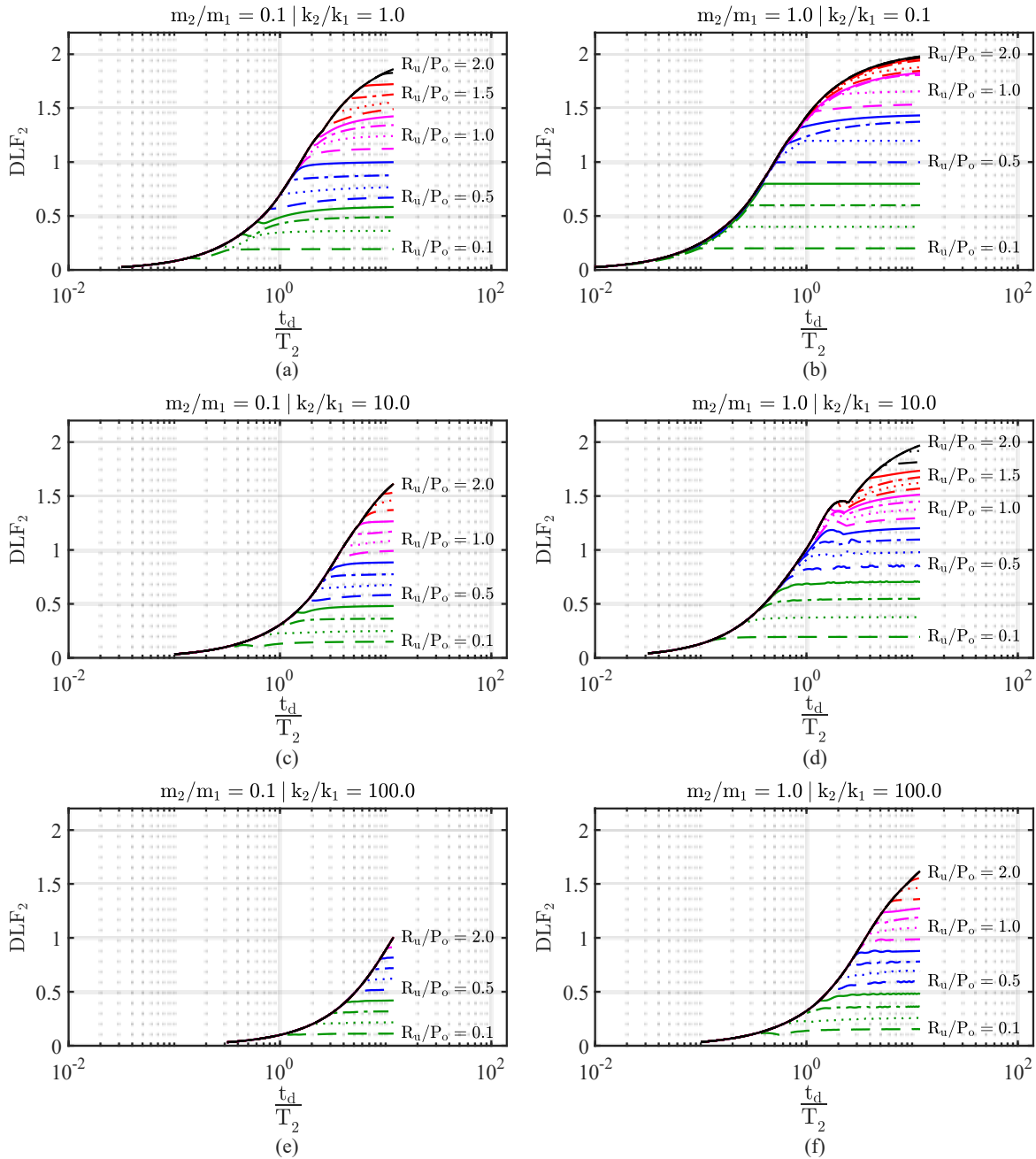


Figure 4-11: Supporting structure DLF_2 for mass ratios $m_2/m_1 = 0.1, 1.0$, for resistance ratios $R_u/P_o = 0.1 - 2.0$ (black curve represents the $R_u/P_o = 2.0$ curve) and typical stiffness ratios k_2/k_1

$DLF_2 \cong 2.0$ is approximately the upper bound static approach value for all mass and stiffness ratios. There are cases that DLF_2 reaches slightly larger values than 2.0. This is due to dynamic interaction of the two degrees of freedom when the natural periods of the two connected components are close to each other. The fact that DLF_2 is slightly over 2.0 is opposed to the balanced design approach (Dusenberry, 2010), where the maximum DLF_2 values applied for the structural design of the components supporting the cladding are 2.0 or lower, assuming the maximum DLF values from professionally

used design charts, e.g. by DoD (2008). This occurs despite the generally applied rule of the two natural periods being different by at least a factor of 2.0 (Biggs, 1964). Further evaluation and remarks for the cases that $DLF_2 > 2.0$ are discussed in subsequent paragraph 4.5.4.

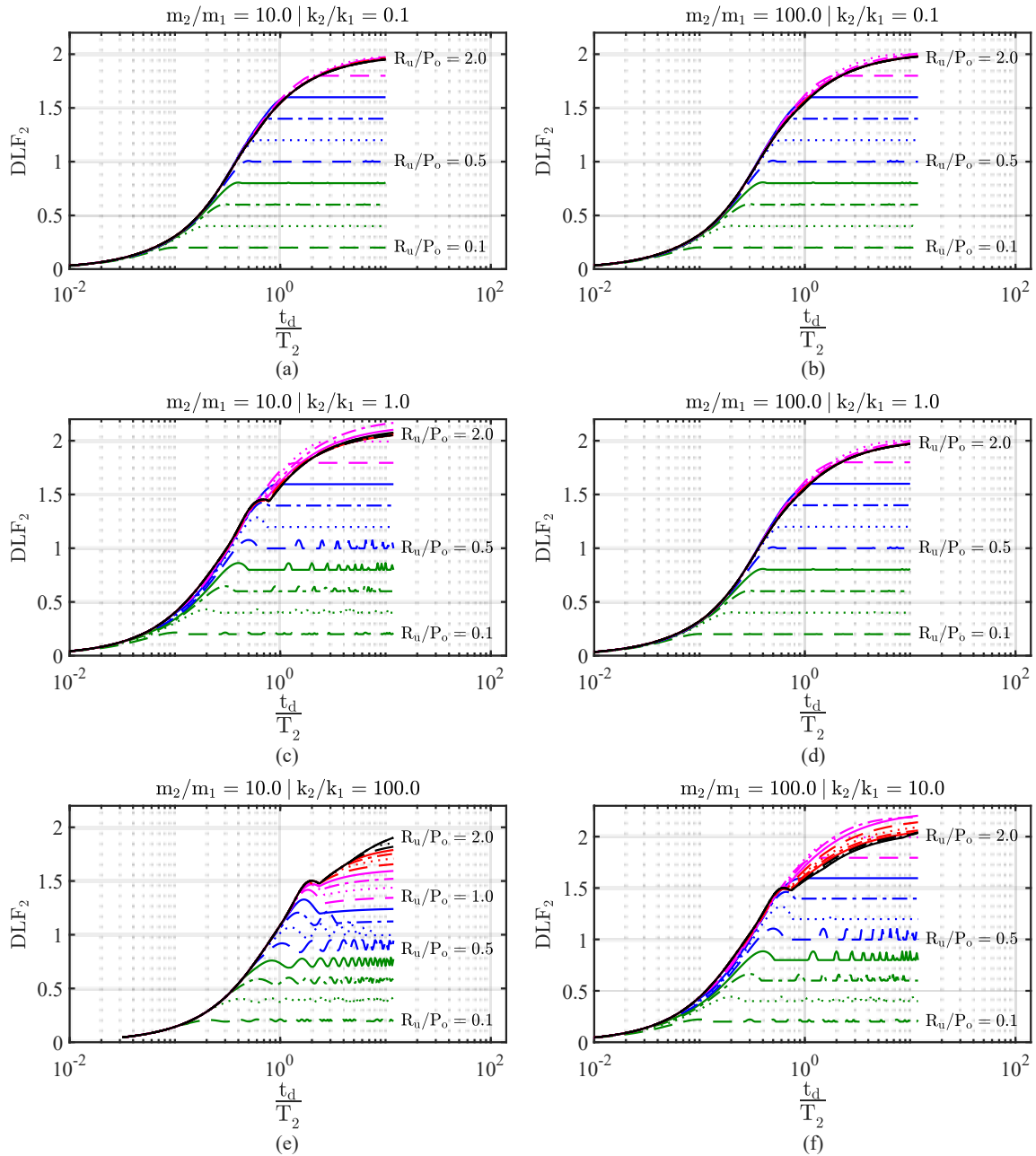


Figure 4-12: Supporting structure DLF_2 for mass ratios $m_2/m_1 = 10.0, 100.0$, for resistance ratios $R_u/P_o = 0.1 - 2.0$ (black curve represents the $R_u/P_o = 2.0$ curve) and typical stiffness ratios k_2/k_1

4.5.2. Effects of cladding ductility on the supporting structure

As already noted, plastic energy absorption is an effective mechanism to limit the demand on the supporting structure. However, certain limitations must be imposed to the structural design of the cladding-to-supporting-structure system in order to benefit from this mechanism. These limitations are associated with the cladding ductility and displacement limits. Ductility is typically dictated by the rupture strain of

the cladding material and displacement by geometric constraints of the structural configuration. According to the observations of Figure 4-11 and Figure 4-12, an apparent approach to design the cladding to achieve a low DLF_2 would be to decrease the resistance R_u in order to have the lowest possible R_u/P_o ratio. However, for the same blast load profile, the lowest R_u/P_o ratio would lead to excessive deformations and plastic strains.

A typical case of the ductility requirements is presented in Figure 4-13, which indicates the points where certain ductility has been reached. The displacements were calculated with Equation (4-2). The ductility limits, illustrated in Figure 4-13, indicate that the limits of the plastic energy absorption mechanism are not infinite. A reasonable ductility value between 5 and 20 (ASCE, 2010), depending on the cladding type for cladding-to-framing systems, is sufficient for a certain range of DLF_2 targets. Below the corresponding ductility limit, there is an inactive zone (illustrated in grey), where the cladding has unacceptable deformations or collapses.

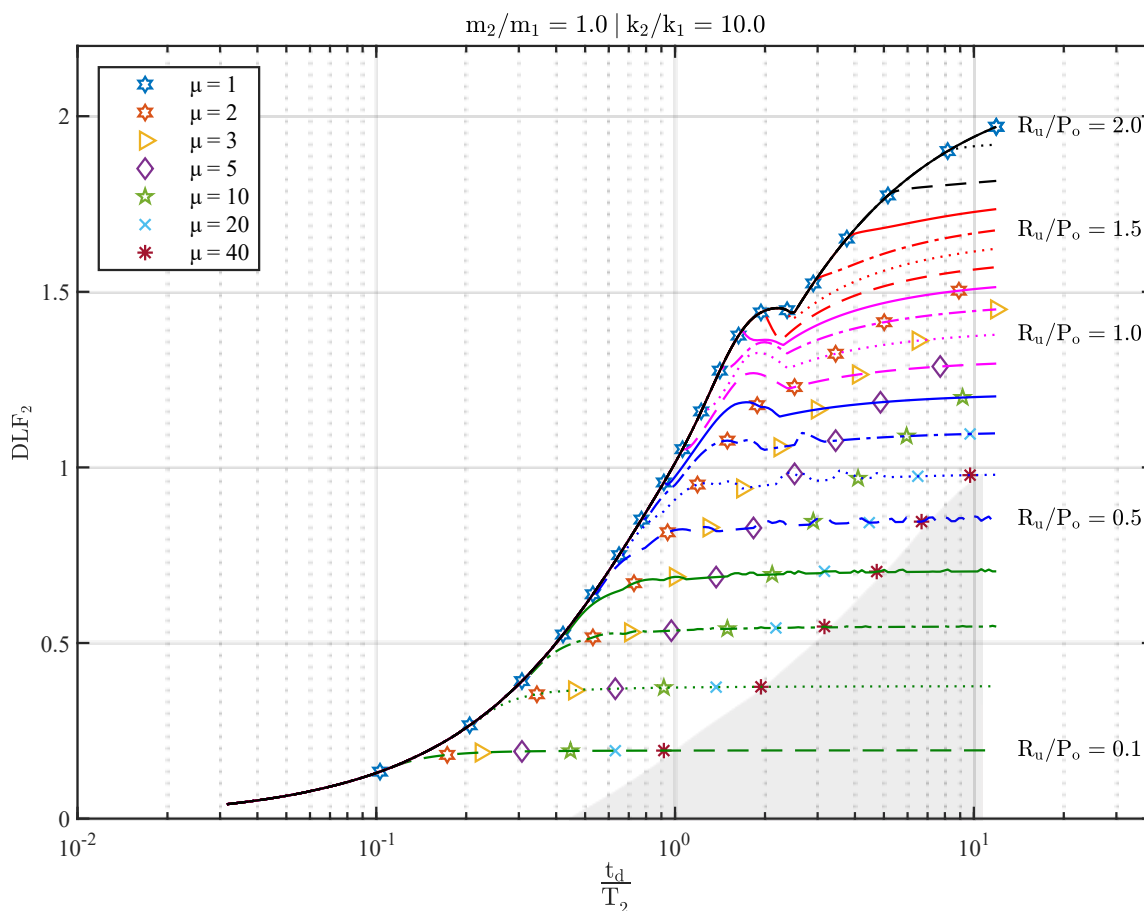


Figure 4-13: Achieved ductility of the cladding for $m_2/m_1 = 1.0$, $k_2/k_1 = 10.0$ and $R_u/P_o = 0.1 - 2.0$

4.5.3. Effects of cladding mass and stiffness on the supporting structure

Figure 4-11 and Figure 4-12 suggest that mass and stiffness have appreciable contribution on DLF_2 of the supporting structure. To further evaluate the effects of mass and stiffness, the $R_u/P_o = 2$ curves for varying mass and stiffness ratios are plotted in Figure 4-14. Regarding the mass and stiffness variables, used in Figure 4-14, the blast duration ratios t_d on the horizontal axis are divided by T_2 , which depends on m_2 and k_2 , while the vertical axis values depend on k_2 . Thus, with regard to the m_2/m_1 and k_2/k_1 ratios at the curves of Figure 4-14, the results cannot be interpreted from the perspective of m_2 and k_2 variation,

because by modifying these parameters, the variables of the axes also change. On the contrary, the variation of parameters m_1 and k_1 can be readily examined, as they do not have any correlation with the axes and they only affect the m_2/m_1 and k_2/k_1 ratios assigned to the respective curves.

An important observation from Figure 4-14 is that the contribution of the first degree of freedom (cladding) to the maximum response of the second degree of freedom (supporting structure) becomes more significant as mass m_1 increases and as stiffness k_1 drops, i.e., representing a heavy and/or flexible cladding system with relatively large natural period. More specifically, in the quasi-static region (to the right of Figure 4-14), the supporting structure DLF_2 is approximately equal to 2.0 for low mass and high stiffness in the cladding, while DLF_2 is reduced for high mass and low stiffness in the cladding. In physical terms, when the cladding has low natural period (reduced mass and increased stiffness) compared to the natural period of the supporting structure, it transfers the blast load practically unchanged to the supporting structure through its dynamic reactions. In other words, the calculated response of the supporting structure with 2DOF analysis is similar to the calculated response of the supporting structure with SDOF analysis, assuming that the mass of the first degree of freedom is rigidly attached to the supporting structure. However, an interesting observation is that when the cladding has large natural period, the supporting structure DLF_2 is lower because of the substantial inertial effects in the corresponding equations of motion. The cladding responds relatively slowly to the blast loading by simultaneously lowering the k_1 spring maximum force and increasing the duration of the excitation, received by the second degree of freedom.

Moreover, inertial resistance also affects the response in the dynamic and impulsive regions (to the left of Figure 4-14), even though this response is not governed by the maximum spring force. Because the excitation on the supporting structure has longer duration, the highly impulsive blast loading is transformed by the cladding into a quasi-static load, even for low t_d/T_2 ratios, but with lower amplitude than the initial blast force P_0 .

4.5.4. The special case of similar natural periods

For the analysis cases in the previous sections, mass and stiffness ratios have been selected in order to avoid dynamic interaction by differentiating the natural periods (calculated separately for each mass) by at least an order of two, as recommended by Biggs (1964). Nonetheless, the case of the two degrees of freedom being in dynamic interaction has also been examined and the results are presented in Figure 4-15.

Equation (4-21) has been used to calculate the ratios of the two natural periods. Since the same ratio can be achieved through multiple m_2/m_1 and k_2/k_1 ratios, each T_1/T_2 curve has been generated by employing different values for the ratios. These values are within the region [0.1, 100.0]. For example, the curve $T_1/T_2 = 1.50$ has been created by the envelope of the eight curves, which correspond to $m_2/m_1 = 0.1, 1.0, 10.0, 100.0$ and $k_2/k_1 = 0.1, 1.0, 10.0, 100.0$.

$$T_1/T_2 = \frac{\left(2\pi\sqrt{\frac{m_1}{k_1}}\right)}{\left(2\pi\sqrt{\frac{m_2}{k_2}}\right)} = \sqrt{\left(\frac{m_2}{m_1}\right)^{-1} \cdot \frac{k_2}{k_1}} \quad (4-21)$$

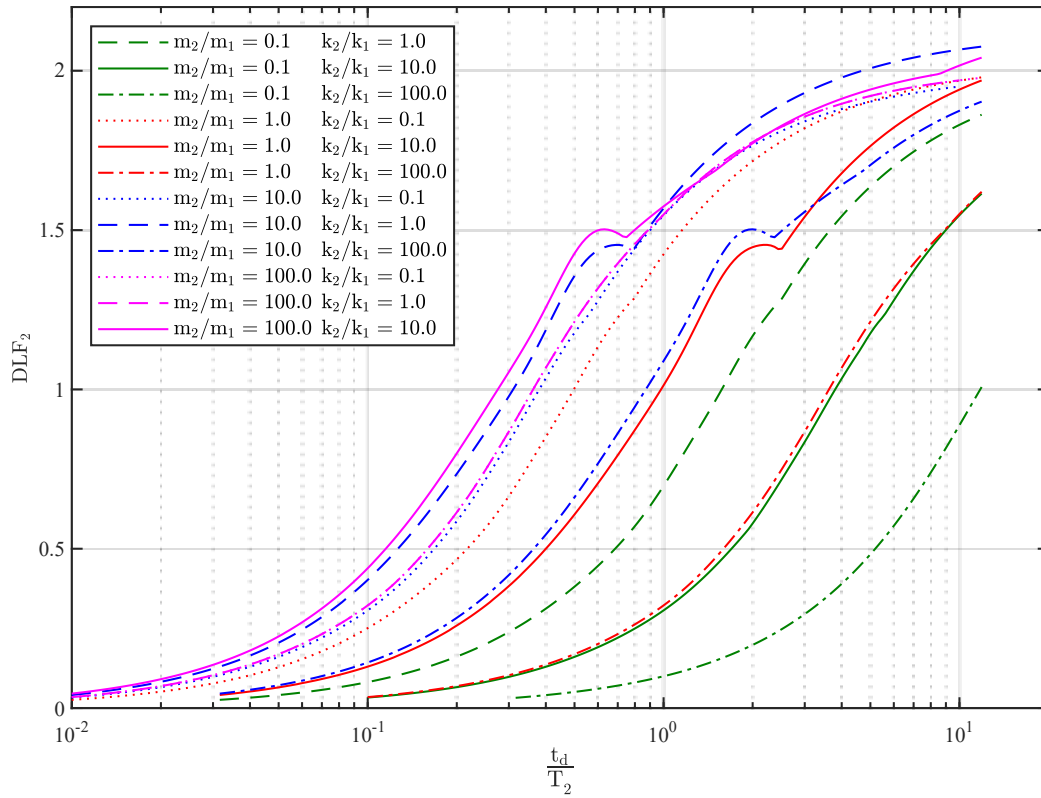


Figure 4-14: Supporting structure DLF_2 for typical mass and stiffness ratios corresponding to resistance ratio $R_u/P_o = 2$

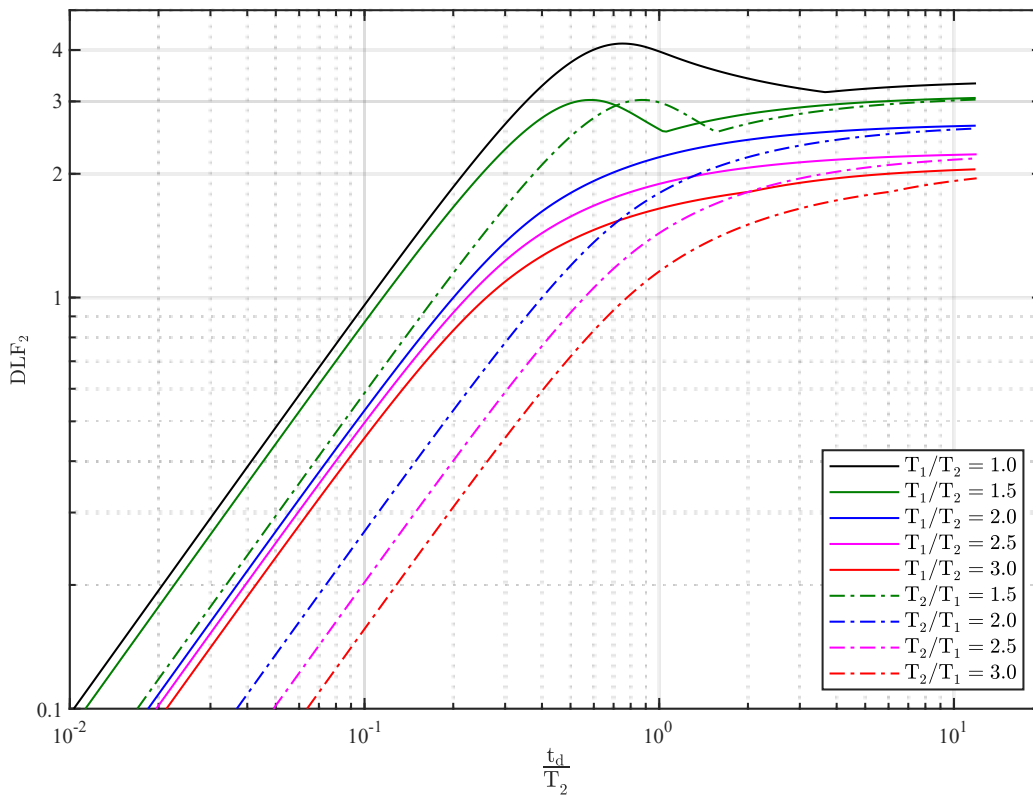


Figure 4-15: $R_u/P_o = 2$ curves when cladding and its supporting structure are in dynamic interaction

As shown in Figure 4-15, the dynamic interaction can be considered negligible only when the natural period ratio is 2.50 or higher. When the natural period ratio is 2.0, there is slight dynamic interaction, which is presented by $DLF_2 \cong 2.50$ in the quasi-static region. This fact negates the limit of 2 for the natural periods ratio, as suggested by Biggs (1964), in order to avoid dynamic interaction effects, i.e., resonance. Furthermore, when the natural period ratio is 1.5 or less, there is significant dynamic interaction, which may lead up to $DLF_2 \cong 4.00$ for equal natural periods, indicating that such design choices should be avoided for structural applications.

However, it is noted that resonance effects on interacting structural members, subjected to blast loading, may be partly disregarded due to mechanisms that attenuate the vibration after a few response cycles. As shown experimentally by PDC (2006), the respective numerical results have been proved to be over-conservative since in actual structural applications resonance effects are not dominant. Hence, as recommended by PDC (2006), DLF_2 can be taken as the peak value of the first response cycle of the supporting structure.

4.6. Interpretation of the 2DOF results and design remarks

Based on the results of the 2DOF parametric analyses that were performed in this study, a number of observations and design remarks that are directly applicable to structural engineering practice can be made, which are summarized in this section.

Regarding the plastic energy absorption mechanism, even though the cladding is designed to dissipate blast energy, this mechanism will not appreciably benefit the response of the supporting structure in the impulsive region ($t_d/T_2 < 0.1$), except only if R_u/P_o is relatively low, in the range of 0.1 to 0.2. On the contrary, mainly in the quasi-static region ($t_d/T_2 > 10.0$) and partly in the dynamic region ($0.1 < t_d/T_2 < 10.0$), the R_u/P_o values seem to be the decisive factor for the maximum displacement of the supporting structure. This observation suggests that the supporting structure should have sufficiently small natural period with respect to the duration of the blast load in order to take advantage of the plastic energy absorption mechanism. The physical meaning of this observation is that in the impulsive region the response is mainly dictated by inertial resistance and not by the plastic energy absorption mechanism. Conversely, in the quasi-static region the response is primarily governed by the plastic energy absorption mechanism, which limits the amplitude of the force exerted on the supporting structure by increasing the duration of reaction force during the response first cycle, while keeping the impulse approximately equal to the impulse of the blast load that is acting on the cladding. Therefore, the supporting structure benefits from the lower amplitude of the applied force due to plastic energy absorption taking place in the cladding. This results in significant decrease of the response of the supporting structure for all m_2/m_1 and k_2/k_1 ratios. Hence, the demand on the supporting structure will benefit from a cladding that is designed for energy absorption, only when the blast duration is such that response is in the quasi-static region and partly in the dynamic region.

However, deformation and plastic strain limits may also control the boundaries of the plastic energy absorption mechanism in the examined 2DOF system as well as in most structural applications. Plastic energy dissipation can take place in the cladding only as long as the cladding does not rupture. As shown in Figure 4-13, ductility may even deplete before the respective R_u/P_o curves enter into the quasi-static region. Thus, even in the regions where the plastic energy absorption mechanism is applicable (as discussed in previous paragraph), there is an upper limit for its utilization, which is dictated from the maximum ductility or excessive deformations of the cladding.

Hence, the plastic energy absorption mechanism has both a lower bound (the inertial resistance mechanism) and an upper bound (the maximum ductility). In order to design a cladding within these bounds, the beforehand estimation of the peak pressure P_o and impulse (through the positive phase duration t_d) is necessary. These parameters are typically known from the design-basis blast loads or may have to be estimated with probabilistic analyses.

Regarding the inertial resistance mechanism, mass and stiffness have compelling role in all regions and they can be useful for all different blast load amplitudes and durations. On the contrary, the plastic energy absorption mechanism is highly dependent on the maximum force P_o and is inactive in the impulsive and partially active in the dynamic region. However, in order to activate the inertial resistance mechanism, a combination of large cladding mass and low cladding stiffness is needed to create a large natural period cladding, with the former leading to increased gravity loads and the latter to high deformations. Thus, the design of a cladding with focus on this mechanism can be cumbersome as it is opposed to typical engineering practice, where it is desirable to minimize dead weight and maximize stiffness. Figure 4-16 summarizes the limits and activation zones of the plastic energy absorption and inertial resistance mechanism.

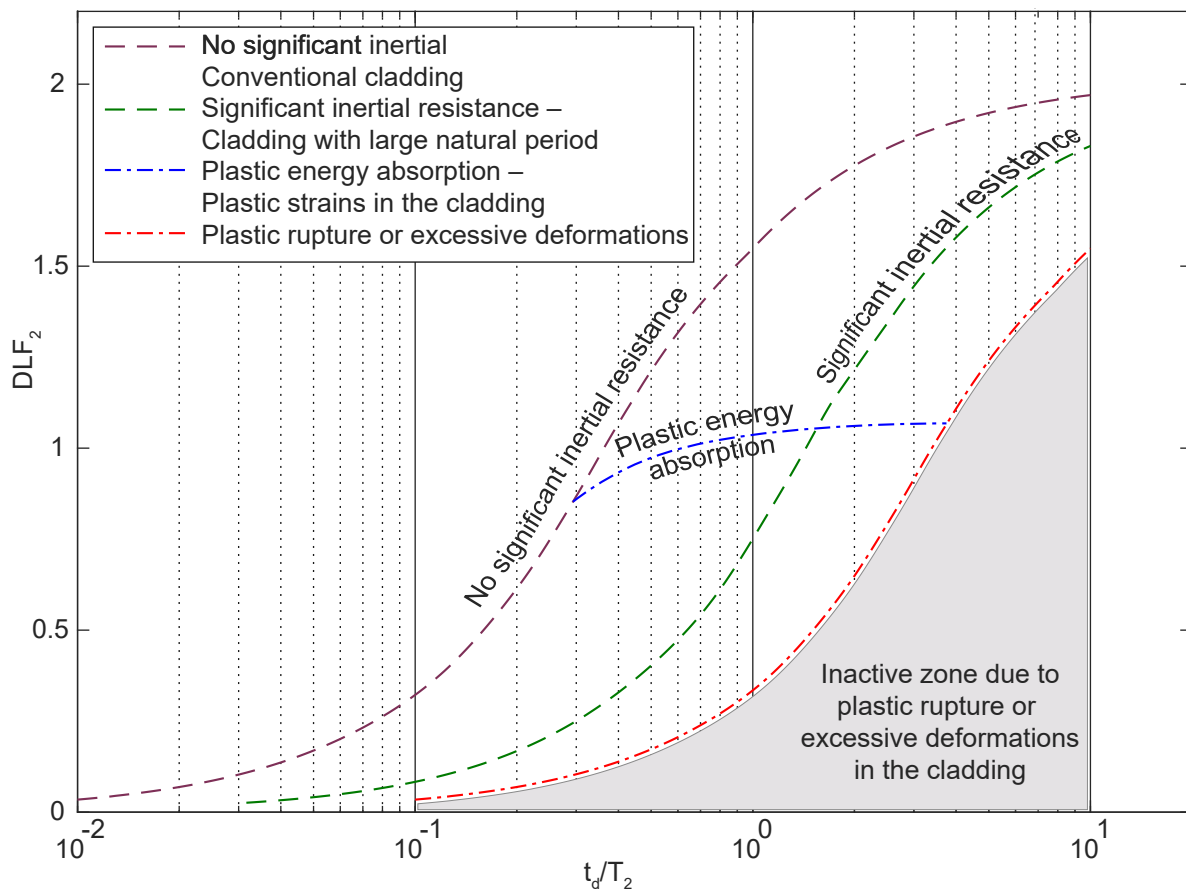


Figure 4-16: Limits and activation zones of the mechanisms of plastic energy absorption and inertial resistance

The results of the 2DOF study are in agreement with the observations made in section 4.4.1, where it is shown that in the impulsive region ($t_d/T_2 = 0.13$), the plastic energy absorption mechanism does not have any significant effect. More specifically, the reduction of steel strength in Alternative A (Figure 4-7), did not yield any appreciable difference in the computed response, even though the panel strength was far

below the peak pressure load and the plastic strains were increased. On the contrary, by altering the panel mass and stiffness in Alternative B (Figure 4-7), leading to a new panel with significantly higher natural period, the maximum beam displacement was decreased by approximately 32%, despite being in the impulsive region. This is attributed to the role of the inertial resistance mechanism, which is prevalent in Figure 4-7(b).

Regarding the dynamic interaction between the cladding and the supporting structure, their natural periods should be differentiated by at least 2.50 in order for a factor of 2 to be applied in the context of a balanced design approach. When this limit is not taken into account, significant dynamic interaction may be exhibited in the response of the respective structural components. Further research may be necessary to better characterize resonance effects for cladding-to-supporting-structure systems.

4.7. Conclusions

In this chapter, a dimensionless 2DOF model was developed. The 2DOF model was used to evaluate the effects of cladding (first DOF) to the dynamic response of the supporting structure (second DOF), when subjected to blast load. The 2DOF model was initially validated and the effects of the plastic energy absorption and inertial resistance mechanism were demonstrated with the numerical modeling, using NTFEA, in a cladding-to-framing system as well as with experimental and analytical results, found in literature. The 2DOF model was found to represent with reasonable accuracy the coupled response of the cladding-to-supporting-structure system.

Using the validated 2DOF model, the response of the cladding-to-supporting-structure system was evaluated for a wide range of different parameters with a series of dimensionless analyses. The examined parameters were the mass and stiffness of the two degrees of freedom and the ultimate resistance and ductility of the first DOF, representing the cladding. Their effects have been presented with a series of diagrams providing the corresponding DLF_2 of the supporting structure, the reduction of which is the main purpose of this research, as a means of protecting the main structure from the blast effects. It was found that by utilizing the plastic energy absorption or the inertial resistance mechanisms, the cladding can be used to mitigate the effects of the blast loading and reduce its consequences to the supporting structure.

More specifically, the most effective techniques for reducing DLF_2 were found to be the reduction of the cladding ultimate resistance, the increase of the cladding mass and the decrease of the cladding stiffness. These approaches for reducing the blast effects on the supporting structure correspond to the two different mechanisms, but both mechanisms have certain limitations. From structural design perspective, these mechanisms and their corresponding limits comprise significant parameters for the selection of a cladding type to mitigate the potential blast effects in the supporting structure. The role and applicability of each mechanism should be taken into account considering the design-basis blast loads that the cladding is designed to resist.

4.8. References

Aleyaasin, M., Harrigan, J. J. and Reid, S. R. (2015) 'Air-blast response of cellular material with a face plate: An analytical–numerical approach', *International Journal of Mechanical Sciences*, 91, pp. 64–70. doi: <https://doi.org/10.1016/j.ijmecsci.2014.03.027>.

American Society of Civil Engineers (2010) *Design of blast-resistant buildings in petrochemical facilities*. doi: 10.1061/9780784410882.

- ANSYS Inc (2017) 'ANSYS Explicit dynamics'.
- Biggs, J. M. (1964) *Introduction to structural dynamics*. United States of America: McGraw-Hill.
- Braconi, A. *et al.* (2015) 'Efficiency of Eurocode 8 design rules for steel and steel-concrete composite structures', *Journal of Constructional Steel Research*, 112, pp. 108–129. doi: <https://doi.org/10.1016/j.jcsr.2015.04.021>.
- British Standards Institution (2019) 'BS EN 10025-2:2019: Hot rolled products of structural steels'.
- Cadoni, E. *et al.* (2018) 'Tensile and compressive behaviour of S355 mild steel in a wide range of strain rates', *European Physical Journal: Special Topics*, 227(1–2), pp. 29–43. doi: 10.1140/epjst/e2018-00113-4.
- Chopra, A. K. (2007) *Dynamics of structures*. Pearson Education. Available at: <https://books.google.gr/books?id=0dU1bDaRyP4C>.
- Cormie, D., Mays, G. and Smith, P. (2009) *Blast effects on buildings*. ICE Publishing. doi: 10.1680/beob.61477.
- Dusenberry, D. O. (2010) *Handbook for blast resistant design of buildings*. John Wiley & Sons. doi: 10.1002/9780470549070.
- Gantes, C. J. and Pnevmatikos, N. G. (2004) 'Elastic-plastic response spectra for exponential blast loading', *International Journal of Impact Engineering*, 30(3), pp. 323–343. doi: 10.1016/S0734-743X(03)00077-0.
- Guruprasad, S. and Mukherjee, A. (2000) 'Layered sacrificial claddings under blast loading Part I — Analytical studies', *International Journal of Impact Engineering*, 24(9), pp. 957–973. doi: [https://doi.org/10.1016/S0734-743X\(00\)00004-X](https://doi.org/10.1016/S0734-743X(00)00004-X).
- Hanssen, A. G., Enstock, L. and Langseth, M. (2002) 'Close-range blast loading of aluminium foam panels', *International Journal of Impact Engineering*, 27(6), pp. 593–618. doi: 10.1016/S0734-743X(01)00155-5.
- Health & Safety Executive (2006) 'Design, materials and connections for blast-loaded structures'.
- Ioannou, O. and Gantes, C. J. (2021) 'Membrane action of cladding subjected to blast loading and effects on the supporting structure', *Vibration*, 4(4), pp. 768–786. doi: 10.3390/vibration4040043.
- Johnson, G. R. and Cook, W. H. (1983) 'A constitutive model and data from metals subjected to large strains, high strain rates and high temperatures', in *Proceedings of the Seventh International Symposium on Ballistics*. The Hague, Netherlands.
- Kambouchev, N., Noels, L. and Radovitzky, R. (2006) 'Nonlinear compressibility effects in fluid-structure interaction and their implications on the air-blast loading of structures', *Journal of Applied Physics*, 100(6), p. 63519. doi: 10.1063/1.2349483.
- Kingery, C. N. and Bulmash, G. (1984) 'Air blast parameters from TNT spherical air burst and hemispherical surface air burst', *U.S. Army Ballistic Research Laboratory*.
- Krauthammer, T. and Altenberg, A. (2000) 'Negative phase blast effects on glass panels', *International Journal of Impact Engineering*, 24(1), pp. 1–17. doi: [https://doi.org/10.1016/S0734-743X\(99\)00043-3](https://doi.org/10.1016/S0734-743X(99)00043-3).
- Ma, G. W. and Ye, Z. Q. (2007) 'Energy absorption of double-layer foam cladding for blast alleviation',

- International Journal of Impact Engineering*, 34(2), pp. 329–347. doi: 10.1016/j.ijimpeng.2005.07.012.
- Mortazavi, M. and Heo, Y. A. (2018) 'Nonlinear dynamic response of steel materials and plain plate systems to impact loads: Review and validation', *Engineering Structures*, 173, pp. 758–767. doi: 10.1016/j.engstruct.2018.07.012.
- Ousji, H. *et al.* (2017) 'Air-blast response of sacrificial cladding using low density foams: Experimental and analytical approach', *International Journal of Mechanical Sciences*, 128–129, pp. 459–474. doi: <https://doi.org/10.1016/j.ijmecsci.2017.05.024>.
- Protective Design Center (2006) 'PDC TR-06-01: Single degree of freedom blast design spreadsheet (SBEDS) Methodology manual', *U.S. Army Corps of Engineers*.
- Rigby, S. E., Tyas, A. and Bennett, T. (2012) 'Single-Degree-of-Freedom response of finite targets subjected to blast loading - The influence of clearing', *Engineering Structures*, 45, pp. 396–404. doi: 10.1016/j.engstruct.2012.06.034.
- Rutner, M. P. and Wright, J. P. (2016) 'Duality of energy absorption and inertial effects: Optimized structural design for blast loading', *International Journal of Protective Structures*, 7(1), pp. 18–44. doi: 10.1177/2041419615622726.
- Taylor, G. I. (1963) *The pressure and impulse of submarine explosion waves on plates*. Cambridge University Press.
- The Mathworks Inc (2018) 'MATLAB'.
- Turkyilmazoglu, M. (2016) 'Air blast response of compaction foam having a deformable front face panel incorporating fluid structure interactions', *International Journal of Mechanical Sciences*, 105, pp. 340–347. doi: <https://doi.org/10.1016/j.ijmecsci.2015.11.010>.
- U.S. Department of Defense (2008) 'UFC 03-340-02: Structures to resist the effects of accidental explosions'.
- U.S. Department of the Army (1957) 'TM5-856-3: Design of structures to resist the effects of atomic weapons'.

Chapter 5

Influence of cladding membrane action

This chapter is a slightly modified version of the following open access paper.

Ioannou, O. and Gantes, C.J. (2021) 'Membrane action of cladding subjected to blast loading and effects on the supporting structure', *Vibration*, 4(4), pp. 768–786. doi: 10.3390/vibration4040043.

5.1. Introduction

Cladding membrane behavior has been found to be critical, as it leads to increased in-plane and out-of-plane reaction forces when subjected to blast loading ([Dharmasena et al., 2008, 2011](#)). Generally, the cladding is designed assuming inelastic flexural action against blast effects, but it may also be designed with catenary action ([Dusenberry, 2010](#)). However, in order for membrane resistance (catenary action) to be efficiently used, large deformations are needed, and the respective connections should be designed accordingly, exhibiting appropriate strength and ductility. These structural implications, associated with membrane action, have limited the exploitation of membrane action in typical structural engineering practice. On the other hand, the opposite is the case in blast-resistant design, as catenary action is extensively applied to safeguard structures against progressive collapse through slabs and tie beams ([Hadjioannou et al., 2018](#)), to protect laminated glass panes with PVB layers ([Zhang and Hao, 2016](#)), or to serve as a reserve safety for structural components that have exhausted their bending strength and ductility ([Dusenberry, 2010](#)).

The effects of panel stiffness on its maximum reaction forces have been analytically examined by [Pan and Watson \(1998\)](#) for the case of a clamped rectangular plate. It was found that in the elastic limit of both the quasi-static and the impulsive regime, the transmitted membrane forces were significantly increased with thickness decrease. Sandwich panels, consisting of a face plate, a core, and a back plate, have also been found to lead to increased reaction stretching forces, when subjected to blast loading ([Dharmasena et al., 2008](#)). When compared with equivalent thickness solid plates with significant membrane behavior, it was shown that the sandwich panels lead to lower out-of-plane reaction forces ([Dharmasena et al., 2011](#)).

The membrane resistance is even more significant for glass panes due to their small thickness. As noted by [Del Linz et al. \(2015\)](#), membrane forces are increased when laminated glass is deformed. This happens up to the post-crack phase, where only membrane resistance is activated, and the respective reaction forces (both in-plane and out-of-plane) are so large that they should be calculated in detail for the glass fixings design.

In the present chapter, the influence of cladding membrane behavior on the supporting structure is examined through dimensionless SDOF models. The dimensionless SDOF models are employed because they can lead to generalized observations about a variety of cladding material and geometric arrangements that can be described by the respective material model. Dimensionless diagrams are produced, offering quantitative and qualitative estimations about the role of cladding membrane behavior over the supporting structure. The observations are demonstrated and verified through a numerical model of a typical steel cladding-to-supporting-structure application.

5.2. Dimensionless SDOF analysis

5.2.1. Derivation of equations of motion

The modeling of the cladding-to-supporting-structure system was accomplished through a two-step SDOF time history analysis, as shown in Figure 5-1.

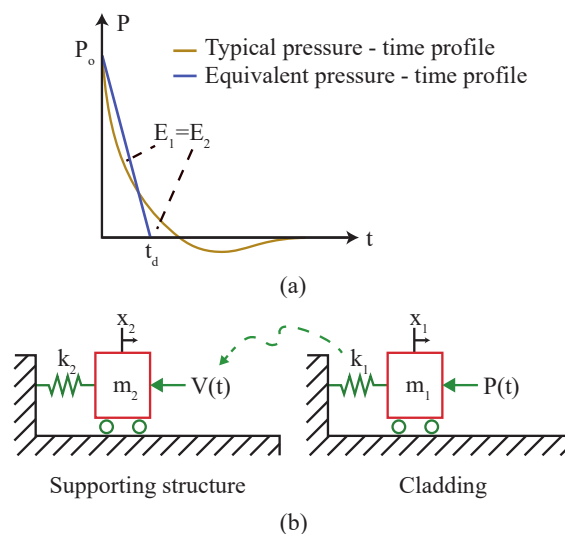


Figure 5-1: Dimensionless SDOF analysis: (a) Pressure time profile for blast loading; (b) Two step SDOF analysis

First, an SDOF analysis was performed representing the cladding subjected to blast loading (first step). Subsequently, another SDOF analysis was performed representing the supporting structure subjected to the dynamic reactions of the cladding (second step). The corresponding displacements are denoted by x_1 (cladding) and x_2 (supporting structure).

The spring that is associated with cladding stiffness is described by the force–displacement diagram of Figure 5-2. Generally, the membrane effects can be incorporated through various methodologies. An analytical methodology for predicting the maximum displacement of a structural component, subjected to blast loading, by taking into account the membrane effects of the cladding, was presented by [Hoffmeister et al. \(2015\)](#). Along with this methodology, extended SDOF approaches with membrane

properties have also been presented in FABIG (2002), NORSOK (2004). In the present chapter, the approach that is prescribed in NORSOK (2004) was adopted. According to this approach, an initial elastic stiffness $k_{1,1}$ is assigned to the SDOF. When the cladding reaches its ultimate resistance R_u , its stiffness is set to zero ($k_{1,2} = 0$), until the cladding develops sufficiently large displacements ($x_{1,mem}$) to initiate membrane action.

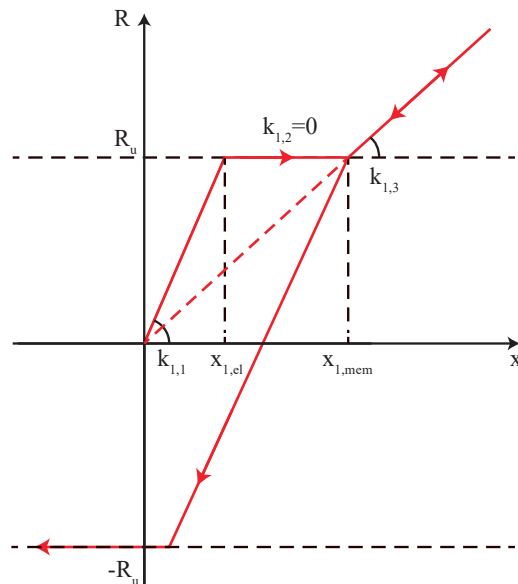


Figure 5-2: Force–displacement diagram of cladding with both bending and membrane stiffness

If the membrane stiffness $k_{1,3}$ is lower than the bending stiffness $k_{1,1}$, the cladding exhibits both bending and membrane behavior. However, if the membrane stiffness $k_{1,3}$ is significantly higher than the bending stiffness $k_{1,1}$, the cladding can be considered to be a purely tensile structure, depending only on $k_{1,3}$ and neglecting both $k_{1,1}$ and the horizontal plasticity branch in the force–displacement diagram. This difference is discussed further in sections 5.3 (both bending and membrane stiffness) and 5.4 (membrane structure).

The unloading curve of the force–displacement diagram was applied as suggested in HSE (2006). More specifically, the unloading curve corresponds to linear material and nonlinear geometry. Thus, the horizontal branch of the loading curve, which accounts for the effects of plasticity, is neglected in the unloading phase. Plasticity is then reactivated during rebound if the force reaches the cladding negative ultimate resistance, $-R_u$.

The cladding and supporting structure masses are denoted by m_1 and m_2 , respectively. Along with mass m_1 , the load–mass transformation factor is employed in order to appropriately convert the cladding component into an SDOF, where $a_{1,1}$, $b_{1,1}$, $a_{1,2}$, and $b_{1,2}$ constitute the respective coefficients for the cladding dynamic reactions (Biggs, 1964). Furthermore, the supporting structure spring is considered as elastic and is denoted by k_2 .

The corresponding equations of motion and dynamic reactions $V(t)$ of the cladding SDOF are described by Equations (5-1)–(5-7), separated into the various regions of cladding response, i.e., the elastic region,

the plastic region, and the membrane action region. The equations are also applicable during the unloading of the cladding SDOF in a similar manner as for the aforementioned regions. In these equations, the blast loading $P(t)$ is applied as an equivalent triangular load, shown in Figure 5-1, while the cladding membrane stiffness is calculated by employing the cladding axial resistance N_p and length L . Moreover, damping has not been accounted for, because it has negligible effects in blast-resistant design (Krauthammer and Altenberg, 2000; Rigby, Tyas and Bennett, 2012). The support reaction $V(t)$ is doubled when applied to the supporting structure because it refers to the reactions of both adjacent cladding components.

$$m_1 \cdot \ddot{x}_1 + k_{1,1} \cdot x_1 = P(t), \quad x_1 < x_{1,el} \quad (5-1)$$

$$V(t) = a_{1,1} \cdot R(t) + b_{1,1} \cdot P(t), \quad x_1 < x_{1,el} \quad (5-2)$$

$$m_1 \cdot \ddot{x}_1 + R_u = P(t), \quad x_{1,el} \leq x_1 < x_{1,mem} \quad (5-3)$$

$$V(t) = a_{1,2} \cdot R_u + b_{1,2} \cdot P(t), \quad x_{1,el} \leq x_1 < x_{1,mem} \quad (5-4)$$

$$m_1 \cdot \ddot{x}_1 + k_{1,3} \cdot x_1 = P(t), \quad x_1 \geq x_{1,mem} \quad (5-5)$$

$$V(t) = (2 \cdot N_p/L) \cdot x_1, \quad x_1 \geq x_{1,mem} \quad (5-6)$$

$$m_2 \cdot \ddot{x}_2 + k_2 \cdot x_2 = 2 \cdot V(t) \quad (5-7)$$

The equations of motion can be further developed in non-dimensional form through the parameters of Equations (5-8)–(5-11). The non-dimensionalization of the displacement is performed by dividing with the static displacement $x_{st2} = P_o/k_2$, while the non-dimensionalization of time is performed by dividing with the ratio of blast positive phase duration t_d to the natural period of the supporting structure T_2 .

$$n_1 = \frac{x_1}{(P_o/k_2)} \quad (5-8)$$

$$n_2 = \frac{x_2}{(P_o/k_2)} \quad (5-9)$$

$$P(t) = P_o \cdot \left(1 - t/t_d\right) \quad (5-10)$$

$$\xi = t/T_2 = t / (2\pi\sqrt{m_2/k_2}) \quad (5-11)$$

By applying a similar procedure with the one described by Biggs (1964), Equations (5-1)–(5-7) can be converted into Equations (5-12)–(5-16). According to these equations, the maximum displacement of the supporting structure can be estimated through the maximum value of n_2 , which constitutes the DLF_2 (Dynamic Load Factor, ratio of maximum displacement x_{max2} to static displacement x_{st2}) of the supporting structure.

$$\frac{m_1}{m_2} \cdot \frac{1}{4\pi^2} \cdot \ddot{n}_1 + \frac{k_{1,1}}{k_2} \cdot n_1 = 1 - \xi \cdot T_2/t_d, \quad n_1 < n_{1,el} \quad (5-12)$$

$$\frac{V(\xi \cdot T_2)}{P_o} = a_{1,1} \cdot \frac{k_{1,1}}{k_2} \cdot n_1 + b_{1,1} \cdot \left(1 - \xi \cdot T_2/t_d\right), \quad n_1 < n_{1,el} \quad (5-13)$$

$$\frac{m_1}{m_2} \cdot \frac{1}{4\pi^2} \cdot \ddot{n}_1 + \frac{R_u}{P_o} = 1 - \xi \cdot T_2/t_d, \quad n_{1,el} \leq n_1 < n_{1,mem} \quad (5-14)$$

$$\frac{V(\xi \cdot T_2)}{P_o} = a_{1,2} \cdot \frac{R_u}{P_o} + b_{1,2} \cdot \left(1 - \xi \cdot T_2/t_d\right), \quad n_{1,el} \leq n_1 < n_{1,mem} \quad (5-15)$$

$$\frac{m_1}{m_2} \cdot \frac{1}{4\pi^2} \cdot \ddot{n}_1 + \frac{k_{1,3}}{k_{1,1}} \cdot \frac{k_{1,1}}{k_2} \cdot n_1 = 1 - \xi \cdot T_2/t_d, \quad n_1 \geq n_{1,mem} \quad (5-16)$$

$$\frac{V(\xi \cdot T_2)}{P_o} = \frac{k_{1,3}}{k_{1,1}} \cdot \frac{k_{1,1}}{k_2} \cdot \frac{1}{2} \cdot n_1, \quad n_1 \geq n_{1,mem} \quad (5-17)$$

$$\frac{1}{4\pi^2} \cdot \ddot{n}_2 + n_2 = 2 \cdot \frac{V(\xi \cdot T_2)}{P_o} \quad (5-18)$$

The above differential equations were solved in MATLAB (The Mathworks Inc, 2018) for a wide range of the five dimensionless parameters m_2/m_1 , $k_2/k_{1,1}$, R_u/P_o , $k_{1,3}/k_{1,1}$, and t_d/T_2 . The Newmark average acceleration method was applied with $\gamma_N = 0.5$, $\beta_N = 0.25$, and a sufficiently small time step in order to capture the maximum displacement at the first oscillation cycle, as noted in PDC (2006).

5.2.2. Assumptions and limitations

The range of validity of the described two-step SDOF analysis is restricted by several limitations, which are summarized as follows:

- The actual cladding-to-supporting-structure system is more complicated with regard to the distribution of mass and stiffness than the employed lumped mass SDOF models. The respective transformation factors are considered uniform throughout the analyses.
- For the sake of simplicity, the dynamic reactions $V(t)$ correspond to simply supported components with uniformly distributed load and uniformly distributed mass [$a_{1,1} = 0.39$, $b_{1,1} = 0.11$, $a_{1,2} = 0.38$, $b_{1,2} = 0.12$ (Cormie, Mays and Smith, 2009)]. It is noted that the respective values of the dynamic reactions in fixed components are approximately equal with the ones in the simply supported components.
- Plasticity can only be captured by the horizontal branch of the force–displacement diagram, while in actual cases the cladding’s response may be composed of multilinear regions with smooth transitions.
- Membrane action, which is considered through stiffness $k_{1,3}$, is only an approximation of the physical system’s response, where the membrane action increases rapidly with increases in displacement, depending also on the cladding’s connections and on the supporting structure stiffness.
- The force–displacement unloading branches and the respective stiffness and resistance values constitute reasonable estimations of the actual behavior. No cyclic loading or buckling was examined.
- Strain-rate effects can efficiently be accounted for with the use of dynamic increase factors, as indicated by Dusenberry (2010).
- Close-in or contact explosions that may lead to shear failure and perforation in the cladding are not taken into account. It is assumed that the charge is positioned at sufficient distance from the cladding, so that the developing blast pressure is uniformly distributed.
- Blast loading was applied as an equivalent triangular load with the same maximum pressure and positive impulse as the actual exponential blast loading, by altering the blast positive phase duration and neglecting the negative phase effects.

5.3. Influence of cladding with both bending and membrane stiffness

The two-step SDOF analysis can be uniquely described by the five parameters identified in paragraph 5.2.1. Appropriate values were assigned to these parameters in order to produce the qualitative and quantitative diagrams shown in the present section. These parameters are further detailed as follows:

- m_2/m_1 : The mass of the supporting structure (m_2) is typically lower than the cladding mass (m_1). Hence, the cases of $m_2/m_1 = 0.1$ and $m_2/m_1 = 1.0$ are presented.
- $k_2/k_{1,1}$: The stiffness of the supporting structure (k_2) is significantly larger than the cladding bending stiffness ($k_{1,1}$). Hence, the cases of $k_2/k_{1,1} = 10.0$ and $k_2/k_{1,1} = 100.0$ are presented.

- R_u/P_o : The ultimate resistance of the cladding (R_u) may be either larger or lower than the maximum blast pressure (P_o). As a consequence, two extreme values were assigned to this ratio ($R_u/P_o = 0.1$ and $R_u/P_o = 2.0$), as well as three intermediate values ($R_u/P_o = 0.5, 1.0, 1.5$).
- $k_{1,3}/k_{1,1}$: Six cases were examined with regard to the cladding membrane stiffness. These cases are presented in Figure 5-3 and can be described by only flexural response without plasticity ($k_{1,3}/k_{1,1} = 1.00, 2.00$), flexural and early membrane response ($k_{1,3}/k_{1,1} = 0.50, 0.75$), and flexural and late membrane response ($k_{1,3}/k_{1,1} = 0.10, 0.25$). The discussed ratios are also examined in NORSOK (2004).
- t_d/T_2 : A wide spectrum of t_d/T_2 ratios was investigated in order to efficiently calculate the DLF_2 at all response types, i.e., at the impulsive regime ($t_d/T_2 < 0.1$), the dynamic regime ($0.1 < t_d/T_2 < 10.0$), and the quasi-static regime ($t_d/T_2 > 10.0$) (Cormie, Mays and Smith, 2009). More specifically, DLF_2 was calculated at 401 points ranging from $t_d/T_2 = 0.01$ to $t_d/T_2 = 100.0$. In the same context with the well-known ductility ratio or DLF diagrams, used in blast-resistant design (DA, 1957), the t_d/T_2 ratio was applied in the horizontal axis of the diagrams that are shown in this chapter.

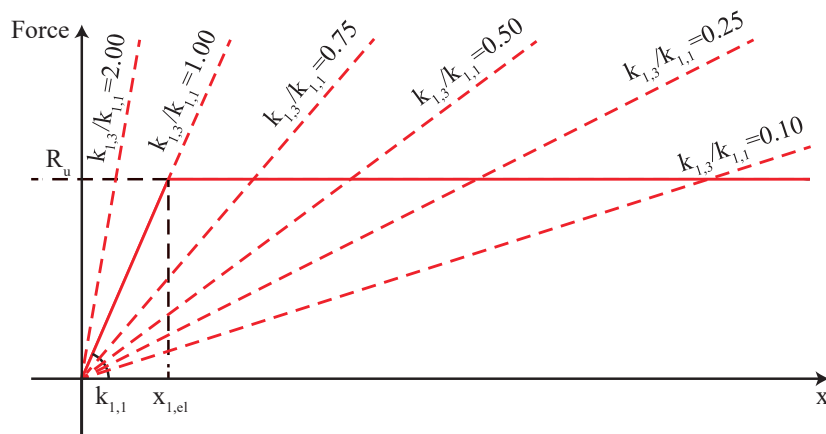


Figure 5-3: Force–displacement diagram of cladding at multiple membrane stiffness ratios ($k_{1,3}/k_{1,1} = 0.10, 0.25, 0.50, 0.75, 1.00, 2.00$)

It is noted that despite the reasonable selection of specific values in the aforementioned parameters, the observations that are made in the present section about the cladding-membrane-behavior influence on the supporting structure were also verified at additional values of the parameters. Hence, these observations can be considered to be of general validity for a wide range of cladding-to-supporting-structure arrangements.

The diagrams included in Figure 5-4 and Figure 5-5 were produced with the aforementioned representative values. More specifically, both figures refer to the same mass and stiffness ratios ($m_2/m_1 = 0.1, 1.0$, $k_2/k_{1,1} = 10.0, 100.0$, and $k_{1,3}/k_{1,1} = 0.1, 0.5, 1.0$) but different resistance ratios ($R_u/P_o = 0.1, 1.0, 2.0$ in Figure 5-4, $R_u/P_o = 0.5, 1.5, 2.0$ in Figure 5-5). The resistance ratio $R_u/P_o = 2.0$ is common between the two figures because it represents the elastic cladding response. Hence, all possible observations should be made by comparing the other curves with the $R_u/P_o = 2.0$ curve (black curve), which is the same for all stiffness ratios.

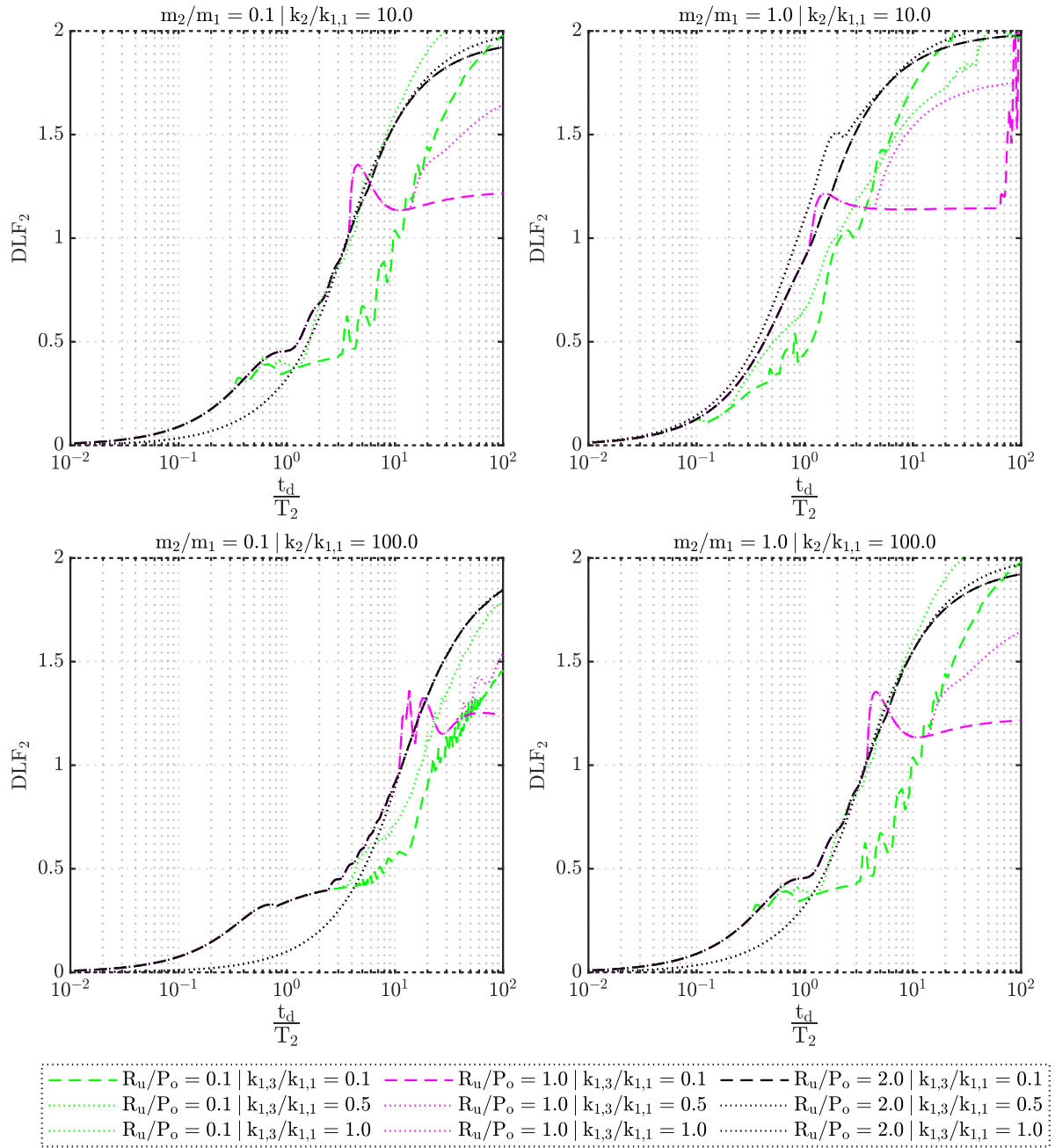


Figure 5-4: DLF_2 of supporting structure for typical mass, bending stiffness, and membrane stiffness arrangements ($m_2/m_1 = 0.1, 1.0, k_2/k_{1,1} = 10.0, 100.0$, and $k_{1,3}/k_{1,1} = 0.1, 0.5, 1.0$) at resistance ratios $R_u/P_o = 0.1, 1.0, 2.0$

Similar diagrams are presented in Figure 5-6 but with fixed values for the mass ratio m_2/m_1 and bending stiffness ratio $k_2/k_{1,1}$, as their main purpose is to capture the effect of membrane stiffness ratio $k_{1,3}/k_{1,1}$ in combination with the resistance ratio R_u/P_o . The selected values were representing typical cladding-to-supporting-structure arrangements, i.e., $m_2/m_1 = 0.1$ and $k_2/k_{1,1} = 10.0$.

The main contribution of the cladding to the response of the supporting structure is presented in the dynamic and quasi-static regime. This observation is supported by the fact that the lower the resistance ratio R_u/P_o is, the lower the positive phase duration to natural period ratio t_d/T_2 is, for which the cladding comes into effect. Hence, the cladding influence could be exhibited in the impulsive regime only for

significantly low resistance ratios R_u/P_o , low stiffness ratios $k_2/k_{1,1}$ and $k_{1,3}/k_{1,1}$, as well as high mass ratios m_2/m_1 .

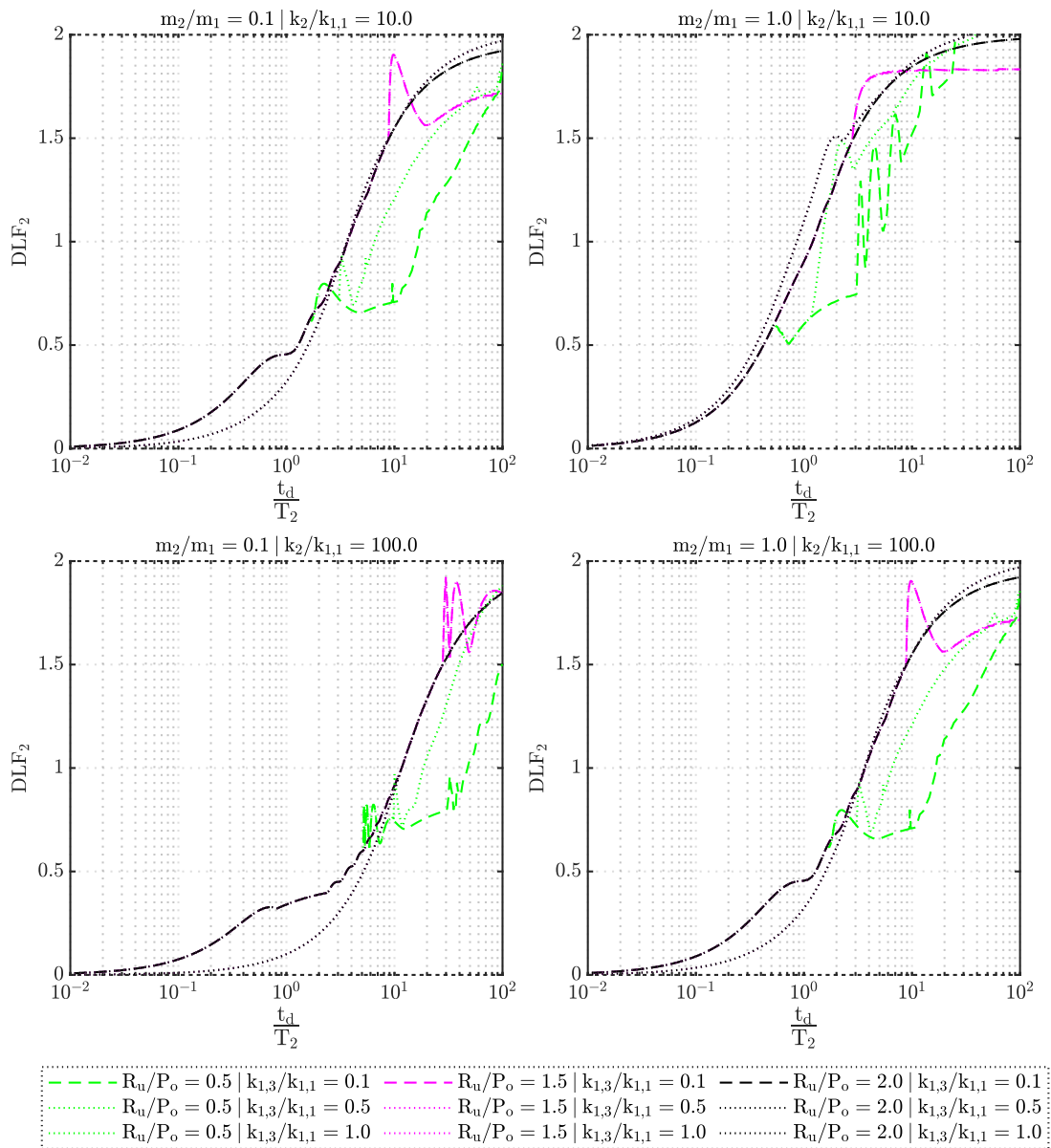


Figure 5-5: DLF_2 of supporting structure for typical mass, bending stiffness, and membrane stiffness arrangements ($m_2/m_1 = 0.1, 1.0$, $k_2/k_{1,1} = 10.0, 100.0$, and $k_{1,3}/k_{1,1} = 0.1, 0.5, 1.0$) at resistance ratios $R_u/P_o = 0.5, 1.5, 2.0$

With regard to the dynamic and the quasi-static regime, the influence of the cladding can be calculated by the reduction in the DLF_2 curve (in black) at the same positive phase duration to natural period ratio t_d/T_2 as the one of interest. The reduction can have limited or extended magnitude and is strongly dependent upon the various examined parameters. Furthermore, the reduction may be present either for only a narrow range or, conversely, for a wide range of t_d/T_2 ratios.

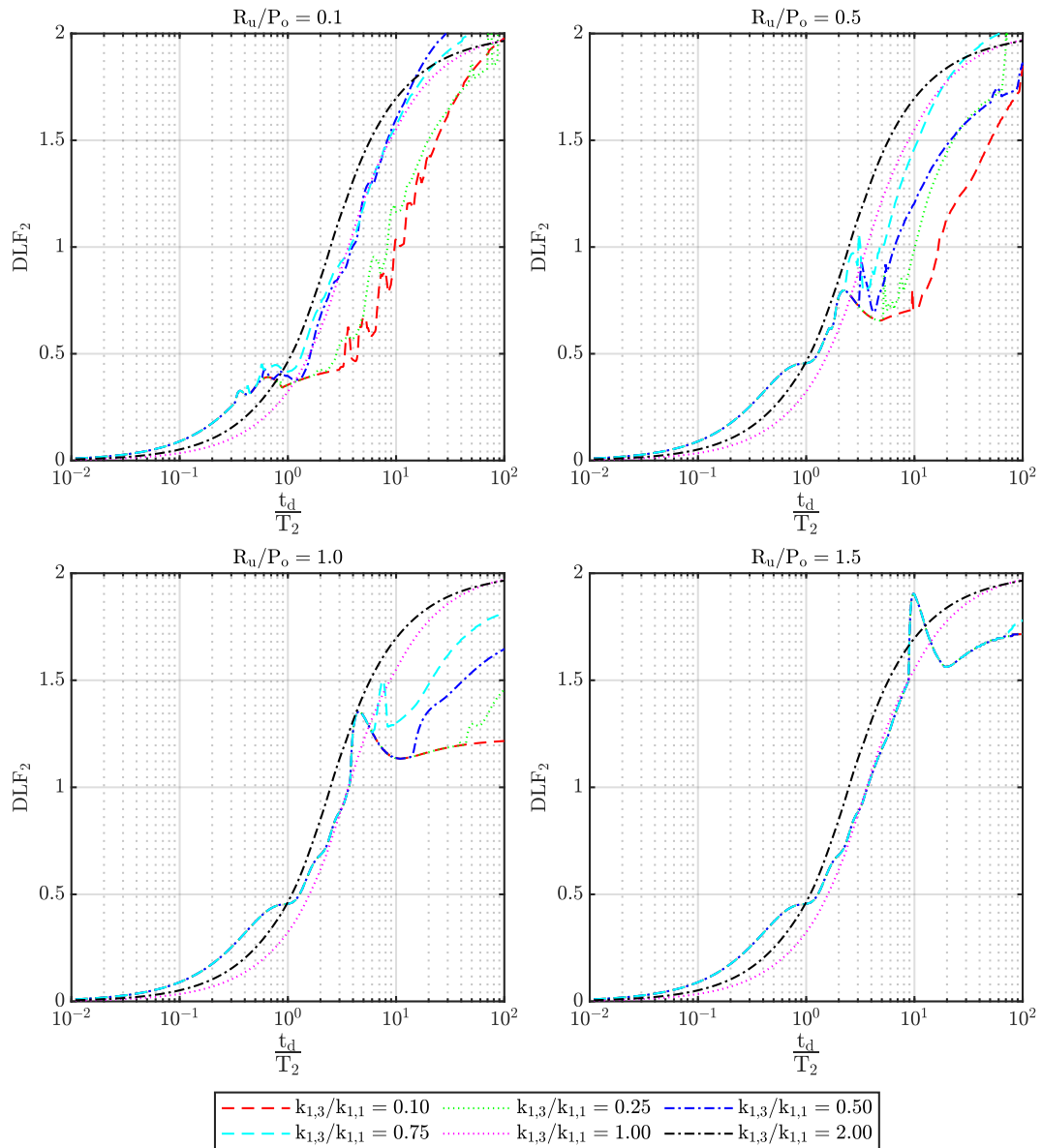


Figure 5-6: DLF_2 of supporting structure for mass ratio $m_2/m_1 = 0.1$, bending stiffness ratio $k_2/k_{1,1} = 10.0$, and various membrane stiffness ratios ($k_{1,3}/k_{1,1} = 0.10, 0.25, 0.50, 0.75, 1.00, 2.00$) at resistance ratios $R_u/P_o = 0.1, 0.5, 1.0, 1.5$

More specifically, the resistance ratio R_u/P_o seems to have a prevalent role in the response of the supporting structure. When R_u/P_o is low (i.e., equal to 0.1 or 0.5), the effects on DLF_2 are exhibited early and can be estimated to have an approximately 30~50% reduction in the displacement of the supporting structure. However, this is not applicable for all membrane stiffness ratios $k_{1,3}/k_{1,1}$ because, when the membrane action is significant ($k_{1,3}/k_{1,1} = 0.5, 1.0$), plastic dissipation cannot be efficiently activated, and the respective effects on DLF_2 are minor. Increases in cladding displacements lead to substantial membrane action with simultaneous increase in the corresponding support reactions acting over the supporting structure. Hence DLF_2 ends up being the same as if blast loading were applied directly to the supporting structure (via the corresponding tributary area), without taking into account the cladding characteristics.

A similar behavior is observed for large resistance ratios R_u/P_o but, in this case, the DLF_2 reduction is applicable for a range of positive phase duration to natural period ratios t_d/T_2 only in the quasi-static regime. Hence, cladding ductility is utilized differently with respect to the supporting structure response regime. Large resistance ratios R_u/P_o should be used only in the quasi-static regime, while small resistance ratios R_u/P_o should be used both in the dynamic and the quasi-static regime. However, at all resistance ratios R_u/P_o , the membrane stiffness ratio $k_{1,3}/k_{1,1}$ should be as small as possible in order for plastic energy absorption to take place.

The effects of mass and bending stiffness are significant and effective at the whole spectrum of positive phase duration to natural period ratios t_d/T_2 . More specifically, it is preferred for mass m_1 to have large values and bending stiffness $k_{1,1}$ to have small values. In this way, the inertial resistance mechanism of the cladding comes into effect. This mechanism is associated with decreased cladding velocity and, thus, with reduced kinetic energy applied to the cladding (Dusenberry, 2010). The reduced kinetic energy is critical because it is subsequently converted into strain energy and, thus, into reduced displacements for the supporting structure.

5.4. Influence of cladding as a membrane structure

Generally, cladding could be designed with negligible bending stiffness in contrast with its membrane stiffness. Then, cladding can be considered as a membrane structure, without bending stiffness $k_{1,1}$ and resistance R_u . This case is indicated by parameters $k_{1,3}/k_{1,1} = 1.0, 2.0$ of Figure 5-3. Pertinent DLF_2 results of this type of structure are presented in Figure 5-7 for multiple mass and stiffness ratios.

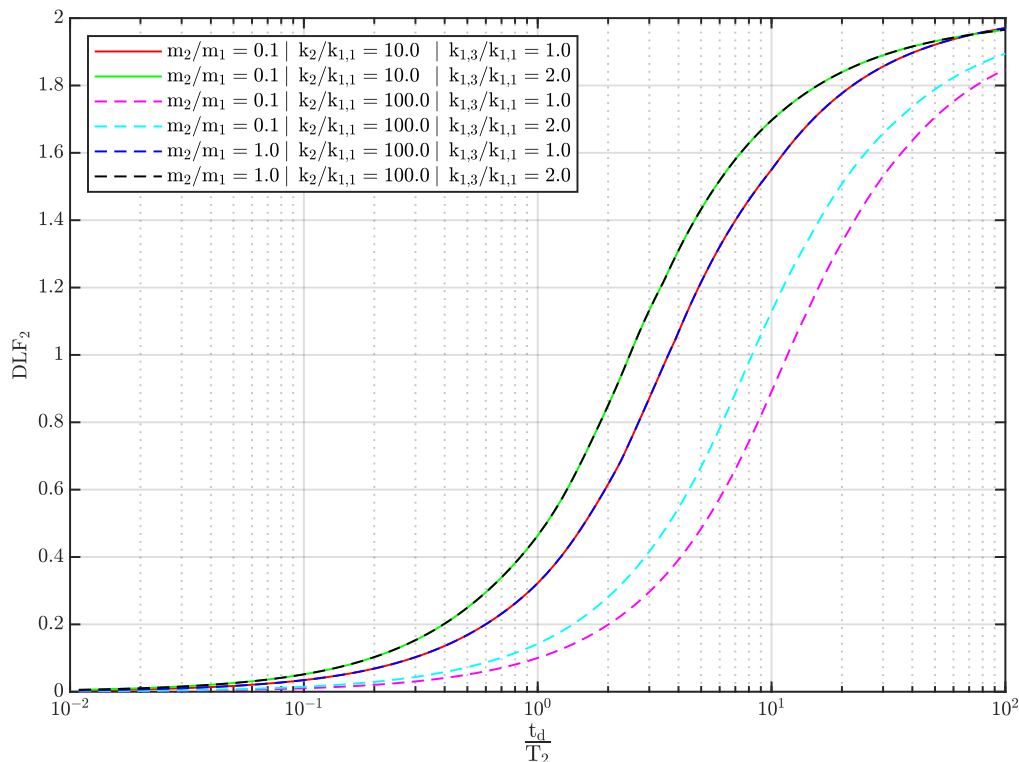


Figure 5-7: DLF_2 of supporting structure when cladding is considered to be a membrane structure with $k_{1,3}/k_{1,1} = 1.0, 2.0$ at mass ratios $m_2/m_1 = 0.1, 1.0$ and bending stiffness ratios $k_2/k_{1,1} = 10.0, 100.0$

As observed, the cladding mass and stiffness exhibit significant influence over the supporting structure. Increases in mass m_1 and decreases of membrane stiffness $k_{1,3}$ may reduce DLF_2 by as much as 70%.

Furthermore, these effects are active across the whole range of positive phase duration to natural period ratios t_d/T_2 , i.e., at the impulsive, dynamic, and quasi-static regime. This fact is of particular interest because the effects of the resistance ratio R_u/P_o are mainly applicable to the dynamic and the quasi-static regime, while they are also dependent upon the maximum pressure P_o for the determination of R_u and the proper design of the cladding. Hence, designing the cladding with low membrane stiffness and increased mass could yield substantial effects over the DLF_2 without the need for the beforehand estimation of maximum blast pressure P_o .

5.5. Case study

A case study of a typical cladding-to-column arrangement was selected in order to verify the proposed two-step SDOF analysis and demonstrate the membrane effects of cladding over the supporting structure. A numerical model was prepared in ANSYS Explicit Dynamics software (ANSYS Inc, 2017), and appropriate Nonlinear Transient Finite Element Analyses (NTFEA) executions were performed.

The considered cladding comprised a steel trapezoidal sheet with a height of 100 mm, a thickness of 5 mm, a crest width of 100 mm, and a valley width of 100 mm, as shown in Figure 5-8. Its geometry was similar to the profiled sheeting that was used by Louca and Boh (2004), and its static pressure–displacement curve was calculated as indicated in Figure 5-9. The supporting structure comprised IPE 330 columns that were considered to be pinned-pinned, while the trapezoidal sheeting was assumed to be welded to the columns through the detail presented in Figure 5-10. The column spacing and length were defined as 4 m and 2 m, respectively.

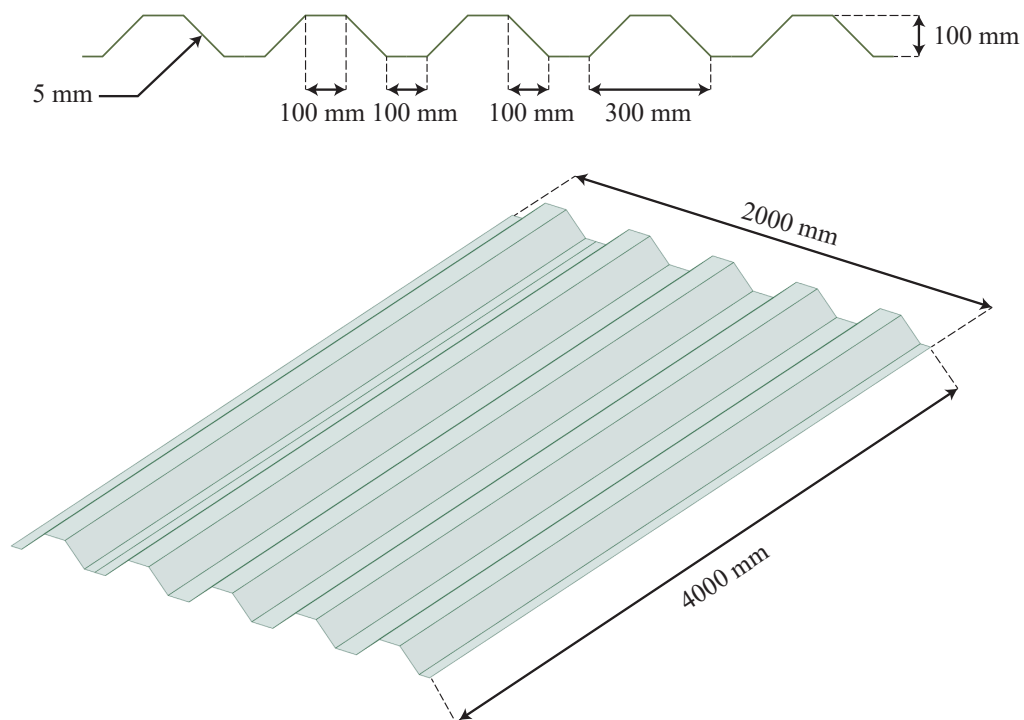


Figure 5-8: Geometry of the trapezoidal sheet considered in the case study

The selected material was steel S355 (BSI, 2019) with a yield strength of 410 MPa (Braconi et al., 2015) due to the static increase factor (representing the difference between the designed steel quality and the actual steel quality). In the numerical model, the hardening effects were taken into account by considering the Johnson-Cook model (Johnson and Cook, 1983), while the strain-rate effects were taken into

account by considering the Cowper-Symonds model (Cowper and Symonds, 1957). These models are described by Equation (5-19), with the relevant values shown in Table 5-1 for the hardening coefficients (B , θ) and for the strain-rate coefficients (D , q) (Cadoni et al., 2018; Mortazavi and Heo, 2018). In Equation (5-19), plastic stress, yield strength, plastic strain, and plastic strain rate are denoted by σ , A , ε_{pl} , and $\dot{\varepsilon}_{pl}$, respectively. These effects were accounted for in the two-step SDOF analysis through the Dynamic Increase Factor (DIF), which was assigned to the resistance R_u .

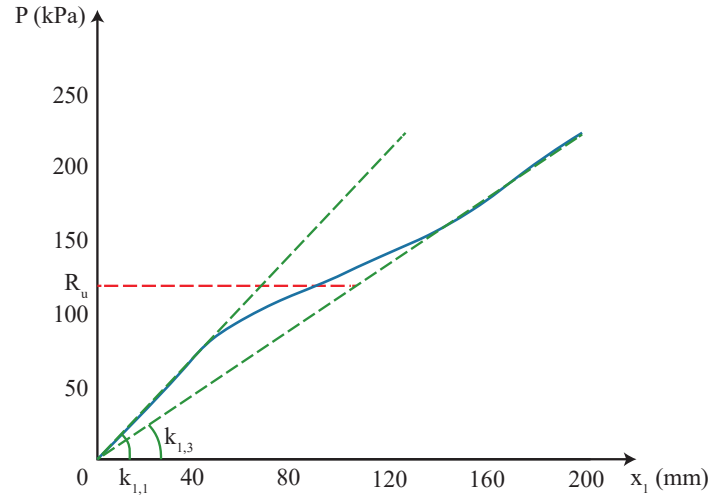


Figure 5-9: Static pressure–displacement curve (resistance curve) of the trapezoidal sheet considered in the case study

$$\sigma = (A + B \cdot \varepsilon_{pl}^{\theta}) \cdot \left(1 + \left(\frac{\dot{\varepsilon}_{pl}}{D}\right)^{1/q}\right) \quad (5-19)$$

Table 5-1: Parameters values of the Johnson-Cook and the Cowper-Symonds models (Cadoni et al., 2018; Mortazavi and Heo, 2018)

Parameter	Value
A	410 MPa
B	782 MPa
θ	0.562
D	4000
q	5

Blast loading was applied as an equivalent triangular pressure, as shown in Figure 5-1. A pressure amplitude of 200 kPa was applied, as it reflects a typical mid-range blast loading (e.g., 20 kg at a stand-off distance of 10 m), which is considered as appropriate, assuming that the panel belongs to a building with perimeter protection (fence and barriers). A variety of peak pressure–impulse combinations was applied to the cladding. All combinations had the same maximum blast pressure but different positive phase duration, as indicated in Figure 5-11. This procedure was chosen, because each curve that was shown at the relevant DLF_2 diagrams of the previous paragraphs can be produced by fixed values at all parameters, except for the positive phase duration t_d , which dictates the ratio t_d/T_2 . It is noted that constant pressure can be achieved through positive phase duration by increasing impulse, which is the integral of pressure over time.

The procedure that was used in the two-step SDOF analysis was the same as the one described in section 5.2. However, along with masses m_1 and m_2 , proper K_{LM} factors (load–mass transformation factors) (Cormie, Mays and Smith, 2009) were applied in order to convert the structural components into SDOF models with approximately the same displacement time history. The contribution of these factors is shown in Equations (5-20)–(5-26), and the respective values are presented in Table 5-2.

$$K_{LM1} \cdot m_1 \cdot \ddot{x}_1 + k_{1,1} \cdot x_1 = P(t), \quad x_1 < x_{1,el} \quad (5-20)$$

$$V(t) = a_{1,1} \cdot R(t) + b_{1,1} \cdot P(t), \quad x_1 < x_{1,el} \quad (5-21)$$

$$K_{LM1} \cdot m_1 \cdot \ddot{x}_1 + DIF \cdot R_u = P(t), \quad x_{1,el} \leq x_1 < x_{1,mem} \quad (5-22)$$

$$V(t) = a_{1,2} \cdot DIF \cdot R_u + b_{1,2} \cdot P(t), \quad x_{1,el} \leq x_1 < x_{1,mem} \quad (5-23)$$

$$K_{LM1} \cdot m_1 \cdot \ddot{x}_1 + k_{1,3} \cdot x_1 = P(t), \quad x_1 \geq x_{1,mem} \quad (5-24)$$

$$V(t) = (2 \cdot N_p/L) \cdot x_1, \quad x_1 \geq x_{1,mem} \quad (5-25)$$

$$K_{LM2} \cdot m_2 \cdot \ddot{x}_2 + k_2 \cdot x_2 = 2 \cdot V(t) \quad (5-26)$$

Table 5-2: Parameters of the two-step SDOF analysis

Parameter	Value	Source
$k_{1,1}$	13,251 N/mm	Figure 5-9
R_u	944,001 N	Figure 5-9
$k_{1,3}$	8883 N/mm	Figure 5-9
m_1	410,000 g	Manual calculation
K_{LM1}	0.72	Average value of fixed-fixed component subjected to distributed loading
I_{yy}	11,770 cm ³	Manual calculation
k_2	237,283 N/mm	$(384 \cdot E \cdot I_{yy}) / (5 \cdot L^3)$
m_2	31,400 g	Manual calculation
K_{LM2}	0.78	Elastic bending of pinned-pinned component subjected to distributed loading
DIF	1.20	(Cormie, Mays and Smith, 2009)
N_p/L	2221 N/mm	$k_{1,3}/4$ (NORSOK, 2004)
$x_{1,el}$	85.5 mm	$DIF \cdot R_u / k_{1,1}$
$x_{1,mem}$	127.5 mm	$DIF \cdot R_u / k_{1,3}$

The numerical model was created with shell elements of sufficiently dense mesh (20 mm), as indicated in Figure 5-13. It was confirmed that the mesh was sufficient through parametric analyses with denser mesh, which exhibited approximately the same results. The duration of the analyses was large enough to capture the maximum displacement and plastic strains of both the cladding and the columns, while the timestep was small enough to satisfy the Courant criterion (ANSYS Inc, 2017). As a whole, twenty analyses were performed with each one having a different blast loading, defined by an increasing positive phase duration from 1 ms to 20 ms with 1 ms step.

The analysis with the 15 ms positive phase duration was selected as an example in order to display both the numerical model and the two-step analysis results. This positive phase duration was selected because it was large enough for the cladding to enter into the membrane branch of its resistance curve. The numerical model results are presented in Figure 5-13, while the comparison with the two-step SDOF analysis is presented in Figure 5-12.

The displacements and plastic strains of the numerical model are displayed at the instances of 10.0 ms and 12.7 ms, where the maximum displacement of the column and the cladding are exhibited, respectively. As shown, cladding maximum displacement was extended beyond $x_{1,mem}$; thus, membrane action of the cladding was initiated. Furthermore, significant plastic strains were observed at the ends and the middle of the cladding, while the columns remained elastic.

Regarding the comparison with the two-step SDOF analysis, the results were verified through the numerical model. The maximum displacements of both the cladding and columns as well as the time of maximum displacement were similar between the two approaches.

Furthermore, useful observations were made through the constant pressure procedure, which was applied to the numerical model in order to check the response of the columns, by constantly increasing impulse. As presented in Figure 5-14, for small positive phase durations t_d , column maximum displacement is linearly increased. Within the range of 4 ms to 8 ms the column displacement is approximately constant, while beyond 8 ms it is further increased until 18 ms. When the positive phase duration is over 18 ms, the column enters into plasticity, and its displacements are rapidly increasing.

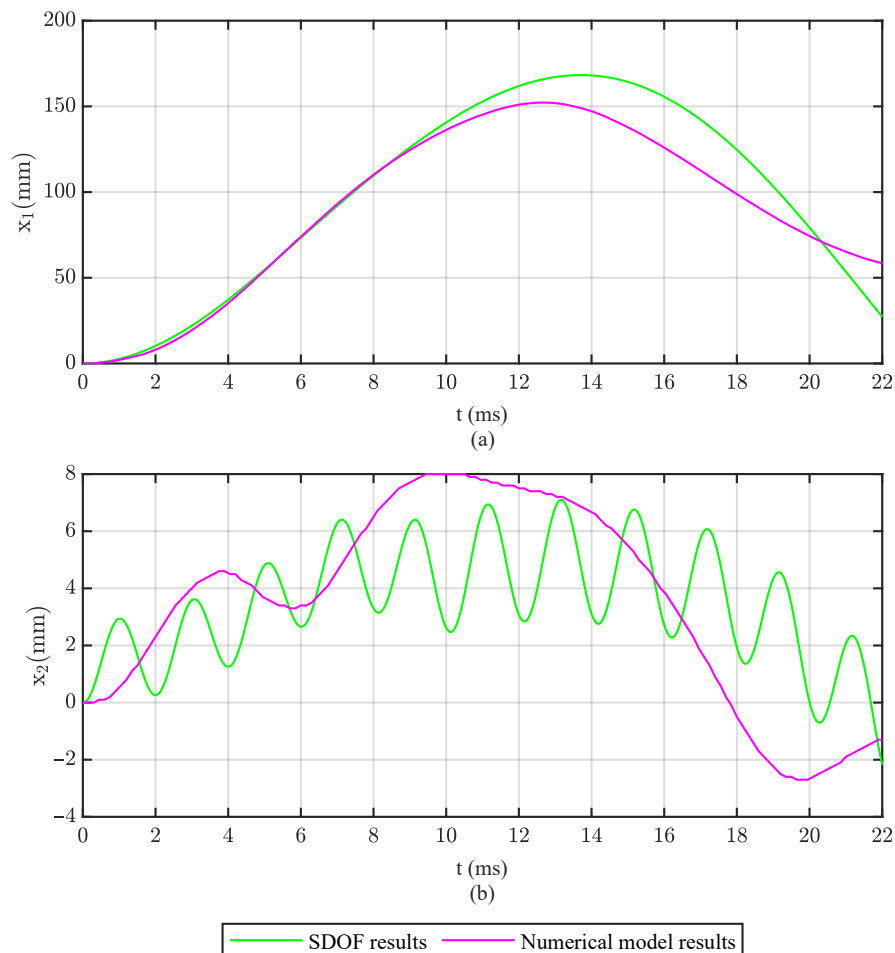


Figure 5-12: Two-step SDOF analysis and numerical model results of the case study (a) cladding and (b) columns, when subjected to maximum blast pressure of 200 kPa and positive phase duration of 15 ms

The negative effects of the cladding membrane action are exhibited through the fact that it constitutes an obstacle to plastic energy dissipation. More specifically, bending-induced plastic strains are beneficial to the supporting structure. However, plastic strains, caused by membrane action, result in larger support reactions, thus leading to significant increase in the supporting structure displacements. When the cladding's response exceeds $x_{1,mem}$, the upper limit of resistance R_U for the support reactions stops being applicable.

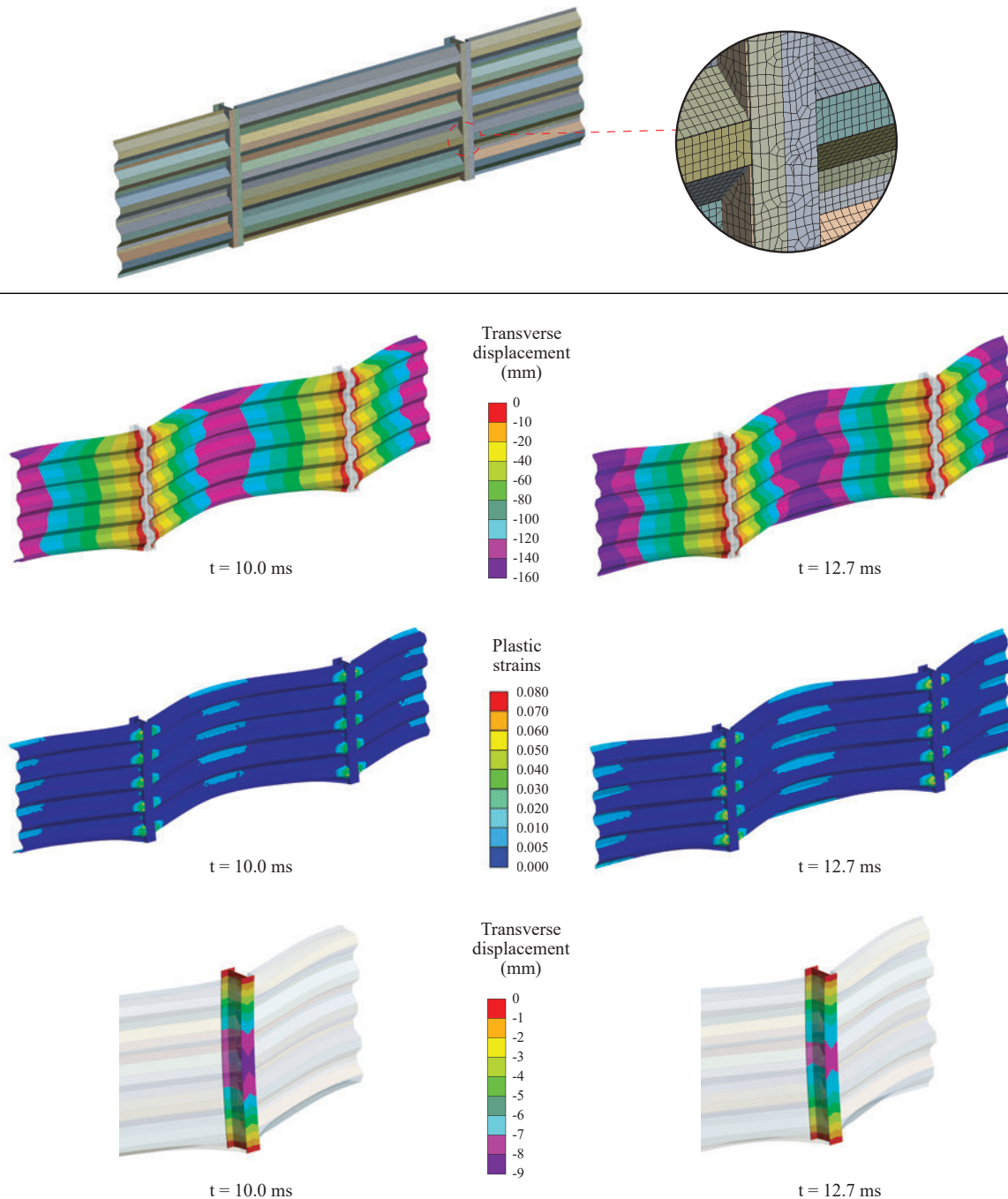


Figure 5-13: Meshing and results of the case study numerical model when cladding is subjected to 200 kPa maximum blast pressure and 1500 kPa ms impulse (15 ms positive phase duration)

5.6. Conclusions

The effects of cladding membrane behavior on the supporting structure were explored, focusing on two cases of cladding response. The first case referred to the response of cladding with both bending and membrane stiffness, while in the second case flexible cladding with only membrane stiffness was considered. The results of the investigation were considered in non-dimensional form so that they would be applicable to multiple cladding-to-supporting-structure configurations. The observations were concentrated on the fundamental parameters of the cladding, i.e., the cladding mass m_1 , resistance R_u , bending stiffness $k_{1,1}$, and membrane stiffness $k_{1,3}$.

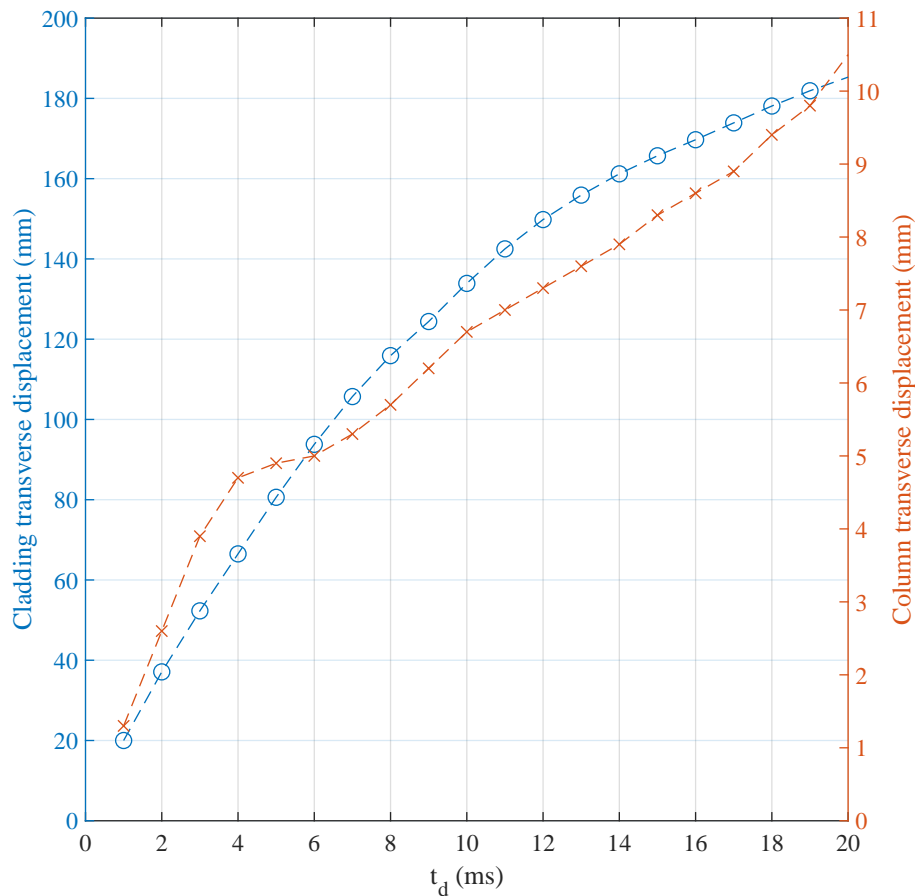


Figure 5-14: Numerical-model transverse displacements of the case-study cladding and column at increasing positive phase duration

It was shown that increased membrane stiffness $k_{1,3}$ leads to the enlargement of the support reactions, thus escalating the displacement of the supporting structure. Moreover, when cladding membrane action is initiated, the beneficial effects of cladding plasticity are countered by the contribution of the axial forces to the support reactions. On the contrary, if membrane stiffness is limited, an upper limit is observed in the support reactions, depending on resistance R_u . Hence, it is preferential that energy absorption is activated through bending behavior instead of membrane behavior.

In addition, when resistance has a low value with regard to maximum blast pressure P_o , the effects of plasticity are observed both in the dynamic and the quasi-static regime, but they are not constant, as they are limited when positive phase duration t_d is increased. However, when resistance has a high value, the effects of plasticity are observed only in the quasi-static regime.

In contradiction to this fact, the effects of mass m_1 and bending stiffness $k_{1,1}$ are applicable to the whole spectrum of positive phase durations t_d and natural periods T_2 , regardless of the impulsive, the dynamic, and the quasi-static regime. More specifically, the supporting structure displacements are limited through increased mass and low bending stiffness in the cladding. In this case, the cladding responds slowly to blast loading, thus yielding low support reactions to the supporting structure. Furthermore, the effects of cladding mass and bending stiffness are applicable to all pressure–impulse combinations, while the effects of resistance depend on the characteristics of blast loading.

As a whole, the observations of the present article are critical for the design of cladding subjected to blast loading. It has been shown that membrane behavior results in adverse consequences for the supporting structure, as it yields unconservative reaction forces, and should not be neglected during the design procedure. Moreover, membrane behavior should only be activated as a reserve, in order to protect cladding from failure. This is of particular interest for a building façade, where displacements and $P-\Delta$ effects at the main lateral resisting system should be limited.

5.7. References

ANSYS Inc (2017) 'ANSYS Explicit dynamics'.

Biggs, J. M. (1964) Introduction to structural dynamics. United States of America: McGraw-Hill.

Braconi, A. et al. (2015) 'Efficiency of Eurocode 8 design rules for steel and steel-concrete composite structures', *Journal of Constructional Steel Research*, 112, pp. 108–129. doi: <https://doi.org/10.1016/j.jcsr.2015.04.021>.

British Standards Institution (2019) 'BS EN 10025-2:2019: Hot rolled products of structural steels'.

Cadoni, E. et al. (2018) 'Tensile and compressive behaviour of S355 mild steel in a wide range of strain rates', *European Physical Journal: Special Topics*, 227(1–2), pp. 29–43. doi: [10.1140/epjst/e2018-00113-4](https://doi.org/10.1140/epjst/e2018-00113-4).

Cormie, D., Mays, G. and Smith, P. (2009) Blast effects on buildings. ICE Publishing. doi: [10.1680/beob.61477](https://doi.org/10.1680/beob.61477).

Cowper, G. and Symonds, P. (1957) 'Strain hardening and strain-rate effects in the impact loading of cantilever beam', Brown University Division of Applied Mathematics.

Dharmasena, K. P. et al. (2008) 'Mechanical response of metallic honeycomb sandwich panel structures to high-intensity dynamic loading', *International Journal of Impact Engineering*, 35(9), pp. 1063–1074. doi: <https://doi.org/10.1016/j.ijimpeng.2007.06.008>.

Dharmasena, K. P. et al. (2011) 'Response of metallic pyramidal lattice core sandwich panels to high intensity impulsive loading in air', *International Journal of Impact Engineering*, 38(5), pp. 275–289. doi: <https://doi.org/10.1016/j.ijimpeng.2010.10.002>.

Dusenberry, D. O. (2010) Handbook for blast resistant design of buildings. John Wiley & Sons. doi: [10.1002/9780470549070](https://doi.org/10.1002/9780470549070).

Fire and Blast Information Group (2002) 'Technical note 7: Simplified methods for analysis of response to dynamic loading'.

Gantes, C. J. and Pnevmatikos, N. G. (2004) 'Elastic-plastic response spectra for exponential blast loading', *International Journal of Impact Engineering*, 30(3), pp. 323–343. doi: [10.1016/S0734-743X\(03\)00077-0](https://doi.org/10.1016/S0734-743X(03)00077-0).

Hadjoannou, M. et al. (2018) 'Large-scale experimental tests of composite steel floor systems subjected to column loss scenarios', *Journal of Structural Engineering*, 144(2).

Health & Safety Executive (2006) 'Design, materials and connections for blast-loaded structures'.

Hoffmeister, B. et al. (2015) 'Advanced design methods for blast loaded steel structures', European Commission Directorate-General for Research and Innovation.

- Johnson, G. R. and Cook, W. H. (1983) 'A constitutive model and data from metals subjected to large strains, high strain rates and high temperatures', in Proceedings of the Seventh International Symposium on Ballistics. The Hague, Netherlands.
- Krauthammer, T. and Altenberg, A. (2000) 'Negative phase blast effects on glass panels', *International Journal of Impact Engineering*, 24(1), pp. 1–17. doi: [https://doi.org/10.1016/S0734-743X\(99\)00043-3](https://doi.org/10.1016/S0734-743X(99)00043-3).
- Del Linz, P. et al. (2015) 'Reaction forces of laminated glass windows subject to blast loads', *Composite Structures*, 131, pp. 193–206. doi: <https://doi.org/10.1016/j.compstruct.2015.04.050>.
- Louca, L. and Boh, J. (2004) 'Analysis and design of profiled blast walls', *Health & Safety Executive*.
- Mortazavi, M. and Heo, Y. A. (2018) 'Nonlinear dynamic response of steel materials and plain plate systems to impact loads: Review and validation', *Engineering Structures*, 173, pp. 758–767. doi: [10.1016/j.engstruct.2018.07.012](https://doi.org/10.1016/j.engstruct.2018.07.012).
- Pan, Y. and Watson, A. (1998) 'Effect of panel stiffness on resistance of cladding panels to blast loading', *Journal of Engineering Mechanics*, 124(7).
- Protective Design Center (2006) 'PDC TR-06-01: Single degree of freedom blast design spreadsheet (SBEDS) Methodology manual', U.S. Army Corps of Engineers.
- Rigby, S. E., Tyas, A. and Bennett, T. (2012) 'Single-Degree-of-Freedom response of finite targets subjected to blast loading - The influence of clearing', *Engineering Structures*, 45, pp. 396–404. doi: [10.1016/j.engstruct.2012.06.034](https://doi.org/10.1016/j.engstruct.2012.06.034).
- The Mathworks Inc (2018) 'MATLAB'.
- The Norwegian Oil Industry Association (2004) 'NORSOK N-004: Design of steel structures'.
- U.S. Department of the Army (1957) 'TM5-856-3: Design of structures to resist the effects of atomic weapons'.
- Zhang, X. and Hao, H. (2016) 'The response of glass window systems to blast loadings: An overview', *International Journal of Protective Structures*, 7(1), pp. 123–154. doi: [10.1177/2041419615626061](https://doi.org/10.1177/2041419615626061).

Chapter 6

Experimental investigation

This chapter is a slightly modified version of the following paper that has been submitted for review and possible publication in a peer-reviewed scientific journal.

Ioannou, O., Hadjioannou, M., Gantes, C.J., and Lignos, X.A. 'Experimental investigation of a cladding-to-girt system subjected to blast loading', submitted for review.

6.1. Introduction

The blast-resistant design trend of reducing the peak reaction force from the cladding to the supporting structure has been investigated experimentally by several researchers. The effectiveness of sandwich panels has been investigated by [Karagiozova et al. \(2009\)](#), [Zhu et al. \(2008\)](#), [McShane et al. \(2006\)](#), [Radford et al. \(2006\)](#), [Tian et al. \(2016\)](#), by measuring the permanent deflection of the rear plate compared to the front plate, and, thus, indirectly estimating the transmitted pulse from the core. Sandwich panels were also examined by [Hanssen et al. \(2002\)](#), [Bornstein and Ackland \(2013\)](#), by measuring the swing of a pendulum or the velocity of a mass, respectively, located at the rear face of the components. It is noted that the response of the rear plate of sandwich panels does not directly facilitate a reduction in the response of the supporting structure, i.e., the structural component where the cladding is attached to, because the reaction forces are not directly correlated with the rear plate response.

In addition, several research studies about sacrificial cladding, directly attached to the supporting structure, have been conducted, involving measurement of the reaction time history and the response of the supporting structure, such as the ones from [Reid and Reddy \(1983\)](#), [Palanivelu et al. \(2011\)](#), [Schenker et al. \(2005\)](#), [Zhao et al. \(2015\)](#), [Chengqing et al. \(2011\)](#). In the same context, [Khalifa et al. \(2017\)](#), [Abada and Ibrahim \(2020\)](#) have experimentally quantified the static resistance curves of various types of sacrificial cladding for blast-resistant applications. Furthermore, the energy-absorbing capacity of panel connectors has been investigated by [Whitney \(1996\)](#), with shock tube tests measuring the maximum reaction to the supporting structure, and by [Oswald \(2018\)](#), who measured the cladding and connectors deflection and reaction time histories.

These studies mainly focused on the plastic energy dissipation characteristics of materials and geometric forms (plastic energy absorption mechanism), located in the core of a sandwich panel, at the face of a protected component or at the connection of a panel. The effects were experimentally investigated through (1) the dynamic response of the cladding, (2) the reaction time history of the cladding, (3) the static resistance curves of the cladding and (4) the dynamic response of the supporting structure.

To further assess the effectiveness of the cladding to limit damage to the underlying structure, a blast test was performed on two specimens, each comprising of a cladding-to-girt system. The girts of the two specimens were identical whereas the cladding types were different, so that only the cladding characteristics would affect the response of the girts. The cladding on the first specimen had relatively low stiffness. Adversely, the cladding on the second specimen was designed to be stiffer and of higher capacity than the cladding on the first specimen. Thus, with specific focus on the effects of the cladding bending and membrane stiffness (inertial resistance mechanism), the interaction between the two different cladding types and their supporting girts, subjected to the same blast loading, are studied in the present chapter.

In the subsequent sections, the test matrix and experimental setup are described, explaining the rationale behind the selected procedure and its steps for the design of the cladding and its supports. Then, the test configuration is described along with the results. The test data are also compared with results obtained from detailed finite element models of the two specimens. Finally, conclusions are drawn regarding the contribution of the cladding stiffness to the response of the supporting structure.

6.2. Description of the experimental setup and instrumentation

Figure 6-1 shows views of the experimental setup. The experimental setup comprised of three components, which are indicated in Figure 6-1(a); (1) the reacting frame, (2) the hanger for the explosive, and (3) the two specimens. The reacting frame was centered to the hanger point of the explosives, so that the two specimens were subjected to the same blast load. All steel members were made of S275 steel. Similar experimental setups with free air bursts were also used by [Silva and Binggeng \(2009\)](#), [Chengqing et al. \(2011\)](#) and [Giovino et al. \(2014\)](#) in blast field experiments. Furthermore, the difference between the two specimens was their cladding type, i.e., specimen 1 with cladding type (cA), denoted as (sA), and specimen 2 with cladding type (cB), denoted as (sB).

6.2.1. Description of the reacting frame

The reacting frame was 1860-mm long, 1940-mm wide, and 1150-mm tall. It comprised of six columns made of HEA 220 sections. Along the 1940-mm long edges, the columns were connected to HEA220 beams and along the 1860-mm long edges, the columns were connected to IPE200 beams. All the beams were rigidly welded to the columns, thus creating moment frames in both directions. The beams and columns were designed to be relatively stiff and remain elastic under the anticipated blast loads with peak expected deflection of less than their length divided by 1500. Each column was anchored on a 500-mm thick reinforced concrete foundation slab, made of C30/37 concrete (Figure 6-1(d)). The two specimens were installed at a height of 1150 mm above the foundation slab (Figure 6-1(b)) to allow sufficient space for the installation of the measuring devices.

6.2.2. Instrumentation

The measurements were mainly focused on the deflection of the cladding and the supporting structure as, along with the support rotation, they constitute the primary engineering demand parameters in blast-

resistant design (PDC 2008). Deflections were measured at characteristic points of the two specimens, mainly at the center points. All locations where displacements were measured on the two specimens are indicated in Figure 6-2(a). Two types of measurements were recorded at these points; the peak transient displacement during the test and the post-test residual displacement. The peak deflection was measured using a single-value measuring device, which is shown in in Figure 6-2(b).

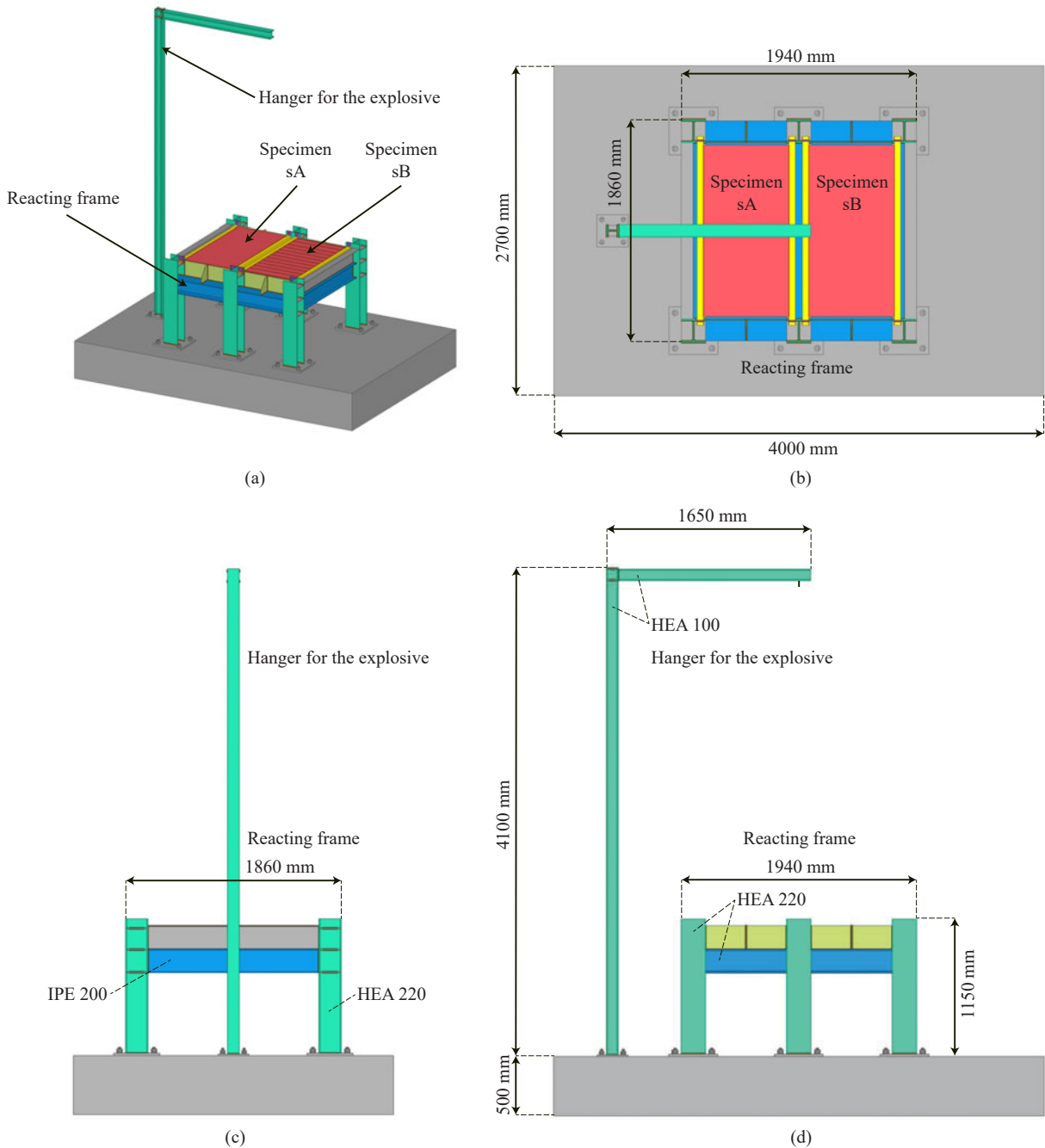


Figure 6-1: Views of the experimental setup: (a) 3D view; (b) Plan view; (c) Front view; (d) Side view

This device was previously used by Schenker et al. (2008) and Giovino et al. (2014) and, owing to its shape, it is known as “displacement comb”. It consists of a series of teeth with linearly decaying length. The maximum displacement occurring during the blast experiment was measured after the test by ob-

servicing the number of bent teeth caused by the deflection of the structural component, which was located above them. One such device was placed below the center of each structural component at specifically designated fastening points [Figure 6-2(b)]. Post-test residual permanent plastic deformations at the same points were measured after the test with the use of a rotary level laser, creating a horizontal laser plane over the cladding components. Then, the vertical distance between the laser plane and the upper face of the cladding was measured with the use of a caliper.

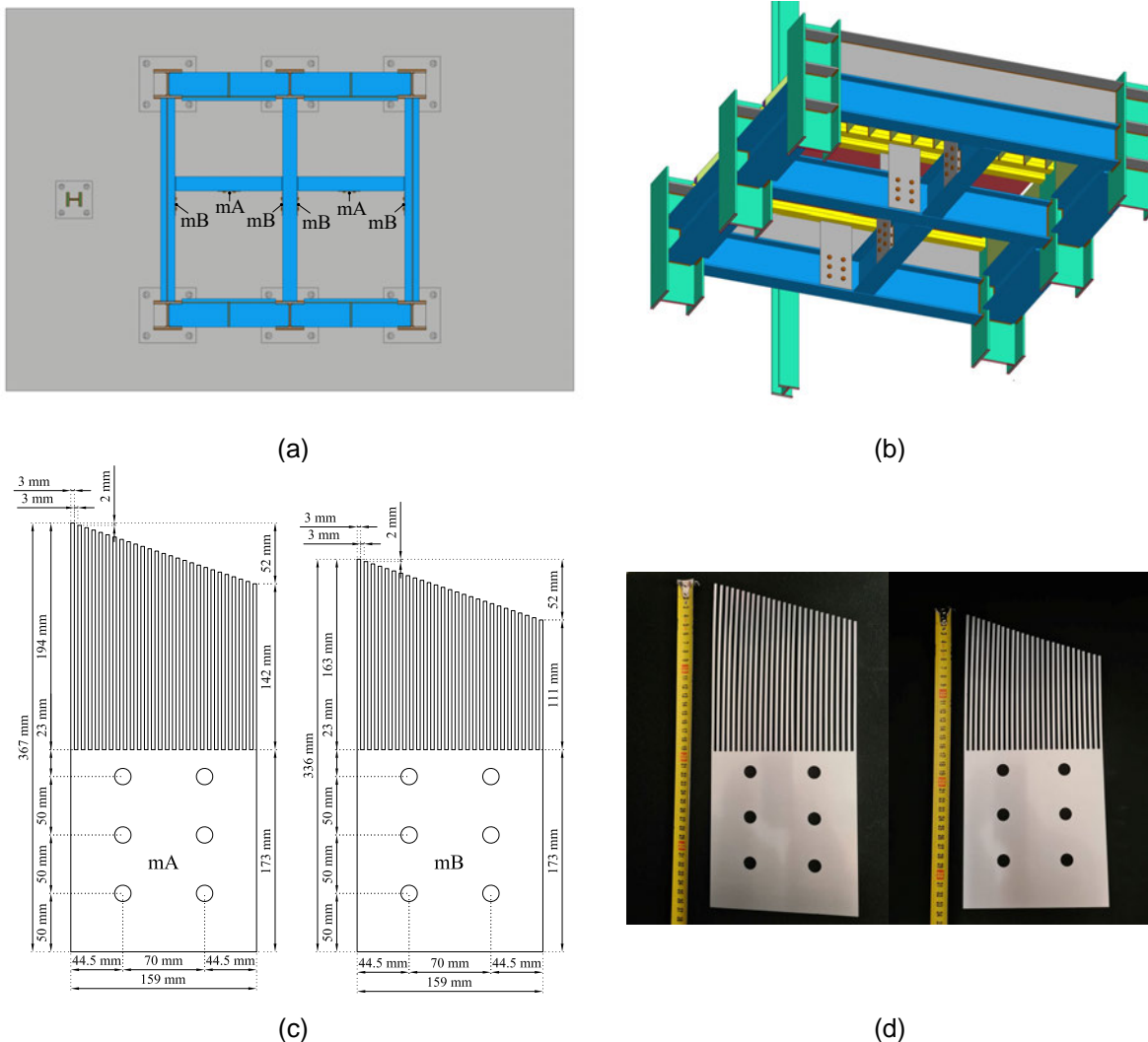


Figure 6-2: Displacement "comb" devices for the measurement of maximum transient deflection: (a) Experimental-setup location of the devices in plan; (b) 3D view of the devices' fastening points below the experimental setup; (c) Geometry of the devices; (d) Photo of the devices before their fastening

Field measurements were not performed with electromechanical sensors, because such sensors have been associated with multiple problems in blast experiments. As mentioned by [Rigby et al. \(2020\)](#), the main challenge about these type of sensors is that they must be covered to be protected from blast loading, while they are simultaneously required to function with spatial and temporal features in the order of mm and μ s, respectively. Thus, they are sensitive recording equipment, frequently associated with ineffective implementation ([Hoffmeister et al., 2015](#)). Mechanical pressure gauges (rupture disks) were also found by [Giovinio et al. \(2014\)](#) to be non-compliant with blast loading.

6.2.3. Field configuration of the experimental setup

All components of the experimental setup were prefabricated in order minimize field work. The components were transported to the testing site, connected to each other and then positioned on a pit with well compacted granular fill, as shown in Figure 6-3. The displacement devices [Figure 6-2(d)] were then installed. Sandbags of different sizes were placed at the perimeter of the setup, similarly as reported by [Giovino et al. \(2014\)](#). Their main function was to prevent the blast wave from entering the area below the panels and protect the displacement devices. Furthermore, the sandbags reduced the clearing effect at the perimeter of the specimens, by extending the horizontal surface upon which blast pressure was applied.

To avoid the development of overpressure in the enclosed space under the specimens, two volume relief gaps were create under two sandbags, arranged symmetrically in plan. These gaps were created using wooden strips, as shown in Figure 6-4. By incorporating these space gaps, the undesirable occurrence of adiabatic compression of the interstitial air at the enclosed volume was effectively averted. Such phenomena were reported in the experimental work of [Naito et al. \(2011\)](#) and [Whitney \(1996\)](#).



Figure 6-3: Installation of the prefabricated experimental setup in the pit



Figure 6-4: Wooden strips for volume relief below the experimental setup

6.2.4. Explosive charge weight

Due to the symmetric layout of the experimental setup and the symmetric position of the explosive charge over the setup [Figure 6-1(b)], the blast loads that were exerted on the two specimens were assumed to be the same. Accordingly, the pressure parameters were estimated per Kingery and Bulmash (1984), Hyde (1993), Hudson (1955). These methods were found to be highly accurate in mid-field explosions according to Cheval et al. (2010), Cheval et al. (2012), Rigby et al. (2020).

The explosive was located at a distance of 2.0 m above the upper face of the specimens, as shown in Figure 6-5. The explosive charge weight was TNT, 2.495 kg (5.5 lb), consisting of five and a half 1-lb containers. The detonation point was at the center of the charge and the shape of the charge was approximately cuboid with dimensions 18 cm × 15 cm × 10 cm; the 18 cm were arranged vertically. The explosion was considered to be a free air burst, without the creation of any Mach waves, due to the low angle between the charge and the limited plan dimensions of the setup. A camera with high frame rate was placed at a distance of 25 m from the experimental setup in order to capture the explosion.



Figure 6-5: View of the experimental setup prior to the detonation

6.3. Description of the test specimens

6.3.1. Specimen geometry

Scaled models with two specimens of different cladding types were tested during the experiment. The first cladding type (cA) was a 4-mm thick solid steel plate, while the second cladding type (cB) comprised of a 2-mm thick solid plate, supported by 5-mm thick welded transverse stiffeners with 110-mm spacing. The cladding types had the same plan dimensions, i.e., a length of 1400 mm and a width of 700 mm. A view of the two specimens is shown in Figure 6-6. The two panels were welded on girts with identical section sizes, since the primary purpose of the experiment was to study the effects of the cladding to the supporting structure, i.e., the girts. A square hollow section with 50-mm edge length and 2.75-mm wall thickness was used for the girt members.

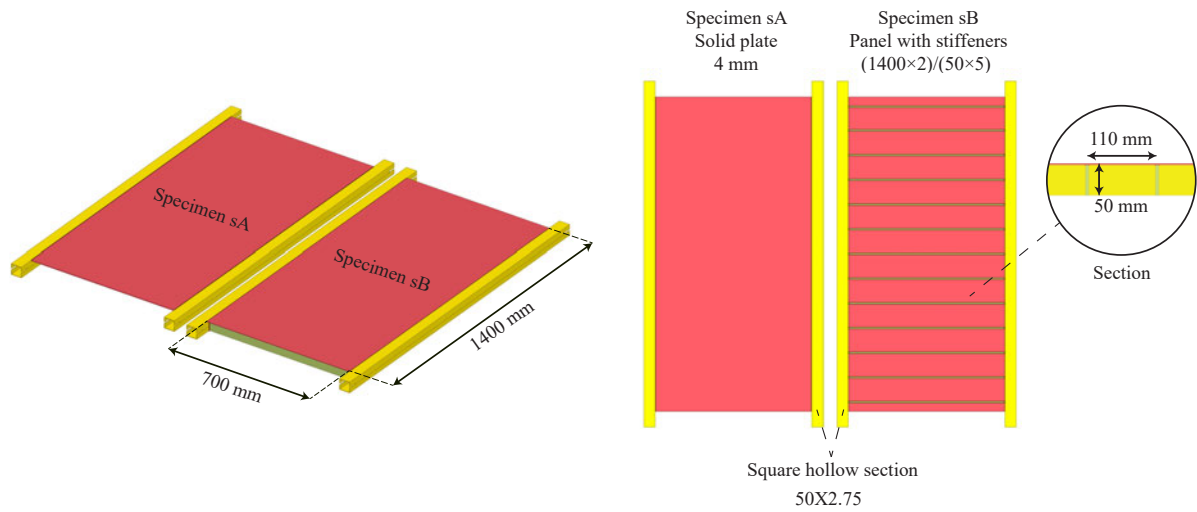


Figure 6-6: Views of the two specimens sA and sB

6.3.2. Specimen design

While the girts on the two specimens were identical, the stiffness characteristics of the two cladding types were different. In type (cA) membrane stiffness dominates due to the deflection restraint in the transverse horizontal direction, provided by the supporting girts. Cladding type (cB) is considered to be a typical panel acting primarily in bending. The total mass of the two cladding types were approximately equal; mass of type (cA) was 30.8 kg and mass of type (cB) was 32.5 kg.

In order to further interpret the stiffness characteristics of the cladding, the static pressure–displacement curves (or resistance curves) were computed and are presented in Figure 6-7. The curves were created by considering the two cladding types isolated from their girts and applying fixity at their boundaries. The pressure was applied with uniform loading at the upper face of the two cladding types.

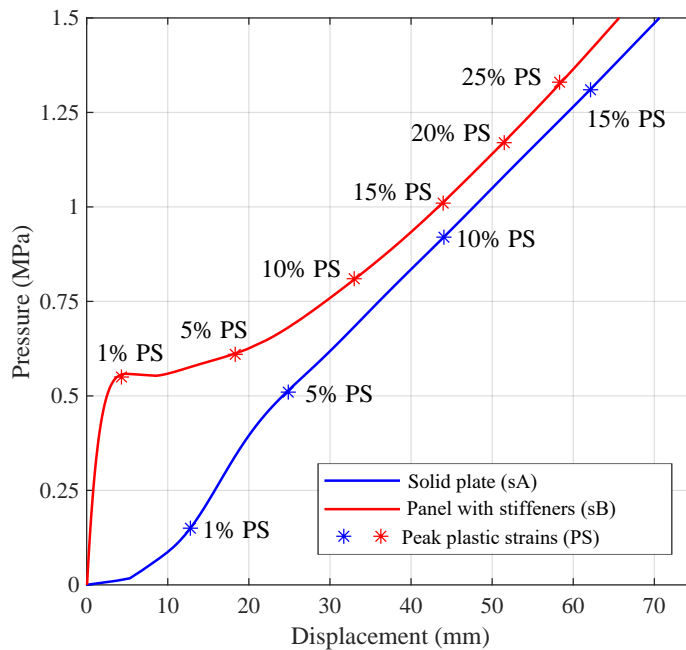


Figure 6-7: Static pressure–displacement curves of the two cladding types

As shown, plastic strains are exhibited in both cladding types. The plastic strains are limited to around 5% for displacements below 25 mm, but they increase substantially with increasing pressure. A prevalent differentiation between the two cladding types is their initial elastic stiffness. The elastic stiffness of the solid plate (cA) is considerably lower than the one of the panel with stiffeners (cB). In the solid plate the initial stiffness is very low and after reaching the displacement threshold of 23 mm, membrane stiffness dominates and continues with a branch of constant slope. It is noted that membrane stiffness becomes steeper at a mid-span displacement beyond 70 mm. However, this branch is neglected in the context of the present paper, as the cladding did not reach this displacement level. Furthermore, the initial stiffness of the panel with stiffeners is significantly higher than the initial stiffness of the solid plate. After reaching its yield displacement of 3 mm, the resistance is approximately constant up to about 10 mm. Then the resistance starts to increase due to the development of membrane action at increasing deformations.

The natural period of the two cladding types were calculated with an eigenvalue analysis as 23 ms in the solid plate (cA) and 3 ms in the panel with stiffeners (cB). It is further noted that, since the mass of the two cladding types is similar, the natural period is affected by the different stiffness characteristics of the two cladding types. Thus, among the main cladding parameters (yield resistance, ductility, mass and stiffness) the primary differentiating factor between the cladding types is their stiffness, which constitutes the main subject of the present chapter, and it was achieved by effectively designing a flexible cladding (cA) and a stiff cladding (cB).

In addition, pre-test simulations of the two specimens indicate that the expected deformation on the girt members were in the order of a few millimeters, which could be measured with reasonable accuracy using measuring combs.

6.3.3. Material properties

The specimens were made of steel. Specifically, the 4-mm, 5-mm solid plates and the square hollow sections of the girts were made of S275, steel while the 2-mm solid plates were made of S235 steel. The actual strength of the steel used in the specimens was measured with a series of direct tension tests on standard size coupons. Three different specimens were employed for each thickness, as shown in Figure 6-8, from spare parts of the material during fabrication. Their exact true stress–true strain characteristics are summarized in Table 6-1. As shown, they have negligible deviations between each other.

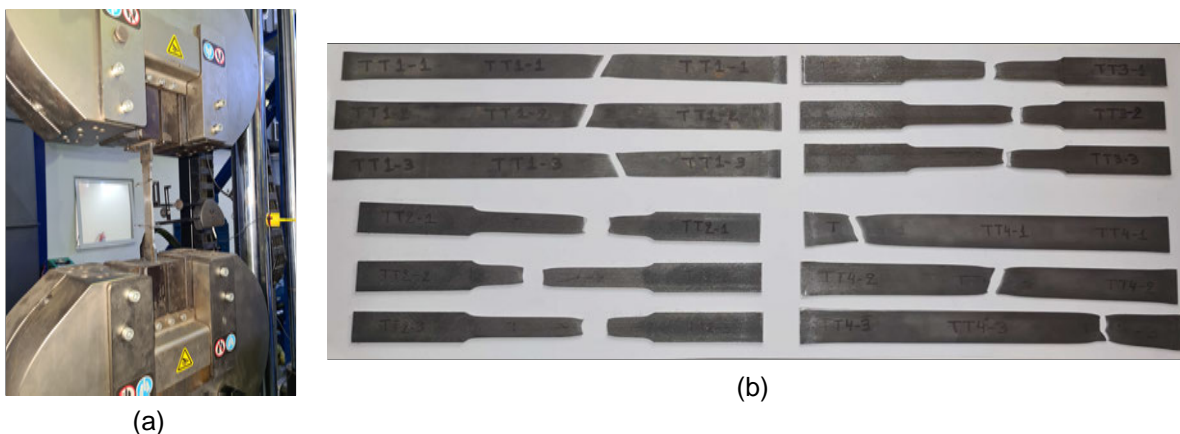


Figure 6-8: Tensile tests in the laboratory: (a) Specimen in Universal Testing Machine (UTM); (b) Specimens after the tensile test

Table 6-1: Experimental measurements of the tensile tests

Specimen	Thickness (mm)	Lower yield strength (MPa)	Upper yield strength (MPa)	Proof strength 0.2 % (MPa)	Code strength (MPa)	Ultimate strength ^a (MPa)	Ultimate strain ^a (%)
TT1-1	1.97 mm	227.9	235.1	-	235	329.7	47.2
TT1-2	1.97 mm	214.4	229.9	-	235	318.8	47.6
TT1-3	1.96 mm	210.3	218.8	-	235	311.7	46.6
TT2-1	4.09 mm	329.0	342.9	-	275	448.3	52.0
TT2-2	4.09 mm	322.7	329.0	-	275	433.0	58.3
TT2-3	4.08 mm	319.6	334.5	-	275	437.4	51.2
TT3-1	5.04 mm	342.2	357.7	-	275	455.3	44.8
TT3-2	5.05 mm	340.2	346.4	-	275	454.1	45.6
TT3-3	5.06 mm	343.6	352.4	-	275	457.7	45.9
TT4-1	2.75 mm	-	-	304.7	275	371.1	33.2
TT4-2	2.75 mm	-	-	302.0	275	360.7	36.3
TT4-3	2.75 mm	-	-	302.5	275	363.4	35.7

^athe values refer to engineering stress and strain properties

6.4. Experimental test results

The detonation of the explosives took place at an ambient air temperature of 24 °C, 55% relative humidity and 1.25 m/s wind velocity. A high-pressure blast wave occurred due to the detonation. Along with this blast wave, an instantaneous fireball appeared, which was captured by the camera shown in Figure 6-9. A photo of the specimens is presented in Figure 6-10.



Figure 6-9: Snapshot of explosion

The displacement “combs” (Figure 6-2) provided accurate measurements of the peak displacements during testing. An example of their behavior is shown in Figure 6-11, where some of the device’s teeth were bent, while the rest remained intact. The peak displacement was measured by identifying the last bent tooth at each device. The specimens also had appreciable permanent plastic deformations, as

indicated in Figure 6-12(a), which shows the central girt of the panel with stiffeners, cladding type (B). In order to accurately measure the permanent deflections, a rotary level laser was effectively used.



Figure 6-10: Photo of the specimens after the explosion



Figure 6-11: Displacement device, before and after the explosion

A summary of the peak and residual displacements at six points across the midspan of the two specimens, as indicated in Figure 6-12(b), are presented in Table 2. As shown, the accuracy was in the order of mm, while the maximum displacements followed the same trend with the permanent deformations. Hence, the results from the two measurement techniques were consistent with each other.



Figure 6-12: Permanent deflections after the explosion: (a) Visual representation of the deflection of the central girt of the panel with stiffeners; (b) Points of interest in plan for the determination of maximum and permanent displacement (solid plate - left, panel with stiffeners - right)

Regarding the structural behavior of the specimens, the highest maximum and permanent displacements were observed in the flexible cladding cA (point P2). On the contrary, significantly lower displacements were observed in the stiff cladding cB (point P5). However, the opposite behavior was exhibited in the response of the girts. More specifically, the displacements of the flexible-cladding girts (point P1 and P3) were lower than the stiff-cladding girts (point P4 and P6). Thus, low stiffness in the cladding leads to enhanced behavior in the supporting structure. Furthermore, both the cladding and the girts exhibited permanent deformations, hence plastic strains were induced in both specimens. More details about the effects of stiffness are given in section 6.3.2 along with several indicators extracted from the numerical model.

Table 6-2: Experimental measurements of the maximum and permanent displacements of the points of interest

Specimen	Point of interest ^a	Maximum displacement (mm)	Permanent displacement (mm)
sA	P1	11	1
	P2	60	35
	P3	26	13
sB	P4	44	27
	P5	40	21
	P6	31	13

^arefer to Figure 6-13(b)

6.5. Numerical modeling

6.5.1. Description of analysis models

The experimental data were compared to results from numerical models of the two specimens. Figure 6-13 shows a view of the detailed finite element model which included the two specimens and the reacting frame. The experimental setup was included in the model in order to more accurately account the effects of the girt-to-column connection stiffness and the fact that the middle columns were subjected to increased forces as two girts were attached to them. Thus, higher rotations were induced at the ends of the central girts than the edge girts. The column bases were modeled as fixed.

The numerical model was developed in ANSYS Explicit Dynamics software (ANSYS Inc, 2017), by performing Nonlinear Transient Finite Element Analyses (NTFEA), accounting for material and geometric

nonlinearity. Numerical stability was achieved by automatically calculating the time step with the Courant number criterion (ANSYS Inc, 2017). The finite element model consisted of a sufficiently dense shell finite element mesh (10 mm) with five through-thickness integration points and with activation of thickness update. The size of the elements was based on the mesh convergence studies of Grisaro et al. (2019) and Ioannou et al. (2022). According to these studies, a size of 10 mm was shown to be accurate for steel components subjected to blast loading.

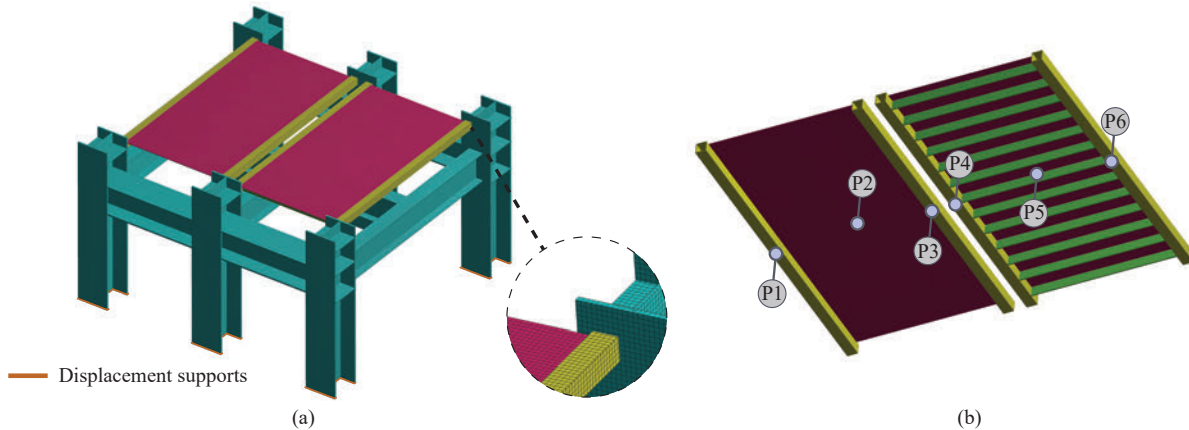


Figure 6-13: Numerical model of both cladding types and their girts: (a) Discretization and partial modeling of the experimental setup; (b) Points of interest at the bottom side of the specimens

6.5.2. Material models

The material properties, used to model the behavior of steel, were informed from the laboratory tensile tests that were performed on coupons, obtained from the test specimens (Figure 6-8). The true plastic stress–true plastic strain diagrams of the three tensile tests, conducted for each plate thickness, are illustrated with grey lines in Figure 6-14. The steel hardening characteristics were implemented in the numerical model by using the Johnson and Cook (1983) hardening model. The Johnson-Cook hardening curve parameters were chosen to match the features of the direct tension tests (Figure 6-14). The strain-rate effects were also included by employing the Cowper and Symonds (1957) model. The Johnson-Cook plasticity model and the Cowper-Symonds strain-rate model are described by Equation (6-1), where σ is the plastic stress, ϵ_{pl} the plastic strain, $\dot{\epsilon}_{pl}$ the plastic strain rate, A the yield strength, B and θ the hardening coefficients and q and D the strain-rate coefficients. q and D were adopted from DNV (2013) for common structural steel with values of 5 and 4000, respectively. All the steel members of the reacting frame (Figure 6-1) were modeled as purely elastic because, as previously mentioned, they were oversized in order to remain elastic under the applied blast loads, something that was confirmed by inspection after the test (no permanent plastic deformations, all welded joints were intact).

$$\sigma = (A + B \cdot \epsilon_{pl}^{\theta}) \cdot \left(1 + \left(\frac{\dot{\epsilon}_{pl}}{D}\right)^{1/q}\right) \quad (6-1)$$

6.5.3. Blast load simulation

The applied blast load to the numerical model was based on the Kingery and Bulmash (1984) semi-empirical blast load equations for free air bursts for the 2.495-kg TNT explosive that was used. These equations can account for the main parameters that affect the resulting blast pressure, i.e., the standoff distance and the charge weight, which are used as input parameters to calculate the values of the maximum reflected pressure, the maximum incident pressure, the positive phase duration, the time of arrival

and the decay coefficients. These values were subsequently used for the formation of the Friedlander equation, as described by Equation (6-2), where t is the time, $P(t)$ the pressure time history, P_o the maximum pressure. P_o is a function of the angle of incidence and varies between the maximum incident pressure P_s and the maximum reflected pressure P_r . t_d is the positive phase duration and b the blast wave decay coefficient. The stand-off distance in these equations was considered by taking the distance between the detonation point and each point on the loaded surface of the specimens. More specifically, the top surface of the specimens was discretized and the blast load time history was applied over the surface according to the local parameters with regard to the explosive source. For example, the stand-off distance of points B1, B2, B3 in Figure 6-15 was 2.20 m, 2.08 m and 2.01 m, respectively.

$$P(t) = P_o \cdot \left(1 - \frac{t}{t_d}\right) \cdot \exp\left(-b \cdot \frac{t}{t_d}\right) \tag{6-2}$$

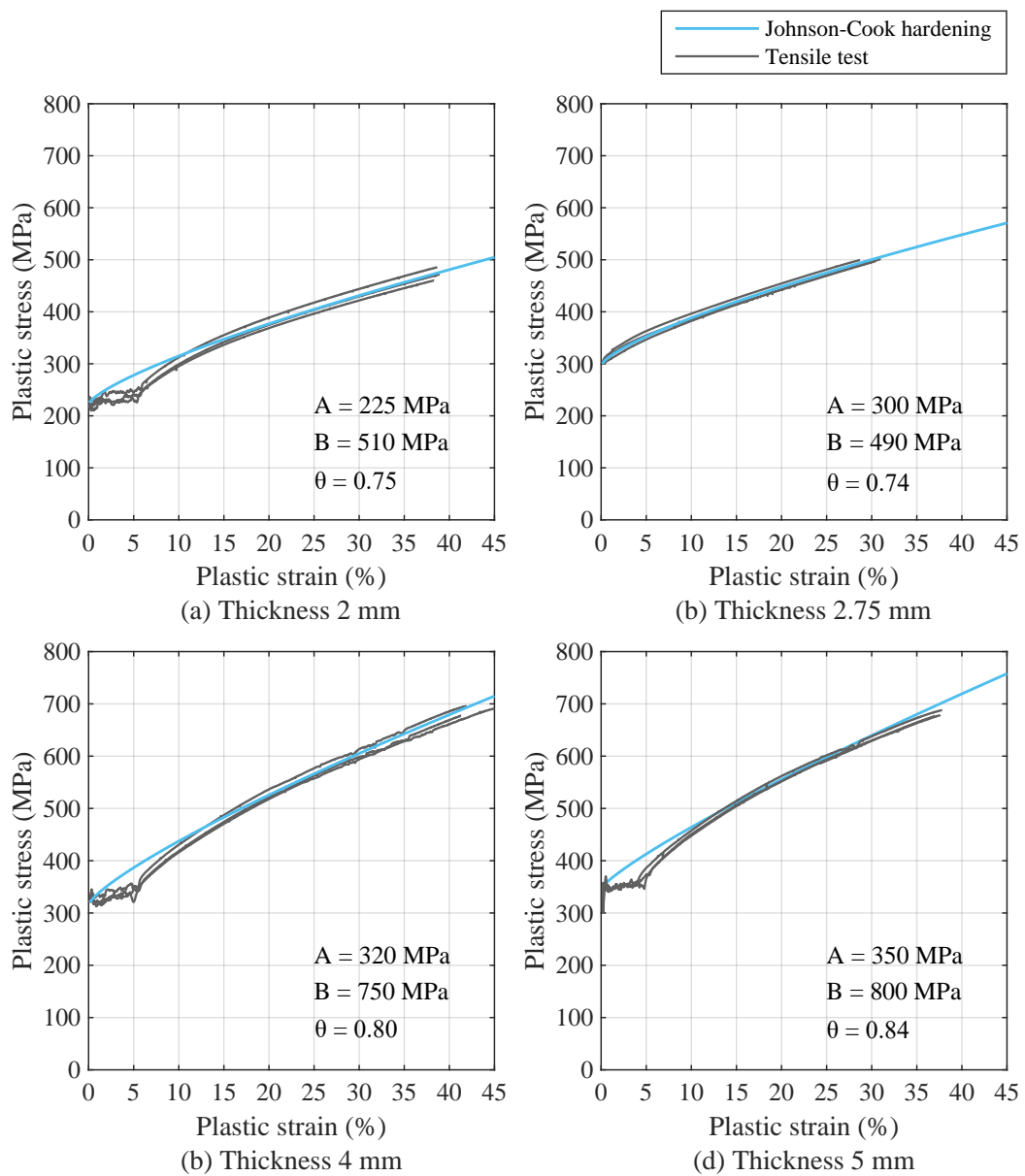


Figure 6-14: True plastic stress–true plastic strain diagrams of the tensile tests accompanied by their fitted Johnson-Cook strain hardening curve. The tensile-test values correspond to the elongation of the specimens up to their ultimate strength, i.e., the post-necking elongation is neglected

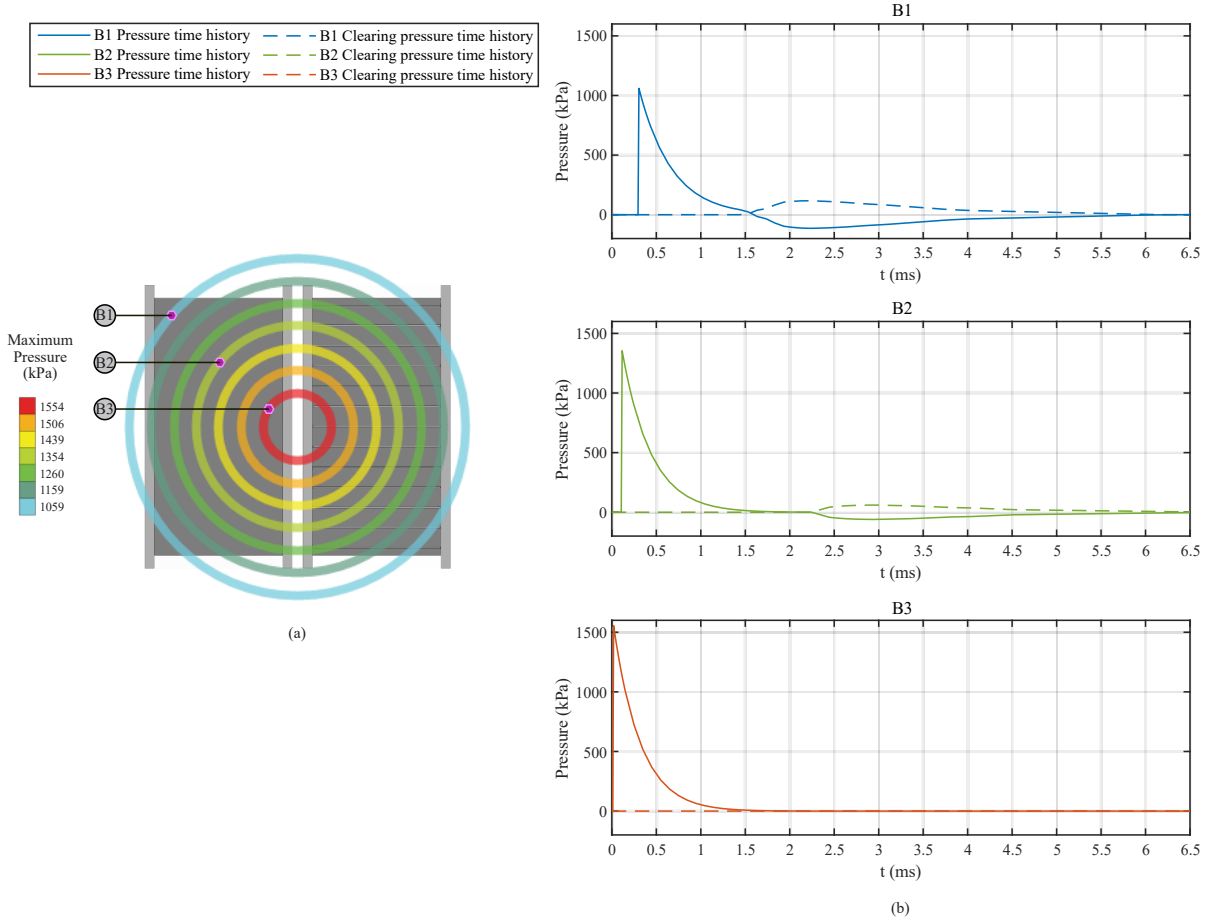


Figure 6-15: Blast pressure over the cladding: (a) Plan distribution of maximum blast pressure over the cladding; (b) Blast pressure time history of points S1, S2, S3 over the cladding

The angle of incidence of a blast wave was also considered using the built-in Loads on Structures (LOS), subroutine of ConWep, as presented by Hyde (1993). More specifically, the pressure time history was calculated according to the circular function of Equation (6-3), where the incident $P_s(t)$ and reflected $P_r(t)$ pressure time histories as well as the angle of incidence φ are incorporated.

$$P_\varphi(t, \varphi) = \begin{cases} P_s(t) \cdot (1 + \cos\varphi - 2\cos^2\varphi) + P_r(t) \cdot \cos^2\varphi, & \cos\varphi \geq 0 \\ P_s(t), & \cos\varphi < 0 \end{cases} \quad (6-3)$$

The aforementioned equations neglect the clearing effects, i.e., the target dimensions are assumed to be infinite. However, in most practical applications as well as in the experimental setup of this study, the target had finite dimensions. This is the reason why blast-wave clearing occurred at the perimeter of the setup. More specifically, horizontal steel beams and sandbags were arranged at the perimeter. After the reflected shock front left the free edge of these objects, an incident shock front diffracted from the free edge. Due the pressure imbalance between the shock fronts, low pressure rarefaction waves propagating towards the center of the setup were created (Rigby, Tyas and Bennett, 2012). These rarefaction waves were calculated by enforcing the Hudson (1955) predictive method through Equations (6-4)–(6-5) and the respective diagram of spatial and temporal properties of the rarefaction wave from Hudson (1955), where n_h is Hudson's non dimensional length scale, x_{edge} is the distance from the point of interest to the free edge, α_0 is the sonic sound speed in air and δ_h is the Hudson's time scale. The objects around the experimental setup were considered to have a size of 50 cm. Relevant clearing-pressure time his-

tories of characteristic points of interest are presented in Figure 6-15. As shown, the effects of the rarefaction waves at the center of the experimental setup are negligible due to the large distance from the free edges. It is noted that the clearing-pressure time history is subtracted from the exponential pressure time history.

$$n_h = \frac{x_{edge}}{\alpha_0 \cdot t_d} \quad (6-4)$$

$$\delta_h = \frac{t}{t_d} - n_h \quad (6-5)$$

6.5.4. Extension of the analysis with an elastic model

As aforementioned, plastic strains appeared in both girts during the experiment. The plastic deformations of the girts could play a key role in the response of the cladding to girt system. Thus, it was deemed valuable to verify the effects of the two cladding types to their girts, by extending the analyses to elastic and stiff girts. These girts were modeled with rectangular hollow sections of 100 mm × 50 mm × 5.00 mm and were expected to respond elastically when subjected to the same blast loading as the experimentally used sections of 50 mm × 50 mm × 2.75 mm.

6.6. Interpretation of the results

The results from the numerical analysis and their comparison to the measured maximum and permanent displacements of the experimental investigation are presented in Figure 6-16. As shown, there are minor deviations between the experimental measurements and the numerical model results, i.e., the maximum difference was 9.8 % in the maximum displacements. In addition, plastic strains were small in the two cladding types, while they were higher in the girts. The plastic strains in the middle of the girts of the panel with stiffeners were around 3%, while the middle of the girts of the solid plate remained elastic. However, the plastic strains of the girts of both cladding types were increased at their ends (6%) due to a combination of large bending moments and shear forces.

Thus, in accordance with the experimental results, the maximum and permanent displacements of the solid panel cA were approximately ~50%-70% times larger than the displacements of the stiffened panel cB. However, the maximum displacements of the sA girts of the solid plate were approximately ~30%-60% of the displacements of the sB girts of the stiffened panel, while the permanent displacements followed a similar trend. This difference was confirmed for the case of elastic response of the girts, as shown in Figure 6-17. In this numerical model, the maximum and permanent displacements of cA were approximately ~170%-230% times larger than the displacements of cB. However, the maximum displacements of the sA girts were approximately ~40%-50% of the displacements of the sB girts. Hence, the displacements were larger in cA than in cB but the displacements of the sA girts were lower than the displacements of the sB girts in both numerical models.

The fact that the displacements of the girts were larger in the case of the stiff cladding than in the case of the flexible cladding is supported by the significant difference in the cladding natural periods, as presented in section 6.3.2. More specifically, when cladding is stiff, the blast loading is transferred unchanged to the supporting structure through the cladding dynamic reactions. On the contrary, when the cladding natural period is increased, low amplitude and increased duration is exhibited in the cladding reaction time history to the girts (Ioannou and Gantes, 2021). This function constitutes the inertial resistance mechanism and is beneficial for the supporting structure as it effectively leads to the reduction of the exhibited displacements and to enhanced structural behavior.

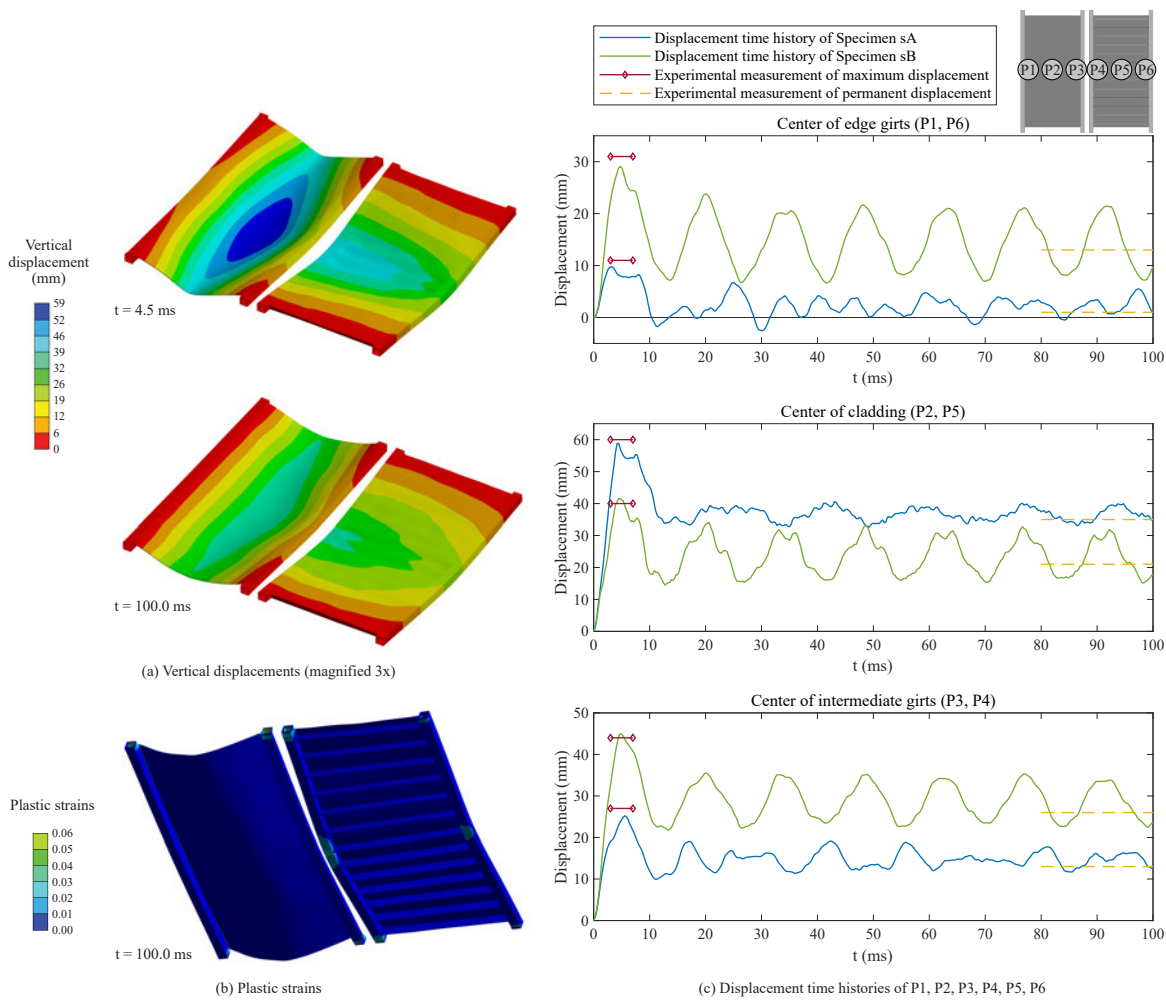


Figure 6-16: Numerical model and experimental results: (a) Vertical displacements in the numerical model at instances $t = 4.5$ ms (peak displacement) and $t = 100.0$ ms (permanent displacement); (b) Plastic strains at instance 100.0 ms (permanent displacement); (c) Numerical model displacement time histories at points P1, P2, P3, P4, P5 and P6 and comparison to experimental measurements

6.7. Conclusions

The effects of cladding stiffness over the response of the supporting structure were demonstrated in the present chapter through the experimental investigation of two cladding-to-girt systems. The girts, which represented the supporting structure, were identical in the two systems, while the claddings had different geometric configuration and, thus, different stiffness characteristics. Both systems were subjected to the same blast loading, as the explosive initiation was made simultaneously and was symmetrical in plan.

The experimental and numerical model results highlighted the fact that low stiffness in the cladding can be beneficial for the supporting structure, as it leads to decreased deformations. This was verified with both elastoplastic and purely elastic response in the girts. The effects of the low stiffness stem from the inertial resistance mechanism, according to which the reaction time history of the cladding has lower amplitude but increased duration, when compared with the time history of the blast loading applied to the cladding.

Hence, low bending and membrane stiffness in the cladding can effectively be used for the blast protection of critical infrastructure in order to guarantee the integrity of the main structure, limit its damages and relevant economic losses as well as to restrain the horizontal displacements of columns as a means to reduce possible P- δ effects.

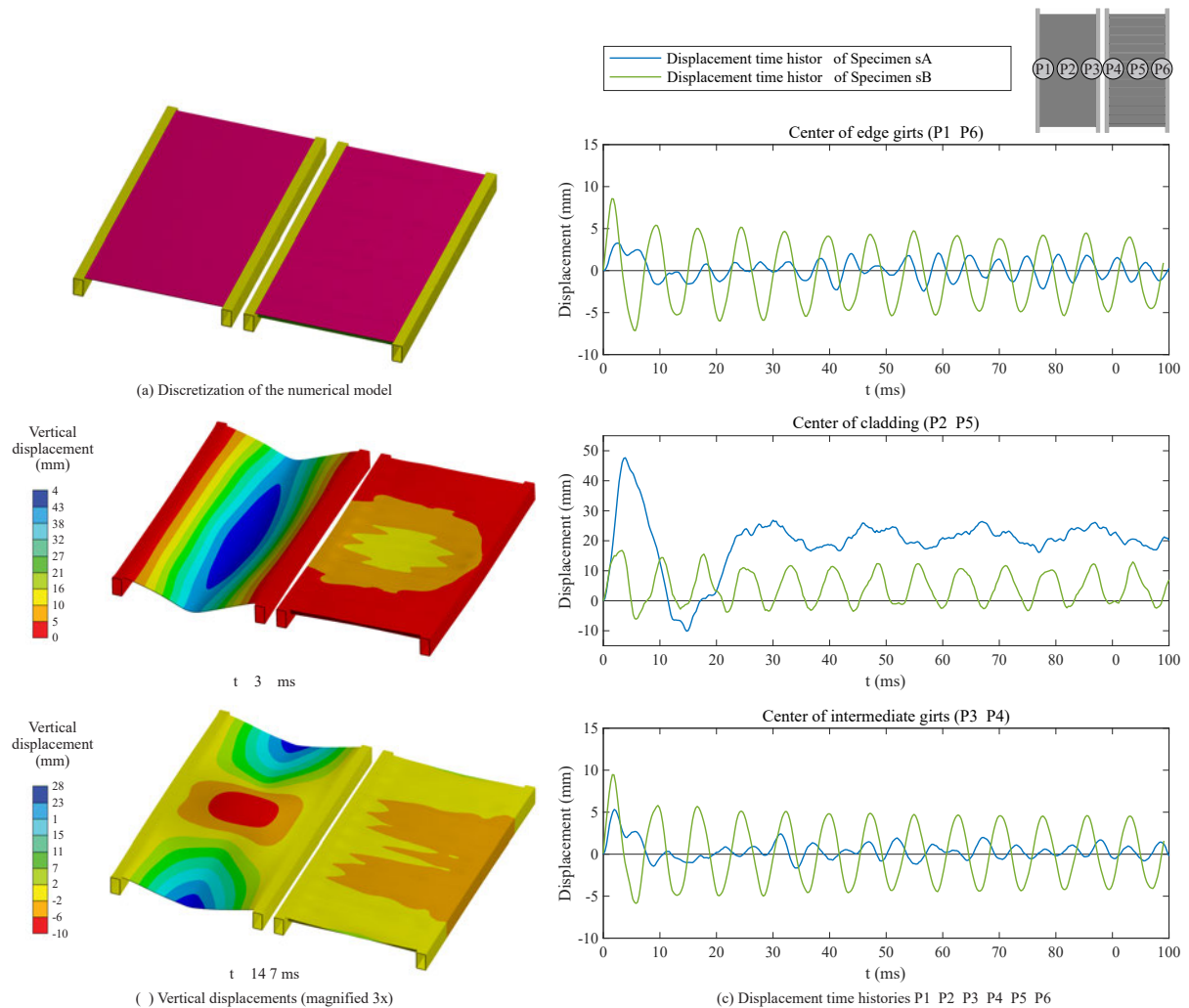


Figure 6-17: Results of the numerical model with elastic girts: (a) Discretization of the numerical model with elastic girts; (b) Vertical displacements in the numerical model at instances of $t = 3.9$ ms (peak displacement) and $t = 14.7$ ms (rebound); (c) Numerical model displacement time histories at points P1, P2, P3, P4, P5 and P6

6.8. Acknowledgements

For the experimental investigation of the response of steel cladding subjected to blast loading, which was conducted by NTUA's Institute of Steel Structures, the explosions were performed by the Land Minefield Clearance and EOD Battalion in the context of the memorandum of cooperation between the National Technical University of Athens (NTUA) and the Engineer Officers' Technical School (EOTS) of the Greek Army. Sponsors and fabricators of the experimental setup were the companies Armos Precast SA (precast reinforced concrete ground slab) and Kataskevastiki J. Dimitriou (steel cladding specimens, main steel support structure). Their support is gratefully acknowledged.

6.9. References

- Abada, M. and Ibrahim, A. (2020) 'Hybrid multi-cell thin-walled tubes for energy absorption applications: Blast shielding and crashworthiness', *Composites Part B: Engineering*, 183. doi: 10.1016/j.compositesb.2019.107720.
- Abouzeid, M. et al. (2020) 'Lebanon's humanitarian crisis escalates after the Beirut blast', *The Lancet*, pp. 1380–1382. doi: 10.1016/S0140-6736(20)31908-5.
- ANSYS Inc (2017) 'ANSYS Explicit dynamics'.
- Bornstein, H. and Ackland, K. (2013) 'Evaluation of energy absorbing materials under blast loading', in *WIT Transactions on Engineering Sciences*, pp. 125–136. doi: 10.2495/MC130111.
- Chengqing, W., Liang, H. and John, O. D. (2011) 'Blast testing of aluminum foam – protected reinforced concrete slabs', *Journal of Performance of Constructed Facilities*, 25(5), pp. 464–474. doi: 10.1061/(ASCE)CF.1943-5509.0000163.
- Cheval, K., Loiseau, O. and Vala, V. (2010) 'Laboratory scale tests for the assessment of solid explosive blast effects. Part I: Free-field test campaign', *Journal of Loss Prevention in the Process Industries*, 23(5), pp. 613–621. doi: <https://doi.org/10.1016/j.jlp.2010.05.001>.
- Cheval, K., Loiseau, O. and Vala, V. (2012) 'Laboratory scale tests for the assessment of solid explosive blast effects. Part II: Reflected blast series of tests', *Journal of Loss Prevention in the Process Industries*, 25(3), pp. 436–442. doi: <https://doi.org/10.1016/j.jlp.2011.11.008>.
- Cowper, G. and Symonds, P. (1957) 'Strain hardening and strain-rate effects in the impact loading of cantilever beam', *Brown University Division of Applied Mathematics*.
- Det Norske Veritas AS (2013) 'DNV-RP-C208: Determination of structural capacity by non-linear FE analysis methods'.
- Dusenberry, D. O. (2010) *Handbook for blast resistant design of buildings*. John Wiley & Sons. doi: 10.1002/9780470549070.
- Giovino, G. et al. (2014) 'Blast resistance assessment of concrete wall panels: experimental and numerical investigations', *International Journal of Protective Structures*, 5(3), pp. 349–366. doi: 10.1260/2041-4196.5.3.349.
- Grisaro, H. Y., Packer, J. A. and Seica, M. V. (2019) 'Weak axis response of steel I-sections subjected to close-in detonations', *Journal of Constructional Steel Research*, 160, pp. 189–206. doi: <https://doi.org/10.1016/j.jcsr.2019.05.025>.
- Hanssen, A. G., Enstock, L. and Langseth, M. (2002) 'Close-range blast loading of aluminium foam panels', *International Journal of Impact Engineering*, 27(6), pp. 593–618. doi: 10.1016/S0734-743X(01)00155-5.
- Hoffmeister, B. et al. (2015) 'Advanced design methods for blast loaded steel structures', *European Commission Directorate-General for Research and Innovation*.
- Hudson, C. C. (1955) 'Sound pulse approximations to blast loading', *Technical Memorandum, SC-TM-191-*.
- Hyde, D. (1993) 'User's guide for microcomputer program CONWEP, applications of TM 5-855-1, "Fundamentals of protective design for conventional weapons"', *U.S. Army Engineer Waterways Experiment Station*.

- Ioannou, O. and Gantes, C. J. (2021) 'Membrane action of cladding subjected to blast loading and effects on the supporting structure', *Vibration*, 4(4), pp. 768–786. doi: 10.3390/vibration4040043.
- Ioannou, O., Hadjioannou, M. and Gantes, C. J. (2022) 'Evaluation of the potential of cladding to mitigate blast effects on the supporting structure', *Practice Periodical on Structural Design and Construction*, (Forthcoming). doi: 10.1061/(ASCE)SC.1943-5576.0000701.
- Johnson, G. R. and Cook, W. H. (1983) 'A constitutive model and data from metals subjected to large strains, high strain rates and high temperatures', in *Proceedings of the Seventh International Symposium on Ballistics*. The Hague, Netherlands.
- Karagiozova, D. et al. (2009) 'Response of flexible sandwich-type panels to blast loading', *Composites Science and Technology*, 69(6), pp. 754–763. doi: 10.1016/j.compscitech.2007.12.005.
- Khalifa, Y. A., Tait, M. J. and El-Dakhkhni, W. W. (2017) 'Out-of-plane behavior of lightweight metallic sandwich panels', *Journal of Performance of Constructed Facilities*, 31(5), p. 4017056. doi: 10.1061/(ASCE)CF.1943-5509.0001018.
- Kingery, C. N. and Bulmash, G. (1984) 'Air blast parameters from TNT spherical air burst and hemispherical surface air burst', U.S. Army Ballistic Research Laboratory.
- McShane, G. J. et al. (2006) 'The response of clamped sandwich plates with lattice cores subjected to shock loading', *European Journal of Mechanics - A/Solids*, 25(2), pp. 215–229. doi: <https://doi.org/10.1016/j.euromechsol.2005.08.001>.
- Naito, C., Dinan, R. and Bewick, B. (2011) 'Use of precast concrete walls for blast protection of steel stud construction', *Journal of Performance of Constructed Facilities*, 25(5), pp. 454–463. doi: 10.1061/(asce)cf.1943-5509.0000228.
- Oswald, C. (2018) 'Blast testing of energy absorbing connectors for blast resistant design', *WIT Transactions on the Built Environment*, 180, pp. 57–67. doi: 10.2495/SUSI180061.
- Palanivelu, S. et al. (2011) 'Close-range blast loading on empty recyclable metal beverage cans for use in sacrificial cladding structure', *Engineering Structures*, 33(6), pp. 1966–1987. doi: <https://doi.org/10.1016/j.engstruct.2011.02.034>.
- Protective Design Center (2008) 'PDC TR-06-08: Single degree of freedom structural response limits for antiterrorism design', U.S. Army Corps of Engineers. Available at: <https://pdc.usace.army.mil/library/tr/06-08>.
- Radford, D. D. et al. (2006) 'The response of clamped sandwich plates with metallic foam cores to simulated blast loading', *International Journal of Solids and Structures*, 43(7), pp. 2243–2259. doi: <https://doi.org/10.1016/j.ijsolstr.2005.07.006>.
- Reader, T. W. and O'Connor, P. (2014) 'The Deepwater Horizon explosion: non-technical skills, safety culture, and system complexity', *Journal of Risk Research*, 17(3), pp. 405–424. doi: 10.1080/13669877.2013.815652.
- Reid, S. R. and Reddy, T. Y. (1983) 'Experimental investigation of inertia effects in one-dimensional metal ring systems subjected to end impact — I. Fixed-ended systems', *International Journal of Impact Engineering*, 1(1), pp. 85–106. doi: [https://doi.org/10.1016/0734-743X\(83\)90014-3](https://doi.org/10.1016/0734-743X(83)90014-3).
- Rigby, S. E. et al. (2020) 'Reflected near-field blast pressure measurements using high speed video', *Experimental Mechanics*, 60(7), pp. 875–888. doi: 10.1007/s11340-020-00615-3.
- Rigby, S. E., Tyas, A. and Bennett, T. (2012) 'Single-Degree-of-Freedom response of finite targets

- subjected to blast loading - The influence of clearing', *Engineering Structures*, 45, pp. 396–404. doi: 10.1016/j.engstruct.2012.06.034.
- Rutner, M. P. and Wright, J. P. (2016) 'Duality of energy absorption and inertial effects: Optimized structural design for blast loading', *International Journal of Protective Structures*, 7(1), pp. 18–44. doi: 10.1177/2041419615622726.
- Schenker, A. et al. (2005) 'Foam-protected reinforced concrete structures under impact: Experimental and numerical studies', *Journal of Structural Engineering*, 131(8), pp. 1233–1242. doi: 10.1061/(ASCE)0733-9445(2005)131:8(1233).
- Schenker, A. et al. (2008) 'Full-scale field tests of concrete slabs subjected to blast loads', *International Journal of Impact Engineering*, 35(3), pp. 184–198. doi: <https://doi.org/10.1016/j.ijimpeng.2006.12.008>.
- Silva, P. F. and Binggeng, L. (2009) 'Blast resistance capacity of reinforced concrete slabs', *Journal of Structural Engineering*, 135(6), pp. 708–716.
- Tian, X. et al. (2016) 'Experimental study of blast mitigation by foamed concrete', *International Journal of Protective Structures*, 7(2), pp. 179–192. doi: 10.1177/2041419616633323.
- Whitney, M. G. (1996) 'Blast damage mitigation using reinforced concrete panels and energy absorbing connectors', in.
- Zhao, H. et al. (2015) 'Blast mitigation effect of the foamed cement-base sacrificial cladding for tunnel structures', *Construction and Building Materials*, 94, pp. 710–718. doi: 10.1016/j.conbuildmat.2015.07.076.
- Zhu, F. et al. (2008) 'Deformation and failure of blast-loaded metallic sandwich panels - Experimental investigations', *International Journal of Impact Engineering*, 35(8), pp. 937–951. doi: <https://doi.org/10.1016/j.ijimpeng.2007.11.003>.

Chapter 7

Evaluation of mitigation potential

This chapter is a slightly modified version of the following paper, republished with permission of American Society of Civil Engineers; permission conveyed through Copyright Clearance Center, Inc.

Ioannou, O., Hadjiioannou, M. and Gantes, C.J. (2022) 'Evaluation of the potential of cladding to mitigate blast effects on the supporting structure', *Practice Periodical on Structural Design and Construction*, 27(3). doi: 10.1061/(ASCE)SC.1943-5576.0000701.

7.1. Introduction

Blast effects can be mitigated for the supporting structure by activating the plastic energy absorption (ductile response) and/or the inertial resistance (mass and stiffness) mechanisms. Quantification of the attenuating effects of certain cladding components has been proposed without taking the supporting structure into consideration, by means of;

- The maximum cladding reaction force or the reaction time history, e.g., [Chen and Hao \(2012\)](#) and [Van Paepegem et al. \(2014\)](#) have measured the boundary reaction forces in order to examine the effectiveness of different panel configuration designs.
- The energy absorbed through plastic deformation, e.g., [Wang et al. \(2020\)](#) and [Li et al. \(2018\)](#) have calculated the energy absorbed in the core of sandwich panels.
- Blast-specific response measurements with assumptions for the explosive weight and stand-off distances, e.g., [Zhao et al. \(2015\)](#) and [Karagiozova et al. \(2009b\)](#) have examined the blast mitigation capacity of structural components with the calculation of the supporting structure stress or the back plate displacement of sandwich panels, which appeared at specific combinations of explosive weight and distance or at specific front plate velocities.

However, the above approaches do not directly take into consideration the interaction of the cladding components with the supporting structure, which can significantly affect the response according to [Lori et al. \(2019\)](#). Furthermore, the attenuating effects of cladding components can also vary for different blast load profiles ([Guruprasad and Mukherjee, 2000](#); [Karagiozova, Nurick and Langdon, 2009](#)), exhibiting better performance for shorter duration and higher magnitude blast loads or vice versa. Overall, a generic approach that can directly estimate the attenuating effects of cladding components, by

taking into consideration their interaction with the supporting structure, for a wide range of blast load combinations, can greatly benefit the structural design process, leading to safer designs against a specified design-basis blast threat. It is noted that the term “mitigation potential” is used to describe the degree of attenuation of blast effects to the supporting structure.

In the present chapter, a new approach to calculate the mitigation potential of cladding components is proposed, taking into consideration the dynamic characteristics of the supporting structure in a dimensionless form, so that it can be generally applicable for a wide range of supporting structure configurations. The dimensionless form is applied using the Dynamic Load Factor (*DLF*), defined in Equation (7-1) as the ratio of the supporting structure’s maximum displacement x_{max} to the corresponding static displacement x_{st} , where P_o is the force amplitude (resultant of peak blast pressure) and k the stiffness of the supporting structure.

$$DLF = x_{max}/x_{st} = x_{max}/(P_o/k) \quad (7-1)$$

With the proposed methodology, the response of the cladding components can be calculated for a wide range of blast loads, regardless of the supporting structure, using Multi-Degree-of-Freedom (MDOF) analyses, Single-Degree-of-Freedom (SDOF) analyses, Finite Element Analyses (FEA) or analytical solutions. The cladding’s response, in the form of dynamic reaction history, is used as applied load for SDOF models to calculate the dimensionless response of the supporting structure, thereby quantifying the cladding’s mitigation potential. The calculated mitigation potential can then be incorporated into a pressure–impulse diagram, which conveniently allows a structural designer to estimate both the mitigation potential of the cladding and its damage levels for various pressure–impulse combinations. Because the proposed methodology is generic, it can be used to evaluate the mitigation potential of different cladding types. As a proof of concept, a case study with the mitigation potential of four cladding types with different geometries and support conditions was prepared, providing key insights for the role of different cladding configuration parameters to the plastic energy absorption and inertial resistance mechanisms.

7.2. Characteristics of cladding response to blast loads

It is further noted that the duration of the reaction time histories has not been experimentally proven to be the same between computational models and experimental tests (PDC 2006). In most cases, after the first oscillation cycle of the reaction time history, the amplitude of the cladding’s reaction is significantly reduced. Computationally-applied numerical damping cannot effectively capture the actual reaction time history and the rapid attenuation of the cladding’s reaction history. For that reason, PDC (2006) suggests to only use the first response cycle of the cladding’s dynamic reaction history to analyze the response of the underlying supporting structure. On that basis, for the present study, the duration of the corresponding time histories, extracted from computational models, representing the cladding are truncated according to Equation (7-2), where T is the natural period of the cladding, t_d the duration of the blast positive phase duration and T_c the duration of the first oscillation cycle.

$$Duration = \max(T, t_d, T_c) \quad (7-2)$$

The support reactions of the cladding comprise force components that are transverse and parallel to the cladding, as well as bending moments. It is noted that cladding panels may often be continuous over the supporting structure, thus subjecting the supporting structure to primarily transverse forces. The in-plane (membrane) force components and moments are counterbalanced between adjacent

cladding segments. Where there is no adjacent cladding segment, next to the segment under consideration, forces that are parallel to the cladding are also transferred to the supporting structure, provided that there is appropriate connection and supporting structure stiffness to allow membrane action to be activated. In this case, the support reaction time history comprises a force vector that is the resultant of the transverse and parallel force components. However, the membrane action could be avoided, by properly detailing the connection (e.g. with slotted holes or flexible connections (Holgado et al., 2012)) and/or considering that the supporting structure is characterized by reduced weak axis stiffness, thus primarily transferring transverse forces to the supporting structure. Furthermore, the case of sacrificial cladding, attached to a protected member, is also included in the present study by neglecting the composite action between the cladding and the protected members, which could induce friction forces in their connection.

7.3. Description of the proposed methodology

The primary objective of the proposed methodology is to enable direct comparison between alternative claddings in terms of their effects to the supporting structure when exposed to blast loads. The mitigation potential that a specific cladding type/configuration provides to the supporting structure is calculated by analyzing the supporting structure for a cladding-specific dynamic reaction history. This process is repeated for a wide range of blast load profiles (pressure–impulse combinations) and for supporting structures with different dynamic characteristics. The pressure–impulse diagram of the cladding is then amended with the calculated mitigation potential characteristics. The following subsections provide a detailed description of this methodology.

7.3.1. Implementation

The proposed methodology can be executed in six steps as described below and illustrated in Figure 7-1.

Step 1: Calculation of the Pressure–Impulse Diagram

The first step is to generate the pressure–impulse diagram of the cladding. Briefly, this procedure involves the determination of a wide range of pressure–impulse pairs for which the cladding has the same performance (or damage) level, such as the same peak deflection (Dusenberry, 2010). The information about the damage levels is produced by performing a series of analyses to the cladding with appropriate search algorithms, which can have basic or advanced nature, as presented by Chernin et al. (2019). All pressure–impulse pairs are eventually plotted in a single plot, as shown in Figure 7-1 (top left).

The purpose of the pressure–impulse diagram in the proposed methodology is to include all relevant information about the damage levels sustained by the cladding (from step 1) and the cladding's mitigation potential, as calculated in the subsequent step 6, in a single plot. It is noted that the pressure–impulse diagrams are constantly used in engineering practice in order to provide for information about the strength of a component subjected to blast loading, from a variety of explosive weight and stand-off distance combinations (PDC 2008). Furthermore, the damage levels are generally associated with specific performance goals for the cladding. Thus, the pressure–impulse diagram could eventually be used as a single reference point for the cladding's damage levels, performance goals and mitigation potential. The analyses to determine the pressure–impulse pairs can be performed with various analytical or numerical methods, depending on the desired level of precision and the availability of computational resources. The outcome of the performed analyses and the applied search method is the repre-

sentation of each specific damage level with a discrete curve (damage curve or iso-damage curve). Thus, a plot is created with different damage curves, with each curve associated with a specific performance goal.

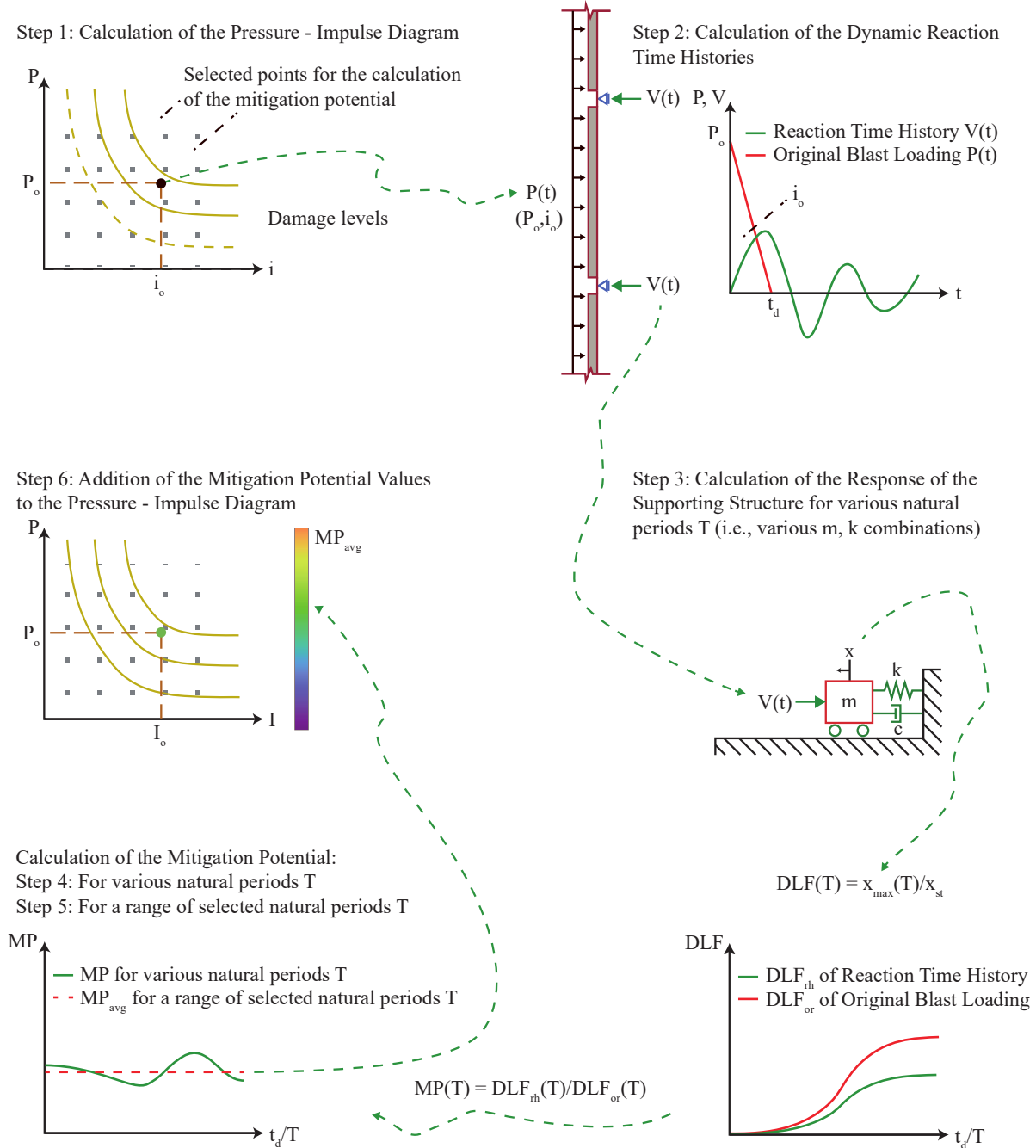


Figure 7-1: Implementation of the proposed methodology through six steps

Step 2: Calculation of the Dynamic Reaction Time Histories

In this step, a variety of pressure–impulse combinations are selected as representative points from the pressure–impulse diagram generated in step 1. The cladding is analyzed for each one of the chosen

pressure–impulse pairs and the computed dynamic reaction history is recorded, as illustrated in Figure 7-1 (top right). The reaction time histories are then truncated according to Equation (7-2).

The goal of this step is to record the reaction time histories of all selected points in order to subsequently use them as applied load to the supporting structure. The selection of the representative points is made according to the pressure–impulse combinations which are of interest. It is clear that the denser the points are, the higher resolution is achieved in the presentation of the mitigation potential at step 6.

Step 3: Calculation of the Response of the Supporting Structure

During this step, the reaction time histories of the cladding (from step 2) are used as applied load to the dimensionless SDOF, that represents the supporting structure, as presented in Figure 7-1 (middle right). For each applied reaction history and for each natural period of the supporting structure, a unique analysis is performed. After each analysis, the corresponding DLF is calculated according to Equation (7-1). Since the goal is to evaluate the effect of the cladding for supporting structures with different dynamic characteristics, several simulations need to be performed to cover a wide range of possible natural periods T of the supporting structure. The equations and procedures which are associated with the dimensionless SDOF are further discussed in the subsequent section "*Derivation of non-Dimensional SDOF Model*".

Key aspect of the methodology is the non-dimensionalization of a SDOF model subjected to an arbitrary time history load. The non-dimensionalization is performed by enforcing the SDOF natural period and the maximum amplitude of the time history in the respective equations of motion of the SDOF. In the case of blast loading, this is used to evaluate the mitigation potential of the cladding and to incorporate it into its pressure–impulse diagram. The SDOF has been selected because it effectively represents the supporting structure through a single parameter, the natural period, which is the key parameter characterizing the blast response regime (impulsive, dynamic, quasi-static) regarding the blast positive-phase duration (Cormie, Mays and Smith, 2009).

Step 4: Calculation of the Mitigation Potential for each Natural Period and each Reaction Time History

The $DLF_{rh}(T)$ value for each natural period of the supporting structure and each reaction time history from the cladding is used to calculate the corresponding mitigation potential, as shown in Figure 7-1 (bottom left). More specifically, the mitigation potential $MP(T)$ is calculated for each natural period as the ratio of the DLF corresponding to the applied reaction time history from the cladding, $DLF_{rh}(T)$, over the DLF for when the blast load is directly applied to the supporting structure, $DLF_{or}(T)$, without accounting for the dynamic interaction with the cladding, as defined by Equation (7-3).

$$MP(T) = \frac{DLF_{rh}(T)}{DLF_{or}(T)} \quad (7-3)$$

Specifically, the difference in the peak displacement of the supporting structure when subjected to the cladding's reaction time history (loading 1) and the original blast loading directly applied to the supporting structure (loading 2) are calculated as the ratio of loading 1 over loading 2. This ratio is the mitigation potential $MP(T)$ for a specific period of the supporting structure. It is noted that for a specific excitation, due to the cladding dynamic reactions, $MP(T)$ varies over the range of the natural periods T of the supporting structure. Furthermore, the value of $DLF_{or}(T)$ can be found in literature (Cormie, Mays

and Smith, 2009) as the response of an elastic dimensionless SDOF subjected to triangular blast loading.

Step 5: Calculation of the Mitigation Potential over a Range of Selected Natural Periods of the Supporting Structure

The arithmetic or geometric mean value MP_{avg} is calculated in this step as a representative MP value across a chosen range of natural periods, as indicated through Figure 7-1 (bottom left). The range of natural periods can be chosen accordingly based on expected natural periods of the supporting structure.

More specifically, in step 5, a single value, MP_{avg} , is calculated for the estimation of the mitigation potential of each reaction time history, regardless of the natural period T . Because the geometric mean is less sensitive to extreme $MP(T)$ values compared to the arithmetic mean, it is used in the present study to estimate MP_{avg} . In order to cover a large range of supporting structural configurations with regard to their stiffness and mass, the (1 ms - 1000 ms) natural period band has been selected, as in Equation (7-4). Equal distribution of the natural periods in the (1 ms - 10 ms), (10 ms - 100 ms) and (100 ms - 1000 ms) sub-bands has been considered, in order to objectively calculate the mitigation potential in logarithmic scale.

$$MP_{avg}(T_1, \dots, T_N) = \left(\prod_{i=1}^N MP(T_i) \right)^{\frac{1}{N}}, T_1 = 1 \text{ ms}, \dots, T_N = 1000 \text{ ms} \quad (7-4)$$

Step 6: Addition of the Mitigation Potential Values to the Pressure–Impulse Diagram

The pressure–impulse diagram, which was generated during step 1, is amended with the corresponding mitigation potential values, calculated in step 5. More specifically, for each pressure–impulse combination selected during step 2, a different MP_{avg} value is calculated (step 5). Each MP_{avg} value is illustrated as a point in the pressure–impulse diagram (Figure 7-1, middle left).

After this step, the pressure–impulse diagram of the cladding will include both the information about the damage level of the cladding (continuous lines of the damage curves) and the mitigation potential of the cladding (represented with discrete dots). The updated pressure–impulse diagram can then be used to check if the cladding is designed with sufficient strength against the pressure–impulse combinations, which constitute the blast demand and, simultaneously, evaluate the ability of the cladding to reduce blast consequences to the supporting structure.

Derivation of non-Dimensional SDOF Model

When a SDOF model is subjected to an arbitrary loading, which in the present work represents the supporting structure that is loaded with the reaction time history of the cladding $V(t)$, the dynamic response of the supporting structure can be obtained by solving the differential equation of motion as described with Equation (7-5) (Arros, 2002). The SDOF comprises of a mass m , an elastic spring with stiffness k and viscous damping coefficient c with damping ratio ζ [Equation (7-6)], as shown in Figure 7-1 (middle right). According to the state of the practice in blast-resistant-design applications, the SDOF model constitutes the prevalent engineering tool in order to calculate the response of a structural component when subjected to blast loading (PDC 2006).

$$m \cdot \ddot{x} + c \cdot \dot{x} + k \cdot x = V(t) \quad (7-5)$$

$$c = 2 \cdot \zeta \cdot m \cdot \omega = 2 \cdot \zeta \cdot m \cdot \frac{2 \cdot \pi}{T} \quad (7-6)$$

The SDOF can be non-dimensionalized using parameters ξ - Equation (7-7) and n - Equations (7-8)–(7-10), with P_o being the peak pressure of the blast loading, $T = 2\pi(m/k)^{0.5}$ being the natural period and P_o/k being the static displacement x_{st} , which leads to Equation (7-11), by following a similar approach with the one described by Biggs (1964). The only variables needed to determine the dynamic response are T , P_o and ζ for a specific reaction time history function $V(\xi \cdot T)$. In order to further simplify the problem, damping ratio ζ is considered to be generally equal to 5%, as typically used for seismic design (Kazantzi and Vamvatsikos, 2015) with spectral acceleration. However, a different damping ratio could be applied to account for the various energy dissipation mechanisms that are available. It should be noted that damping does not affect significantly the response of a member to blast (Krauthammer and Altenberg, 2000; Rigby, Tyas and Bennett, 2012), since the peak response typically occurs during the first cycle, where damping has negligible effect. Furthermore, variable P_o is constant at each selected point (step 1 in Figure 7-1) and variable T is constant at each SDOF calculation (step 3 in Figure 7-1). Thus, the only differentiating factor between each SDOF calculation is the reaction time history function $V(\xi \cdot T)$, which is determined by the different characteristics of each cladding type and constitutes the main point of interest of the present study.

$$\xi = t/T = t / (2\pi\sqrt{m/k}) \quad (7-7)$$

$$n = x / (P_o/k) \quad (7-8)$$

$$\dot{n} = T \cdot \dot{x} / (P_o/k) \quad (7-9)$$

$$\ddot{n} = T^2 \cdot \ddot{x} / (P_o/k) \quad (7-10)$$

$$\frac{1}{4\pi^2} \cdot \ddot{n} + \frac{\zeta}{\pi} \cdot \dot{n} + n = \frac{V(\xi \cdot T)}{P_o} \quad (7-11)$$

Solving Equation (7-11), the effect of the reaction time history can be evaluated for a wide range of natural periods by obtaining the maximum value of n , which is the $DLF_{rh}(T)$ of the supporting structure, as defined in Equation (7-1). $DLF_{rh}(T)$ is unique for each combination of reaction time history and natural period, and can be used to quantify the mitigation potential, since it represents the displacement of the supporting structure, which is a widely applied engineering demand parameter in blast-resistant design applications (Cormie, Mays and Smith, 2009). Considering the cladding as sacrificial and aiming at protecting the supporting components (Guruprasad and Mukherjee, 2000; Hanssen, Enstock and Langseth, 2002), the SDOF is modelled as linear elastic.

7.3.2. Assumptions and limitations

The proposed methodology has the following assumptions and limitations:

- The reaction time history is composed only of force components acting in the direction of blast loading. Eventual moments and/or forces, which do not have the same direction, as the blast force are ignored.
- The dimensionless SDOF model is purely elastic, as it is considered non-sacrificial in the same context as described by Guruprasad and Mukherjee (2000), Hanssen et al. (2002).

- The MP_{avg} parameter is a representative value for a wide range of SDOF natural periods and constitutes an estimation of the mitigation potential. When the supporting structure's natural period is known, the MP_{avg} can be calculated with increased accuracy at the vicinity of the known natural period.
- The mitigation potential is determined herein using the peak displacement of the dimensionless SDOF, which is a representative indicator of the demand in most practical cases.

7.4. Case study

This section provides a detailed description of the implementation of the proposed methodology for calculating the mitigation potential of four different cladding types. The four cladding types were strategically chosen to demonstrate how different activated response mechanisms can contribute to the mitigation potential of each cladding type. Discussion about their behavior and design recommendations are also included in this section.

7.4.1. Cladding description

Four steel cladding types with different geometry and boundary conditions are examined, all having plan dimensions 1000 mm × 1750 mm. The first cladding type (CT1), shown in Figure 7-2(a), consists of a 9-mm monolithic plate with transverse and in-plane supports at the two long opposite edges, allowing the development of membrane action. CT2 (second cladding type), shown in Figure 7-2(b), consists of a 30-mm monolithic plate with transverse supports only, to enable flexural action and eliminate development of membrane action. Figure 7-2(c) shows the CT3 (third cladding type), a sandwich panel consisting of transverse core plates with a thickness of 3 mm, spacing of 250 mm and height of 110 mm, face plates with a thickness of 3 mm and endplates with a thickness of 7 mm. The equal thickness of front plate, back plate and core plates was selected as the one offering the highest energy dissipation in the parametric studies that were performed by Alberdi et al. (2013). This geometry is characterized as macro-architectural (Yuen et al., 2010), while the supports are both transverse and in-plane. CT4 (fourth cladding type), which is illustrated in Figure 7-2(d), is geometrically the same as the third, but having only transverse supports to prevent development of membrane action. In view of various research studies by Dharmasena et al. (2011), Vaziri and Hutchinson (2007), Xue and Hutchinson (2003), where the performance of sandwich panels was compared with their equivalent mass-monolithic plates in terms of panel deflection, the monolithic plate of CT1 was selected with an approximately equal mass to types CT3 and CT4. CT2 was selected with significantly larger mass to demonstrate the effects of inertial resistance mechanism, which is important for this cladding type, contrary to the other types, as will be further discussed in a subsequent section below. The four cladding types are illustrated in Figure 7-2. The material for all cladding types is S355 structural steel (BSI 2019).

7.4.2. Finite element models of claddings

In order to assess the response of the examined cladding types, dynamic analyses (Nonlinear Transient Finite Element Analysis - NTFEA) were performed with the ANSYS Explicit Dynamics software (ANSYS Inc, 2017), using shell elements with five through-thickness integration points. Results from mesh sensitivity studies demonstrated that shell elements with 20-mm long edges were sufficiently dense to capture the response of the four cladding types, which is consistent with the mesh sized used by Kang et al. (2013) and Eslami-majd and Rahbar-Ranji (2014). As an example, the mesh sensitivity study of CT2 with pressure 5.0 MPa and impulse 2.0 MPa-ms is shown in Figure 7-3. Simulations with finer mesh size showed that the response remained practically the same both in terms of maximum

displacement at midspan and reaction force time history. It is noted that the mesh sensitivity study focused on identifying a mesh size that was sufficiently small to provide consistent dynamic reaction force, since this was the only quantity that was used as applied load on the SDOF model (step 3). Convergence studies did not focus on other quantities, such as stresses and strains, since they were out of the scope of the primary purpose of the finite element models. The analysis durations were large enough to capture the maximum displacement of both the cladding and, subsequently, the dimensionless SDOF model of the supporting structure, upon which the reaction time history of the cladding was exerted, while the time step was selected to be sufficiently small per the Courant number (ANSYS Inc, 2017) for numerical stability. A total of 90, 110, 100 and 95 FE analyses were performed for types CT1, CT2, CT3 and CT4, respectively.

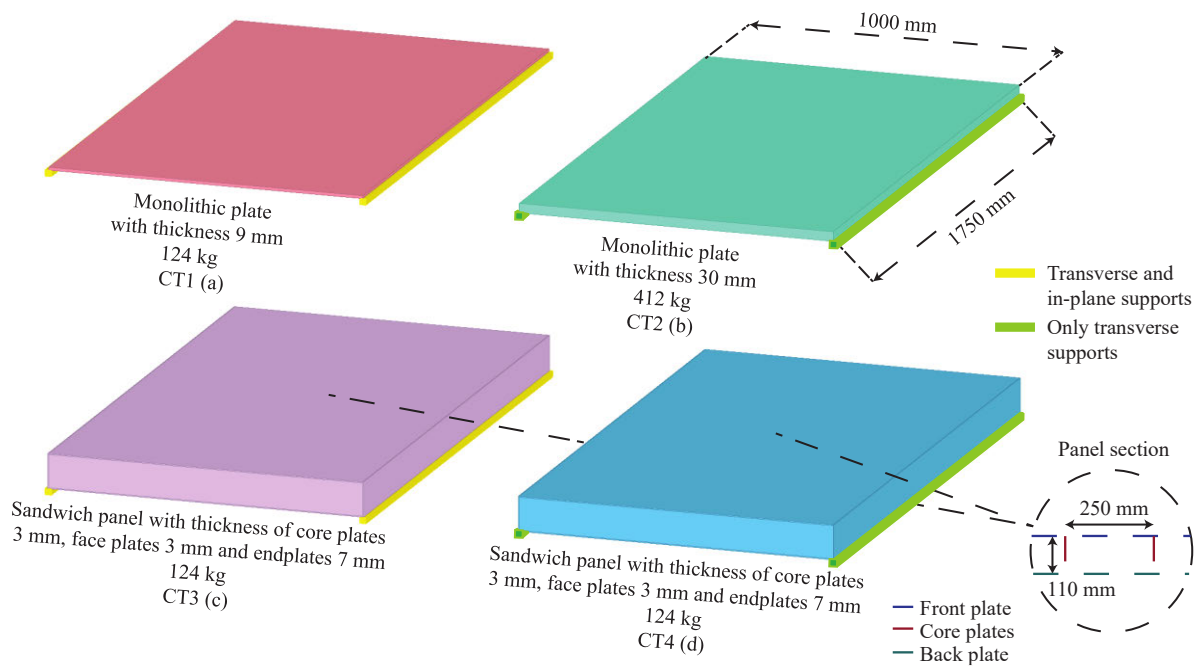


Figure 7-2: Illustration of the four case study cladding types: (a) CT1; (b) CT2; (c) CT3; (d) CT4

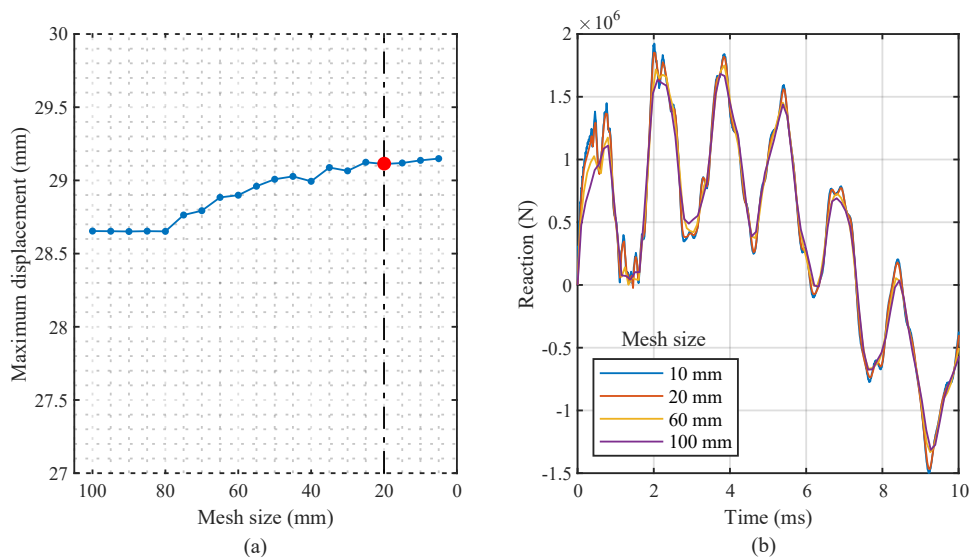


Figure 7-3: Mesh sensitivity study for cladding type CT2 with pressure 5.0 MPa and impulse 2.0 MPa-ms: (a) Maximum displacement; (b) Reaction time history

Blast loading was idealized as an equivalent triangular load with the same positive impulse as the corresponding exponential blast shape (Figure 7-4), which has been shown to lead to negligible deviations (Gantes and Pnevmatikos, 2004). Thus, the parameters dictating blast loading were only the pressure and impulse (or equivalently the blast loading duration).

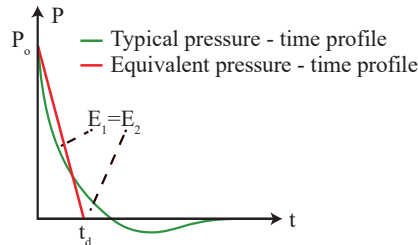


Figure 7-4: Description of the blast loading

The Cowper-Symonds Strength material model (ANSYS Inc, 2017) was adopted for all steel plates, described in Equation (7-12), where the terms of the first and second parenthesis account for the hardening effects per the Johnson-Cook material model (Johnson and Cook, 1983) and for the strain-rate effects per Cowper-Symonds model (Cowper and Symonds, 1957), respectively. In this equation, ε_{pl} is the plastic strain, $\dot{\varepsilon}_{pl}$ the plastic strain rate, A the yield stress, B and θ the hardening coefficients and q , D the strain-rate coefficients. The values of these parameters were adopted from Braconi et al. (2015), Forni et al. (2016), Mortazavi and Heo (2018), and are summarized in Table 7-1.

$$\sigma = (A + B \cdot \varepsilon_{pl}^{\theta}) \cdot \left(1 + \left(\frac{\dot{\varepsilon}_{pl}}{D} \right)^{1/q} \right) \quad (7-12)$$

Table 7-1: Parameters of the Cowper-Symonds Strength model

Parameter	Value
Yield stress A	410 MPa
Hardening coefficient B	782 MPa
Hardening coefficient θ	0.562
Strain-rate coefficient q	5.0
Strain-rate coefficient D	4000

7.4.3. Step 1: Calculation of the pressure–impulse diagrams

The generation of the pressure–impulse diagrams was performed using unidirectional search algorithms, as described by Chernin et al. (2019), with multiple pairs of pressure and impulse. More specifically, the pressure-controlled, the impulse-controlled and the mixed approach were applied to capture the impulse asymptote, the pressure asymptote and the hyperbola constant, respectively. According to these approaches, pressure and impulse were gradually increased until specific performance goals matched the target damage level. It is assumed that all cladding types are subjected to near-field and mid-range blast loadings with uniformly applied pressure at their exterior face.

The performance goals were associated with the cladding conditions, where specific structural damage was achieved, when subjected to a variety of pressure–impulse combinations. Three component damage levels were enforced. More specifically, these were the moderate, heavy and hazardous component damage level, which are considered to be associated with the performance goals of property preservation (PP), life safety (LS) and collapse prevention (CP), respectively (Dusenberry, 2010).

The damage levels of all cladding types were calculated using the response parameter of maximum ductility ratio μ . Furthermore, for CT2 and CT4 an extra response parameter was used based on maximum in-plane slippage s . The two response parameters are illustrated in Figure 7-5. More specifically, the damage curves of types CT1 and CT3 were developed for maximum ductility ratios of 3, 6, 12, as prescribed by PDC (2008), with each one referring to the aforementioned three performance goals, respectively. In a comparable scale, the damage curves of CT2 and CT4 were developed for the same ductility ratios and for maximum in-plane slippage limits equal to 5 mm, 10 mm, 20 mm, assuming that the cladding has sufficiently long slotted holes to allow in-plane slippage. Similar approach for in-plane slippage limits are used for glazing, where the bites of the glazing on the framing should be large enough to allow the glazing to remain attached to its frame during blast events (ASTM 2019). Also, per PDC (2012), in-plane displacement may be critical and dictate the damage level of the glazing. Thus, the worst condition between the maximum ductility ratio and maximum in-plane slippage was used in types CT2 and CT4.

The discrete response values on the pressure–impulse diagrams were fitted to a continuous curve that is consistent with the hyperbola used by Sperrazza (1963), according to the values included in Table 7-2. The pressure–impulse diagrams for all cladding types are presented in Figure 7-6.

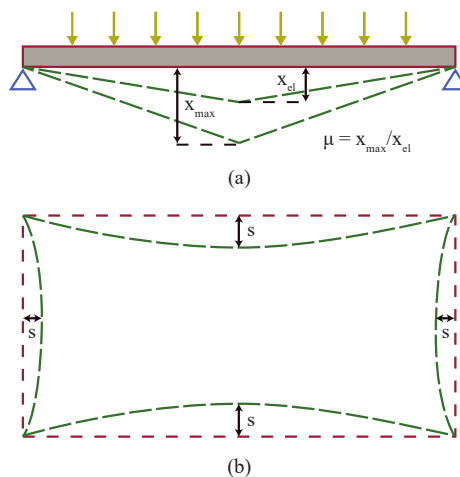


Figure 7-5: Description of: (a) The maximum ductility ratio at a section of the examined cladding; (b) The in-plane slippage at the plan view of the examined cladding

Table 7-2: Pressure–impulse hyperbola parameters

Cladding type	Performance goal	Pressure asymptote	Impulse asymptote	Hyperbola constant	Damage level
CT1	Property preservation (PP)	1.50 MPa	2.0 MPa-ms	0.5	$\mu = 3$
	Life safety (LS)	3.00 MPa	4.1 MPa-ms	3.0	$\mu = 6$
	Collapse prevention (CP)	6.00 MPa	11.0 MPa-ms	25.0	$\mu = 12$
CT2	Property preservation (PP)	0.8 MPa	3.0 MPa-ms	6.0	$s = 5 \text{ mm}^a$
	Life safety (LS)	0.90 MPa	4.0 MPa-ms	7.0	$s = 10 \text{ mm}^a$
	Collapse prevention (CP)	1.00 MPa	5.5 MPa-ms	8.0	$s = 20 \text{ mm}^a$
CT3	Property preservation (PP)	0.50 MPa	0.9 MPa-ms	0.1	$\mu = 3$
	Life safety (LS)	0.65 MPa	1.3 MPa-ms	0.7	$\mu = 6$
	Collapse prevention (CP)	0.80 MPa	3.0 MPa-ms	2.0	$\mu = 12$

	Property preservation (PP)	0.50 MPa	0.9 MPa-ms	0.1	$\mu = 3^a$
CT4	Life safety (LS)	0.55 MPa	1.3 MPa-ms	0.7	$\mu = 6^a$
	Collapse prevention (CP)	0.60 MPa	2.5 MPa-ms	2.0	$s = 20 \text{ mm}^a$

^a Damage level is controlled by the most critical parameter between the in-plane slippage and the maximum ductility ratio

As an indicative analysis example, the transverse displacements, plastic strains and in-plane displacements of the cladding types, subjected to a pressure–impulse combination of 1.0 MPa and 3.0 MPa-ms, are presented in Figure 7-6. As shown, the damage level of $\mu = 3$ or $s = 5 \text{ mm}$ has not been reached in CT1 and CT2. Hence, their performance is below the property preservation (PP) goal and the corresponding pressure–impulse combination has not reached any designated damage level (Figure 7-7). On the contrary, it is shown that the maximum achieved deflection ($t = 5.0 \text{ ms}$) is equal to approximately 66 mm in CT3 and CT4. Therefore, increased plastic strains have been induced over the panel and the panel is not reusable. With yield displacement equal to 11.0 mm, the maximum achieved ductility ratio is equal to 6, thus the damage level $\mu = 6$ has been reached. In-plane slippage is limited, hence the response parameter of maximum ductility ratio prevails for the performance goal of life safety (LS).

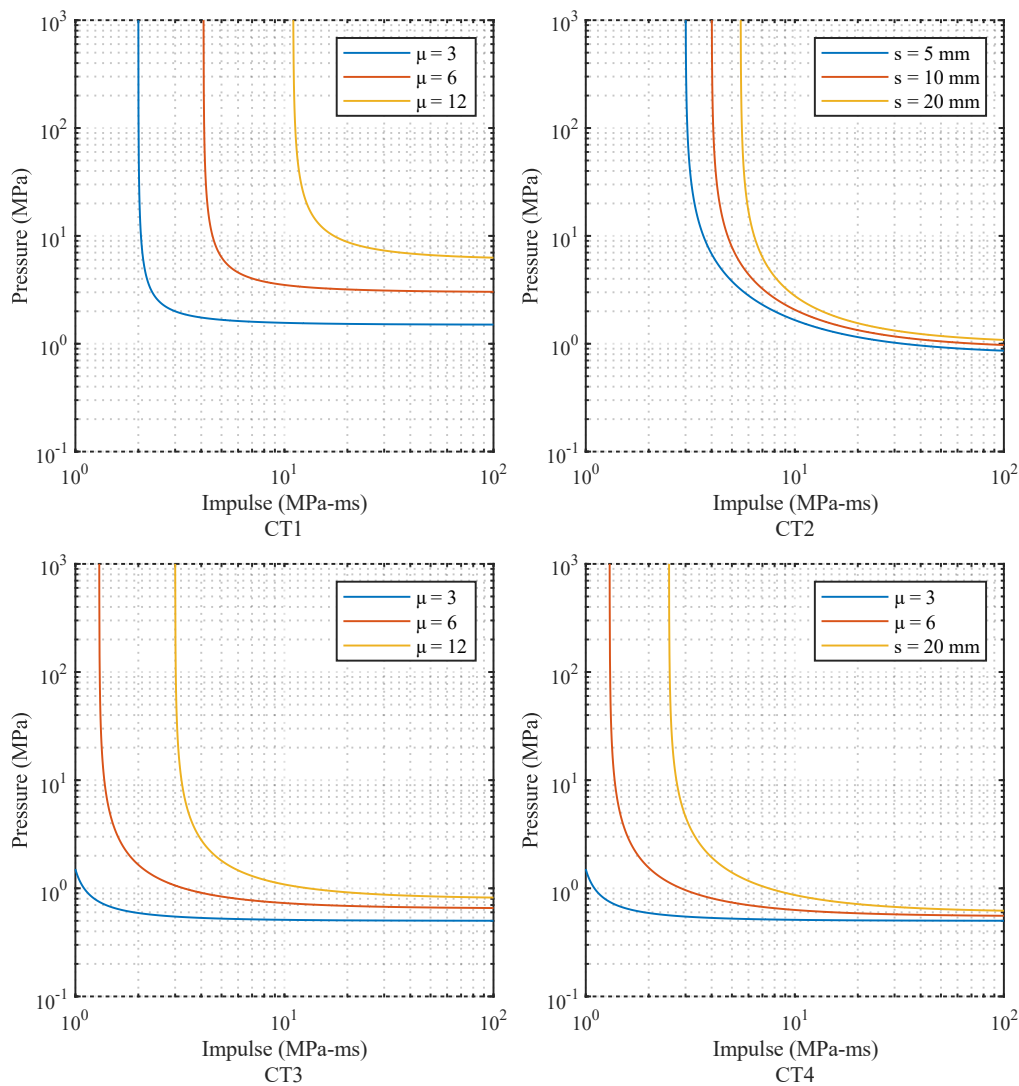


Figure 7-6: Pressure–impulse diagrams for all case study cladding types

7.4.4. Step 2: Calculation of the dynamic reaction time histories

On the pressure–impulse diagram, each pressure–impulse pair that is below the performance goal of collapse prevention corresponds to a specific combination of pressure and impulse, thus it is associated with a unique reaction time history. For this case study, characteristic positions of the pressure–impulse diagram of each cladding type were selected to extract the corresponding reaction time histories and proceed with the subsequent steps of the methodology, in accordance with Figure 7-1. The durations of the reaction time histories are subject to the limitations of Equation (7-2). In Figure 7-8, the reaction time histories, as computed with the FE models of the four cladding types for pressure of 5.0 MPa and impulse 2.0 MPa-ms, are plotted as an example. It is observed that the four dynamic reactions are quite different, and they are therefore expected to have different effect on the supporting structure. Namely, the peak dynamic reaction force of cladding type CT1 (2.2×10^6 N) is higher than the peak dynamic reactions of the other types CT2, CT3 and CT4, which are approximately equal to each other (1.8×10^6 N). It is noted that the reaction time histories are truncated when applied to the supporting structure with the rule described by Equation (7-2). The truncated portions of the reaction histories are illustrated with the dotted lines in Figure 7-8.

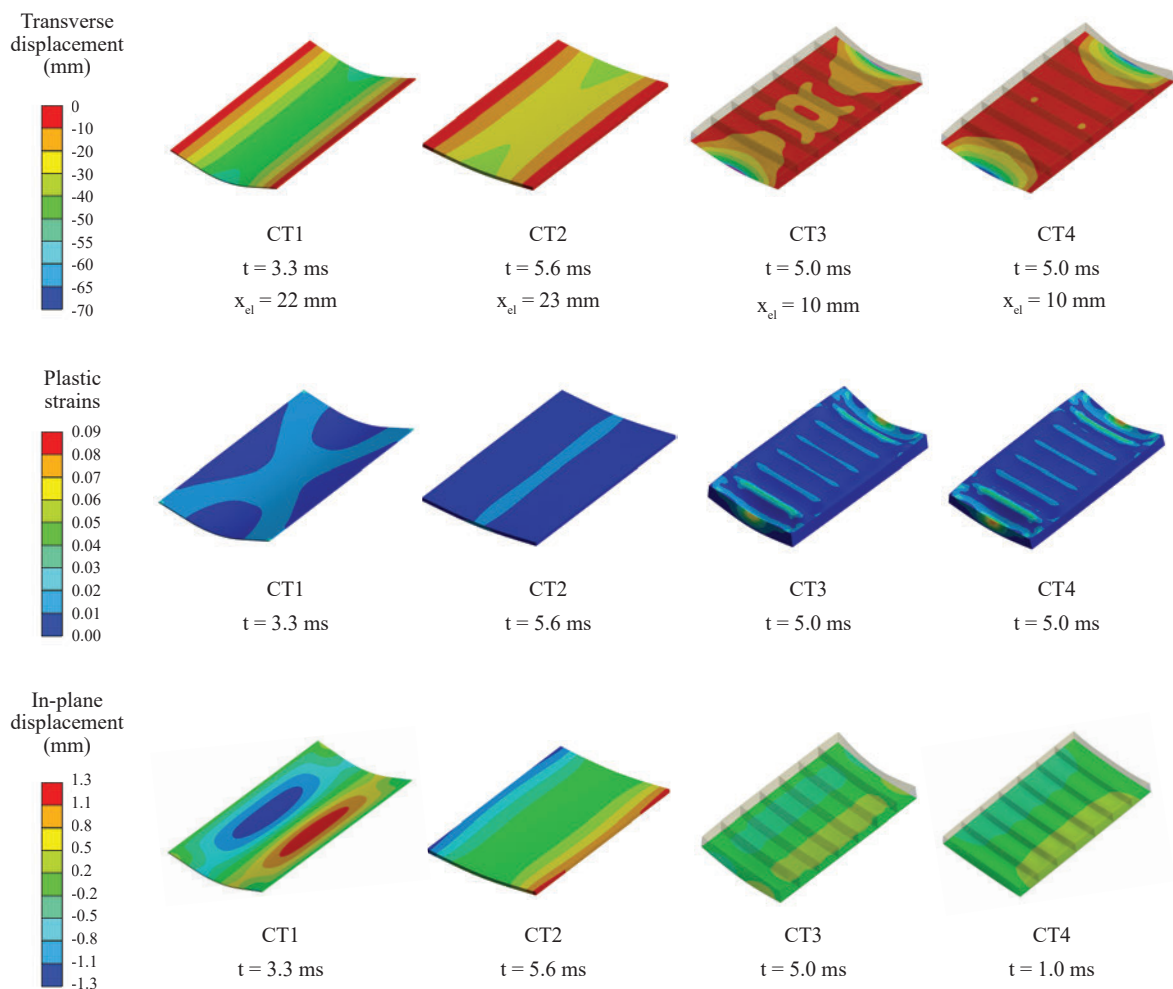


Figure 7-7: Transverse displacements, plastic strains and in-plane displacements of the case study cladding types subjected to a pressure–impulse combination of 1.0 MPa and 3.0 MPa-ms

7.4.5. Step 3: Calculation of the response of the supporting structure

Each truncated time history from the four cladding types was subsequently applied, as applied load, to the dimensionless SDOF (Equation (7-11)). For each reaction time history, a series of dimensionless SDOF analyses were performed across the considered range of natural periods of the supporting structure, and the corresponding $DLF_{rh}(T)$ was calculated from each analysis. The calculated $DLF_{rh}(T)$ of the pressure–impulse combination of 5.0 MPa, 2.0 MPa-ms, are plotted in Fig. (7-9) for the four cladding types.

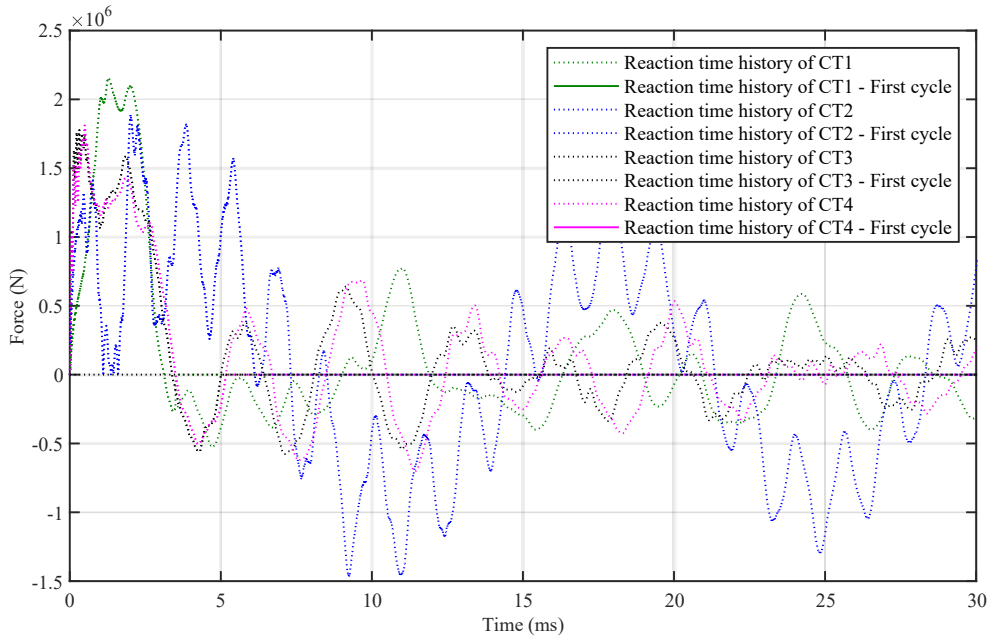


Figure 7-8: Reaction time histories for the case study cladding types with pressure 5.0 MPa and impulse 2.0 MPa-ms

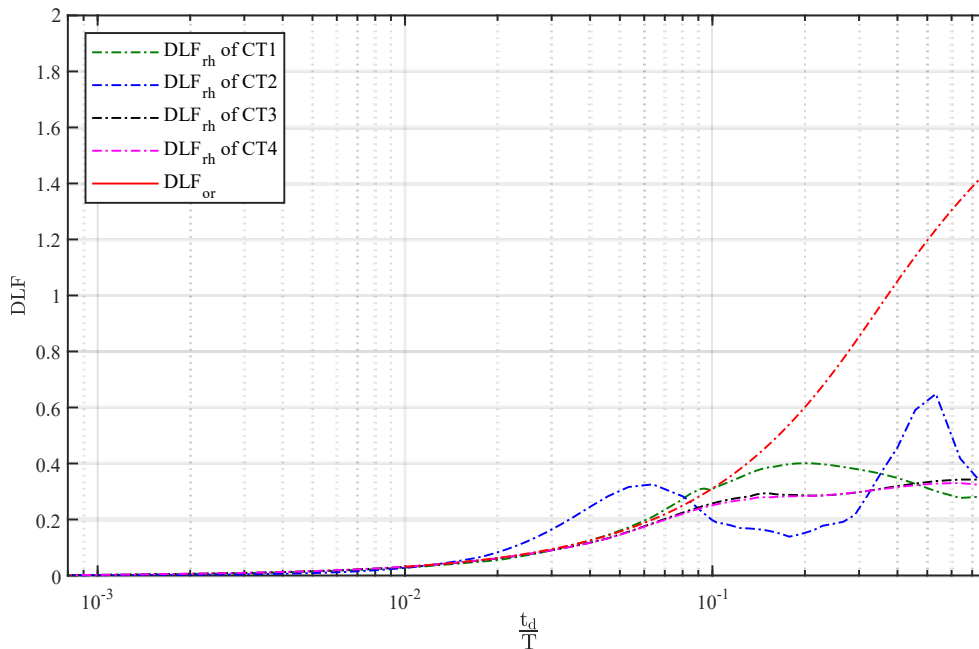


Figure 7-9: $DLF(T)$ at different natural periods of the dimensionless SDOF for the examined cladding types for pressure 5.0 MPa and impulse 2.0 MPa-ms

The DLF_{or} curve of the SDOF, when the pressure–impulse combination is directly applied to the supporting structure, is plotted with a solid red line on Figure 7-9. It is worth noting that the solution of the dimensionless SDOF, subjected to the original blast loading, is available in the bibliography for simple loading shapes (Biggs, 1964), including the triangular one employed here. It can be observed that the highest DLF_{th} reduction is exhibited differently between the cladding types, depending on the blast positive-phase duration to natural period ratio. Furthermore, there is a local peak of CT2, which leads to a DLF_{th} greater than the DLF_{or} , that the supporting structure would have if there was no cladding.

7.4.6. Step 4: Calculation of the mitigation potential at each natural period and for each reaction time history

The mitigation potential at each natural period was calculated with Equation (7-3), i.e., by dividing the $DLF_{th}(T)$ of the dimensionless SDOF when subjected to the cladding reaction time history with the $DLF_{or}(T)$ of the dimensionless SDOF when subjected to the original blast loading. As observed in Fig. Figure 7-9, where the mitigation potential for the four cladding types is presented, the mitigation potential varies significantly between the different cladding types. The difference between the cladding types is illustrated through the deviation between the red line, which represents $DLF_{or}(T)$ of the original blast loading, and the respective reaction time histories. As shown, the dynamic interaction of the cladding with the supporting structure can significantly change the response of the supporting structure.

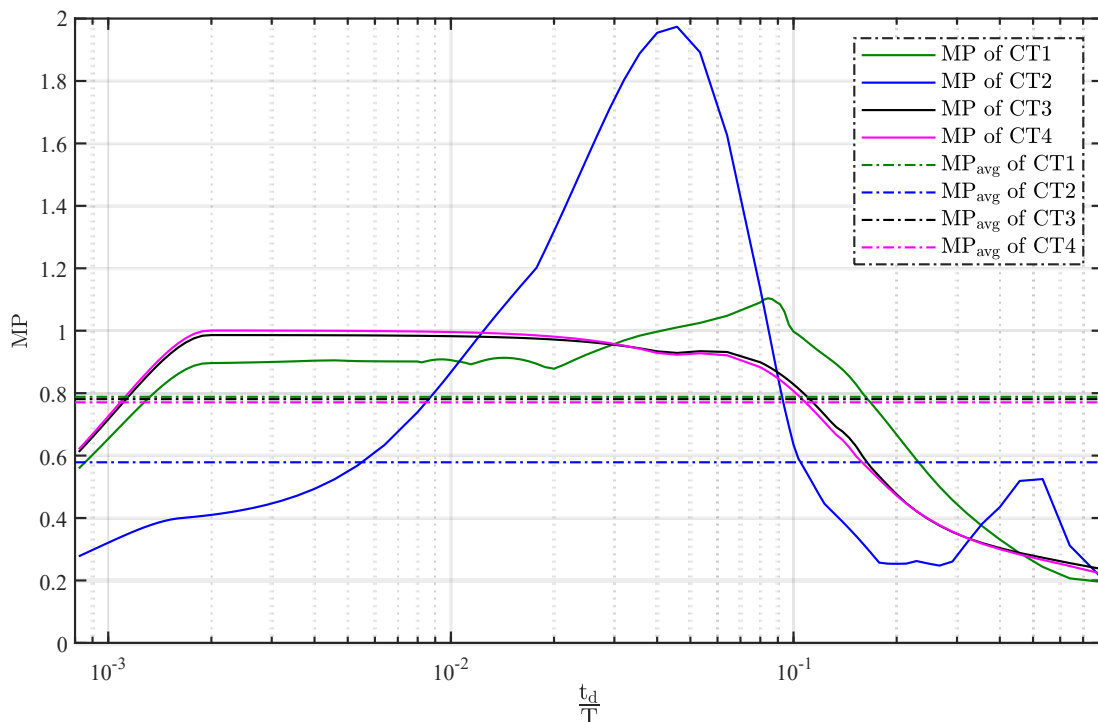


Figure 7-10: Mitigation potential for different natural periods of the dimensionless SDOF for the case study cladding types with pressure 5.0 MPa and impulse 2.0 MPa-ms

7.4.7. Step 5: Calculation of the mitigation potential over a range of selected natural periods of the supporting structure

Furthermore, the MP_{avg} values, which are also plotted in Figure 7-10, indicate the overall mitigation potential of each cladding type across the full range of considered t_d/T ratios. It is noted that CT2 has

the best overall performance, i.e., lowest MP_{avg} . It is also worth noting that the MP_{avg} of this cladding type is calculated as the geometric mean of the $MP(T)$, by being slightly affected by the local peak at $t_d/T \approx 0.045$, which corresponds only to a relatively small region, while a generally advantageous mitigation potential is exhibited at lower and higher t_d/T ratios. Because the mitigation potential peaks are mainly created when the cladding natural period is approximately equal to the supporting structure natural period, appropriate measures should be taken to avoid having a supporting structure with natural period within (or close) to mitigation potential peaks.

7.4.8. Step 6: Addition of the mitigation potential values to the pressure–impulse diagrams

The figures (Figure 7-10, Figure 7-11, Figure 7-12) in the previous steps 2 through 5 were associated with the pressure–impulse combination of 5.0 MPa and 2.0 MPa-ms. This combination constitutes only one dot in Figure 7-11, where more pressure–impulse combinations have been included. This dot is indicated with a square marker in Figure 7-11. More specifically, the procedure of the aforementioned steps (step 2 to step 5) has been repeated for several other pressure and impulse combinations and the obtained mitigation potential values have been incorporated in Figure 7-11 for all four cladding types at characteristic points of the pressure–impulse diagrams. The MP_{avg} values have been presented in color scale for direct comparison. It is observed that there are regions where the mitigation potential is as low as 0.5 and regions where it is around 1.0 or even larger.

7.4.9. Discussion of the results

In general, the effects of cladding mass and stiffness are directly correlated with the activated mechanism of inertial resistance, representing the slow response of a structural element against blast loading with respect to blast duration. Inertial resistance mechanism is defined in the current study as the mechanism where the mass of a component is relatively large and/or its stiffness is relatively low, leading to a large natural period and decreased $DLF_{rh}(T)$ against blast loading for the supporting structure, as shown by Cormie et al. (2019). Another important response mechanism is the plastic energy absorption mechanism. According to this mechanism, the component absorbs the blast energy through plastic deformation. With regard to these two mechanisms, some interesting points are exhibited in the case study results.

More specifically, the pressure–impulse diagrams (Figure 7-6) are differentiated significantly between each other. In terms of damage levels, CT1 seems to have the highest strength against the performance goals of collapse prevention and life safety, while CT2 exhibits the best results against the performance goal of property preservation. On the contrary, the worst performance is exhibited by types CT3 and CT4, which have lower pressure and impulse asymptotes. It is noted that CT1, CT3 and CT4 have approximately the same mass, while type CT2 has triple mass. With regard to stiffness, types CT3 and CT4 have larger elastic stiffness than CT1 and CT2, while a stiffening phase due to membrane effects is presented in CT1 and CT3, as shown in Figure 7-12. CT1 can be considered to be a membrane structure with negligible bending stiffness.

In terms of mitigation potential (Figure 7-11), the superior performance of CT2 is mainly attributed to a combination of the aforementioned inertial resistance and plastic energy absorption mechanisms. In all types, the desirable lower mitigation potential values follow the damage curves which are associated with increased plastic strains. Thus, it is inferred that the plastic energy absorption mechanism has an important role on the mitigation potential at the corresponding pressure–impulse combinations. On the contrary, the undesirable high mitigation potential values are exhibited at points where the cladding types behave elastically.

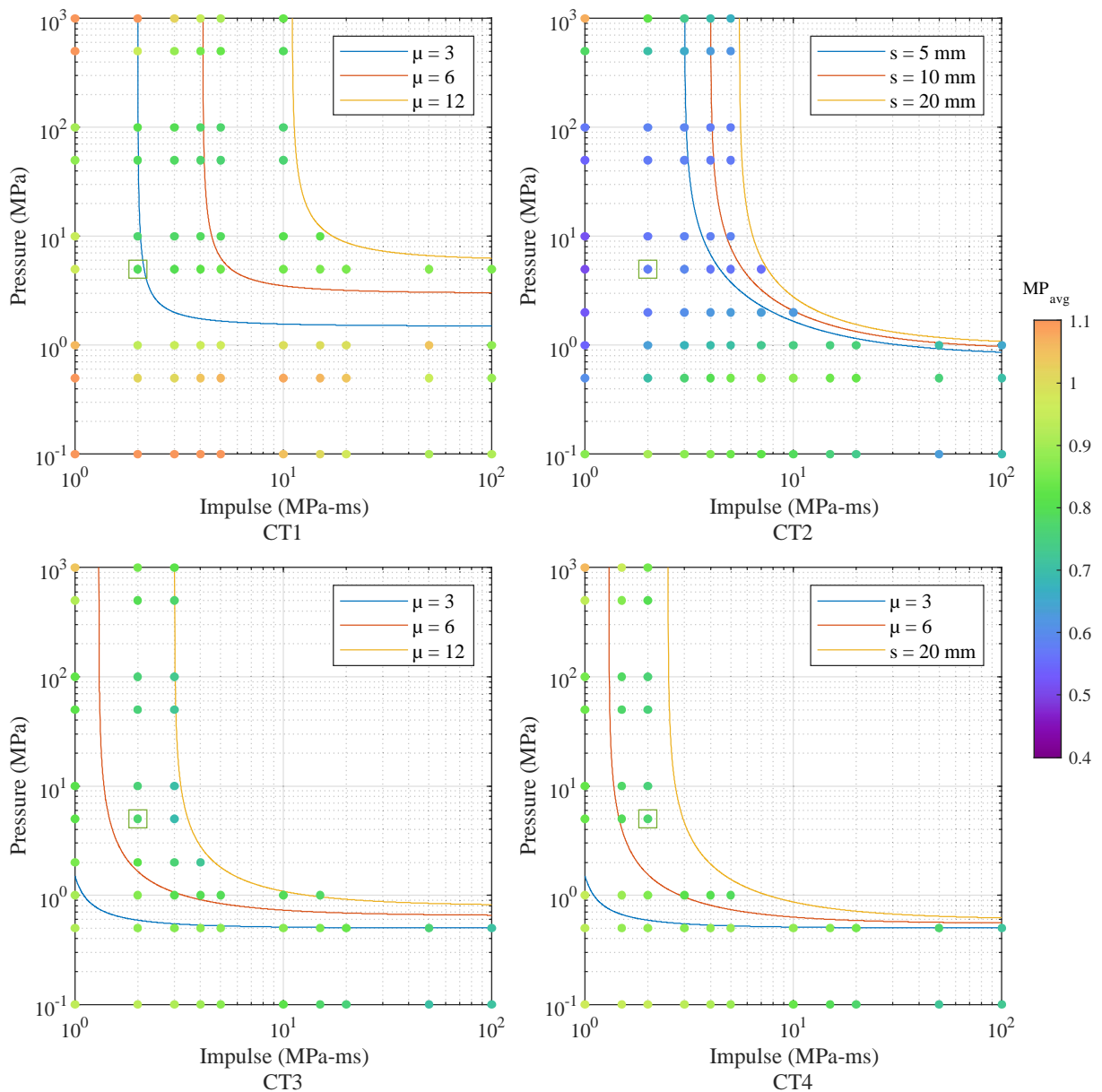


Figure 7-11: Pressure–Impulse diagrams including the mitigation potential values for the case study cladding types

Furthermore, the inertial resistance mechanism seems to also be in effect. CT2, which is characterized by the largest mass and no membrane effects, has the lowest mitigation potential of all cladding types. Interestingly, the worst performance with respect to mitigation potential is exhibited by CT1, since its response is dictated by membrane action which leads to increased stiffness and, thus, to increased reaction forces (Ioannou and Gantes, 2021). When there are significant membrane effects, the load transferred to the supporting components with the respective resistance curves is also increased. Results for CT3 and CT4 are similar because, due to the increased bending stiffness of the sandwich panels, the membrane effects are prevented. In addition, there are points where the mitigation potential is over 1.0. In these cases the dynamic reaction time histories, which are exhibited through the respective cladding type, are unconservative with regard to the effects of the original blast loading.

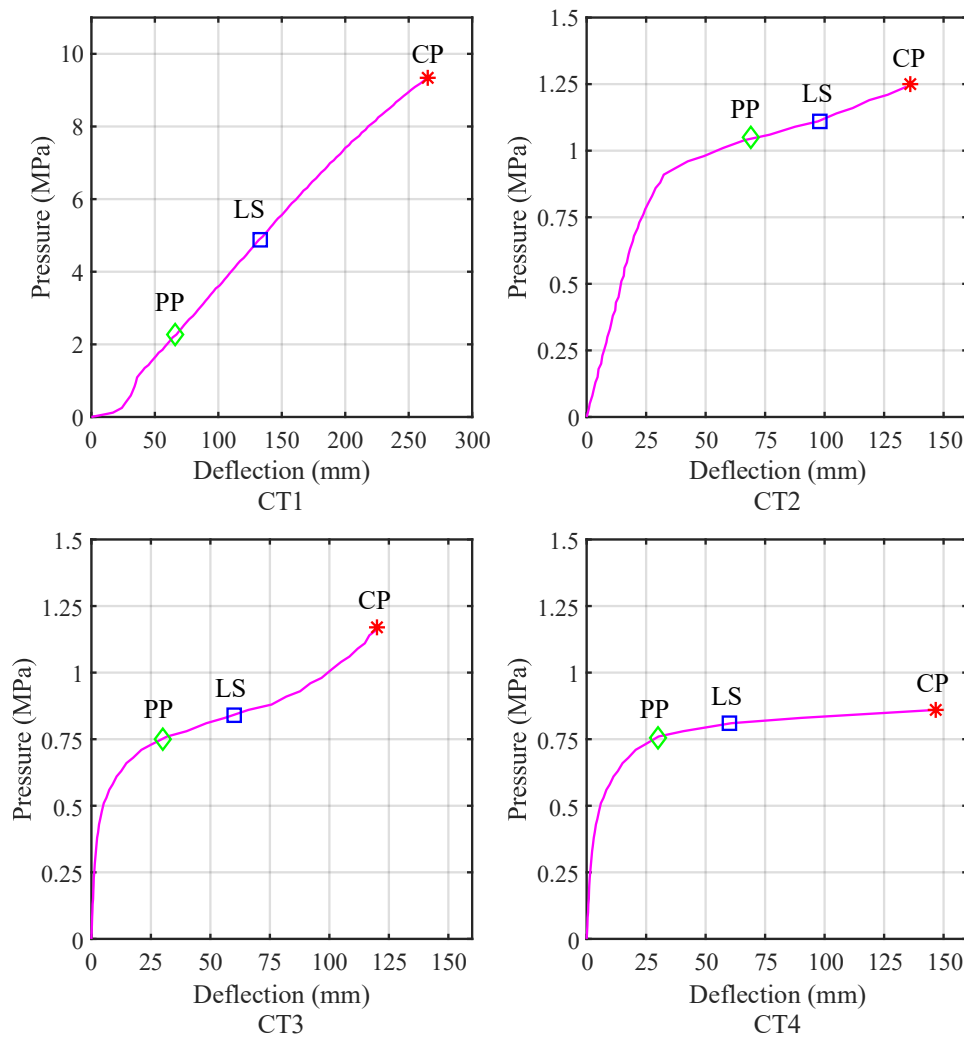


Figure 7-12: Static resistance curves for the case study cladding types in combination with the respective static damage levels and the associated performance goals

7.5. Conclusions

A methodology to evaluate the mitigation potential of a cladding to minimize the blast consequences to its supporting structure is proposed. The advantages of this methodology, in comparison to the existing ones, can be summarized as follows:

- The approach is not limited to specific combinations of explosive weight and stand-off distance, hence to specific peak pressure–impulse combinations. Instead, it can be used to evaluate the response of the cladding's supporting structure for various combinations of pressure and impulse.
- The effects of the cladding to the supporting structure can be directly estimated by calculating its response using the *DLF*.
- The approach is generic to all possible supporting structure arrangements.
- The mitigation potential can be incorporated in the respective pressure–impulse diagram of the cladding, which allows the structural engineer to associate the mitigation potential with the

cladding damage levels and directly compare the mitigation potential between different cladding types.

More specifically, the examined cladding is first analyzed for a variety of blast pressure and impulse combinations, in isolation from the supporting structure. The corresponding pressure–impulse diagrams of the cladding are constructed, and the reaction time histories are extracted for each pressure and impulse combination. These reaction time histories are subsequently used in order to calculate the $DLF_{rh}(T)$ of a dimensionless SDOF representing supporting structures with a wide range of natural periods. A proposed mitigation potential indicator is then obtained for each pressure and impulse combination and is added to the pressure–impulse diagrams of the cladding for direct reference.

The application of the methodology was implemented for four steel cladding types. Interesting insights into the role of the inertial resistance and the plastic energy absorption mechanisms emerged, showing that the plastic energy absorption mechanism is activated along the damage curves, while the inertial resistance mechanism seems to be in effect at each cladding type as a whole, and is significantly reduced when the cladding supports allow membrane action to develop.

7.6. References

- Alberdi, R., Przywara, J. and Khandelwal, K. (2013) 'Performance evaluation of sandwich panel systems for blast mitigation', *Engineering Structures*, 56, pp. 2119–2130. doi: <https://doi.org/10.1016/j.engstruct.2013.08.021>.
- American Society for Testing and Material (2019) 'F2248-19: Standard practice for specifying an equivalent 3-second duration design loading for blast resistant glazing fabricated with laminated glass'.
- ANSYS Inc (2017) 'ANSYS Explicit dynamics'.
- Arros, J. K. (2002) *Dynamics of structures, Earthquake Engineering Handbook*. United States of America: Pearson Education. doi: 10.1139/I90-078.
- Biggs, J. M. (1964) *Introduction to structural dynamics*. United States of America: McGraw-Hill.
- Braconi, A. et al. (2015) 'Efficiency of Eurocode 8 design rules for steel and steel-concrete composite structures', *Journal of Constructional Steel Research*, 112, pp. 108–129. doi: <https://doi.org/10.1016/j.jcsr.2015.04.021>.
- British Standards Institution (2019) 'BS EN 10025-2:2019: Hot rolled products of structural steels'.
- Chen, W. and Hao, H. (2012) 'Numerical study of a new multi-arch double-layered blast-resistance door panel', *International Journal of Impact Engineering*, 43, pp. 16–28. doi: 10.1016/j.ijimpeng.2011.11.010.
- Chernin, L. et al. (2019) 'Pressure-impulse diagram method - A fundamental review', *Proceedings of the Institution of Civil Engineers: Engineering and Computational Mechanics*, pp. 55–69. doi: 10.1680/jencm.17.00017.
- Cormie, D., Mays, G. and Smith, P. (2009) *Blast effects on buildings*. ICE Publishing. doi: 10.1680/beob.61477.
- Cowper, G. and Symonds, P. (1957) 'Strain hardening and strain-rate effects in the impact loading of cantilever beam', *Brown University Division of Applied Mathematics*.

- Dharmasena, K. P. et al. (2011) 'Response of metallic pyramidal lattice core sandwich panels to high intensity impulsive loading in air', *International Journal of Impact Engineering*, 38(5), pp. 275–289. doi: <https://doi.org/10.1016/j.ijimpeng.2010.10.002>.
- Dusenberry, D. O. (2010) *Handbook for blast resistant design of buildings*. John Wiley & Sons. doi: 10.1002/9780470549070.
- Eslami-majd, A. and Rahbar-Ranji, A. (2014) 'Blast response of corroded steel plates', *Journal of Mechanical Science and Technology*, 28, pp. 1683–1690.
- Forni, D., Chiaia, B. and Cadoni, E. (2016) 'Strain rate behaviour in tension of S355 steel: Base for progressive collapse analysis', *Engineering Structures*, 119, pp. 164–173. doi: <https://doi.org/10.1016/j.engstruct.2016.04.013>.
- Gantes, C. J. and Pnevmatikos, N. G. (2004) 'Elastic-plastic response spectra for exponential blast loading', *International Journal of Impact Engineering*, 30(3), pp. 323–343. doi: 10.1016/S0734-743X(03)00077-0.
- Guruprasad, S. and Mukherjee, A. (2000) 'Layered sacrificial claddings under blast loading Part I — Analytical studies', *International Journal of Impact Engineering*, 24(9), pp. 957–973. doi: [https://doi.org/10.1016/S0734-743X\(00\)00004-X](https://doi.org/10.1016/S0734-743X(00)00004-X).
- Hanssen, A. G., Enstock, L. and Langseth, M. (2002) 'Close-range blast loading of aluminium foam panels', *International Journal of Impact Engineering*, 27(6), pp. 593–618. doi: 10.1016/S0734-743X(01)00155-5.
- Holgado, D. et al. (2012) 'Connection design of steel members subjected to blast loading', in *83rd Shock and vibration symposium*. New Orleans, Louisiana.
- Ioannou, O. and Gantes, C. J. (2021) 'Membrane action of cladding subjected to blast loading and effects on the supporting structure', *Vibration*, 4(4), pp. 768–786. doi: 10.3390/vibration4040043.
- Ioannou, O., HadjiIoannou, M. and Gantes, C. J. (2022) 'Evaluation of the potential of cladding to mitigate blast effects on the supporting structure', *Practice Periodical on Structural Design and Construction*, 27(3). doi: 10.1061/(ASCE)SC.1943-5576.0000701.
- Johnson, G. R. and Cook, W. H. (1983) 'A constitutive model and data from metals subjected to large strains, high strain rates and high temperatures', in *Proceedings of the Seventh International Symposium on Ballistics*. The Hague, Netherlands.
- Kang, K. W., Lee, S. C. and Liew, R. J. Y. (2013) 'Analysis of steel-concrete composite column subject to blast', *Proceedings of the Institution of Civil Engineers - Structures and Buildings*, 166(1), pp. 15–27. doi: 10.1680/stbu.9.00092.
- Karagiozova, D. et al. (2009) 'Response of flexible sandwich-type panels to blast loading', *Composites Science and Technology*, 69(6), pp. 754–763. doi: 10.1016/j.compscitech.2007.12.005.
- Karagiozova, D., Nurick, G. N. and Langdon, G. S. (2009) 'Behaviour of sandwich panels subject to intense air blasts - Part 2: Numerical simulation', *Composite Structures*, 91(4), pp. 442–450. doi: 10.1016/j.compstruct.2009.04.010.
- Kazantzi, A. K. and Vamvatsikos, D. (2015) 'Intensity measure selection for vulnerability studies of building classes', *Earthquake Engineering and Structural Dynamics*, 44(15), pp. 2677–2694. doi: 10.1002/eqe.2603.
- Krauthammer, T. and Altenberg, A. (2000) 'Negative phase blast effects on glass panels', *International*

- Journal of Impact Engineering, 24(1), pp. 1–17. doi: [https://doi.org/10.1016/S0734-743X\(99\)00043-3](https://doi.org/10.1016/S0734-743X(99)00043-3).
- Li, Z., Chen, W. and Hao, H. (2018) 'Blast mitigation performance of cladding using square dome-shape kirigami folded structure as core', *International Journal of Mechanical Sciences*, 145, pp. 83–95. doi: <https://doi.org/10.1016/j.ijmecsci.2018.06.035>.
- Lori, G. et al. (2019) 'Sustainable facade design for glazed buildings in a blast resilient urban environment', *Glass Structures and Engineering*, 4(2), pp. 145–173. doi: [10.1007/s40940-018-0088-3](https://doi.org/10.1007/s40940-018-0088-3).
- Mortazavi, M. and Heo, Y. A. (2018) 'Nonlinear dynamic response of steel materials and plain plate systems to impact loads: Review and validation', *Engineering Structures*, 173, pp. 758–767. doi: [10.1016/j.engstruct.2018.07.012](https://doi.org/10.1016/j.engstruct.2018.07.012).
- Van Paepegem, W. et al. (2014) 'Blast performance of a sacrificial cladding with composite tubes for protection of civil engineering structures', *Composites Part B: Engineering*, 65, pp. 131–146. doi: <https://doi.org/10.1016/j.compositesb.2014.02.004>.
- Protective Design Center (2006) 'PDC TR-06-01: Single degree of freedom blast design spreadsheet (SBEDS) Methodology manual', U.S. Army Corps of Engineers.
- Protective Design Center (2008) 'PDC TR-08-07: Component explosive damage assessment workbook', U.S. Army Corps of Engineers.
- Protective Design Center (2012) 'PDC TR-10-02: Blast Resistant design methodology for window systems designed statically and dynamically', U.S. Army Corps of Engineers.
- Rigby, S. E., Tyas, A. and Bennett, T. (2012) 'Single-Degree-of-Freedom response of finite targets subjected to blast loading - The influence of clearing', *Engineering Structures*, 45, pp. 396–404. doi: [10.1016/j.engstruct.2012.06.034](https://doi.org/10.1016/j.engstruct.2012.06.034).
- Sperrazza, J. (1963) 'Modelling of air blast', in *Use of models and scaling in shock and vibration*. Philadelphia, Pennsylvania.
- Vaziri, A. and Hutchinson, J. W. (2007) 'Metal sandwich plates subject to intense air shocks', *International Journal of Solids and Structures*, 44(6), pp. 2021–2035. doi: <https://doi.org/10.1016/j.ijsolstr.2006.08.038>.
- Wang, E., Li, Q. and Sun, G. (2020) 'Computational analysis and optimization of sandwich panels with homogeneous and graded foam cores for blast resistance', *Thin-Walled Structures*, 147. doi: [10.1016/j.tws.2019.106494](https://doi.org/10.1016/j.tws.2019.106494).
- Xue, Z. and Hutchinson, J. W. (2003) 'Preliminary assessment of sandwich plates subject to blast loads', *International Journal of Mechanical Sciences*, 45(4), pp. 687–705. doi: [https://doi.org/10.1016/S0020-7403\(03\)00108-5](https://doi.org/10.1016/S0020-7403(03)00108-5).
- Yuen, S. C. K. et al. (2010) 'Sandwich panels subjected to blast loading - Dynamic failure of materials and structures', in Shukla, A., Ravichandran, G., and Rajapakse, Y. D. S. (eds). Boston, MA: Springer US, pp. 297–325. doi: [10.1007/978-1-4419-0446-1_10](https://doi.org/10.1007/978-1-4419-0446-1_10).
- Zhao, H. et al. (2015) 'Blast mitigation effect of the foamed cement-base sacrificial cladding for tunnel structures', *Construction and Building Materials*, 94, pp. 710–718. doi: [10.1016/j.conbuildmat.2015.07.076](https://doi.org/10.1016/j.conbuildmat.2015.07.076).

Chapter 8

Conclusions

8.1. Summary

The primary objective of the present thesis is to offer further insight into the cladding's capacity to mitigate potential blast effects on the supporting structure. To that effect, a combined experimental, numerical and analytical investigation has been performed and design considerations have been formulated.

Following the two introductory chapters, in chapter 3, the cladding-design philosophy was presented. The key properties cladding should have when subjected to blast loading were analyzed. The cladding's potential to mitigate blast effects on the supporting structure was highlighted as one of these properties. The mechanisms that can be activated in order to achieve blast mitigation, were described thoroughly. More specifically, both the inertial resistance and the plastic energy absorption mechanisms were found leading to the same behavior, i.e., the reduction of blast-pressure amplitude and the increase of blast duration in the cladding support-reaction time histories that are transferred to the supporting structure. It was noted that the inertial resistance mechanism is activated through increased mass and decreased stiffness in the cladding, while the plastic energy absorption is activated through plastic strains in the cladding (ultimate resistance lower than blast pressure and high ductility). Furthermore, significant literature findings on the capacity of cladding to mitigate blast pressure were presented, with particular emphasis on the effects of cladding properties, the way they were calculated and their experimental investigation.

In chapter 4, the influence of the two aforementioned mechanisms on the supporting structure's response were investigated through a dimensionless, Two-Degree-of-Freedom (2DOF) model representing the cladding (first DOF) and the supporting structure (second DOF). The 2DOF model was validated

through nonlinear dynamic finite element analyses of a specific cladding-to-framing system and by comparing 2DOF results with experimental and analytical results found in the literature. Using the validated 2DOF model, the effects of the cladding's mass, stiffness, ultimate resistance and ductility were explored through parametric studies for a wide range of parameters. The differentiating factors between the corresponding spectrum regions, where the two mechanisms are activated, were thoroughly examined and their limits were highlighted. It was shown that the plastic energy absorption mechanism is activated in specific spectrum regions, while the inertial resistance mechanism can be activated throughout the entire spectrum.

Cladding components may exhibit significant membrane action, and its effects may be critical for the supporting structure. So, the main focus of chapter 5 was to examine these effects through two-step dimensionless SDOF analyses, aimed at reaching conclusions that are applicable to a large variety of cladding-to-supporting-structure arrangements. The results of these analyses were presented by employing the dynamic load factor, representing the maximum supporting structure displacement. It was found that cladding membrane action has adverse effects over its supporting structure, as it does not allow for extensive plastic dissipation to occur and leads to higher support reactions. On the contrary, insignificant membrane action leads to lower dynamic load factor for the supporting structure. Thus, membrane behavior should be activated only as a safety backup action in order to prevent cladding failure. A case study of a typical cladding-to-supporting-structure system was presented to demonstrate and verify the proposed two-step SDOF results.

In chapter 6, the capacity of cladding to mitigate potential blast effects was examined through a blast test on two specimens with different stiffness and strength characteristics. Specifically, two steel cladding types with different geometry were examined, one comprising of a solid plate and the other one comprising of a stiffened panel. Scaled models of both types were attached to girts of identical geometry, representing the supporting structure, and were exposed to the same explosion. Maximum and permanent (plastic) displacements of the girts were measured as an index of the cladding's influence on the response of the supporting structure. Significantly lower displacements were exhibited in the girts of the solid plate in contrast to those of the panel, highlighting that the lower membrane stiffness of the solid plate, regarding the bending stiffness of the panel, was advantageous for the supporting structure. Furthermore, nonlinear transient finite element analyses of the test were performed and compared well against the experimental data.

It is desirable to develop a generally applicable method for evaluating the cladding performance in terms of blast pressure mitigation. For that purpose, in chapter 7, a methodology for calculating this mitigation potential was proposed, employing the Dynamic Load Factor (*DLF*) of a dimensionless Single-Degree-of-Freedom (SDOF) model subjected to blast for multiple pressure and impulse combinations. The *DLF* of multiple SDOF analyses was used to calculate an overall indicator of the mitigation potential of a cladding. To further demonstrate the proposed methodology, four steel cladding types were analyzed, and their mitigation potential was mapped into their pressure–impulse diagrams. Furthermore, the effects of the activated mechanisms of plastic energy absorption and inertial resistance were presented through performance observations regarding the different geometry and boundary configurations of the four cladding types. Among the four cladding types, the best and worst performing ones were found to be a thick and a thin monolithic plate respectively, while the performance of sandwich-type panels was moderate. Generally, the analysis results suggest that the increased mass and plastic dissipation in the cladding are beneficial for the building frame, while increased stiffness may overload the building frame.

8.2. Concluding remarks

The main conclusions of the present thesis are summarized below:

Chapter 4

- The most effective techniques in order to reduce blast consequences on the supporting structure were found to be the reduction of the cladding ultimate resistance, the increase of cladding ductility, the increase of the cladding mass and the decrease of the cladding stiffness.
- The plastic energy absorption mechanism is only effective in a specific region (out of the impulsive, dynamic and quasi-static regimes) that is dictated by the inertial resistance mechanism (lower bound) and the maximum ductility (upper bound). The lower bound is defined by the prevalent effects of the mass and stiffness over the effects of ultimate resistance in the response of the supporting structure. The upper bound is defined by the level of peak deformations and corresponding plastic strains, which may lead to cladding rupture, thus allowing the blast wave to enter the building, or core densification in sacrificial cladding solutions, thus transmitting unchanged blast pressure to the protected member.
- The inertial resistance mechanism is effective in all regions (impulsive, dynamic and quasi-static regimes), but it may have adverse effects on other performance objectives and serviceability requirements in typical structural applications, because of the need for increased mass or low stiffness in the cladding, leading to increased gravity loads and increased lateral deformations, respectively.
- The two mechanisms could be applied either separately or jointly, aiming at increased effectiveness over a wide range of blast pressures P_o and durations t_d .
- The activation of the plastic energy absorption mechanism depends on the blast loading characteristics (peak pressure, impulse), while the inertial resistance mechanism is activated regardless. Hence, the latter mechanism is advantageous, as there is no need for the beforehand estimation of the blast loading characteristics.
- The natural periods of the cladding and the supporting structure should differentiate by at least a factor of 2.50, in order to have negligible dynamic interaction.

Chapter 5

- It was found that the membrane branch of the cladding is not beneficial for the supporting structure. On the contrary, membrane stiffness leads to unconservative reactions to the supporting structure.
- The effects of the mechanism of plastic energy absorption are countered by the cladding membrane behavior.
- The membrane reaction forces, which occur from the cladding, should not be neglected during the structural-design phase, as it has adverse effects on the supporting structure.

Chapter 6

- The effects of the cladding bending and membrane stiffness were experimentally verified through an actual explosion, confirming that low bending and membrane stiffness in the cladding is beneficial for the supporting structure.

- The numerical model of the experiment was successfully validated through the experimental measurements. Thus, reliable numerical modelling can be performed in order to effectively capture the actual response of a cladding and its supporting structure, when subjected to blast loads.

Chapter 7

- A methodology evaluating the mitigation potential of a cladding against blast loading was proposed by using a dimensionless SDOF model.
- The methodology is not limited to specific combinations of explosive weight and stand-off distance. It is generic to all possible cladding and supporting arrangements. Hence, the direct comparison between different cladding types can be established.
- The methodology can be incorporated in the pressure–impulse diagram of the designed cladding, associating the mitigation potential with the respective damage levels of the cladding.

8.3. Research contribution

The main contributions of the present thesis to the advancement of engineering science and practice are summarized below:

- Quantitative and qualitative diagrams were created by using a validated 2DOF model (Ioannou et al., 2022a) in order to examine the effects of the cladding's mass, stiffness, ultimate resistance and ductility over the cladding mitigation potential. According to these diagrams, the differentiating factors between the activated mechanisms were highlighted.
- Quantitative and qualitative diagrams were created by using a two-step analysis (Ioannou and Gantes, 2021), in order to examine the effects of the cladding's membrane stiffness on the cladding's mitigation potential.
- An experimental investigation of two steel cladding types subjected to the blast loading of an actual explosion was conducted (Ioannou et al., 2022c). Insights into the role of the membrane and bending stiffness of the two claddings were provided and a numerical model was validated through the experimental results.
- The geometric and material arrangements which could be used for the mitigation of blast effects on the supporting structure is vast (Ioannou et al., 2020). Since there is a large variety of cladding types, a methodology for calculating the mitigation potential was proposed (Ioannou et al., 2022b).

8.4. Suggestions for future research

The findings of the thesis can be extended in the future along the following lines:

- The limitations of the lumped-mass models of chapters 4 and 5 could be overcome by taking into account more sophisticated models regarding the distribution of mass and stiffness, support reactions, force–displacement diagrams of the cladding, strain rate effects and blast loading.
- Comparative studies between different cladding geometries and materials are proposed, e.g., for the comparison of structural steel and reinforced concrete panels, the cost-effectiveness of different cladding types, etc.
- In addition to the experimental investigation of chapter 6, further experiments are suggested for validating the numerical-model results of the suggested comparative studies.

- The overall mitigation potential indicator MP_{avg} in the proposed methodology of chapter 7 is based on a selection of a wide range of natural periods. The selection of natural periods could be further explored in order to cover a typical range representing a variety of actual panel typologies and supporting structures.
- Truncation of the cladding reaction time histories in the proposed methodology of chapter 7 should be studied further and compared with experimental results. The effective duration of the reactions from the cladding on the supporting structure should be prescribed accurately.
- The variety of blast loadings that can be applied over a cladding is vast. Thus, their probabilistic analysis is considered crucial for the calculation of the cladding mitigation potential. This research work is in process (Ioannou et al., 2022d).

8.5. References

- Ioannou, O., and Gantes, C. J. (2021). "Membrane action of cladding subjected to blast loading and effects on the supporting structure." *Vibration*, 4(4), 768–786. doi: 10.3390/vibration4040043.
- Ioannou, O., Hadjioannou, M., and Gantes, C. J. (2022a). "A 2DOF method to study the influence of cladding characteristics on the response of the supporting structure under blast loading." *Journal of Structural Engineering*. doi: 10.1061/(ASCE)ST.1943-541X.0003494.
- Ioannou, O., Hadjioannou, M., and Gantes, C. J. (2022b). "Evaluation of the potential of cladding to mitigate blast effects on the supporting structure." *Practice Periodical on Structural Design and Construction*, 27(3). doi: 10.1061/(ASCE)SC.1943-5576.0000701.
- Ioannou, O., Hadjioannou, M., Gantes, C. J., and Lignos, X. A. (2022c). "Experimental investigation of a cladding to girt system subjected to blast loading." Submitted in peer-reviewed scientific journal.
- Ioannou, O., Mantzourani, A. P., and Gantes, C. J. (2020). "Energy absorption of steel cladding subjected to blast loading." 10th Greek National Steel Structures Conference (to be presented), Athens, Greece.
- Ioannou, O., Rigoutsos, G., Vamvatsikos, D., and Gantes, C. J. (2022d). "A baseline approach for probabilistic blast risk analysis of building façades under far-field explosions." In preparation for submission in peer-reviewed scientific journal.

Appendix A

Code fragments

A1. Matlab code for SDOF

The Matlab code used for the SDOF investigation of a structural component subjected to an equivalent triangular blast loading is presented in the following code fragment. The force–displacement curve for the SDOF is considered to be elastic-perfectly plastic.

Main

```
%  
%-----  
%  
% INPUT  
%  
% S1 : Degree of freedom  
% A : Area of S1 (mm2)  
% k1 : S1 stiffness (N/m)  
% m1 : S1 mass (gr)  
% r1 : S1 yield force (N)  
% c1 : S1 viscous damping coefficient  
% g : Newmark gamma coefficient  
% b : Newmark beta coefficient  
% dur : Total duration (ms)  
% dt : Timestep (ms)  
% Pr : Maximum pressure of triangular load (MPa)  
% td : Blast duration of triangular load (ms)  
%  
% OUTPUT  
%  
% di(1,dof,step) : Displacement time history  
% ve(1,dof,step) : Velocity time history
```

```

% ac(1,dof,step)      : Acceleration time history
% fs(1,dof,step)     : Resistance force time history
% rr(1,dof,step)     : Spring force time history
% tt(step)           : Timestep table
% steps              : Number of steps
% P                  : Pressure time history
%
%
% Input
A = 10^6; % mm2
k1 = 50; % N/mm
m1 = 1000; % gr
r1 = 1000; % N
c1 = 1000; % gr/ms

g = 1/2;
b = 1/4;

dur = 400; % ms
dt = 0.005; % ms
Pr = 1; % MPa
td = 5; % ms

% Execution

T1 = 2*pi*(m1/k1)^0.5; % Natural period of DOF

[di,ve,ac,fs,rr,tt,steps,P] = SDOF(dur,dt,A,k1,m1,r1,c1,g,b,Pr,td);

```

SDOF Function

```

function [di,ve,ac,fs,rr,tt,steps,P] = SDOF(dur,dt,A,k1,m1,r1,c1,g,b,Pr,td)

deviation = 1.00;

dof = 1;

M = [m1]; % Mass matrix
C = [c1]; % Damping matrix

k(:, :, 1) = k1; % Stiffness matrix

el(dof) = k1; % Stiffness table
re(dof) = r1; % Resistance table

P = [Pr; 0]; % Pressure table

t = [0; td]; % Pressure time table

stepss = size(P,1); %Number of pressure steps
steps = int32(dur/dt); %Number of all steps

pa = zeros(1,dof,steps+1);
ac = zeros(1,dof,steps+1);
ve = zeros(1,dof,steps+1);
di = zeros(1,dof,steps+1);
rr = zeros(1,dof,steps+1);
fs = zeros(1,dof,steps+1);
dp = zeros(1,dof,steps);
dpt = zeros(1,dof,steps);

```

```

ddi = zeros(1,dof,steps);
dve = zeros(1,dof,steps);
dac = zeros(1,dof,steps);
k = zeros(dof,dof,steps);
kt = zeros(dof,dof,steps);
tt = zeros(steps+1,1);

% Pressure table at each DOF multiplied by the area

for i = 1:1:dof
    pa(1,i,1) = A*P(1,i);
    pa(1,i,2) = 0;
end

% Pressure table at each DOF discretized into the individual timesteps i

tt(1) = 0;
j = 2;
i = 2;
while (j <= stepss)
    tt(i) = tt(i-1)+dt;
    if (round(tt(i),9) == round(t(j),9))
        for n = 1:1:dof
            pa(1,n,i) = P(j,n)*A;
        end
        j = j+1;
        if (j > stepss)
            break;
        end
    else
        while (tt(i) > t(j))
            j = j+1;
            if (j > stepss)
                break;
            end
        end
        if (j <= stepss)
            for n = 1:1:dof
                pa(1,n,i) = (tt(i)-tt(i-1))/(t(j)-tt(i-1))*(P(j,n)*A...
                    -pa(1,n,i-1))+pa(1,n,i-1);
            end
        end
    end
    i = i+1;
end

% Timestep table

tt(1) = 0;
for i = 2:1:(steps+1)
    tt(i) = tt(i-1)+dt;
end

% Force table applied at each timestep

for i = 1:1:steps
    for j = 1:1:dof
        dp(1,j,i) = pa(1,j,i+1)-pa(1,j,i);
    end
end

%Initial conditions

ve(1,1,1) = 0;
di(1,1,1) = 0;

%Initial calculations

```

```

ac(1,:,1) = (inv(M)*(pa(1,:,1).'-C*ve(1,:,1).'-k(:, :, 1)*di(1,:,1).')).';

% Dynamic analysis and Newton-Raphson calculations

for i = 1:1:steps
    dpt(1,:,i) = (dp(1,:,i).'+(M/b/dt+C*g/b)*ve(1,:,i).'+(M/(2*b)-C*dt*...
        (1-g/(2*b)))*ac(1,:,i).')).';

    w = 1;
    if (rr(1,w,i)*deviation<re(w) && rr(1,w,i)*deviation>-re(w))
        ktr(w) = el(w);
    else
        ktr(w) = 0;
    end

    k(:, :, i) = ktr(1);
    kt(:, :, i) = k(:, :, i)+g/(b*dt)*C+1/b/(dt^2)*M;

    % Newton-Raphson

    dr(2,:) = dpt(1,:,i);
    fsj(1,:) = fs(1,:,i);
    rj(1,:) = rr(1,:,i);
    diplus(1,:) = di(1,:,i);
    err = max(abs(max(dr(2,:))), abs(min(dr(2,:))));
    j = 2;
    while (err>0.0000001)
        dd(j,:) = (inv(kt(:, :, i))*dr(j,:)).';
        diplus(j,:) = diplus(j-1,:)+dd(j,:);

        if (rj(j-1,1)+(dd(j,1))*el(1) > re(1))
            rj(j,1) = re(1);
        elseif (rj(j-1,1)+(dd(j,1))*el(1) < -re(1))
            rj(j,1) = -re(1);
        else
            rj(j,1) = rj(j-1,1)+(dd(j,1))*el(1);
        end

        fsj(j,1) = rj(j,1);

        df(j,:) = fsj(j,:)-fsj(j-1,:)+((g/(b*dt)*C+1/b/dt^2*M)*(dd(j,:)).').';
        dr(j+1,:) = dr(j,:)-df(j,:);
        err = max(abs(max(dd(j,:))), abs(min(dd(j,:))));
        j = j+1;
    end
    di(1,:,i+1) = diplus(j-1,:);
    fs(1,:,i+1) = fsj(j-1,:);
    rr(1,:,i+1) = rj(j-1,:);
    ddi(1,:,i) = di(1,:,i+1)-di(1,:,i);
    dve(1,:,i) = g/(b*dt)*ddi(1,:,i)-g/b*ve(1,:,i)+dt*(1-g/(2*b))*ac(1,:,i);
    dac(1,:,i) = 1/(b*dt^2)*ddi(1,:,i)-1/(dt*b)*ve(1,:,i)-1/(2*b)*ac(1,:,i);
    ve(1,:,i+1) = ve(1,:,i)+dve(1,:,i);
    ac(1,:,i+1) = ac(1,:,i)+dac(1,:,i);
    dd = zeros(size(dd));
    df = zeros(size(df));
    dr = zeros(size(dr));
    fsj = zeros(size(fsj));
    rj = zeros(size(rj));
    diplus = zeros(size(diplus));
    err = 0;
end

```

A2. Matlab code for 2DOF

The Matlab code used for the 2DOF investigation of two structural components subjected to an equivalent triangular blast loading is presented in the following code fragment. The force–displacement curve for the first DOF is considered to be elastic–perfectly plastic, while the force–displacement curve for the second DOF is considered to be elastic.

Main

```

%
%
% INPUT
%
% S1          : First degree of freedom
% S2          : Second degree of freedom
% A           : Area of S1 (mm2)
% k1          : S1 stiffness (N/m)
% m1          : S1 mass (gr)
% r1          : S1 yield force (N)
% c1          : S1 viscous damping coefficient
% k2          : S2 stiffness (N/mm)
% m2          : S2 mass (gr)
% c2          : S2 viscous damping coefficient
% g           : Newmark gamma coefficient
% b           : Newmark beta coefficient
% dur         : Total duration (ms)
% dt          : Timestep (ms)
% Pr          : Maximum pressure of triangular load (MPa)
% td         : Blast duration of triangular load (ms)
%
% OUTPUT
%
% di(1,dof,step) : Displacement time history
% ve(1,dof,step) : Velocity time history
% ac(1,dof,step) : Acceleration time history
% fs(1,dof,step) : Resistance force time history
% rr(1,dof,step) : Spring force time history
% tt(step)       : Timestep table
% steps          : Number of steps
% P              : Pressure time history
%
%
% Input
A = 10^6; % mm2
k1 = 50; % N/mm
m1 = 1000; % gr
r1 = 1000; % N
c1 = 1000; % gr/ms

k2 = 50; % N/mm
m2 = 1000; % gr
c2 = 1000; % gr/ms

g = 1/2;
b = 1/4;

dur = 400; % ms
dt = 0.005; % ms
Pr = 1; % MPa

```

```

td = 5; % ms

% Execution

T1 = 2*pi*(m1/k1)^0.5; % Natural period of first DOF
T2 = 2*pi*(m2/k2)^0.5; % Natural period of second DOF

[di,ve,ac,fs,rr,tt,steps,P] = TwoDOF(dur,dt,A,k1,m1,r1,c1,k2,m2,c2,g,b,Pr,td
);

```

2DOF Function

```

function [di,ve,ac,fs,rr,tt,steps,P] =
TwoDOF(dur,dt,A,k1,m1,r1,c1,k2,m2,c2,g,b,Pr,td)

deviation = 1.00;
dof = 2;

M = [m1 0;0 m2]; % Mass matrix
C = [c1 0;0 c2]; % Damping matrix

ktr = [k1;k2]; % Stiffness table
el = [k1;k2]; % Stiffness table
k(:, :, 1) = [ktr(1) -ktr(1);-ktr(1) ktr(1)+ktr(2)]; % Stiffness matrix

r2 = 10^10; % Infinite
re = [r1;r2]; % Resistance table

P = [Pr 0;0 0]; % Pressure table at each DOF

t = [0; td]; % Pressure time table

stepss = 2; % Number of pressure steps
steps = int32(dur/dt); % Number of all steps

pa = zeros(1,dof,steps+1);
ac = zeros(1,dof,steps+1);
ve = zeros(1,dof,steps+1);
di = zeros(1,dof,steps+1);
rr = zeros(1,dof,steps+1);
fs = zeros(1,dof,steps+1);
dp = zeros(1,dof,steps);
dpt = zeros(1,dof,steps);
ddi = zeros(1,dof,steps);
dve = zeros(1,dof,steps);
dac = zeros(1,dof,steps);
k = zeros(dof,dof,steps);
kt = zeros(dof,dof,steps);
tt = zeros(steps+1,1);

% Pressure table at each DOF multiplied by the area

for i = 1:1:dof
    pa(1,i,1) = P(1,i)*A;
    pa(1,i,3) = 0;
end

% Pressure table at each DOF discretized into the individual timesteps i

tt(1) = 0;
j = 2;
i = 2;
while (j <= stepss)

```

```

        tt(i) = tt(i-1)+dt;
    if (round(tt(i),7) == round(t(j),7))
        for n = 1:1:dof
            pa(1,n,i) = P(j,n)*A;
        end
        j = j+1;
        if (j > stepss)
            break;
        end
    else
        while (tt(i) > t(j))
            j = j+1;
            if (j > stepss)
                break;
            end
        end
        if (j <= stepss)
            for n = 1:1:dof
                pa(1,n,i) = (tt(i)-tt(i-1))/(t(j)-tt(i-1))*(P(j,n)*A...
                    -pa(1,n,i-1))+pa(1,n,i-1);
            end
        end
    end
    i = i+1;
end

% Timestep table
for i = i:1:steps+1
    tt(i) = tt(i-1)+dt;
end

% Force table applied at each timestep
for i = 1:1:steps
    for j = 1:1:dof
        dp(1,j,i) = pa(1,j,i+1)-pa(1,j,i);
    end
end

% Initial conditions
ve(1,1,1) = 0;
di(1,1,1) = 0;
ve(1,2,1) = 0;
di(1,2,1) = 0;

% Initial calculations
ac(1,:,1) = (inv(M)*(pa(1,:,1) .* -C*ve(1,:,1) .* -k(:, :, 1)*di(1,:,1) .'));

% Dynamic analysis and Newton-Raphson calculations
for i = 1:1:steps
    dpt(1,:,i) = (dp(1,:,i) .* +(M/b/dt+C*g/b)*ve(1,:,i) .* +(M/(2*b)-C*dt*...
        (1-g/(2*b)))*ac(1,:,i) .');

    for w=1:1:1
        if (rr(1,w,i)*deviation<re(w) && rr(1,w,i)*deviation>-re(w))
            ktr(w) = el(w);
        else
            ktr(w) = 0;
        end
    end

    k(:, :, i) = [ktr(1) -ktr(1); -ktr(1) ktr(1)+ktr(2)];
    kt(:, :, i) = k(:, :, i)+g/(b*dt)*C+1/b/(dt^2)*M;
end

```

```

% Newton-Raphson

dr(2,:) = dpt(1,:,i);
fsj(1,:) = fs(1,:,i);
rj(1,:) = rr(1,:,i);
diplus(1,:) = di(1,:,i);
err = max(abs(max(dr(2,:))),abs(min(dr(2,:))));
j = 2;
while (err>0.0000001)
    dd(j,:) = (inv(kt(:, :, i))*dr(j,:).');
    diplus(j,:) = diplus(j-1,:)+dd(j,:);

    if (rj(j-1,1)+(dd(j,1)-dd(j,2))*el(1) > re(1))
        rj(j,1) = re(1);
    elseif (rj(j-1,1)+(dd(j,1)-dd(j,2))*el(1) < -re(1))
        rj(j,1) = -re(1);
    else
        rj(j,1) = rj(j-1,1)+(dd(j,1)-dd(j,2))*el(1);
    end

    rj(j,2) = rj(j-1,2)+(dd(j,2))*el(2);

    fsj(j,1) = rj(j,1);
    fsj(j,2) = rj(j,2)-rj(j,1);

    df(j,:) = fsj(j,:)-fsj(j-1,:)+((g/(b*dt))*C+1/b/dt^2*M)*(dd(j,:).').';
    dr(j+1,:) = dr(j,:)-df(j,:);
    err = max(abs(max(dd(j,:))),abs(min(dd(j,:))));
    j = j+1;
end
di(1,:,i+1) = diplus(j-1,:);
fs(1,:,i+1) = fsj(j-1,:);
rr(1,:,i+1) = rj(j-1,:);
ddi(1,:,i) = di(1,:,i+1)-di(1,:,i);
dve(1,:,i) = g/(b*dt)*ddi(1,:,i)-g/b*ve(1,:,i)+dt*(1-g/(2*b))*ac(1,:,i);
dac(1,:,i) = 1/(b*dt^2)*ddi(1,:,i)-1/(dt*b)*ve(1,:,i)-1/(2*b)*ac(1,:,i);
ve(1,:,i+1) = ve(1,:,i)+dve(1,:,i);
ac(1,:,i+1) = ac(1,:,i)+dac(1,:,i);
dd = zeros(size(dd));
df = zeros(size(df));
dr = zeros(size(dr));
fsj = zeros(size(fsj));
rj = zeros(size(rj));
diplus = zeros(size(diplus));
err = 0;
end

```

A3. Matlab code for dimensionless SDOF

The Matlab code used for the dimensionless SDOF investigation of a structural component subjected to arbitrary loading (cladding reaction time history) is presented in the following code fragment. The force-displacement curve for the dimensionless SDOF is considered to be elastic and the initial blast loading is considered to have an equivalent triangular form.

Main

```

%
%
% INPUT
%

```

```

% A          : Tributary area of force reaction (mm2)
% g          : Newmark gamma coefficient
% b          : Newmark beta coefficient
% dur        : Total duration (ms)
% dt         : Timestep (ms)
% Pr         : Maximum pressure of triangular load (MPa)
% td         : Blast duration of triangular load (ms)
% RT         : Reaction time history (1st column: Load (MPa))
%           : (2nd column: Time (ms))
%
% OUTPUT
%
% DLF        : Dynamic load factor
% maxd       : DLF table for each natural period
% MP         : Mitigation potential of each natural period
% MPavg      : Averaged mitigation potential
% typicaldlf : DLF for triangular load with regard to td/T1
%
% Input
g = 1/2;
b = 1/4;

dur = 400; % ms
dt = 0.005; % ms
Pr = 1; % MPa
td = 5; % ms
A = 1000/2*1000; % mm2

RT = [500000 0;200000 1;0 2]; % N

k1 = 1; % Typical value for stiffness

% Execution

% DLF calculation

for z=1:1:108 % Natural period discretization
    T1 = (1+mod((z-1)/4,9))*10^fix((z-1)/36);
    dt = min(T1/100, 0.0001);
    m1 = (T1/2/pi)^2*k1;
    [di,ve,ac,fs,rr,tt,steps,pa] = SDOF(g,b,dur,dt,RT,k1,m1);
    DLF = max(max(di(1,1,:)),abs(min(di(1,1,:))))/((Pr*A)/(k1));
    maxd(1,z,1) = DLF;
    maxd(1,z,2) = td/(T1);
end

load('typicaldlf.mat'); % It is given at Typical DLF

% Mitigation potential calculation

DLFavg = 1;
ar = 0;
for j=1:1:108
    if (maxd(1,j,2)<0.01)
        T = (1+mod((j-1)/4,9))*10^fix((j-1)/36);
        x = pi*td/T;
    elseif (maxd(1,j,2)>1)
        x = 2;
    else
        x = interp1q(maxtypd(:,2),maxtypd(:,1),maxd(1,j,2));
    end
    MP = maxd(1,j,1)/x;
    DLFavg = DLFavg*MP;
end

```

```

    ar = ar+1;
end

MPavg = (DLFavg)^(1/ar);

```

Dimensionless SDOF Function

```

function [di,ve,ac,fs,rr,tt,steps,pa] = SDOF(g,b,dur,dt,RT,k1,m1);

deviation = 1.00;

dof = 1;

P = RT(:,1); % Pressure table
t = RT(:,2); % Time table

eigen = 2*pi*(m1/k1)^0.5;
z = 0.05; % Damping ratio
c1 = 2*m1*z*2*pi/eigen; % Damping coefficient
r1 = 10^10; % Infinite

M = [m1]; % Mass matrix
C = [c1]; % Damping matrix

k(:,:,1) = k1; % Stiffness table
el(dof) = k1; % Stiffness table
re(dof) = r1; % Resistance table

stepss = size(P,1); % Number of pressure steps
steps = int32(dur/dt); % Number of all steps

pa = zeros(1,dof,steps+1);
ac = zeros(1,dof,steps+1);
ve = zeros(1,dof,steps+1);
di = zeros(1,dof,steps+1);
rr = zeros(1,dof,steps+1);
fs = zeros(1,dof,steps+1);
dp = zeros(1,dof,steps);
dpt = zeros(1,dof,steps);
ddi = zeros(1,dof,steps);
dve = zeros(1,dof,steps);
dac = zeros(1,dof,steps);
k = zeros(dof,dof,steps);
kt = zeros(dof,dof,steps);
tt = zeros(steps+1,1);

% Pressure (resultant) table at each DOF multiplied by the area

for i = 1:1:dof
    pa(1,i,1) = P(1,i);
end

% Pressure(resultant) table at each DOF discretized into the individual timesteps
i

tt(1) = 0;
j = 2;
i = 2;
while (j <= stepss)
    tt(i) = tt(i-1)+dt;
    if (round(tt(i),9) == round(t(j),9))
        for n = 1:1:dof

```

```

        pa(1,n,i) = P(j,n);
    end
    j = j+1;
    if (j > stepss)
        break;
    end
else
    while (tt(i) > t(j))
        j = j+1;
        if (j > stepss)
            break;
        end
    end
    if (j <= stepss)
        for n = 1:1:dof
            pa(1,n,i) = (tt(i)-tt(i-1))/(t(j)-tt(i-1))*(P(j,n)-...
            pa(1,n,i-1))+pa(1,n,i-1);
        end
    end
end
i = i+1;
end

% Timestep table
clear tt;
tt(1) = 0;
for i = 2:1:(steps+1)
    tt(i) = tt(i-1)+dt;
end

% Force table applied at each timestep
for i = 1:1:steps
    for j = 1:1:dof
        dp(1,j,i) = pa(1,j,i+1)-pa(1,j,i);
    end
end

% Initial conditions
ve(1,1,1) = 0;
di(1,1,1) = 0;

% Initial calculations
ac(1,:,1) = (inv(M)*(pa(1,:,1) .* -C*ve(1,:,1) .* -k(:, :, 1)*di(1,:,1) .'));

% Dynamic analysis and Newton-Raphson calculations
dd = 0;
df = 0;
for i = 1:1:steps
    dpt(1,:,i) = (dp(1,:,i) .* (M/b/dt+C*g/b)*ve(1,:,i) .* (M/(2*b)-C*...
    dt*(1-g/(2*b)))*ac(1,:,i) .');

    w = 1;
    if (rr(1,w,i)*deviation<re(w) && rr(1,w,i)*deviation>-re(w))
        ktr(w) = el(w);
    else
        ktr(w) = 0;
    end

    k(:, :, i) = ktr(1);
    kt(:, :, i) = k(:, :, i)+g/(b*dt)*C+1/b/(dt^2)*M;

% Newton-Raphson

```

```

dr(2,:) = dpt(1,:,i);
fsj(1,:) = fs(1,:,i);
rj(1,:) = rr(1,:,i);
diplus(1,:) = di(1,:,i);
err = max(abs(max(dr(2,:))),abs(min(dr(2,:))));
j = 2;
while (err>0.0000001)
    dd(j,:) = (inv(kt(:, :, i))*dr(j,:).');
    diplus(j,:) = diplus(j-1,:)+dd(j,:);

    if (rj(j-1,1)+(dd(j,1))*el(1) > re(1))
        rj(j,1) = re(1);
    elseif (rj(j-1,1)+(dd(j,1))*el(1) < -re(1))
        rj(j,1) = -re(1);
    else
        rj(j,1) = rj(j-1,1)+(dd(j,1))*el(1);
    end

    fsj(j,1) = rj(j,1);

    df(j,:) = fsj(j,:)-fsj(j-1,:)+((g/(b*dt)*C+1/b/dt^2*M)*(dd(j,:).')).';
    dr(j+1,:) = dr(j,:)-df(j,:);
    err = max(abs(max(dd(j,:))),abs(min(dd(j,:))));
    j = j+1;
end
di(1,:,i+1) = diplus(j-1,:);
fs(1,:,i+1) = fsj(j-1,:);
rr(1,:,i+1) = rj(j-1,:);
ddi(1,:,i) = di(1,:,i+1)-di(1,:,i);
dve(1,:,i) = g/(b*dt)*ddi(1,:,i)-g/b*ve(1,:,i)+dt*(1-g/(2*b))*ac(1,:,i);
dac(1,:,i) = 1/(b*dt^2)*ddi(1,:,i)-1/(dt*b)*ve(1,:,i)-1/(2*b)*ac(1,:,i);
ve(1,:,i+1) = ve(1,:,i)+dve(1,:,i);
ac(1,:,i+1) = ac(1,:,i)+dac(1,:,i);
dd = zeros(size(dd));
df = zeros(size(df));
dr = zeros(size(dr));
fsj = zeros(size(fsj));
rj = zeros(size(rj));
diplus = zeros(size(diplus));
err = 0;
end

```

Typical DLF

The typical DLF curve refers to the response of an elastic SDOF subjected to an equivalent triangular load. The response of the SDOF is undimensionalized regarding the ratio of blast load duration to the SDOF natural period.

```

maxtypd(:,1) = [0.0314145815078217 0.0323317923883323 0.0332757506485545
0.0342472299228916 0.0352470265752000 0.0362759738658638 0.0373348993824340
0.0384246886462925 0.0395462217245455 0.0407004211994161 0.0418882321441422
0.0431106244968925 0.0443685978154325 0.0456631764988717 0.0469954148632018
0.0483664012078016 0.0497772447755837 0.0512305177120362 0.0527262842192085
0.0542655849838191 0.0558496732062680 0.0574798181163132 0.0591573965557830
0.0608837080914336 0.0626601657119049 0.0644882008059889 0.0663692866592323
0.0683049289842837 0.0702966461434069 0.0723461345358318 0.0744549186525893
0.0766247104670980 0.0788598047586537 0.0811607801894940 0.0835283521012943
0.0859644224141073 0.0884709381926705 0.0910498205427886 0.0937030929200103
0.0964328173956753 0.0992411129735442 0.102130145606521 0.105103680812749
0.108167660931759 0.111319738961005 0.114562294511498 0.117897783539987
0.121328713918918 0.124857653386152 0.128487210329891 0.132222719335847

```

0.136071968698932 0.140030772254300 0.144102075663287 0.148288706353002
0.152593670278254 0.157019978728085 0.161582632500600 0.166276052084195
0.171101282799869 0.176061560650146 0.181160158476919 0.186408898613512
0.191813649159713 0.197368224746150 0.203076097353151 0.208940749314818
0.214985463746033 0.221199470855279 0.227582609238293 0.234138361576731
0.240893196908825 0.247835835680944 0.254963986119518 0.262287330764681
0.269832053556298 0.277575231646360 0.285520378048748 0.293708391608104
0.302110095076425 0.310725158048810 0.319605828229717 0.328708973865782
0.338053206015446 0.347665262910837 0.357511404576023 0.367641609850867
0.378024167343074 0.388683836852318 0.399621666855635 0.410836283529419
0.422346579854473 0.434140684132841 0.446238598073702 0.458634999248127
0.471327499923343 0.484351819092646 0.497661791153645 0.511316973675027
0.525276510888295 0.539547561766676 0.554166860452580 0.569098701565887
0.584346781063565 0.599931804422787 0.615846612999847 0.632078877096249
0.648627015601373 0.665492097574747 0.682667608704254 0.700149348654982
0.717932518948474 0.736003326431311 0.754350670432670 0.772965566925329
0.791829893738839 0.810925389908484 0.830231266151902 0.849724237702909
0.869380673263492 0.889183856026373 0.909087211035124 0.929060774882204
0.949071833103563 0.969070788935245 0.989015773119539 1.00885350931545
1.02855504113862 1.04805172699741 1.06747354550215 1.08666267669827
1.10565952155840 1.12450837274091 1.14307179612400 1.16148772534661
1.17967515691828 1.19756945426366 1.21528198976346 1.23277216860382
1.24996863964324 1.26687458116053 1.28360025344143 1.30007207759248
1.31625640314078 1.33215779501385 1.34778096988346 1.36313055961913
1.37821087170391 1.39303443155667 1.40760333836421 1.42189182175984
1.43590083282645 1.44967149649062 1.46317887218301 1.47641865770221
1.48938455213956 1.50206811711525 1.51445866133724 1.52657090423856
1.53854515047373 1.55020524338930 1.56153066847244 1.57274468596564
1.58364263873737 1.59427795704653 1.60473753057949 1.61488260020326
1.62486947559838 1.63459059070671 1.64404565434251 1.65338381409483
1.66242637630630 1.67120543878710 1.67989182643304 1.68834741086804
1.69657898118306 1.70460276099340 1.71243066589049 1.72007018805324
1.72752436079388 1.73479176491317 1.74186658035485 1.74873868119004
1.75548593050406 1.76209184717442 1.76846534803737 1.77471007855995
1.78080358114539 1.78671588082383 1.79248813300336 1.79813704492419
1.80358501335877 1.80891195295557 1.81414109867682 1.81921608428354
1.82415097337234 1.82895255329602 1.83362066448377 1.83814857624248
1.84260406895088 1.84694251990716 1.85110897131666 1.85523655837235
1.85917536556658 1.86309405841080 1.86686961102005 1.87053147767102
1.87409854888765 1.87757982947002 1.88097515280813 1.88427592086172
1.88746586141958 1.89059032331191 1.89362321342444 1.89658449817059
1.89944381158270 1.90222606510757 1.90494398877028 1.90759920953416
1.91018332604543 1.91267897106066 1.91511412374488 1.91746976314476
1.91978418447566 1.92202501392334 1.92420005551121 1.92630539912662
1.92837831281023 1.93037168945583 1.93232937881516 1.93422393839718
1.93606495974879 1.93784915981769 1.93959385621668 1.94128069988089
1.94293294932887 1.94453263608920 1.94608062665235 1.94760522878793
1.94907069723792 1.95049790042982 1.95189288526219 1.95324784374905
1.95455922342129 1.95583412790248 1.95707944848100 1.95828762148968
1.95946175925898 1.96060249056771 1.96171142376964 1.96278804083347
1.96383430227690 1.96485583848620 1.96584323101946 1.96680740771070
1.96773939582419 1.96865351758438 1.96953743704394 1.97039360701629
1.97123115198991 1.97204174791826 1.97283146975460 1.97359805767925
1.97434278764121 1.97506764196496 1.97576908643932 1.97645488412965
1.97711884885443 1.97776508502233 1.97839426915628 1.97900394495525
1.97959837835098 1.98017487193871 1.98073416824481 1.98127945692289
1.98180790486523 1.98232303416249 1.98282262286735 1.98330854682623
1.98377940620350 1.98423852083499 1.98468402108451 1.98511792359535
1.98553881935681 1.98594831391031 1.98634585740735 1.98673222917240
1.98710758369936 1.98747184856038 1.98782691843133 1.98817150663401
1.98850593073076 1.98883177989428 1.98914758733123 1.98945487454703
1.98975367656742 1.99004383154823 1.99032568132336 1.99059924754324
1.99086592911409 1.99112459685639 1.99137599127227 1.99161985484069
1.99185741134212 1.99208807521819 1.99231214581240 1.99253002999683
1.99274148727423 1.99294741205708 1.99314723612566 1.99334135806548
1.99352997375438 1.99371327359791 1.99389151142050 1.99406462735830

```

1.99423284648349 1.99439628396554 1.99455509789193 1.99470935014881
1.99485934196726 2];

maxtypd(:,2) = [0.0100000000000000 0.0102920052719443 0.0105925372517729
0.0109018449238513 0.0112201845430196 0.0115478198468946 0.0118850222743702
0.0122320711904993 0.0125892541179417 0.0129568669751702 0.0133352143216332
0.0137246096100756 0.0141253754462275 0.0145378438560766 0.0149623565609443
0.0153992652605949 0.0158489319246111 0.0163117290922784 0.0167880401812256
0.0172782598050786 0.0177827941003892 0.0183020610631106 0.0188364908948980
0.0193865263595221 0.0199526231496888 0.0205352502645715 0.0211348903983665
0.0217520403401952 0.0223872113856834 0.0230409297605585 0.0237137370566166
0.0244061906804198 0.0251188643150958 0.0258523483956219 0.0266072505979881
0.0273841963426436 0.0281838293126445 0.0290068119869315 0.0298538261891796
0.0307255736526745 0.0316227766016838 0.0325461783498046 0.0334965439157828
0.0344746606573149 0.0354813389233576 0.0365174127254838 0.0375837404288444
0.0386812054633052 0.0398107170553497 0.0409732109813542 0.0421696503428582
0.0434010263644744 0.0446683592150963 0.0459726988530872 0.0473151258961481
0.0486967525165863 0.0501187233627272 0.0515822165072306 0.0530884444230989
0.0546386549881854 0.0562341325190349 0.0578761988349121 0.0595662143529011
0.0613055792149821 0.0630957344480193 0.0649381631576211 0.0668343917568615
0.0687859912308808 0.0707945784384138 0.0728618174513228 0.0749894209332456
0.0771791515585012 0.0794328234724282 0.0817523037943650 0.0841395141645195
0.0865964323360066 0.0891250938133746 0.0917275935389780 0.0944060876285924
0.0971627951577107 0.1000000000000000 0.102920052719443 0.105925372517729
0.109018449238513 0.112201845430196 0.115478198468946 0.118850222743702
0.122320711904993 0.125892541179417 0.129568669751702 0.133352143216332
0.137246096100756 0.141253754462275 0.145378438560766 0.149623565609443
0.153992652605949 0.158489319246111 0.163117290922784 0.167880401812256
0.172782598050786 0.177827941003892 0.183020610631106 0.188364908948980
0.193865263595221 0.199526231496888 0.205352502645715 0.211348903983665
0.217520403401952 0.223872113856834 0.230409297605585 0.237137370566166
0.244061906804198 0.251188643150958 0.258523483956219 0.266072505979881
0.273841963426436 0.281838293126445 0.290068119869315 0.298538261891796
0.307255736526745 0.316227766016838 0.325461783498046 0.334965439157828
0.344746606573150 0.354813389233575 0.365174127254838 0.375837404288444
0.386812054633052 0.398107170553497 0.409732109813542 0.421696503428582
0.434010263644744 0.446683592150963 0.459726988530872 0.473151258961481
0.486967525165863 0.501187233627272 0.515822165072306 0.530884444230989
0.546386549881854 0.562341325190349 0.578761988349121 0.595662143529011
0.613055792149821 0.630957344480193 0.649381631576211 0.668343917568615
0.687859912308808 0.707945784384138 0.728618174513228 0.749894209332456
0.771791515585012 0.794328234724282 0.817523037943650 0.841395141645195
0.865964323360065 0.891250938133746 0.917275935389780 0.944060876285924
0.971627951577107 1.02920052719443 1.05925372517729 1.09018449238513
1.12201845430196 1.15478198468946 1.18850222743702 1.22320711904993
1.25892541179417 1.29568669751702 1.33352143216332 1.37246096100756
1.41253754462275 1.45378438560766 1.49623565609443 1.53992652605949
1.58489319246111 1.63117290922784 1.67880401812256 1.72782598050786
1.77827941003892 1.83020610631106 1.88364908948980 1.93865263595221
1.99526231496888 2.05352502645715 2.11348903983665 2.17520403401952
2.23872113856834 2.30409297605585 2.37137370566166 2.44061906804198
2.51188643150958 2.58523483956219 2.66072505979881 2.73841963426436
2.81838293126446 2.90068119869315 2.98538261891796 3.07255736526745
3.16227766016838 3.25461783498046 3.34965439157828 3.44746606573149
3.54813389233575 3.65174127254838 3.75837404288444 3.86812054633052
3.98107170553497 4.09732109813541 4.21696503428582 4.34010263644744
4.46683592150963 4.59726988530872 4.73151258961480 4.86967525165863
5.01187233627273 5.15822165072306 5.30884444230989 5.46386549881854
5.62341325190349 5.78761988349121 5.95662143529010 6.13055792149821
6.30957344480193 6.49381631576211 6.68343917568615 6.87859912308808
7.07945784384138 7.28618174513227 7.49894209332456 7.71791515585013
7.94328234724281 8.17523037943650 8.41395141645195 8.65964323360065
8.91250938133746 9.17275935389780 9.44060876285924 9.71627951577106 10
10.2920052719443 10.5925372517729 10.9018449238513 11.2201845430196
11.5478198468946 11.8850222743702 12.2320711904993 12.5892541179417
12.9568669751702 13.3352143216332 13.7246096100756 14.1253754462275
14.5378438560766 14.9623565609443 15.3992652605949 15.8489319246111

```

```
16.3117290922784 16.7880401812256 17.2782598050786 17.7827941003892
18.3020610631106 18.8364908948980 19.3865263595221 19.9526231496888
20.5352502645715 21.1348903983665 21.7520403401952 22.3872113856834
23.0409297605585 23.7137370566166 24.4061906804198 25.1188643150958
25.8523483956219 26.6072505979881 27.3841963426436 28.1838293126445
29.0068119869315 29.8538261891796 30.7255736526745 31.6227766016838
32.5461783498046 33.4965439157828 34.4746606573149 35.4813389233575
36.5174127254838 37.5837404288444 38.6812054633052 39.8107170553497
40.9732109813541 42.1696503428582 43.4010263644744 44.6683592150963
45.9726988530872 47.3151258961480 48.6967525165863 50.1187233627273
51.5822165072306 53.0884444230989 54.6386549881854 56.2341325190349
57.8761988349121 59.5662143529010 61.3055792149821 63.0957344480193
64.9381631576211 66.8343917568615 68.7859912308807 70.7945784384138
72.8618174513228 74.9894209332456 77.1791515585013 79.4328234724281
81.7523037943650 84.1395141645195 86.5964323360065 89.1250938133746
91.7275935389779 94.4060876285924 97.1627951577106 100];
```

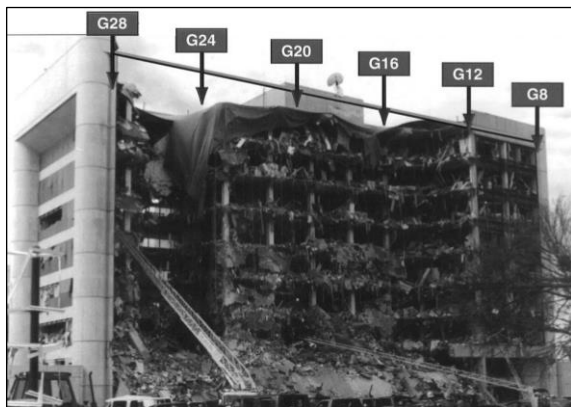

Appendix B

Extended summary (in Greek) Εκτενής περίληψη

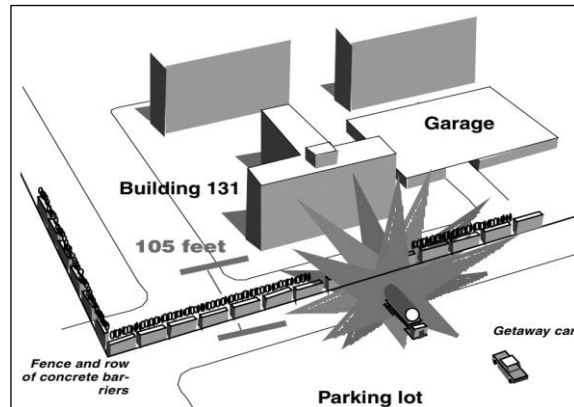
B1. Εισαγωγή

Παρότι ανέκαθεν αποτελούσαν ένα σπάνιο συμβάν, οι εκρήξεις πλέον αυξάνονται όλο και περισσότερο με την πάροδο του χρόνου, εξαιτίας της ανθρώπινης παρέμβασης, με τις συνέπειές τους να είναι εξαιρετικά δυσμενείς για την κοινωνία (IEP, 2015). Ο τρόπος σύμφωνα με τον οποίο προκύπτουν είναι είτε λόγω επιθέσεων είτε λόγω ατυχημάτων. Και στις δύο περιπτώσεις, υπάρχουν χαρακτηριστικά παραδείγματα εκρήξεων που έχουν οδηγήσει στην ενεργοποίηση του κράτους και των ερευνητών για την προστασία των κατασκευών και της ανθρώπινης ζωής. Στην περίπτωση των επιθέσεων, δύο περιστατικά που έχουν συνταράξει την κοινή γνώμη αποτελούν η επίθεση στο Alfred P. Murrah Federal Building στην πόλη Oklahoma των ΗΠΑ (1995) και στους Πύργους Khobar στη Dhahran της Σαουδικής Αραβίας (1996). Αντίστοιχα παραδείγματα στην περίπτωση εκρήξεων λόγω ατυχήματος, αποτελούν οι εκρήξεις στο Λιμάνι Tianjin της Κίνας (2015) και στο Λιμάνι της Βηρυτού στον Λίβανο (2020). Αποτελέσματα των παραδειγμάτων απεικονίζονται στο Σχήμα 1.

Όταν λαμβάνει χώρα μια έκρηξη κοντά σε ένα κτίριο, τα πρώτα δομικά στοιχεία που δέχονται τις αναπτυσσόμενες πιέσεις είναι τα εξωτερικά στοιχεία επικάλυψης. Για την ασφάλεια των χρηστών του κτιρίου, τα στοιχεία επικάλυψης πρέπει να έχουν επαρκή αντοχή έναντι της έκρηξης, να συμπεριφέρονται με ελεγχόμενο τρόπο και να μην επιτρέπουν την είσοδο του ωστικού κύματος στον εσωτερικό χώρο (Cormie, Mays and Smith, 2009). Μια πρόσφατη τάση αποτελεί ο σχεδιασμός της επικάλυψης με τέτοιο τρόπο, ώστε να μπορεί να απορροφήσει σημαντικό μέρος της ενέργειας που προκύπτει από την έκρηξη. Με αυτόν τον τρόπο, το φορτίο που μεταφέρεται από τα στοιχεία επικάλυψης στα κύρια δομικά μέλη (υποστυλώματα, δοκοί κ.τ.λ.) δύναται να είναι χαμηλότερο σε σχέση με αυτό που θα μεταφερόταν εάν τα στοιχεία επικάλυψης δεν είχαν σχεδιαστεί με δυνατότητα μείωσης των συνεπειών στον υποκείμενο φορέα.



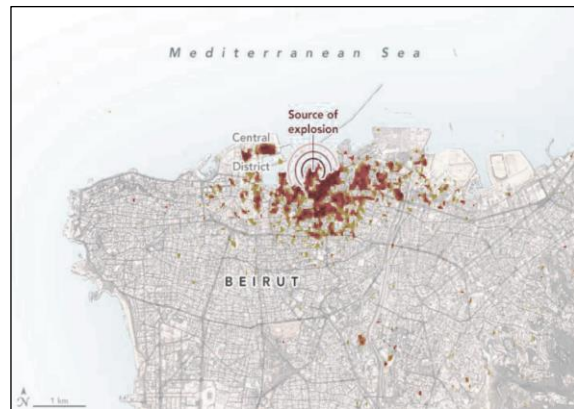
(α)



(β)



(γ)



(δ)

Σχήμα 1: Χαρακτηριστικές περιπτώσεις εκρήξεων που έχουν συνταράξει την κοινή γνώμη: (α) Έκρηξη στο Alfred P. Murrah Federal Building [αναπαραγωγή από FEMA (1996)], (β) Απεικόνιση του σημείου της έκρηξης σε σχέση με τους Πύργους Khobar [αναπαραγωγή από Grant (1998)], (γ) Ζημιές σε κτίριο που βρίσκεται σε απόσταση 300 m από την έκρηξη στο Λιμάνι Tianjin της Κίνας [αναπαραγωγή από Yu et al. (2022)] και (δ) Χάρτης ζημιών γύρω από το Λιμάνι της Βηρυτού [αναπαραγωγή από Sivaraman and Varadharajan (2021)]

Ωστόσο, υπάρχουν διάφορα ζητήματα, σε σχέση με την αξιοποίηση αυτής της τάσης, τα οποία δεν έχουν καλυφθεί ερευνητικά. Αυτά είναι:

- Η ποικιλία των πιθανών τύπων επικάλυψης, που μπορούν να τοποθετηθούν σε ένα κτίριο στο οποίο μπορεί να συμβεί έκρηξη, είναι ευρεία. Κατά συνέπεια, χρειάζονται οδηγίες σχεδιασμού σε σχέση με την κατάλληλη επιλογή των ιδιοτήτων της επικάλυψης, προκειμένου να επιτυγχάνεται μείωση των δυνάμεων στον υποκείμενο φορέα.
- Τα αποτελέσματα των αριθμητικών μοντέλων επικάλυψης και υποκείμενου φορέα χρειάζονται πιστοποίηση μέσω πειραματικών μετρήσεων, ούτως ώστε να επιβεβαιωθεί ότι είναι ρεαλιστικά.
- Χρειάζεται μια μεθοδολογία για την εκτίμηση της δυνατότητας ενός τύπου επικάλυψης για μείωση των συνεπειών από έκρηξη. Αυτή η μεθοδολογία πρέπει να είναι γενικευμένη, ούτως ώστε να μπορεί να γίνει άμεση σύγκριση μεταξύ των διαφόρων τύπων της επικάλυψης και κατάλληλη επιλογή του επικρατέστερου.

Οπότε, σε μια προσπάθεια αντιμετώπισης αυτών των ζητημάτων το αντικείμενο της διατριβής είναι:

- Ο υπολογισμός με ποιοτικά και ποσοτικά διαγράμματα του τρόπου επιρροής της μάζας, δυσκαμψίας, αντοχής και ολκιμότητας της επικάλυψης στον υποκείμενο φορέα.
- Ο υπολογισμός με ποιοτικά και ποσοτικά διαγράμματα του τρόπου επιρροής της μεμβρανικής δράσης της επικάλυψης στον υποκείμενο φορέα.
- Η πειραματική διερεύνηση ενός συστήματος χαλύβδινης επικάλυψης–υποκείμενου φορέα (με την εφαρμογή πραγματικής έκρηξης) και η προετοιμασία ενός αριθμητικού μοντέλου, του οποίου τα αποτελέσματα πιστοποιούνται από τις πειραματικές μετρήσεις.
- Η ανάπτυξη μεθοδολογίας για τη γενικευμένη εκτίμηση της δυνατότητας μιας τυχαίας επικάλυψης για μείωση των συνεπειών στον υποκείμενο φορέα και, κατ' επέκταση, την άμεση σύγκριση μεταξύ των διαφόρων τύπων επικάλυψης.

B2. Μηχανισμοί λειτουργίας και βιβλιογραφική επισκόπηση

Σύμφωνα με τους [Hetherington and Smith \(1994\)](#), [Dusenberry \(2010\)](#) και [Palanivelu et al. \(2011\)](#), όταν σχεδιάζεται κάποιο κτίριο έναντι έκρηξης, τα εξωτερικά στοιχεία επικάλυψής του πρέπει να έχουν συγκεκριμένες ειδικές ιδιότητες:

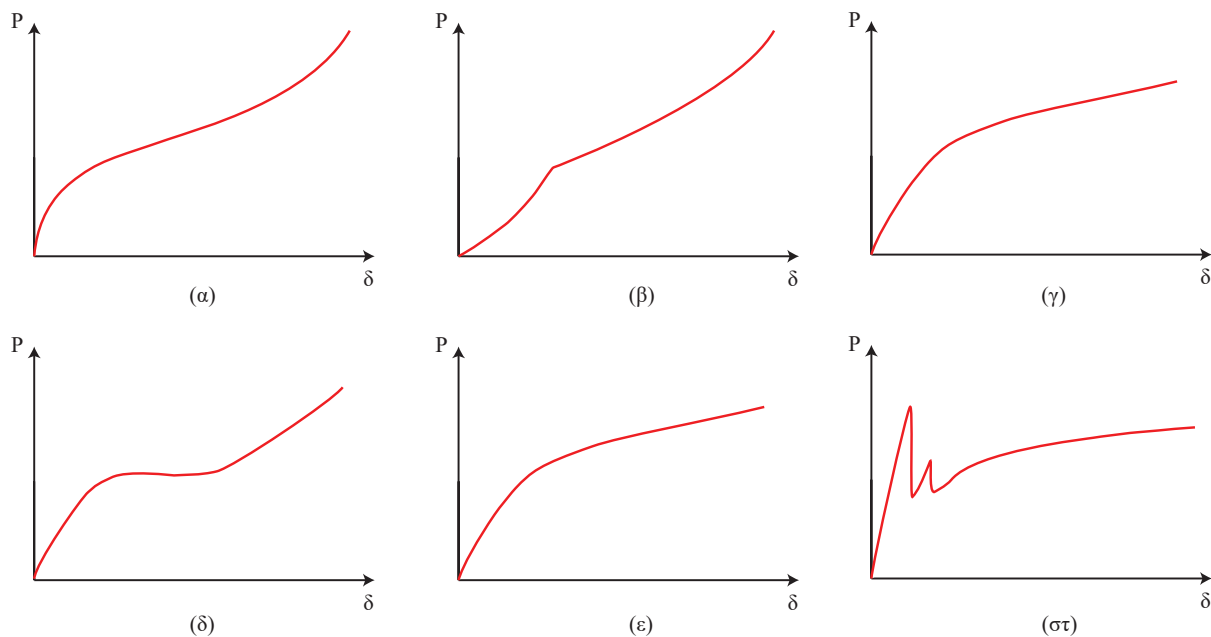
- 1) Να έχουν επαρκή αντοχή, ούτως ώστε να περιορίζονται οι αστοχίες και οι ζημιές υπό φορτία έκρηξης.
- 2) Να μη διαρρηγνύονται, με σκοπό να μη δύναται να εισέλθει το ωστικό κύμα εντός του κτιρίου, προκαλώντας απώλεια ανθρώπινων ζωών και καταστροφές στο εσωτερικό.
- 3) Να διατηρείται η ακεραιότητά τους, υπό την έννοια του να μη μετατρέπονται τα ίδια τα στοιχεία επικάλυψης σε θρυμματισμούς που μπορεί να οδηγήσουν σε τραυματισμούς (π.χ. θρυμματισμοί από το γυαλί ενός υαλοπίνακα).
- 4) Να απορροφούν την ενέργεια της έκρηξης με τρόπο ώστε να μεταφέρονται χαμηλότερες δυνάμεις στον υποκείμενο φορέα (αντικείμενο της διατριβής).

Για την επίτευξη του τέταρτου στόχου, ο τρόπος σχεδιασμού της επικάλυψης μπορεί να διαχωριστεί σε τρεις διακριτούς τύπους:

- Σε συστήματα επικάλυψης που γεφυρώνουν ανοίγματα. Χαρακτηριστικά παραδείγματα τέτοιων περιπτώσεων παρουσιάζονται στις εργασίες των [Xue and Hutchinson \(2004\)](#), [Chen and Hao \(2012\)](#), [Chen and Hao \(2013\)](#), [Hoffmeister et al. \(2015\)](#), [Goel, Matsagar and Gupta \(2011\)](#) και [Sun et al. \(2019\)](#).
- Σε θυσιαζόμενες καλύψεις που συνδέονται απευθείας πάνω στα στοιχεία προς προστασία (π.χ. επί ενός υποστυλώματος). Χαρακτηριστικά παραδείγματα τέτοιων περιπτώσεων παρουσιάζονται στις εργασίες των [Guruprasad and Mukherjee \(2000\)](#), [Alberdi, Przywara and Khandelwal \(2013\)](#) και [Palanivelu et al. \(2011\)](#).
- Σε συστήματα στα οποία η απορρόφηση της ενέργειας πραγματοποιείται στις συνδέσεις των επικαλύψεων. Χαρακτηριστικό παράδειγμα μιας τέτοιας περίπτωσης παρουσιάζεται στην εργασία του [Oswald \(2018\)](#).

Και στις τρεις περιπτώσεις, οι τύποι επικάλυψης μπορούν να χαρακτηριστούν από τις καμπύλες φορτίου–παραμόρφωσής τους, ή αλλιώς από τις καμπύλες αντίστασής τους. Σημειώνεται ότι οι καμπύλες αναφέρονται σε στατική φόρτιση. Παραδείγματα τέτοιων καμπυλών παρουσιάζονται στο Σχήμα 2. Αυτές οι καμπύλες είναι ιδιαίτερα σημαντικές για τη δυνατότητα μείωσης των συνεπειών στον υποκείμενο φορέα, καθώς μέσα από αυτές ρυθμίζονται οι μέγιστες μεταφερόμενες αντιδράσεις στήριξής τους. Όπως παρατηρείται και από το Σχήμα 2, η αντίσταση της επικάλυψης (δηλαδή η ελαστική δυσκαμψία, η

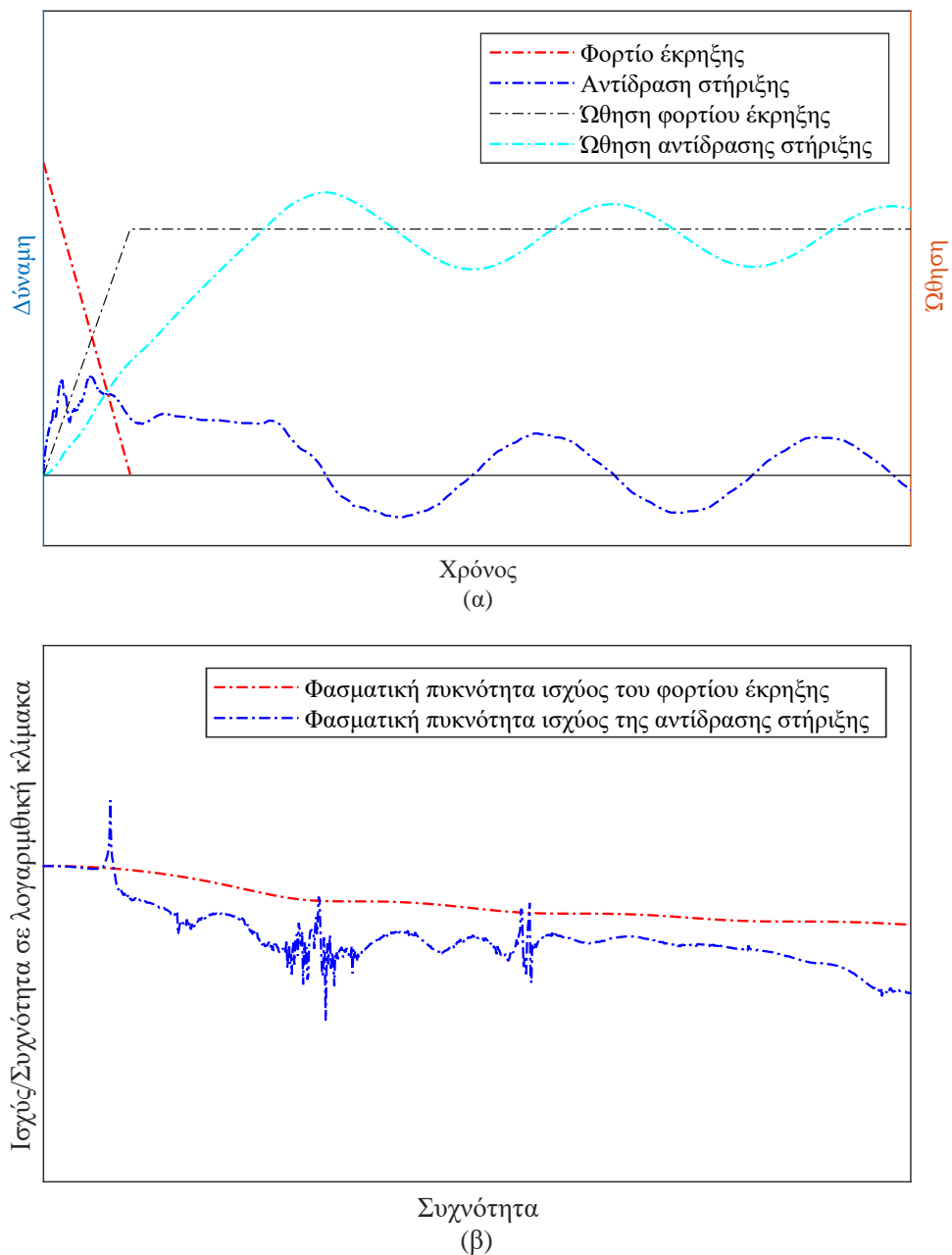
μέγιστη αντοχή και τα μεταλαστικά χαρακτηριστικά) εξαρτώνται τόσο από τις μηχανικές ιδιότητες του υλικού, όσο και από τις συνοριακές συνθήκες.



Σχήμα 2: Τυπικές καμπύλες αντίστασης διαφορετικών τύπων επικάλυψης: (α) Χαλύβδινο σάντουιτς πάνελ με συνθήκες πάκτωσης στα άκρα [δεδομένα από Xue and Hutchinson (2004)], (β) Μονολιθικό χαλύβδινο έλασμα με συνθήκες πάκτωσης στα άκρα [δεδομένα από Xue and Hutchinson (2004)], (γ) Χαλύβδινο σάντουιτς πάνελ με συνθήκες στήριξης που δεν επιτρέπουν μεμβρανική δράση [δεδομένα από Khalifa, Tait and El-Dakhkhni (2017)], (δ) Πάνελ σκυροδέματος με συνθήκες πάκτωσης στα άκρα [δεδομένα από Gouverneur, Caspeepe and Taerwe (2013)], (ε) Πάνελ σκυροδέματος με συνθήκες στήριξης που δεν επιτρέπουν μεμβρανική δράση [δεδομένα από Gouverneur, Caspeepe and Taerwe (2013)]; και (στ) Τρίπλεξ υαλοπίνακας [δεδομένα από Zobec et al. (2015)]

Επιπλέον, το φάσμα φορτίων έκρηξης που μπορούν να επιδράσουν επί μιας επικάλυψης είναι ευρύ, αφού μπορούν να επενεργήσουν διάφοροι συνδυασμοί μέγιστης πίεσης - ώθησης. Ο κάθε συνδυασμός προκαλεί διαφορετικό τρόπο απόκρισης, οδηγώντας σε διαφορετικές αντιδράσεις στήριξης. Κατά συνέπεια, η απόκριση του υποκείμενου φορέα στον οποίο στηρίζεται η επικάλυψη είναι μοναδική και εξαρτάται από: (1) Χαρακτηριστικά της επικάλυψης (αντίδραση, μάζα) και (2) Τη χρονοϊστορία φόρτισης.

Με άλλα λόγια, η επικάλυψη μπορεί να θεωρηθεί ως ένας ταλαντωτής που μετατρέπει τη χρονοϊστορία φόρτισης σε μια διαφορετική χρονοϊστορία δύναμης προς τον υποκείμενο φορέα. Μια χαρακτηριστική περίπτωση αποτελεί το παράδειγμα στο Σχήμα 3 που έχει δημιουργηθεί μέσα από ένα προσομοίωμα πεπερασμένων στοιχείων αμφιέριστης επικάλυψης. Όπως παρατηρείται στο Σχήμα 3(α), η επικάλυψη εισέρχεται στον πλαστικό της κλάδο. Κατά συνέπεια, το αρχικό φορτίο έκρηξης μετατρέπεται από ένα υψηλής τιμής και σύντομης διάρκειας φορτίο σε μια μειωμένης τιμής και αυξημένης διάρκειας πρώτου κύκλου χρονοϊστορία δύναμης, η οποία μετά τον πρώτο κύκλο φέρεται να έχει περίοδο κοινή με την ιδιοπερίοδο της επικάλυψης. Η ώθηση παραμένει ίδια. Μάλιστα, εφαρμόζοντας ταχύ μετασχηματισμό Fourier (Yang, 2009) στις δυο χρονοϊστορίες, προκύπτει το Σχήμα 3(β). Σύμφωνα με αυτό, υπάρχουν συγκεκριμένες ιδιοσυχνότητες στις οποίες το φασματικό περιεχόμενο της αντίδρασης εμφανίζει αιχμές.

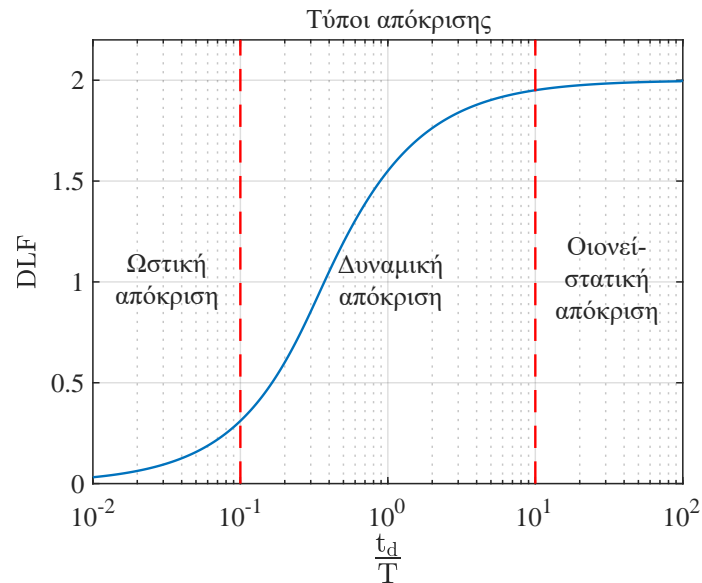


Σχήμα 3: Τυπική περίπτωση απόκρισης επικάλυψης σε έκρηξη: (α) Φορτίο και αντίδραση στήριξης, καθώς και (β) Φασματική ανάλυση του φορτίου και της αντίδρασης στήριξης

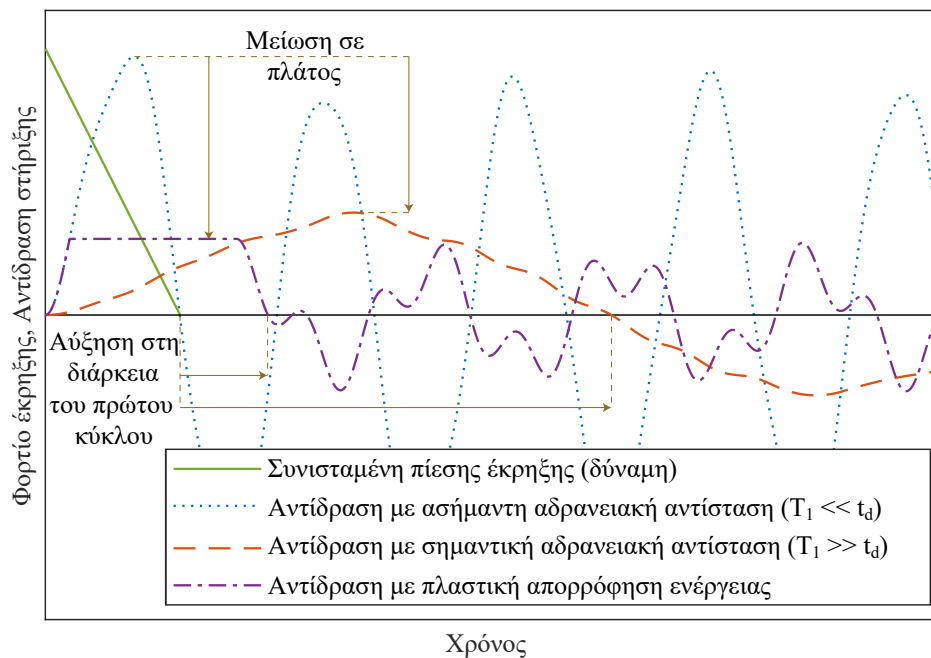
Αυτού του είδους η απόκριση παρατηρείται στις επικαλύψεις με την ενεργοποίηση δύο διαφορετικών μηχανισμών (Rutner and Wright, 2016): (α) Του μηχανισμού πλαστικής απορρόφησης ενέργειας και (β) Του μηχανισμού αδρανειακής αντίστασης. Και με τους δύο μηχανισμούς η τιμή του φορτίου της έκρηξης μειώνεται και η διάρκεια του πρώτου κύκλου αντίδρασης αυξάνεται (Palanivelu et al., 2011; Bornstein and Ackland, 2013). Πιο συγκεκριμένα, ο μηχανισμός πλαστικής απορρόφησης ενέργειας καθορίζεται μέσα από την αντοχή διαρροής της επικάλυψης ενώ ο μηχανισμός αδρανειακής αντίστασης ενεργοποιείται μέσα από τη μάζα και δυσκαμψία της επικάλυψης (αργή απόκριση της επικάλυψης στο φορτίο της έκρηξης).

Σε σχέση με τον μηχανισμό αδρανειακής αντίστασης, η επικάλυψη μπορεί να χαρακτηριστεί από τρεις τύπους απόκρισης, όπως φαίνονται στο Σχήμα 4. Αυτοί οι τύποι διαχωρίζονται μεταξύ τους μέσω του

λόγου της διάρκειας θετικής φάσης της έκρηξης t_d και της ιδιοπεριόδου του στοιχείου T . Θεωρώντας τον συσχετισμό μιας τυχαίας επικάλυψης με αυτούς τους τύπους απόκρισης, μια επικάλυψη με ιδιοπερίοδο T_1 μπορεί να έχει οιονεί-στατική απόκριση με ασήμαντη αδρανειακή αντίσταση, ωστική απόκριση με σημαντική αδρανειακή αντίσταση ή δυναμική απόκριση με μέτρια αδρανειακή αντίσταση. Η διαφορά μεταξύ αυτών των καταστάσεων παρουσιάζεται στο Σχήμα 5, όπου για ασήμαντη αδρανειακή αντίσταση το μέγιστο φορτίο έκρηξης εμφανίζεται αυτούσιο στη χρονοϊστορία της αντίδρασης ενώ για σημαντική αδρανειακή αντίσταση η μέγιστη τιμή αντίδρασης είναι αρκετά χαμηλότερη σε σχέση με το μέγιστο φορτίο έκρηξης.



Σχήμα 4: Τύποι απόκρισης ελαστικού μονοβάθμιου ταλαντωτή έναντι έκρηξης



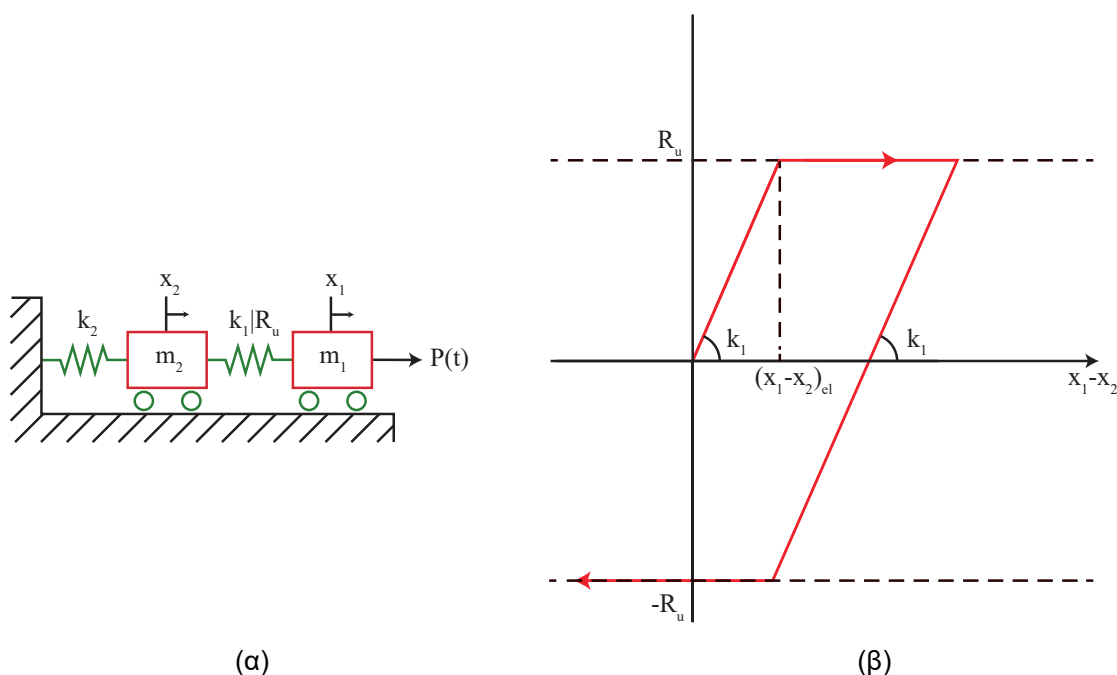
Σχήμα 5: Επίδραση των μηχανισμών αδρανειακής αντίστασης και πλαστικής απορρόφησης ενέργειας στη χρονοϊστορία αντίδρασης επικάλυψης

Σε σχέση με τον μηχανισμό πλαστικής απορρόφησης ενέργειας, η μέγιστη τιμή αντίδρασης της επικάλυψης συσχετίζεται με την αντοχή διαρροής. Αφού η επικάλυψη εισέλθει στη διαρροή, η ενέργεια της έκρηξης μετατρέπεται σε πλαστική ενέργεια παραμορφώσεων και η μέγιστη αντίδραση παραμένει σταθερή μέχρις ότου αρχίσει η ταλάντωση της επικάλυψης, οπότε και η αντίδραση αλλάζει φορά και βαίνει μειούμενη.

B3. Επιρροή της μάζας, δυσκαμψίας, αντοχής και ολκιμότητας της επικάλυψης

Υπάρχει μεγάλη ποικιλία τύπων επικάλυψης που μπορούν να εφαρμοστούν, προκειμένου να επιτευχθεί μείωση των συνεπειών στον υποκείμενο φορέα. Κατά συνέπεια, κρίνεται χρήσιμη η διερεύνηση των βασικών ιδιοτήτων που χρειάζεται να έχουν, ούτως ώστε να οδηγούν στο καλύτερο δυνατό αποτέλεσμα και να προκρίνεται η επιλογή ενός συγκεκριμένου τύπου επικάλυψης έναντι κάποιου άλλου. Σε αυτήν την ενότητα, λοιπόν, αναζητείται η επιρροή της μάζας, δυσκαμψίας, αντοχής και ολκιμότητας της επικάλυψης στην ικανότητά της για μείωση των συνεπειών.

Αυτή η αναζήτηση επιτυγχάνεται με την επιστράτευση ενός διβάθμιου ταλαντωτή, ο οποίος συντίθεται από την επικάλυψη στον πρώτο βαθμό ελευθερίας και από τον υποκείμενο φορέα στον δεύτερο βαθμό ελευθερίας. Το επακριβές μοντέλο παρουσιάζεται στο Σχήμα 6(α). Όπως φαίνεται, η επικάλυψη αναπαρίσταται μέσω της μάζας m_1 , ενώ ο υποκείμενος φορέας αναπαρίσταται μέσω της μάζας m_2 . Μεταξύ τους συνδέονται μέσω ενός μη γραμμικού ελατηρίου που αναπαριστά την ελαστοπλαστική συμπεριφορά της επικάλυψης [Σχήμα 6(β)], έχοντας ελαστική δυσκαμψία k_1 και αντοχή διαρροής R_u . Αντιθέτως, επειδή βασική επιδίωξη αποτελεί ο υποκείμενος φορέας να παραμένει ελαστικός υπό φορτία έκρηξης, ο υποκείμενος φορέας στηρίζεται μέσω ελαστικού ελατηρίου με δυσκαμψία k_2 .



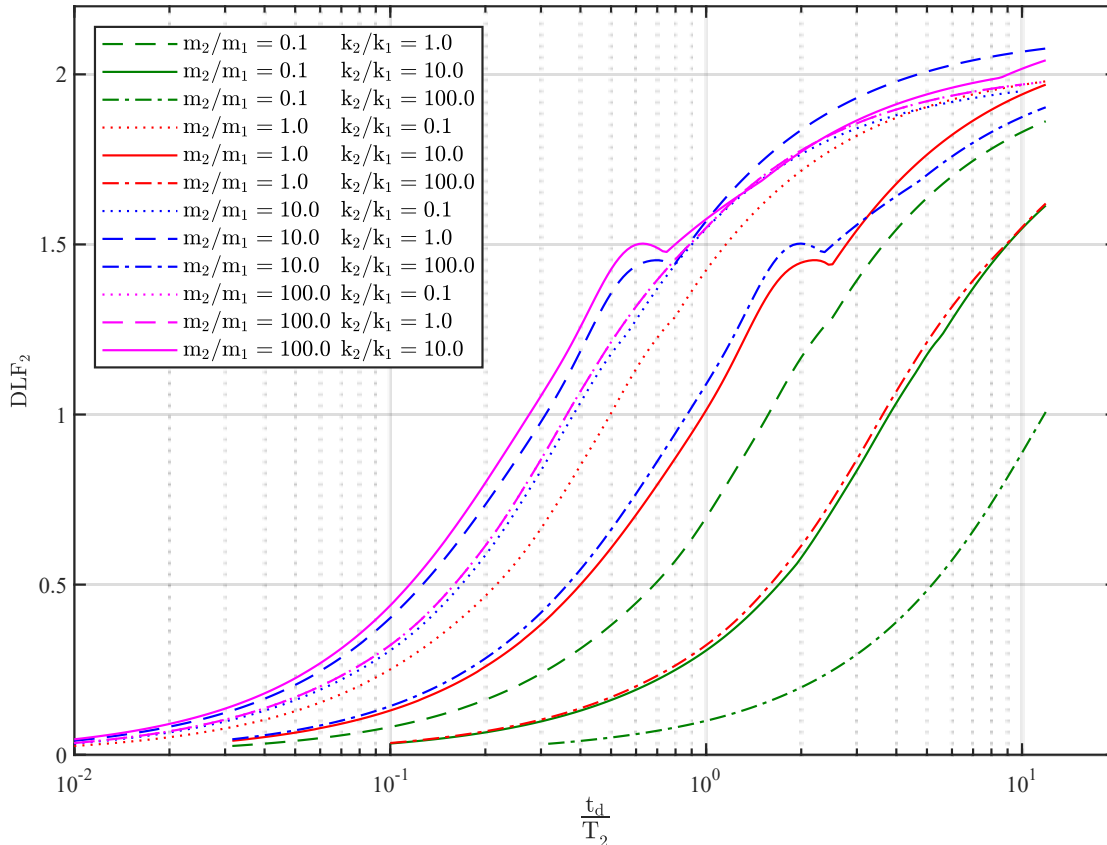
Σχήμα 6: Αναπαράσταση του διβάθμιου ταλαντωτή: (α) Παράμετροι μάζας, δυσκαμψίας, αντοχής διαρροής και μετακίνησης, και (β) Διάγραμμα δύναμης–μετακίνησης του ελατηρίου k_1 μεταξύ των δύο βαθμών ελευθερίας

Οι εξισώσεις κίνησης του διβάθμιου ταλαντωτή είναι αδιάστατες, ούτως ώστε τα αποτελέσματα και συμπεράσματα να ανταποκρίνονται σε όλους τους πιθανούς συνδυασμούς επικάλυψης και υποκείμενου

φορέα. Πιο συγκεκριμένα, ο χρόνος αδιαστατοποιείται μέσω του λόγου της διάρκειας του φορτίου της έκρηξης t_d προς την ιδιοπερίοδο T_2 του υποκείμενου φορέα, η οποία υπολογίζεται ως να ήταν ο δεύτερος βαθμός ελευθερίας απομονωμένος. Ενώ, το πλάτος της απόκρισης αδιαστατοποιείται μέσω της στατικής μετακίνησης, η οποία προκύπτει από τον λόγο της μέγιστης πίεσης P_0 προς τη δυσκαμψία k_2 . Σημειώνεται ότι η μέγιστη μετακίνηση του υποκείμενου φορέα προς τον λόγο P_0/k_2 ισούται με την παράμετρο DLF_2 , η οποία συνδέεται άρρηκτα με το αντικείμενο της διατριβής. Όσο μικρότερη είναι η παράμετρος DLF_2 , τόσο μικρότερη η μέγιστη μετακίνηση του υποκείμενου φορέα και, άρα, τόσο καλύτερη η συμπεριφορά της επικάλυψης.

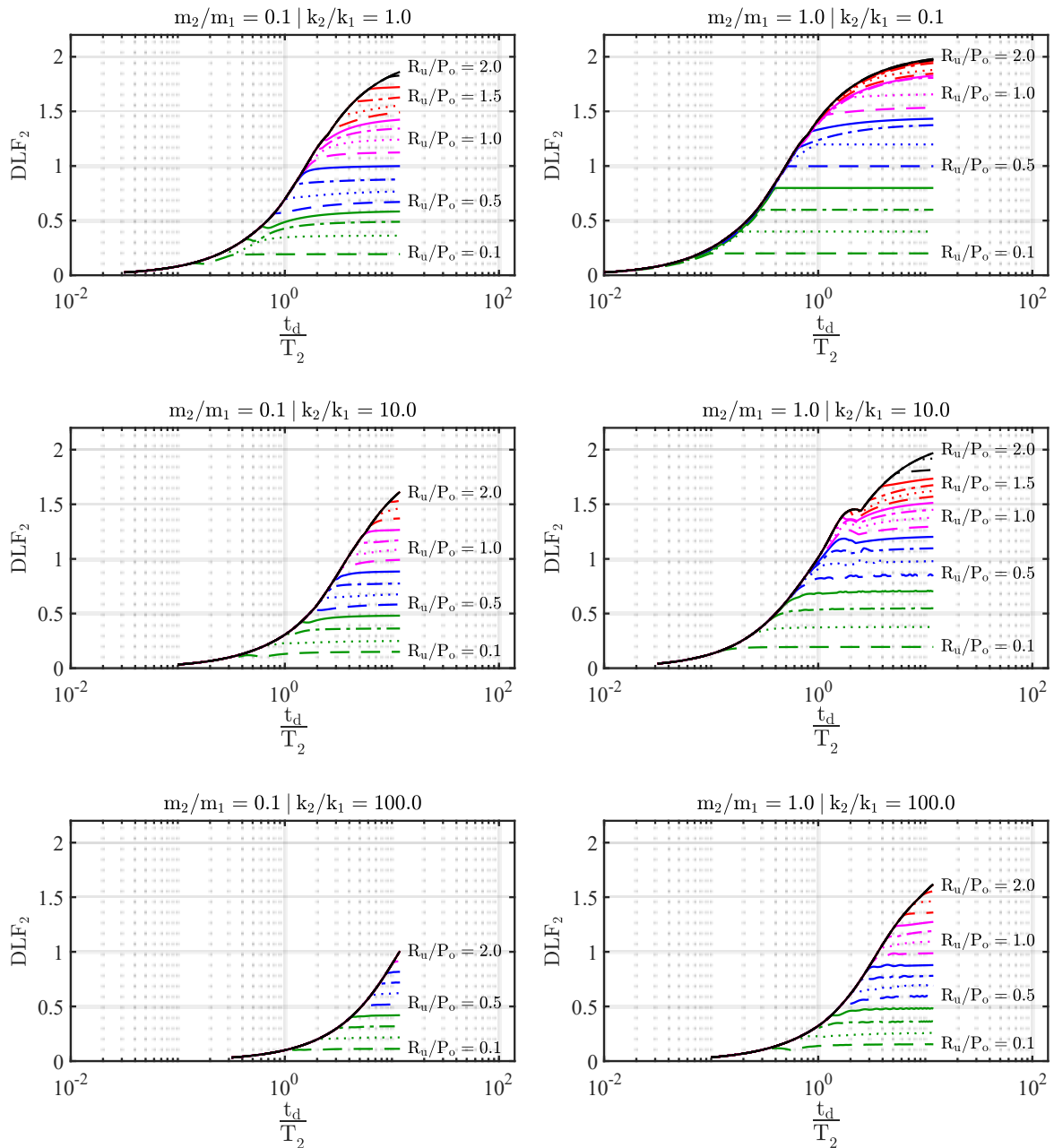
Ως αποτέλεσμα των διαφόρων μετασχηματισμών στις εξισώσεις κίνησης, οι παράμετροι αδιαστατοποίησης είναι οι λόγοι m_2/m_1 , k_2/k_1 , t_d/T_2 και R_u/P_0 . Βάσει αυτών των παραμέτρων, μπορεί να προσδιοριστεί μοναδικά η τιμή DLF_2 του υποκείμενου φορέα. Δεδομένου ότι στον οριζόντιο άξονα βρίσκεται η ιδιοπερίοδος T_2 που προκύπτει από τις παραμέτρους m_2 και k_2 , οι λόγοι μαζών και δυσκαμψιών μέσα σε κάθε διάγραμμα μπορούν χρησιμοποιηθούν μόνο για την εξέταση του τρόπου επιρροής της επικάλυψης (m_1, k_1), θεωρώντας σταθερές τις παραμέτρους του υποκείμενου φορέα (m_2, k_2).

Στην προκειμένη περίπτωση, το Σχήμα 7 μπορεί να χρησιμοποιηθεί για την εξέταση του τρόπου επιρροής της μάζας και της δυσκαμψίας της επικάλυψης στον υποκείμενο φορέα (μηχανισμός αδρανειακής αντίστασης). Οι διάφορες καμπύλες έχουν προκύψει για λόγο αντοχής $R_u/P_0 = 2$, κατά τον οποίο εμφανίζεται ελαστική συμπεριφορά στην επικάλυψη. Όπως παρουσιάζεται, όσο χαμηλότερη είναι η δυσκαμψία και όσο υψηλότερη η μάζα της επικάλυψης, τόσο χαμηλότερη είναι η τιμή του DLF_2 . Επιπλέον, η συμπεριφορά αυτή εμφανίζεται σε όλο το φάσμα τιμών t_d/T_2 , δηλαδή σε όλους τύπους απόκρισης (ω -στική, δυναμική και οωνει-στατική απόκριση) του υποκείμενου φορέα.



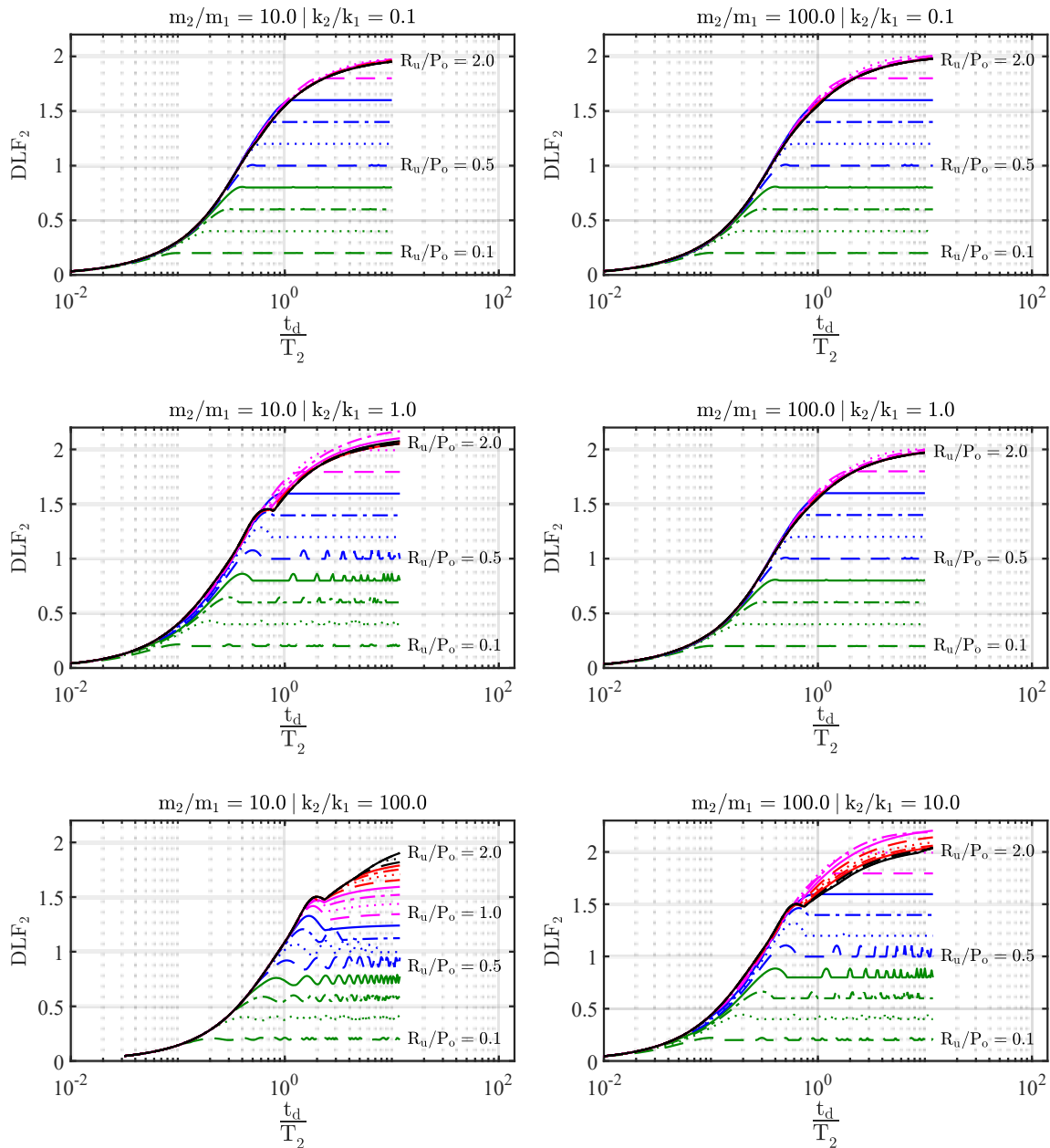
Σχήμα 7: DLF_2 του υποκείμενου φορέα για διάφορους λόγους μαζών και δυσκαμψιών στην περίπτωση λόγου αντοχής $R_u/P_0 = 2$

Το Σχήμα 8 και το Σχήμα 9 μπορούν να χρησιμοποιηθούν για την εξέταση του τρόπου επιρροής της αντοχής (μηχανισμός πλαστικής απορρόφησης ενέργειας). Θεωρώντας σταθερή τη μέγιστη πίεση P_o των φορτίων έκρηξης, παρατηρείται ότι στη ζώνη ωστικής απόκρισης δεν υπάρχει κάποια διαφοροποίηση, παρά μόνο για εξαιρετικά χαμηλές τιμές αντοχής. Αντιθέτως, στη ζώνη δυναμικής απόκρισης και, κυρίως, στη ζώνη οιονεί-στατικής απόκρισης παρατηρείται σημαντική απομείωση του DLF_2 , ανάλογη με το πόσο χαμηλή είναι η αντοχή. Ενώ, η ευνοϊκή συμπεριφορά της επικάλυψης εμφανίζεται μέσω σχεδόν οριζώντιων γραμμών.



Σχήμα 8: DLF_2 του υποκείμενου φορέα για λόγο μαζών $m_2/m_1 = 0.1, 1.0$, για λόγους αντοχής $R_u/P_o = 0.1 - 2.0$ (η μαύρη γραμμή αναπαριστά την καμπύλη $R_u/P_o = 2.0$) και διάφορους λόγους δυσκαμψιών k_2/k_1

Αυτή η συμπεριφορά υπάρχει σε όλους τους πιθανούς λόγους δυσκαμψιών και μαζών. Επιπλέον, για σταθερή πίεση και μεταβαλλόμενη ώθηση, μέσω αύξησης της διάρκειας του φορτίου t_d , παρατηρείται ότι αρχικά δεν υπάρχει κάποια διαφοροποίηση. Στην πορεία, και όσο αυξάνεται η ώθηση, η επικάλυψη εισέρχεται στον πλαστικό της κλάδο και αρχίζει να έχει ευνοϊκή συμπεριφορά για τον υποκείμενο φορέα.

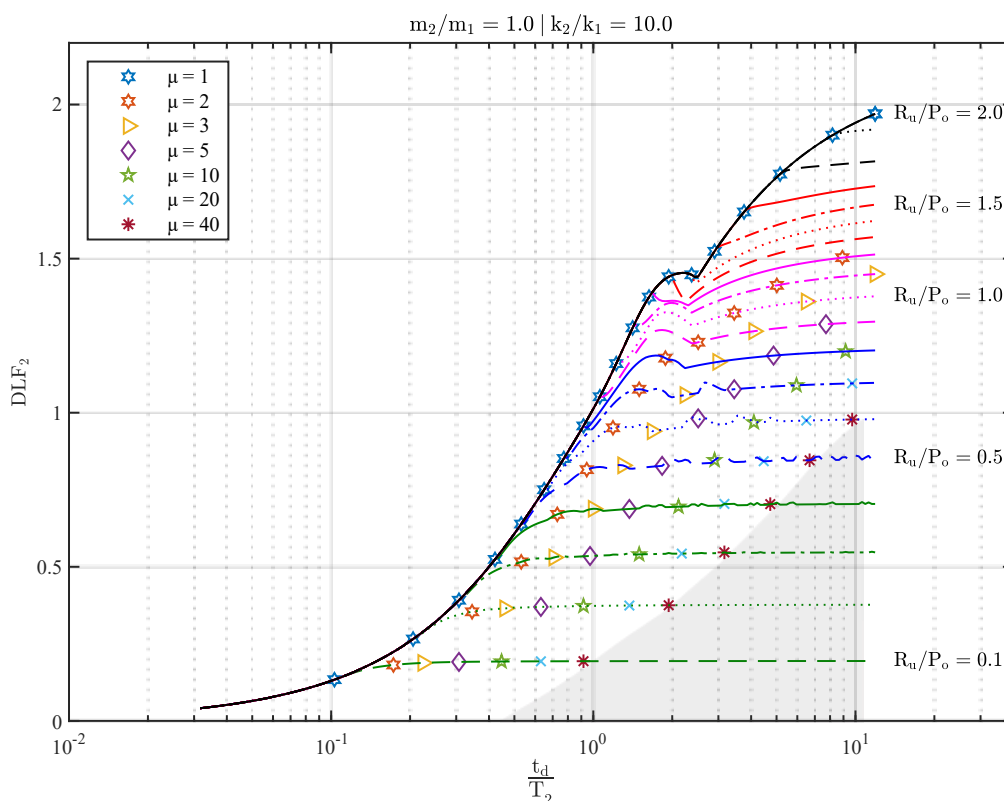


Σχήμα 9: DLF_2 του υποκείμενου φορέα για λόγο μαζών $m_2/m_1 = 10.0, 100.0$, για λόγους αντοχής $R_u/P_o = 0.1 - 2.0$ (η μαύρη γραμμή αναπαριστά την καμπύλη $R_u/P_o = 2.0$) και διάφορους λόγους δυσκαμψιών k_2/k_1

Ωστόσο, όπως φαίνεται στο Σχήμα 10 για τυχαίους λόγους μαζών και δυσκαμψιών, με την αύξηση της ώθησης και αφού έχει εισέλθει η επικάλυψη στον πλαστικό της κλάδο, εξαντλείται η ολκιμότητά της και προκαλούνται μεγάλες μετακινήσεις. Μάλιστα, φέρεται να υπάρχει ομαλή κατανομή της επιτευχθείσας

ολκιμότητας. Ως εκ τούτου, υπάρχει μια περιοχή (η οποία έχει αναπαρασταθεί με γκρι χρώμα) που είναι ανενεργή.

Στην ουσία, σε αυτήν την περιοχή δε μπορεί να εισέλθει με ευκολία η επικάλυψη καθώς απαιτείται δυνατότητα για εξαιρετικά όλκιμη συμπεριφορά και υψηλές επιτρεπόμενες μετακινήσεις. Κατά συνέπεια, η ζώνη λειτουργίας του μηχανισμού πλαστικής απορρόφησης ενέργειας βρίσκεται ανάμεσα στην άνω-αριστερά καμπύλη $R_{u1}/P_o = 2.0$, η οποία συσχετίζεται με τον μηχανισμό αδρανειακής αντίστασης [Σχήμα 7], και στην κάτω-δεξιά καμπύλη που αντιστοιχεί στη μέγιστη ολκιμότητα, η οποία δύναται να εμφανιστεί στην επικάλυψη.

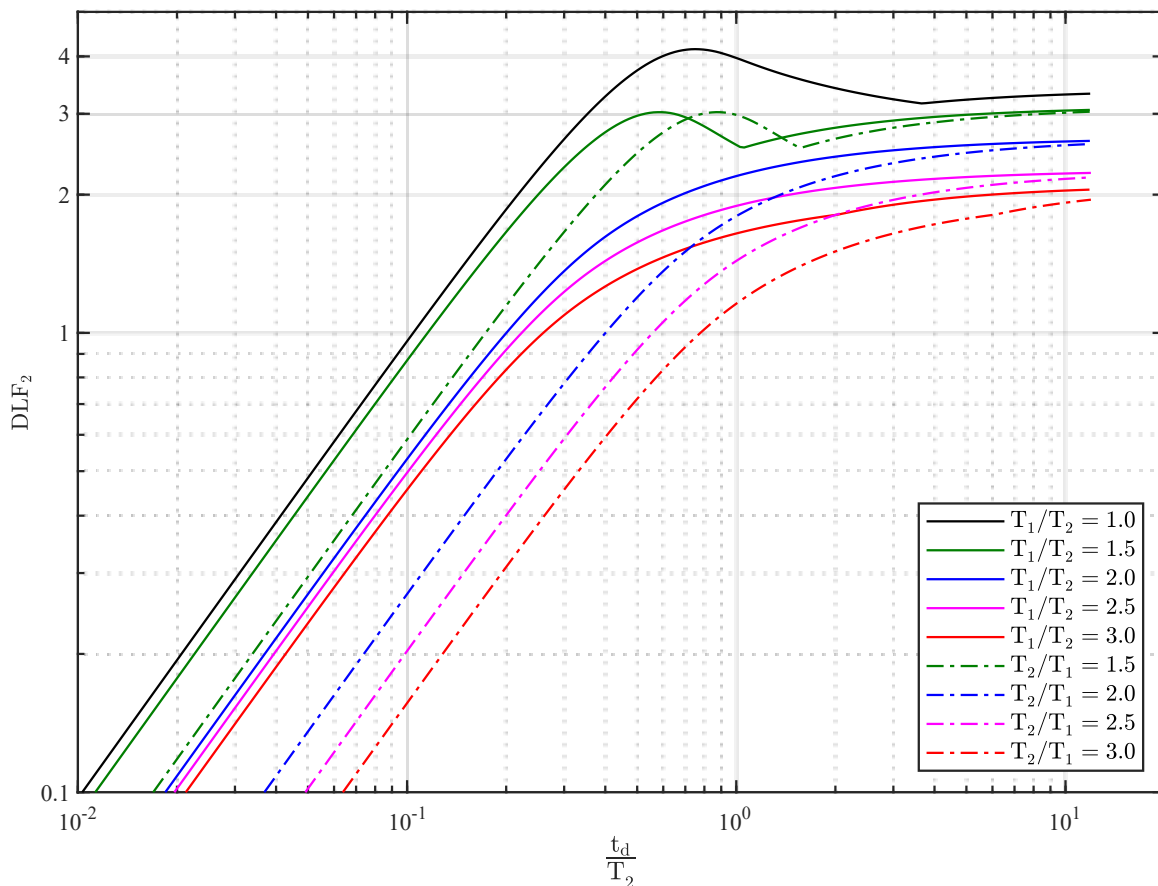


Σχήμα 10: Ολκιμότητα της επικάλυψης για λόγους $m_2/m_1 = 1.0$, $k_2/k_1 = 10.0$ και $R_{u1}/P_o = 0.1 - 2.0$

Επιπροσθέτως, και δεδομένου ότι οι δύο βαθμοί ελευθερίας είναι συζευγμένοι σε έναν διβάθμιο ταλαντωτή, δίνεται η δυνατότητα να διερευνηθούν οι περιοχές στις οποίες μπορεί να εμφανιστεί συντονισμός στο σύστημα επικάλυψης και υποκείμενου φορέα, καθώς και το πώς επηρεάζεται ο υποκείμενος φορέας στο ενδεχόμενο συντονισμού.

Σε αυτήν την κατεύθυνση, ο βασικός παράγοντας που φέρεται να παίζει σημαντικό ρόλο στον συντονισμό είναι ο λόγος ιδιοπεριόδων της επικάλυψης T_1 και του υποκείμενου φορέα T_2 . Σημειώνεται ότι οι ιδιοπεριόδοι υπολογίζονται στον εκάστοτε βαθμό ελευθερίας, σαν να είναι ανεξάρτητοι και όχι σαν κομμάτι ενός συζευγμένου συστήματος.

Όπως φαίνεται στο Σχήμα 11, σε περίπτωση που οι ιδιοπεριόδοι είναι ίσες, προκύπτει η μέγιστη τιμή του DLF_2 . Σημαντικός συντονισμός προκαλείται, επίσης, για λόγους ιδιοπεριόδων μέχρι και 2.5, ενώ για μεγαλύτερες τιμές δεν εμφανίζεται συντονισμός. Οπότε, λόγοι ιδιοπεριόδων μικρότεροι του 2.5 πρέπει να αποφεύγονται, για να εμφανίζονται όσο γίνεται χαμηλότερες μετακινήσεις τόσο στον υποκείμενο φορέα, όσο και στην επικάλυψη.

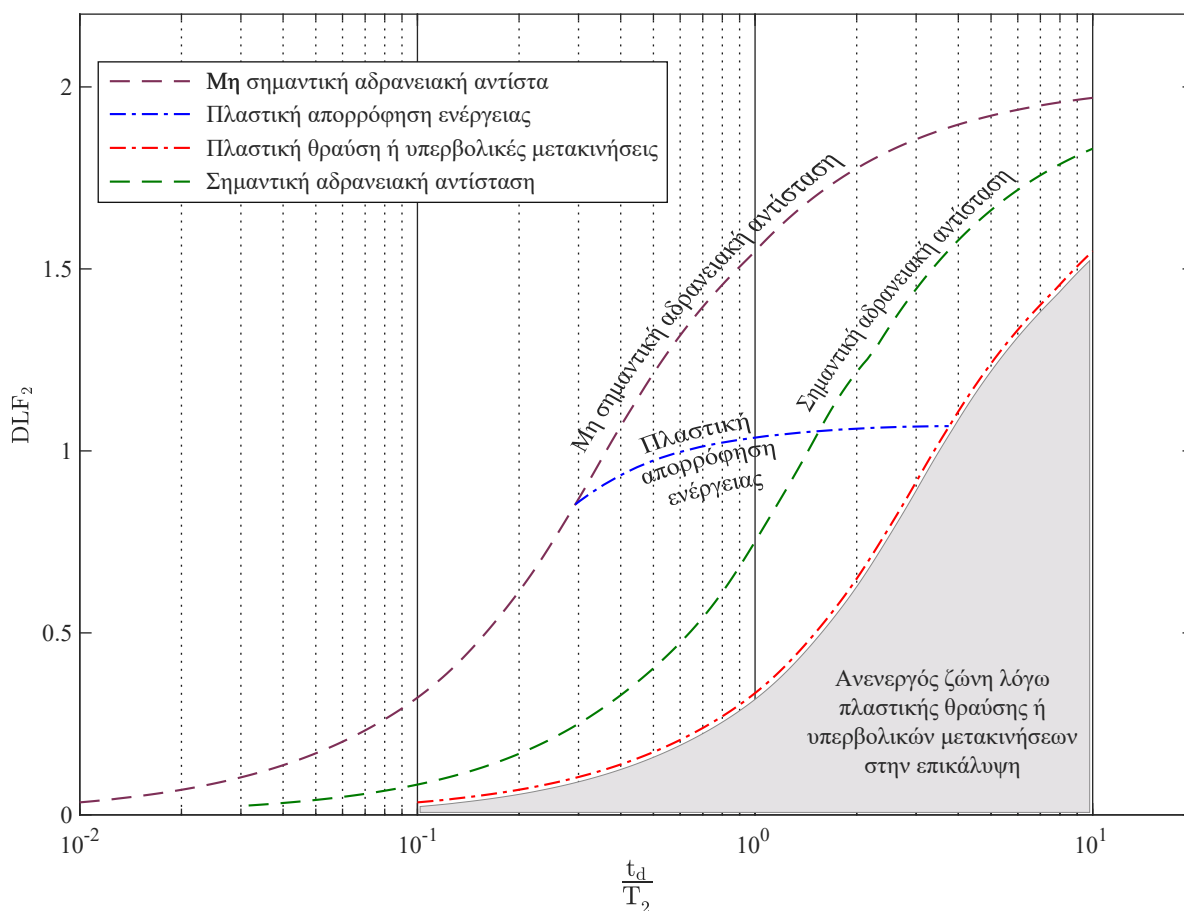


Σχήμα 11: Καμπύλες $R_u/P_o = 2$ όταν η επικάλυψη και ο υποκείμενος φορέας βρίσκονται σε συντονισμό

Οι προαναφερθείσες παρατηρήσεις συνοψίζονται στο Σχήμα 12, σημειώνοντας τις διάφορες ζώνες ενεργοποίησης των μηχανισμών αδρανειακής αντίστασης και πλαστικής απορρόφησης ενέργειας, καθώς και τα συνακόλουθα όριά τους. Συμπερασματικά, προκύπτουν τα εξής:

- Ο μηχανισμός αδρανειακής αντίστασης είναι ενεργός σε όλο το φάσμα των λόγων t_d/T_2 , ενώ ο μηχανισμός πλαστικής απορρόφησης ενέργειας είναι ενεργός κυρίως στη ζώνη δυναμικής και οιωνεί-στατικής απόκρισης.
- Για την ενεργοποίηση του μηχανισμού πλαστικής απορρόφησης ενέργειας απαιτείται όλκιμη επικάλυψη, ενώ για την ενεργοποίηση του μηχανισμού αδρανειακής αντίστασης απαιτείται χαμηλή ιδιοπερίοδος στην επικάλυψη, δηλαδή επικάλυψη είτε με αυξημένη μάζα είτε με μειωμένη δυσκαμψία.
- Οι δύο μηχανισμοί μπορούν να χρησιμοποιηθούν είτε ανεξάρτητα ο ένας από τον άλλο, είτε σε συνδυασμό μεταξύ τους. Για να επιτευχθεί αυτό, απαιτείται τόσο χαμηλή ιδιοπερίοδος όσο και χαμηλή αντοχή και υψηλή ολκιμότητα στην επικάλυψη.
- Ο μηχανισμός αδρανειακής αντίστασης εμφανίζεται σε όλους τους πιθανούς συνδυασμούς μέγιστης πίεσης και ώθησης. Αντιθέτως, ο μηχανισμός πλαστικής απορρόφησης ενέργειας εμφανίζεται για συγκεκριμένους συνδυασμούς, οπότε απαιτείται η εκ των προτέρων εκτίμηση της μέγιστης πίεσης και ώθησης.
- Γενικότερα, επιδιώκεται υψηλή μάζα, χαμηλή δυσκαμψία, χαμηλή αντοχή και υψηλή ολκιμότητα στην επικάλυψη, ούτως ώστε να υπάρχει βέλτιστη λειτουργία για τον υποκείμενο φορέα. Τα τρία από τα τέσσερα αυτά χαρακτηριστικά, δηλαδή η υψηλή μάζα, η χαμηλή δυσκαμψία και η χαμηλή

αντοχή, γενικά δεν επιλέγονται στην πράξη αφού αυξάνουν τα βάρη και τις σεισμικές δυνάμεις, αυξάνουν τις μετακινήσεις και μειώνουν την ασφάλεια, αντιστοίχως.

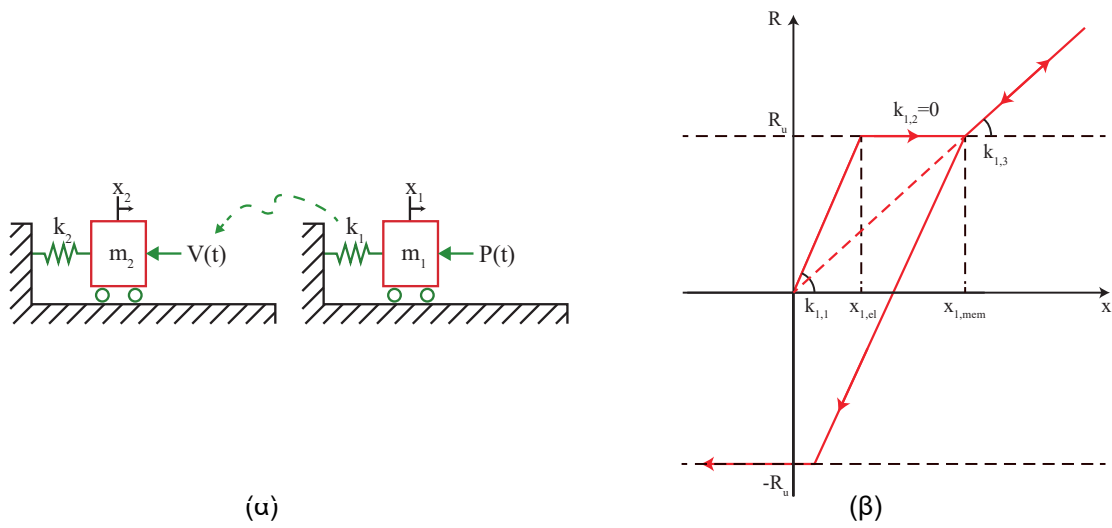


Σχήμα 12: Όρια και ζώνες ενεργοποίησης των μηχανισμών πλαστικής απορρόφησης ενέργειας και αδρανειακής αντίστασης

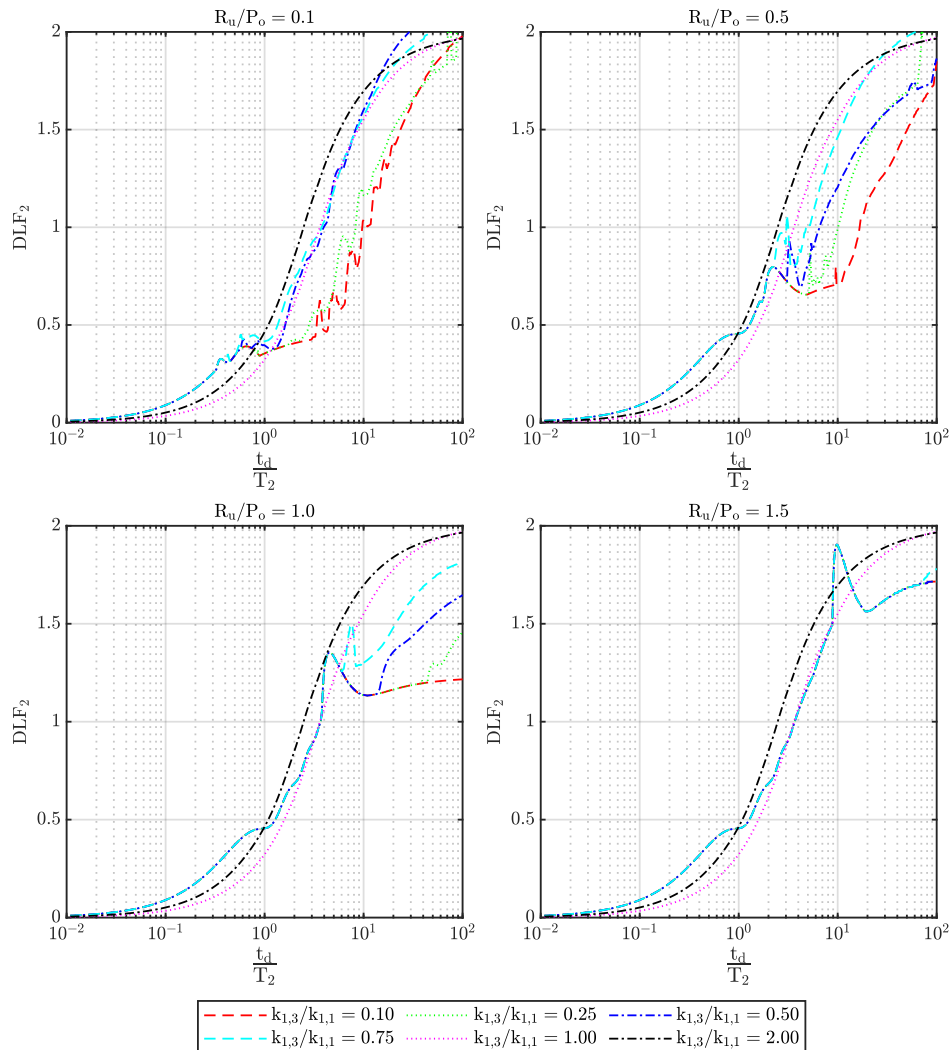
B4. Επιρροή της μεμβρανικής δράσης της επικάλυψης

Στην περίπτωση του τύπου επικάλυψης ο οποίος χρησιμοποιείται για τη γεφύρωση ανοιγμάτων, στο διάγραμμα δύναμης–μετακίνησης αρχικά επενεργεί ελαστικά η καμπτική δυσκαμψία της επικάλυψης, στην πορεία εμφανίζεται ο οριζόντιος πλαστικός κλάδος και, τέλος, υπεισέρχεται η μεμβρανική δυσκαμψία της επικάλυψης. Αυτό συμβαίνει όταν οι συνοριακές συνθήκες έχουν διαμορφωθεί με τέτοιο τρόπο ώστε να επιτρέπουν την ανάπτυξη μεμβρανικής δράσης. Ο τρόπος επιρροής της μεμβρανικής δράσης στον υποκείμενο φορέα αναζητείται στην παρούσα ενότητα.

Για την εξέταση της επιρροής, εφαρμόζεται ανάλυση δύο βημάτων με τη χρήση μονοβάθμιων ταλαντωτών. Η ανάλυση είναι αδιαστατοποιημένη, προκειμένου να έχει γενική εφαρμογή σε όλους τους πιθανούς συνδυασμούς επικάλυψης και υποκείμενου φορέα. Μέσα από την αδιαστατοποίηση, προκύπτουν πέντε παράμετροι που καθορίζουν μοναδικά το αποτέλεσμα σύμφωνα με τις εξισώσεις κίνησης. Οι τέσσερις εκ των πέντε είναι οι ίδιες παράμετροι με την προηγούμενη ενότητα, ενώ η επιπλέον παράμετρος είναι ο λόγος μεμβρανικής δυσκαμψίας $k_{1,3}/k_{1,1}$. Το μοντέλο που χρησιμοποιείται παρουσιάζεται στο Σχήμα 13, ενώ τα σχετικά αποτελέσματα για συγκεκριμένες τιμές στις παραμέτρους εμφανίζονται στο Σχήμα 14.



Σχήμα 13: Μοντέλο για την εξέταση επιρροής του μεμβρανικής δράσης: (α) Ανάλυση δύο βημάτων με τη χρήση μονοβάθμιων ταλαντωτών και (β) Μη γραμμικό ελατήριο k_1



Σχήμα 14: DLF_2 του υποκείμενου φορέα για λόγο μαζών $m_2/m_1 = 0.1$, λόγο δυσκαμψιών $k_2/k_{1,1} = 10.0$, και διάφορους λόγους μεμβρανικής δυσκαμψίας ($k_{1,3}/k_{1,1} = 0.10, 0.25, 0.50, 0.75, 1.00, 2.00$) στους λόγους αντοχής $R_u/P_o = 0.1, 0.5, 1.0, 1.5$

Το Σχήμα 14 είναι σε συμφωνία με τα σχήματα της προηγούμενης ενότητας και οδηγεί σε κοινά συμπεράσματα. Επιπλέον σε αυτά, παρατηρείται ότι σε περίπτωση που υπάρχει σημαντική μεμβρανική δράση, επί της ουσίας απενεργοποιείται η ευμενής επιρροή της πλαστικής απορρόφησης ενέργειας. Από τη μία υπάρχουν πλαστικές παραμορφώσεις αλλά από την άλλη η αντίσταση και οι αντίστοιχες αντιδράσεις βαίνουν αυξανόμενες λόγω μεμβρανικής δράσης.

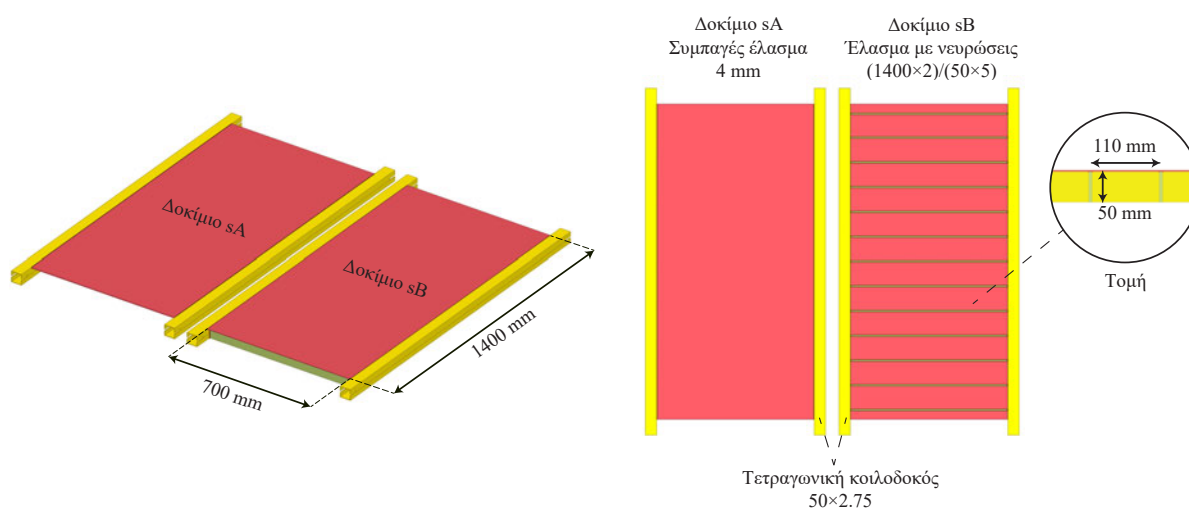
Αντιθέτως, όταν η μεμβρανική δράση δεν είναι σημαντική, τότε παρατηρείται ευμενής επιρροή στον υποκείμενο φορέα. Διατηρώντας σταθερή τη μέγιστη πίεση και αυξάνοντας την ώθηση (μέσω αύξησης της διάρκειας της έκρηξης), αρχικά η τιμή του DLF_2 ορίζεται μέσα από τον μηχανισμό αδρανειακής αντίστασης. Με περαιτέρω αύξηση της ώθησης, η επικάλυψη εισέρχεται στον πλαστικό της κλάδο (καμπτική συμπεριφορά) και οι αντιδράσεις μεταφέρονται μειωμένες στον υποκείμενο φορέα. Αλλά, τέλος, σε περαιτέρω αύξηση της ώθησης, η τιμή του DLF_2 αρχίζει να αυξάνεται λόγω της μεμβρανικής δράσης.

Κατά συνέπεια, πέρα από την πλαστική θραύση και τις υπερβολικές μετακινήσεις, η μεμβρανική δράση αποτελεί ένα επιπλέον όριο για τη ζώνη ενεργοποίησης του μηχανισμού πλαστικής απορρόφησης ενέργειας. Σε κάθε περίπτωση το βασικό συμπέρασμα είναι ότι η μεμβρανική δράση θα πρέπει να αποφεύγεται ή/και να χρησιμοποιείται μόνο για την παροχή επιπλέον ασφάλειας στην αντοχή της επικάλυψης.

B5. Πειραματική διερεύνηση μεταλλικής επικάλυψης σε έκρηξη

Τα συμπεράσματα των προηγούμενων ενότητων επιβεβαιώθηκαν μερικώς μέσα από την πειραματική διερεύνηση δύο συστημάτων επικάλυψης και υποκείμενου φορέα. Πιο συγκεκριμένα, θεωρήθηκαν οι τύποι επικάλυψης που παρουσιάζονται στο Σχήμα 15, δηλαδή ένα συμπαγές μεταλλικό έλασμα πάχους 4 mm και ένα έλασμα πάχους 2 mm με νευρώσεις των 5 mm. Αυτοί οι δύο τύποι συγκρίθηκαν μεταξύ τους ως προς τον τρόπο που επηρεάζουν τον υποκείμενο φορέα, δηλαδή τις μηκίδες που είναι διατομής τετραγωνικής κοιλοδοκού 50 mm × 2.75 mm.

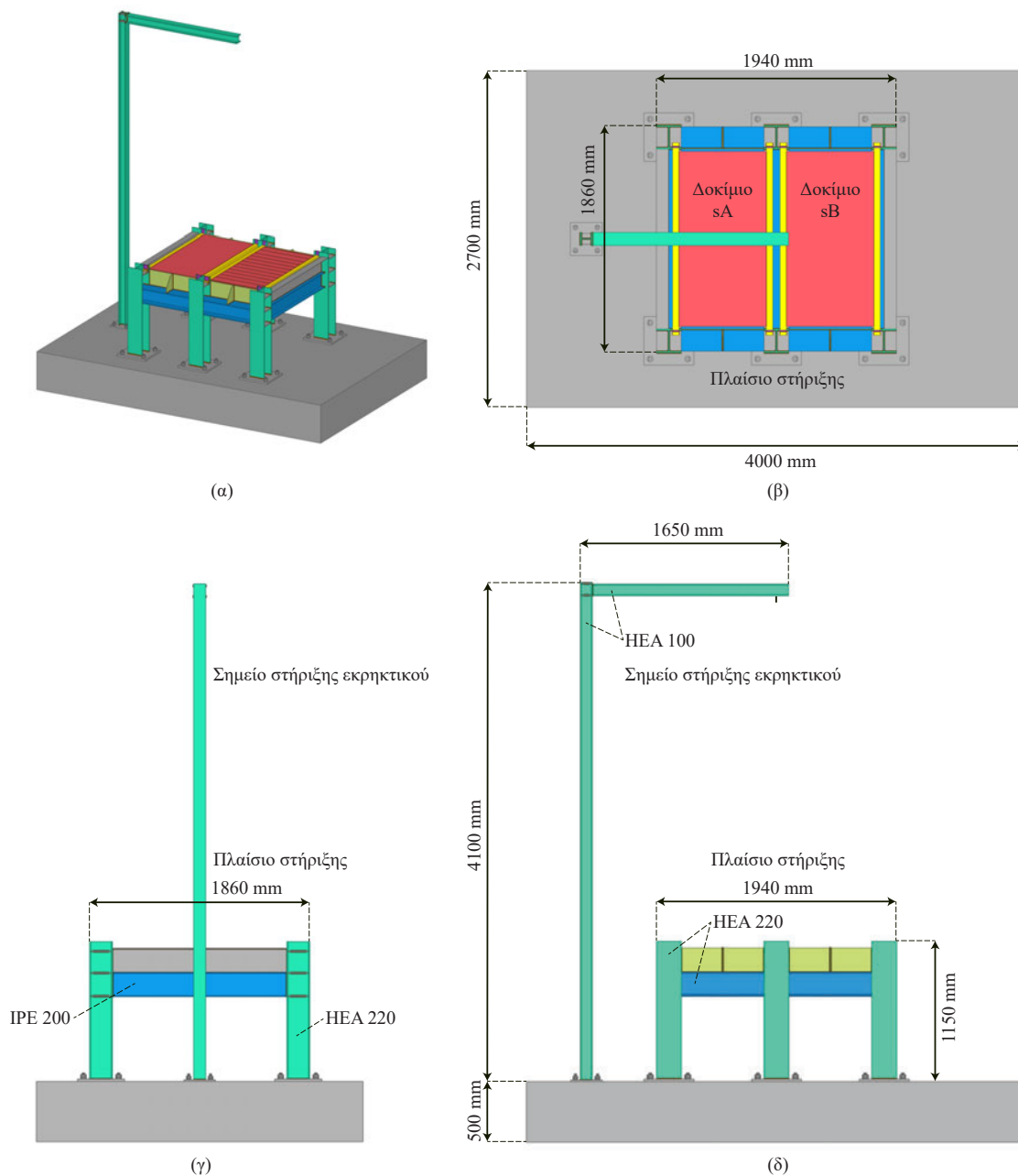
Η ουσιαστική διαφορά μεταξύ των δύο τύπων είναι το γεγονός ότι στο συμπαγές έλασμα εμφανίστηκε χαμηλής δυσκαμψίας μεμβρανική δράση, ενώ στο έλασμα με νευρώσεις εμφανίστηκε ισχυρή καμπτική δυσκαμψία με πλαστικό κλάδο. Σημειώνεται ότι οι δύο τύποι επικάλυψης είχαν περίπου ίση μάζα. Επομένως, ο τρόπος απόκρισης αυτών των δύο τύπων έχουν άμεση συσχέτιση με τις προηγούμενες ενότητες και, ιδιαίτερα, με τα συμπεράσματα όσον αφορά στον τρόπο επιρροής της καμπτικής δυσκαμψίας και της μεμβρανικής δυσκαμψίας της επικάλυψης.



Σχήμα 15: Όψη δοκιμίων sA και sB

Για τη διεξαγωγή του πειράματος κατασκευάστηκε η πειραματική διάταξη που εμφανίζεται στο Σχήμα 16. Σχεδιάστηκαν ένας πολύστηλος μεταλλικός φορέας και μια παχιά βάση σπλισμένου σκυροδέματος με τρόπο τέτοιο, ώστε να είναι άκαμπτα και να παραμένουν ελαστικά υπό τα φορτία της έκρηξης. Αυτές οι σχεδιαστικές επιλογές έγιναν προκειμένου να μην επηρεάζεται το σύστημα επικάλυψης και υποκείμενου φορέα, αλλά και για να είναι επαναχρησιμοποιούμενη η πειραματική διάταξη.

Το εκρηκτικό τοποθετήθηκε στην κορυφή του Γ, η οποία ήταν τοποθετημένη συμμετρικά σε κάτωψη, όσον αφορά στους δύο τύπους επικάλυψης. Επιπλέον, όπως αναφέρθηκε ήδη, ο υποκείμενος φορέας (οι μηκίδες) είχαν κοινή διατομή. Οπότε, τόσο το φορτίο (λόγω συμμετρίας) όσο και η γεωμετρία του υποκείμενου φορέα (λόγω κοινών διατομών) ήταν κοινά μεταξύ των δύο συστημάτων επικάλυψης και υποκείμενου φορέα. Το μόνο που διέφερε ήταν η γεωμετρία των ίδιων των τύπων επικάλυψης.



Σχήμα 16: Όψεις πειραματικής διάταξης: (α) 3D όψη, (β) Κάτοψη, (γ) Μπροστινή όψη και (δ) Πλευρική όψη

Το εκρηκτικό βάρους 2.495 kg TNT (5.5 lb) τοποθετήθηκε σε απόσταση 2 m από την άνω παρειά των επικαλύψεων και αποτελούνταν από πέντε συσκευασίες TNT μίας λίβρας, καθώς και μία συσκευασία μισής λίβρας, όπως φαίνεται στο Σχήμα 17. Η περίμετρος της πειραματικής κλείστηκε με σακιά άμμου, προκειμένου να μη μπορεί να εισέλθει το ωστικό κύμα στην κάτω πλευρά της πειραματικής διάταξης και, άρα, να μην επηρεάζει τις επικαλύψεις από την κάτω πλευρά τους.



(α)



(β)

Σχήμα 17: Φωτογραφίες πειραματικής διάταξης: (α) Εκρηκτικό και (β) Πειραματική διάταξη με σακιά άμμου στην περίμετρο

Η έκρηξη [Σχήμα 18(α)] δημιούργησε μια στιγμιαία μπάλα φωτιάς. Πραγματοποιήθηκαν δύο διαφορετικά είδη μετρήσεων. Το ένα αφορούσε τη μέγιστη μετακίνηση της επικάλυψης και του υποκείμενου φορέα, ενώ το άλλο αφορούσε την παραμένουσα μετακίνησή τους. Η μέτρηση της μέγιστης μετακίνησης επετεύχθη με διατάξεις μορφής χτένας [Σχήμα 18(β)] ενώ η μέτρηση της παραμένουσας μετακίνησης έγινε με χρήση μετρητικού laser μετά την έκρηξη.



(α)

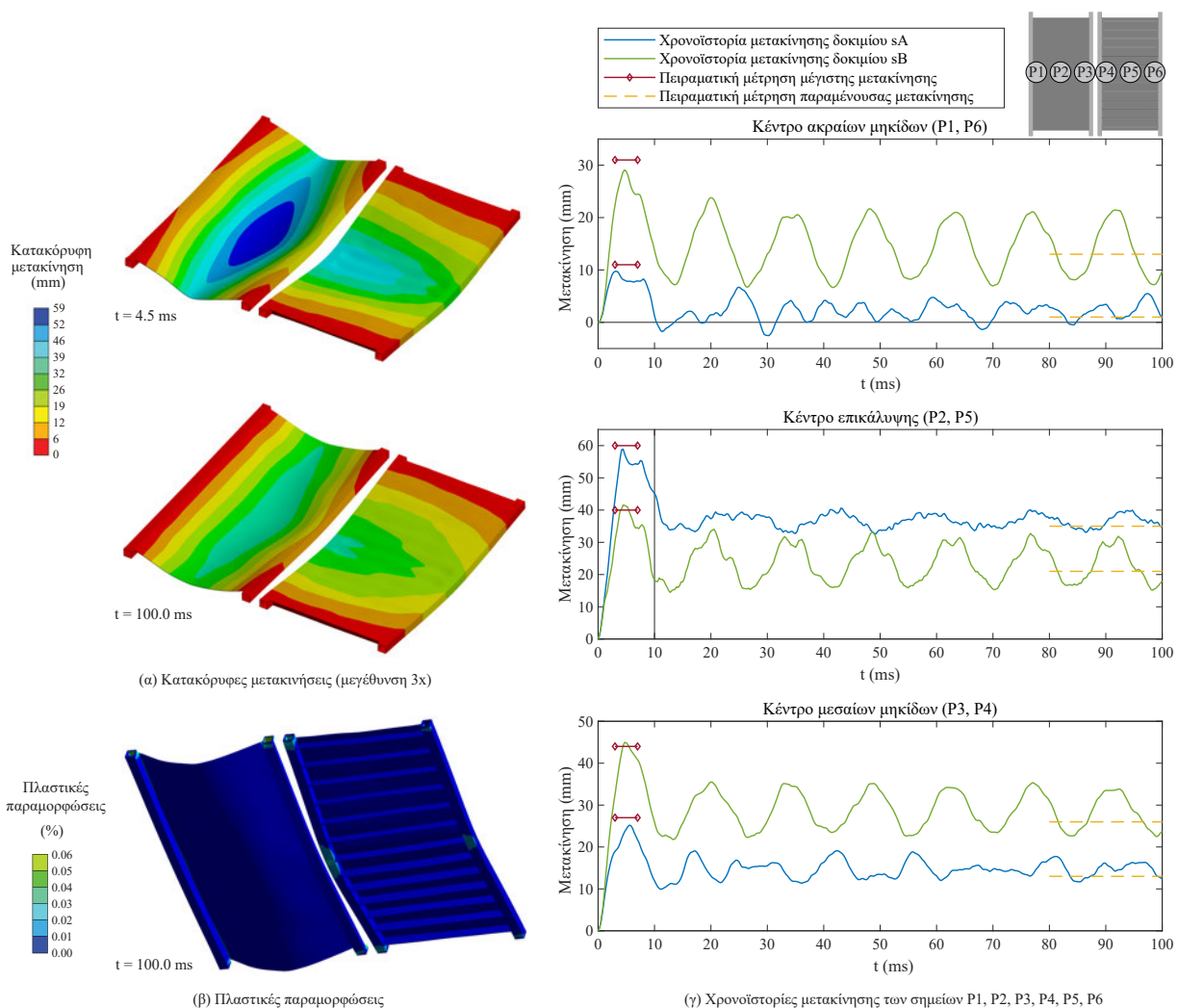


(β)

Σχήμα 18: Πρόκληση έκρηξης: (α) Στιγμιότυπο έκρηξης και (β) Παραμόρφωση μετρητικών διατάξεων

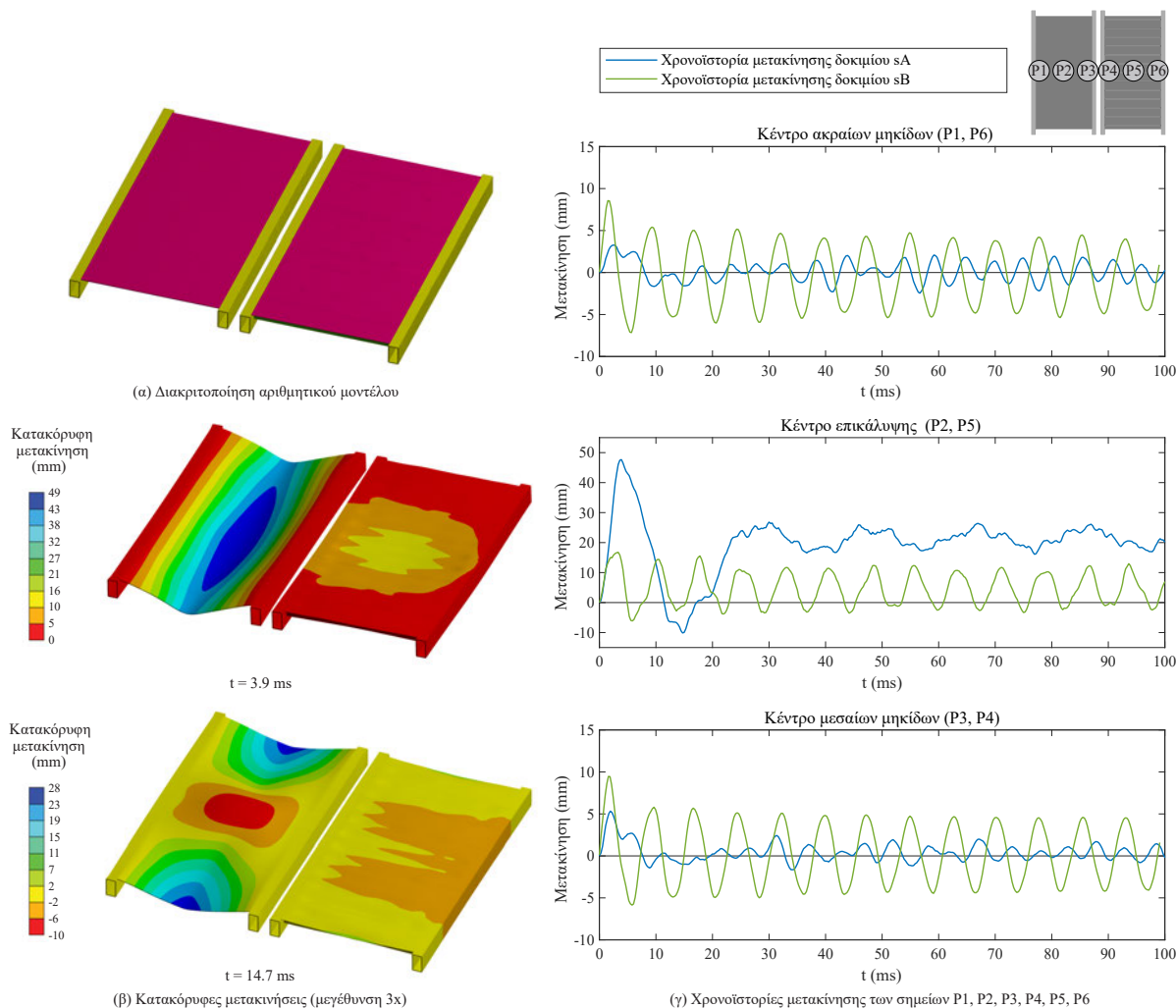
Επιπλέον, στα πλαίσια της διατριβής, πραγματοποιήθηκαν δύο διαφορετικά μοντέλα σε σχέση με την απόκριση του συστήματος επικάλυψης και υποκείμενου φορέα του πειράματος. Πιο συγκεκριμένα, το ένα (Σχήμα 19) αφορά επακριβώς τα στοιχεία που χρησιμοποιήθηκαν στο πείραμα ενώ το άλλο (Σχήμα 20) αφορά τις ίδιες επικαλύψεις με αυτές του πειράματος αλλά μεγαλύτερης διατομής μηκίδες με ελαστική απόκριση. Μέσα από τα αριθμητικά μοντέλα, λοιπόν, τα οποία επιβεβαιώνονται από τις πειραματικές μετρήσεις, επιδιώκεται η τεκμηρίωση του τρόπου προετοιμασίας ενός αριθμητικού μοντέλου σε έκρηξη και η πιστοποίηση κάποιων εκ των συμπερασμάτων των προηγούμενων ενοτήτων.

Όπως φαίνεται στο Σχήμα 19, οι τιμές των πειραματικών μετρήσεων έχουν μικρή απόκλιση σε σύγκριση με τα αποτελέσματα του αριθμητικού μοντέλου. Επιπλέον, η επικάλυψη με συμπαγές έλασμα φέρεται να οδηγεί σε μικρότερες μετακινήσεις στον υποκείμενο φορέα σε σχέση με την επικάλυψη με νευρώσεις. Το αντίστροφο ισχύει για την ίδια την επικάλυψη, αφού εμφανίζονται μεγαλύτερες μετακινήσεις στο συμπαγές έλασμα σε σύγκριση με την επικάλυψη με νευρώσεις.



Σχήμα 19: Πειραματικά αποτελέσματα: (α) Κατακόρυφες μετακινήσεις στο αριθμητικό μοντέλο στα στιγμιότυπα $t = 4.5$ ms (μέγιστη μετακίνηση) και $t = 100.0$ ms (παραμένουσα μετακίνηση), (β) Πλαστικές παραμορφώσεις στο στιγμιότυπο 100.0 ms (παραμένουσα μετακίνηση) και (γ) Χρονοϊστορίες μετακίνησης αριθμητικού μοντέλου στα σημεία P1, P2, P3, P4, P5 και P6, καθώς και σύγκριση με τις πειραματικές μετρήσεις

Αυτό σημαίνει ότι η χαμηλότερης δυσκαμψίας και, άρα, υψηλότερης ιδιοπεριόδου επικάλυψη του συμπαγούς ελάσματος έχει ευνοϊκότερη επιρροή στον υποκείμενο φορέα σε σύγκριση με την υψηλότερης δυσκαμψίας και, άρα, χαμηλότερης ιδιοπεριόδου επικάλυψη με νευρώσεις. Αυτό το συμπέρασμα επιδιώκεται να επιβεβαιωθεί μέσα από τις πιο δύσκαμπτες και ελαστικές μηκίδες που παρουσιάζονται στο Σχήμα 20. Οι μετακινήσεις και σε αυτήν την περίπτωση έχουν κοινό μοτίβο με τις μετακινήσεις στο Σχήμα 19. Κατά συνέπεια, επιβεβαιώνεται πειραματικά πως η χαμηλή δυσκαμψία στην επικάλυψη οδηγεί σε μείωση των συνεπειών στον υποκείμενο φορέα, έχοντας είτε ελαστική είτε ελαστοπλαστική απόκριση.



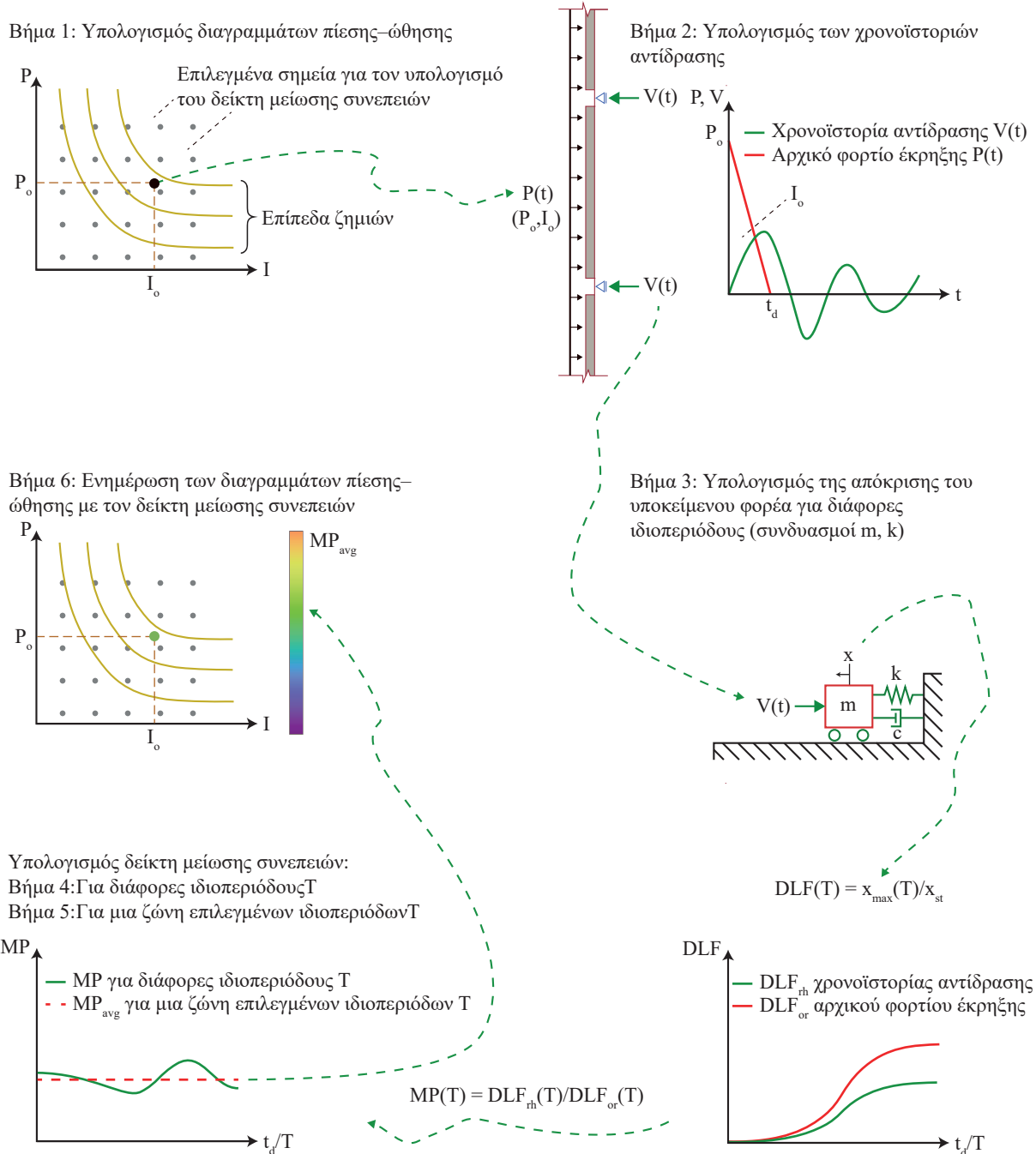
Σχήμα 20: Αποτελέσματα αριθμητικού μοντέλου με ελαστικές μηκίδες: (α) Διακριτοποίηση αριθμητικού μοντέλου, (β) Κατακόρυφες μετακινήσεις αριθμητικού μοντέλου στα στιγμιότυπα $t = 3.9$ ms (μέγιστη μετακίνηση) και $t = 14.7$ ms (αρνητική φάση) και (γ) Χρονοϊστορίες μετακίνησης αριθμητικού μοντέλου στα σημεία P1, P2, P3, P4, P5 και P6

B6. Μεθοδολογία εκτίμησης της ικανότητας της επικάλυψης για μείωση των συνεπειών από έκρηξη

Γενικότερα, υπάρχει πλειάδα τύπων επικάλυψης που δύναται να εφαρμοστούν έναντι έκρηξης. Ωστόσο, δεν υπάρχει κάποια γενικευμένη μέθοδος μέσα από την οποία να μπορεί να γίνει σύγκριση μεταξύ τους και επιλογή του καλύτερου δυνατού, ούτως ώστε να επιτυγχάνεται μείωση των συνεπειών στον

υποκείμενο φορέα. Σε αυτήν την ενότητα αναπτύσσεται μια μεθοδολογία που να επιτρέπει την άμεση σύγκριση μεταξύ των διαφόρων τύπων επικάλυψης, ανεξαρτήτως γεωμετρίας ή υλικού.

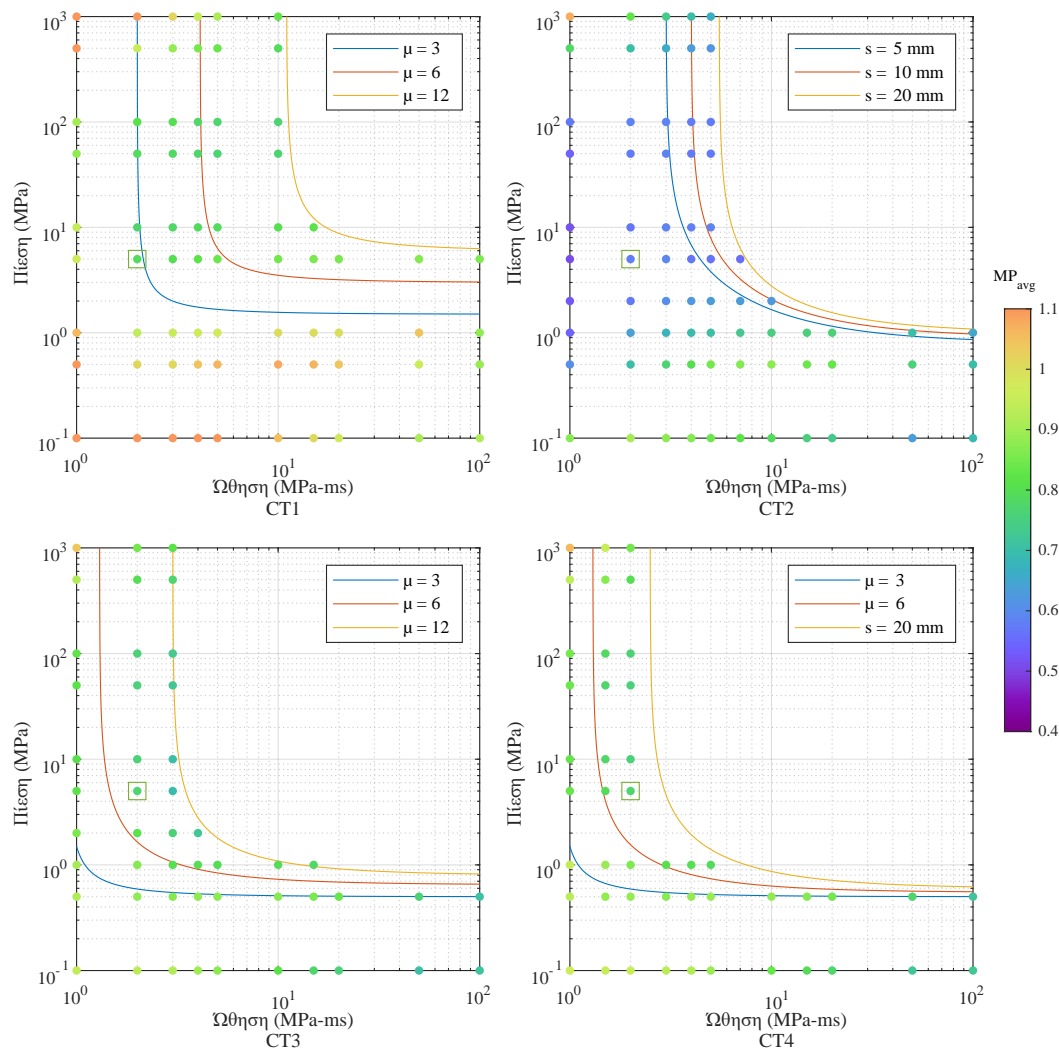
Αυτή η μεθοδολογία εφαρμόζεται μέσα από τα βήματα που περιγράφονται στο Σχήμα 21. Πιο συγκεκριμένα, κατά το βήμα 1 υπολογίζεται το διάγραμμα πίεσης-ώθησης μιας τυχαίας επικάλυψης. Στην πορεία (βήμα 2), για διάφορους επιλεγμένους συνδυασμούς πίεσης-ώθησης υπολογίζονται οι χρονοϊστορίες αντίδρασης της επικάλυψης. Για κάθε συνδυασμό υπολογίζεται η απόκριση αδιάστατου και ελαστικού μονοβάθμιου ταλαντωτή σε διάφορες ιδιοπεριόδους (βήμα 3).



Σχήμα 21: Εφαρμογή της προτεινόμενης μεθοδολογίας για εκτίμηση της δυνατότητας της επικάλυψης για μείωση των συνεπειών στον υποκείμενο φορέα

Ο δείκτης μείωσης συνεπειών προκύπτει μέσα από τον λόγο της απόκρισης του μονοβάθμιου ταλαντωτή στη χρονοϊστορία αντίδρασης προς την απόκρισή του στο αρχικό φορτίο έκρηξης (βήμα 4). Με αυτόν τον τρόπο δίνεται ο δείκτης μείωσης συνεπειών σε κάθε ιδιοπερίοδο του ταλαντωτή. Μέσα από την αριθμητική εκτίμηση του δείκτη σε ένα σύνολο ιδιοπεριοδών, προκύπτει ένας ενιαίος δείκτης συνεπειών για κάθε συνδυασμό πίεσης-ώθησης (βήμα 5), ο οποίος δύναται να ενσωματωθεί στο διάγραμμα πίεσης-ώθησης της επικάλυψης (βήμα 6). Έτσι, μπορεί να γίνει άμεση σύγκριση μεταξύ των διαφόρων τύπων επικάλυψης απευθείας, έχοντας τα διαγράμματα πίεσης-ώθησής τους, τα οποία χρησιμοποιούνται ευρέως στην πράξη.

Ένα τυχαίο παράδειγμα σύγκρισης δίνεται στο Σχήμα 22, όπου παρουσιάζονται τα διαγράμματα πίεσης-ώθησης τεσσάρων διαφορετικών ειδών επικάλυψης, συμπεριλαμβάνοντας τον ενιαίο δείκτη μείωσης συνεπειών. Όπως φαίνεται, η επικάλυψη CT2 έχει την καλύτερη συμπεριφορά, η επικάλυψη CT1 τη χειρότερη, ενώ οι επικαλύψεις CT3 και CT4 έχουν ενδιάμεση συμπεριφορά. Επομένως, αν υπήρχε ως μοναδικό κριτήριο επιλογής η δυνατότητα μείωσης συνεπειών, τότε θα επιλεγόταν η επικάλυψη CT2, αφού οδηγεί στις χαμηλότερες μετακινήσεις σε έναν τυχαία ιδιοπεριόδου υποκείμενο φορέα. Σημειώνεται ότι αν είναι γνωστή η ιδιοπερίοδος του υποκείμενου φορέα, τότε μπορεί να γίνει πιο ακριβής ανά-λυση, χωρίς ανάγκη χρήσης ενιαίου δείκτη μείωσης συνεπειών.



Σχήμα 22: Παράδειγμα διαγράμματος πίεσης-ώθησης για τα τέσσερα είδη επικάλυψης CT1, CT2, CT3 και CT4, συμπεριλαμβάνοντας τον δείκτη μείωσης συνεπειών

B7. Σύνοψη και συμπεράσματα

Αντικείμενο της παρούσας διδακτορικής διατριβής αποτελεί η διερεύνηση των επικαλύψεων όσον αφορά στη δυνατότητά τους για μείωση των συνεπειών στον υποκείμενο φορέα υπό φορτίο έκρηξης. Για την επίτευξη αυτού του στόχου, επιστρατεύονται δύο διαφορετικοί μηχανισμοί: ο μηχανισμός πλαστικής απορρόφησης ενέργειας και ο μηχανισμός αδρανειακής αντίστασης. Ο πρώτος μηχανισμός αφορά την πρόκληση πλαστικών παραμορφώσεων στην επικάλυψη, μέσα από τις οποίες απορροφάται μέρος της ενέργειας της έκρηξης. Ο δεύτερος μηχανισμός αφορά την αργή απόκριση της επικάλυψης στα φορτία της έκρηξης λόγω μεγάλης ιδιοπεριόδου. Και στις δύο περιπτώσεις το αποτέλεσμα είναι κοινό. Πιο συγκεκριμένα, το υψηλό πλάτους και σύντομης διάρκειας φορτίο έκρηξης μετατρέπεται σε χαμηλότερο πλάτους και μεγαλύτερης διάρκειας αντίδραση για τον υποκείμενο φορέα.

Στο πλαίσιο της διατριβής, λοιπόν, αναζητούνται θεωρητικά τα πεδία εφαρμογής των δύο μηχανισμών, καθώς και πώς αυτά επηρεάζονται από τις διάφορες παραμέτρους της επικάλυψης. Οι παράμετροι προς εξέταση είναι η μάζα, η δυσκαμψία, η αντοχή και η ολκιμότητα της επικάλυψης, όπως επίσης και η πιθανή εμφάνιση μεμβρανικής δράσης. Παράλληλα, πραγματοποιείται πειραματική διερεύνηση για την επιβεβαίωση κάποιων εκ των συμπερασμάτων της θεωρητικής ανάλυσης. Τέλος, αναπτύσσεται σειρά βημάτων για την εκτίμηση της δυνατότητας μιας επικάλυψης για μείωση των συνεπειών έκρηξης.

Τα βασικά συμπεράσματα που προκύπτουν από το σύνολο της διατριβής συνοψίζονται ως ακολούθως:

- Αυξημένη μάζα, μειωμένη δυσκαμψία, μειωμένη αντοχή και αυξημένη ολκιμότητα στην επικάλυψη οδηγούν σε ευμενή συμπεριφορά όσον αφορά στις αντιδράσεις στον υποκείμενο φορέα.
- Ο μηχανισμός πλαστικής απορρόφησης ενέργειας ενεργοποιείται σε συγκεκριμένες ζώνες απόκρισης εν αντιθέσει με τον μηχανισμό αδρανειακής αντίστασης, ο οποίος εμφανίζεται σε όλο το φάσμα.
- Η μεμβρανική δράση της επικάλυψης έχει δυσμενή ρόλο για τον υποκείμενο φορέα. Ως εκ τούτου, πρέπει να αποφεύγεται ή να υπάρχει υπό τη μορφή επιπλέον ασφάλειας για την ίδια την επικάλυψη.
- Τα υπολογιστικά μοντέλα που χρησιμοποιήθηκαν για την εξαγωγή των διαφόρων συμπερασμάτων έχουν ρεαλιστικά αποτελέσματα, γεγονός που αποδείχθηκε πειραματικά.
- Μια τυχαίας γεωμετρίας και υλικού επικάλυψη μπορεί να υπολογιστεί με γενικευμένο τρόπο, όσον αφορά στην ικανότητά της για μείωση των συνεπειών έκρηξης, γεγονός που βοηθάει στο να μπορεί να συγκριθεί άμεσα με άλλους τύπους επικάλυψης και να γίνει κατάλληλη επιλογή.

B8. Πρωτότυπη συμβολή και προτάσεις για περαιτέρω έρευνα

Η πρωτότυπη συμβολή της διατριβής στην επιστήμη του μηχανικού και την επαγγελματική πρακτική συνοψίζεται στις εξής εργασίες:

- Δεδομένου ότι υπάρχει μεγάλη ποικιλία τύπων επικάλυψης που μπορούν να εφαρμοστούν (Ioannou, Mantzourani and Gantes, 2020), υπολογίστηκε με ποιοτικά και ποσοτικά διαγράμματα ο τρόπος επιρροής της μάζας, δυσκαμψίας, αντίστασης και ολκιμότητας μιας επικάλυψης στον υποκείμενο φορέα. Τα αποτελέσματα συμβάλλουν στον κατάλληλο σχεδιασμό της επικάλυψης όσον αφορά στη δυνατότητα της για μείωση των συνεπειών (Ioannou et al., 2022a).
- Υπολογίστηκε με ποιοτικά και ποσοτικά διαγράμματα ο τρόπος επιρροής της μεμβρανικής δράσης της επικάλυψης στον υποκείμενο φορέα και εξήχθη το συμπέρασμα ότι η μεμβρανική δράση έχει δυσμενή ρόλο για τον υποκείμενο φορέα (Ioannou and Gantes, 2021).

- Πραγματοποιήθηκε η πειραματική διερεύνηση ενός συστήματος χαλύβδινης επικάλυψης–υποκείμενου φορέα μέσα από το οποίο πιστοποιήθηκαν τα αποτελέσματα των θεωρητικών μοντέλων και αναδείχθηκε το γεγονός ότι τα θεωρητικά αποτελέσματα μπορούν να δώσουν ρεαλιστικά αποτελέσματα (Ioannou et al., 2022c).
- Αναπτύχθηκε μεθοδολογία για τη γενικευμένη εκτίμηση της δυνατότητας μιας τυχαίας επικάλυψης για μείωση των συνεπειών στον υποκείμενο φορέα, γεγονός που επιτρέπει την άμεση σύγκρισή της με άλλους τύπους επικάλυψης για την τελική επιλογή του επικρατέστερου (Ioannou et al., 2022b). Η μεθοδολογία περιλαμβάνει όλους τους πιθανούς συνδυασμούς πίεσης και ώθησης που μπορεί να προκύψουν σε μια επικάλυψη, οι οποίοι είναι στοχαστικής φύσεως.

Για τη μελλοντική επέκταση των ευρημάτων της διατριβής προτείνονται τα εξής:

- Οι περιορισμοί των ταλαντωτών για τις θεωρητικές αναλύσεις των παραμέτρων της επικάλυψης μπορούν να ξεπεραστούν με τη χρήση πιο σύνθετων μοντέλων, σύμφωνα με τα οποία να λαμβάνεται υπόψη κατανεμημένη μάζα και δυσκαμψία, καθώς και ακριβέστερες χρονοϊστορίες αντίδρασης, διαγράμματα δύναμης–μετακίνησης και χρονοϊστορίες πίεσης.
- Συγκριτικές αναλύσεις προτείνονται για την εξέταση διαφόρων τύπων επικάλυψης όσον αφορά στην επιλεγμένη γεωμετρία και το υλικό, όπως σύγκριση δομικού χάλυβα και οπλισμένου σκυροδέματος, κόστος μεταξύ των διαφορετικών τύπων κ.α.
- Επιπλέον στην πειραματική διερεύνηση που έγινε, προτείνεται να εξεταστούν πειραματικά και άλλα συστήματα επικάλυψης–υποκείμενου φορέα για την πιστοποίηση των αποτελεσμάτων των πειραματικών μοντέλων των συγκριτικών αναλύσεων.
- Ο δείκτης μείωσης συνεπειών βασίζεται σε ένα επιλεγμένο εύρος ιδιοπεριόδων. Αυτό το εύρος μπορεί να ερευνηθεί περαιτέρω, ώστε η επιλογή των ιδιοπεριόδων να είναι ακριβέστερη σε σχέση με τα κτίρια που στην πράξη υπόκεινται σε έκρηξη.
- Οι χρονοϊστορίες αντίδρασης που χρησιμοποιούνται για τον υπολογισμό του δείκτη μείωσης συνεπειών υπόκεινται σε κατάλληλη επεξεργασία, ούτως ώστε να ανταποκρίνονται όσο γίνεται καλύτερα στα πειραματικά αποτελέσματα. Αυτές οι χρονοϊστορίες χρειάζονται επιπλέον διερεύνηση για την εφαρμογή τους στο μοντέλο του μονοβάθμιου ταλαντωτή.
- Τα φορτία εκρήξεων που ενδέχεται να εφαρμοστούν επί μιας επικάλυψης χαρακτηρίζονται από μεγάλη ποικιλία συνδυασμών πίεσης και ώθησης. Κατά συνέπεια, κρίνεται σημαντική η πιθανολογική εκτίμηση αυτών των φορτίων. Αυτή η εργασία είναι σε εξέλιξη (Ioannou et al., 2022d).

B9. Βιβλιογραφία

- Alberdi, R., Przywara, J. and Khandelwal, K. (2013) 'Performance evaluation of sandwich panel systems for blast mitigation', *Engineering Structures*, 56, pp. 2119–2130. doi: <https://doi.org/10.1016/j.engstruct.2013.08.021>.
- Bornstein, H. and Ackland, K. (2013) 'Evaluation of energy absorbing materials under blast loading', in *WIT Transactions on Engineering Sciences*, pp. 125–136. doi: 10.2495/MC130111.
- Chen, W. and Hao, H. (2012) 'Numerical study of a new multi-arch double-layered blast-resistance door panel', *International Journal of Impact Engineering*, 43, pp. 16–28. doi: 10.1016/j.ijimpeng.2011.11.010.
- Chen, W. S. and Hao, H. (2013) 'Preliminary study of sandwich panel with rotational friction hinge device against blast loadings', in *Advances in Engineering Plasticity XI*. Trans Tech Publications Ltd (Key Engineering Materials), pp. 530–533. doi: 10.4028/www.scientific.net/KEM.535-536.530.
- Cormie, D., Mays, G. and Smith, P. (2009) *Blast effects on buildings*. ICE Publishing. doi:

10.1680/beob.61477.

- Dusenberry, D. O. (2010) Handbook for blast resistant design of buildings. John Wiley & Sons. doi: 10.1002/9780470549070.
- Federal Emergency Management Agency (1996) 'FEMA 277: The Oklahoma city bombing: Improving building performance through multi-hazard mitigation'.
- Goel, M. D., Matsagar, V. A. and Gupta, A. K. (2011) 'Dynamic response of stiffened plates under air blast', *International Journal of Protective Structures*, 2(1), pp. 139–156. doi: 10.1260/2041-4196.2.1.139.
- Gouverneur, D., Caspeepele, R. and Taerwe, L. (2013) 'Experimental investigation of the load–displacement behaviour under catenary action in a restrained reinforced concrete slab strip', *Engineering Structures*, 49, pp. 1007–1016. doi: <https://doi.org/10.1016/j.engstruct.2012.12.045>.
- Grant, R. (1998) 'Khobar Towers', *Air Force Magazine*, pp. 41–77.
- Guruprasad, S. and Mukherjee, A. (2000) 'Layered sacrificial claddings under blast loading Part I — Analytical studies', *International Journal of Impact Engineering*, 24(9), pp. 957–973. doi: [https://doi.org/10.1016/S0734-743X\(00\)00004-X](https://doi.org/10.1016/S0734-743X(00)00004-X).
- Hetherington, J. and Smith, P. (1994) Blast and ballistic loading of structures. New York: Taylor & Francis.
- Hoffmeister, B. et al. (2015) 'Advanced design methods for blast loaded steel structures', European Commission Directorate-General for Research and Innovation.
- Institute for Economics and Peace (2015) 'Global Terrorism Index 2015, measuring the impact of terrorism'.
- Ioannou, O., and Gantes, C. J. (2021). "Membrane action of cladding subjected to blast loading and effects on the supporting structure." *Vibration*, 4(4), 768–786. doi: 10.3390/vibration4040043.
- Ioannou, O., Hadjioannou, M., and Gantes, C. J. (2022a). "A 2DOF method to study the influence of cladding characteristics on the response of the supporting structure under blast loading." *Journal of Structural Engineering*. doi: 10.1061/(ASCE)ST.1943-541X.0003494.
- Ioannou, O., Hadjioannou, M., and Gantes, C. J. (2022b). "Evaluation of the potential of cladding to mitigate blast effects on the supporting structure." *Practice Periodical on Structural Design and Construction*, 27(3). doi: 10.1061/(ASCE)SC.1943-5576.0000701.
- Ioannou, O., Hadjioannou, M., Gantes, C. J., and Lignos, X. A. (2022c). "Experimental investigation of a cladding to girt system subjected to blast loading." Submitted in peer-reviewed scientific journal.
- Ioannou, O., Mantzourani, A. P., and Gantes, C. J. (2020). "Energy absorption of steel cladding subjected to blast loading." 10th Greek National Steel Structures Conference (to be presented), Athens, Greece.
- Ioannou, O., Rigoutsos, G., Vamvatsikos, D., and Gantes, C. J. (2022d). "A baseline approach for probabilistic blast risk analysis of building façades under far-field explosions." In preparation for submission in peer-reviewed scientific journal.
- Khalifa, Y. A., Tait, M. J. and El-Dakhakhni, W. W. (2017) 'Out-of-plane behavior of lightweight metallic sandwich panels', *Journal of Performance of Constructed Facilities*, 31(5), p. 4017056. doi: 10.1061/(ASCE)CF.1943-5509.0001018.

- Oswald, C. (2018) 'Blast testing of energy absorbing connectors for blast resistant design', *WIT Transactions on the Built Environment*, 180, pp. 57–67. doi: 10.2495/SUSI180061.
- Palanivelu, S. et al. (2011) 'Close-range blast loading on empty recyclable metal beverage cans for use in sacrificial cladding structure', *Engineering Structures*, 33(6), pp. 1966–1987. doi: <https://doi.org/10.1016/j.engstruct.2011.02.034>.
- Rutner, M. P. and Wright, J. P. (2016) 'Duality of energy absorption and inertial effects: Optimized structural design for blast loading', *International Journal of Protective Structures*, 7(1), pp. 18–44. doi: 10.1177/2041419615622726.
- Sivaraman, S. and Varadharajan, S. (2021) 'Investigative consequence analysis: A case study research of beirut explosion accident', *Journal of Loss Prevention in the Process Industries*, 69, p. 104387. doi: <https://doi.org/10.1016/j.jlp.2020.104387>.
- Sun, G. et al. (2019) 'Dynamic response of sandwich panel with hierarchical honeycomb cores subject to blast loading', *Thin-Walled Structures*. doi: 10.1016/j.tws.2019.04.029.
- Xue, Z. and Hutchinson, J. W. (2004) 'A comparative study of impulse-resistant metal sandwich plates', *International Journal of Impact Engineering*, 30(10), pp. 1283–1305. doi: 10.1016/j.ijimpeng.2003.08.007.
- Yang, W. Y. (2009) *Signals and systems with MATLAB*, Signals and Systems with MATLAB. doi: 10.1007/978-3-540-92954-3.
- Yu, G. et al. (2022) 'Holistic case study on the explosion of ammonium nitrate in Tianjin port', *Sustainability*. doi: 10.3390/su14063429.
- Zobec, M. et al. (2015) 'Innovative design tool for the optimization of blast-enhanced facade systems', *Journal of Facade Design and Engineering*, 2(3–4), pp. 183–200. doi: 10.3233/fde-150019.

